

Electronic Thesis and Dissertation Repository

8-21-2013 12:00 AM

Development of Advanced Nanomaterials for Potential Lithium-Ion Battery Application

Jian Liu, *The University of Western Ontario*

Supervisor: Xueliang Sun, *The University of Western Ontario*

A thesis submitted in partial fulfillment of the requirements for the Doctor of Philosophy degree in Mechanical and Materials Engineering

© Jian Liu 2013

Follow this and additional works at: <https://ir.lib.uwo.ca/etd>



Part of the [Nanoscience and Nanotechnology Commons](#)

Recommended Citation

Liu, Jian, "Development of Advanced Nanomaterials for Potential Lithium-Ion Battery Application" (2013). *Electronic Thesis and Dissertation Repository*. 1443.
<https://ir.lib.uwo.ca/etd/1443>

This Dissertation/Thesis is brought to you for free and open access by Scholarship@Western. It has been accepted for inclusion in Electronic Thesis and Dissertation Repository by an authorized administrator of Scholarship@Western. For more information, please contact wlsadmin@uwo.ca.

**DEVELOPMENT OF ADVANCED NANOMATERIALS FOR POTENTIAL LITHIUM-
ION BATTERY APPLICATIONS**

(Thesis format: Integrated Article)

by

Jian Liu

Graduate Program in Mechanical and Materials Engineering

A thesis submitted in partial fulfillment
of the requirements for the degree of
Doctor of Philosophy

The School of Graduate and Postdoctoral Studies
The University of Western Ontario
London, Ontario, Canada

© Jian Liu 2013

Abstract

Lithium-ion batteries (LIBs) are promising energy storage media under serious consideration for practical applications in electric vehicle (EVs) and hybrid electric vehicles (HEVs). However, to meet the requirements for EVs and HEVs, the performance of commercially available LIBs needs to be greatly improved in terms of the energy density, cycling life, rate capability, safety and cost. It is well known that the LIB performance is highly dependent on the choice of electrode materials. Therefore, it is greatly important to develop new electrode materials as replacements for graphite/LiCoO₂ used in commercial LIBs, in order to achieve high-performance LIBs desirable for EV and HEV applications.

In this thesis, to achieve the above goal, efforts made in this thesis followed into two sections. The first section was to develop novel nanostructured electrode materials, which could be directly used in LIBs. The other section was to develop various surface-modification materials, which could be applied to further improve the LIB performance of electrode materials. Various advanced characterization techniques, including field-emission scanning electron microscope (FE-SEM), energy dispersive X-ray spectroscopy (EDS), transmission electron microscope (TEM), high-resolution TEM (HRTEM), Raman spectroscopy, X-ray diffraction (XRD), X-ray photoelectron spectroscopy (XPS), Fourier transform-infrared spectroscopy (FT-IR), X-ray absorption near edge structure (XANES) spectroscopy, and electrochemical methods, have been applied to analyze the prepared nanomaterials, understand their growth mechanisms, and evaluate their battery performance.

The nanostructured electrode materials included nitrogen-doped carbon nanotubes (NCNTs), phosphorus-nitrogen doped carbon nanotubes (PNCNTs), and lithium titanate (Li₄Ti₅O₁₂). A scalable method, ultrasonic spray pyrolysis, was developed inhouse to produce NCNTs with tunable structure as potential anode materials. Further attempt to incorporate P element into CNTs was made, and it was successful when P and N elements were doped together. The P doping effect on the structure of NCNTs was investigated in detail. Furthermore, novel nanostructured Li₄Ti₅O₁₂ were prepared by a microwave-assisted hydrothermal method in a fast and energy-efficient way. Their electrochemical performance was evaluated, and nanoflower-like Li₄Ti₅O₁₂ showed better LIB performance than nanoparticle Li₄Ti₅O₁₂.

Three different surface-modification materials, ZrO_2 , AlPO_4 and LiTaO_3 solid-state electrolyte, were developed by atomic layer deposition (ALD), for potential use to improve the chosen electrode materials. Deposition of these materials on different substrates, including NCNTs, graphene nanosheets, Si (100) and anodic aluminum oxide (AAO) template, showed that as-grown thin films of ZrO_2 , AlPO_4 and LiTaO_3 were precisely controllable in terms of film thickness, film crystallinity and film composition. These characteristics enabled by ALD promised ZrO_2 , AlPO_4 and LiTaO_3 great potential as surface-modification materials. One application example of these materials was demonstrated by using ALD- ZrO_2 coating to enhance the performance of nanoflower-like $\text{Li}_4\text{Ti}_5\text{O}_{12}$.

Keywords

Lithium-ion battery, Nanomaterial, Nanocomposite, Carbon nanotubes, graphene nanosheets, Nitrogen doping, Phosphorus doping, Lithium titanate, Zirconium oxide, Aluminum phosphate, Lithium tantalate, Solid-state electrolyte, Atomic layer deposition, Chemical vapor deposition, Ultrasonic spray pyrolysis, Microwave-assisted hydrothermal synthesis.

Co-Authorship Statement

1.

Title: Nitrogen-doped carbon nanotubes with tunable structure and high yield produced by ultrasonic spray pyrolysis

Authors: Jian Liu, Yong Zhang, Mihnea Ioan Ionescu, Ruying Li, Xueliang Sun

The experimental and theoretical work was carried out by Jian Liu under the supervision of Dr. Xueliang Sun. This manuscript was organized and wrote by Jian Liu under the guidance of Dr. Xueliang Sun. Coauthors contributed to the formation of the final version by means of helping related characterization, providing valuable discussions and polishing the draft. The final version of this manuscript has been published in *Appl. Surf. Sci.* **2011**, 257, 7837-7844.

2.

Title: Synthesis and characterization of phosphorus-nitrogen doped multiwalled carbon nanotubes

Authors: Jian Liu, Hao Liu, Yong Zhang, Ruying Li, Guoxian Liang, Michel Gauthier, Xueliang Sun

The experimental and theoretical work was carried out by Jian Liu under the supervision of Dr. Xueliang Sun. This manuscript was organized and wrote by Jian Liu under the guidance of Dr. Xueliang Sun. Coauthors contributed to the formation of the final version by means of helping related characterization, providing valuable discussions and polishing the draft. The final version of this manuscript has been published in *Carbon* **2011**, 49, 5014-5021.

3.

Title: Microwave-assisted hydrothermal synthesis of nanostructured spinel $\text{Li}_4\text{Ti}_5\text{O}_{12}$ as anode materials for lithium ion batteries

Authors: Jian Liu, Xifei Li, Jinli Yang, Dongsheng Geng, Yongliang Li, Dongniu Wang, Ruying Li, Xueliang Sun, Mei Cai, Mark W. Verbrugge

The experimental and theoretical work was carried out by Jian Liu under the supervision of Dr. Xueliang Sun. This manuscript was organized and wrote by Jian Liu under the guidance of Dr. Xueliang Sun. Coauthors contributed to the formation of the final version by means of helping related characterization, providing valuable discussions and polishing the draft. The final version of this manuscript has been published in *Electrochim. Acta* **2012**, *63*, 100-104.

4.

Title: Crystallinity-controlled synthesis of zirconium oxide thin films on nitrogen-doped carbon nanotubes by atomic layer deposition

Authors: Jian Liu, Xiangbo Meng, Mohammad N. Banis, Mei Cai, Ruying Li, Xueliang Sun

The experimental and theoretical work was carried out by Jian Liu under the supervision of Dr. Xueliang Sun. This manuscript was organized and wrote by Jian Liu under the guidance of Dr. Xueliang Sun. Coauthors contributed to the formation of the final version by means of helping related characterization, providing valuable discussions and polishing the draft. The final version of this manuscript has been published in *J. Phys. Chem. C* **2012**, *116*, 14656-14664.

5.

Title: Controlled synthesis of zirconium oxide on graphene nanosheets by atomic layer deposition and its growth mechanism

Authors: Jian Liu, Xiangbo Meng, Yuhai Hu, Dongsheng Geng, Mohammad N. Banis, Mei Cai, Ruying Li, Xueliang Sun

The experimental and theoretical work was carried out by Jian Liu under the supervision of Dr. Xueliang Sun. This manuscript was organized and wrote by Jian Liu under the guidance of Dr. Xueliang Sun. Coauthors contributed to the formation of the final version by means of helping related characterization, providing valuable discussions and polishing the draft. The final version of this manuscript has been published in *Carbon* **2013**, *52*, 74-82.

6.

Title: Ultrathin atomic layer deposited ZrO_2 coating to enhance the electrochemical performance of $\text{Li}_4\text{Ti}_5\text{O}_{12}$ as an anode material

Authors: Jian Liu, Xifei Li, Mei Cai, Ruying Li, Xueliang Sun

The experimental and theoretical work was carried out by Jian Liu under the supervision of Dr. Xueliang Sun. This manuscript was organized and wrote by Jian Liu under the guidance of Dr. Xueliang Sun. Coauthors contributed to the formation of the final version by means of helping related characterization, providing valuable discussions and polishing the draft. The final version of this manuscript has been published in *Electrochim. Acta* **2013**, 93, 195-201.

7.

Title: Atomic layer deposited aluminum phosphate thin films on N-doped CNTs

Authors: Jian Liu, Yongji Tang, Biwei Xiao, Tsun-Kong Sham, Ruying Li, Xueliang Sun

The experimental and theoretical work was carried out by Jian Liu under the supervision of Dr. Xueliang Sun. This manuscript was organized and wrote by Jian Liu under the guidance of Dr. Xueliang Sun. Coauthors contributed to the formation of the final version by means of helping related characterization, providing valuable discussions and polishing the draft. The final version of this manuscript has been published in *RSC Adv.* **2013**, 3, 4492-4495.

8.

Title: Atomic layer deposition of lithium tantalate solid-state electrolytes

Authors: Jian Liu, Mohammad N. Banis, Xifei Li, Andrew Lushington, Mei Cai, Ruying Li, Tsun-Kong Sham, Xueliang Sun

The experimental and theoretical work was carried out by Jian Liu under the supervision of Dr. Xueliang Sun. This manuscript was organized and wrote by Jian Liu under the guidance of Dr. Xueliang Sun. Coauthors contributed to the formation of the final version by means of helping related characterization, providing valuable discussions and polishing the draft. The final version of this manuscript is to be submitted.

Dedication

I dedicate this thesis to my family

my wife, Shuo Zhang, and my son, Cameron Ninghui Liu.

I love you both dearly.

Acknowledgments

The work included in this thesis was carried out in Dr. Sun's Nanomaterials and Energy Group at the University of Western Ontario (UWO). Herein, it is my tremendous pleasure to express my acknowledgements to every individual who contributed to my research work in various ways during the past four years.

First of all, I would like to express my deepest gratitude to my supervisor, Dr. Xueliang (Andy) Sun, a Professor in Department of Mechanical and Materials Engineering (MME) at UWO and Canada Research Chair in Development of Nanomaterials for Clean Energy, for providing me this greatest opportunity to work in his group and giving me strongest support on my PhD project during the past four years. I got to know Dr. Sun in his course "Nanomaterials and Nanotechnology" taught in the fall of 2009, when I started as a M. Eng. student at UWO. I was greatly impressed by the fantastic research work done in Dr. Sun's group and presented in this course. In the following term, I joined Dr. Sun's group initially for my M. Eng. project. But a few days later, I decided to transfer to a PhD student under the supervision of Dr. Sun, and luckily, was accepted. This was the quickest decision I had ever made, and has proven a right one. During the past four years, Dr. Sun has been always supporting my research work with his insightfulness, passion and patience, and encouraging me to pursue my dreams. He is the best advisor and one of the smartest people I know. He is the reason I decided to pursue a career in research. I hope that I could be as lively, enthusiastic, and energetic as Dr. Sun and to someday be able to command an audience as well as he can.

I will forever be thankful to Mrs. Ruying (Kathy) Li, Dr. Sun's wife and a research engineer in our group, for her kindest help and strongest support not only in my work, but also in my life. Kathy trained me in everything in this group, beginning with carbon nanotube growth on the first day of my time in this group (Jan 4th, 2010) which I remembered clearly, and helped me solve lots of problems in different kinds of experiments. She is the best research engineer I know. Kathy is always ready to give me a hand whenever I need, and she helped me through my darkest days in the past years. I cannot thank Kathy enough for all her help!

I am also grateful to my former supervisor, Dr. Xiping Song, a Professor in State Key Laboratory for Advanced Metals and Materials (SKLAMM) at University of Science and Technology Beijing, China. Dr. Song gave me a hand-by-hand and comprehensive training from experiment designs, experiment carry-out, data analysis, and paper organization in my two and half years in SKLAMM, with his extraordinary patience and selfless efforts. I will never forget the moments Dr. Song helped me revise my papers word by word.

I would like to sincerely thank my advisory committee members, Dr. Liying Jiang and Dr. Jun Yang, professors in MME at UWO, for their valuable advice in every stage of my PhD study. I also would like to deeply appreciate my doctoral thesis examination board members, Dr. Sean Barry, a professor in Department of Chemistry at Carleton University and an expert in ALD, Dr. Hugo de Lasa, a professor in Department of Chemical and Biochemical Engineering at UWO, Dr. Samuel F. Asokanathan and Dr. O. Remus Tutunea-Fatan, professors in MME at UWO, for their careful examinations and important suggestions on this thesis.

I am deeply grateful to all current and former members in Dr. Sun's Nanomaterials and Energy Group at UWO. I am so proud of being part of such a strong research group. Especially, I would like to thank Dr. Hao Liu, Dr. Yong (Bryan) Zhang and Dr. Mihnea I. Ionescu, for their help on carbon nanotube related projects, Dr. Xiangbo (Henry) Meng for his training, help and discussions on ALD, Dr. Xifei Li for his help and discussions on lithium-ion battery project, Dr. Mohammad N. Banis for his help on XRD, sputtering and XANES analysis, Dr. Yongji Tang for his help on XANES analysis, and Dr. Dongsheng Geng for his help on graphene related projects. I also would like to extend my appreciation to my colleagues, Jingli Yang, Yongliang Li and Dongniu Wang, for your help and being side during the four years of my PhD study. It was my great pleasure to work with other former group members, Dr. Yu Zhong, Dr. Shuhui Sun, Dr. Gaixia Zhang, Dr. Jiajun Wang, Dr. Yougui (Alex) Chen, Dr. Liang Li, Dr. Ying Chen, Dr. Kun Chang, Mr. Hamid N. Banis, and current group members, Dr. Niancai Cheng, Dr. Yuhai Hu, Mr. Andrew Lushington, Miss. Xia Li, Mr. Biwei Xiao, Miss. Biqiong Wang, and Mr. Hossein Yadegari.

I am also indebted to Dr. Tsun-Kong Sham in Department of Chemistry at UWO, for his help on XANES testing and analysis, and Dr. Yanhua Cui, a visiting professor from Chinese

Academy of Engineering Physics Mianyang China, for her help on solid-state electrolyte testing.

I would like to express my acknowledgement to all scientists and technicians who helped me on the characterization of my samples. They are Mr. Fred Pearson and Mrs. Karmen Andrei (former and current coordinator, respectively, for HRTEM at the Canadian Centre for Electron Microscopy (CCEM) at McMaster University), Mr. Mark Biesinger (senior scientist in XPS at Surface Science Western at UWO) and Mrs. Ying Zhang (CMLP Common Lab Manager at UWO).

I am grateful to funding supports from Nature Sciences and Engineering Research Council of Canada (NSERC), General Motors (GM) of Canada, Canada Research Chair (CRC) program, Canada Foundation of Innovation (CFI), Ontario Early Researcher Award (ERA), Phostech Lithium Inc., and the University of Western Ontario.

I also thank all my friends (too many to list herein, and I apology for this) for providing support and friendship that I needed during the past four years.

In particularly, I would like to express thank from the bottom of my heart to my parents, brother, and parents-in-law. My parents, Yueming Liu and Sumin Jia, provided me unconditional love and supported me all the time of my life. My elder brother, Wei Liu, was always encouraging me to explore the world, and helping me take care of my parents by being with them. I love them so much, and I would not have made it this far without them. Epecial thank to my parents-in-law, Jishan Zhang and Hua Cui. Mr. Zhang always gave me insightful suggestions on my research career, and Mrs. Cui was always supporting me and my family, and she was the reason I could meet and finally marry my life partner, her daughter, Shuo (Suzy) Zhang.

There are no words to convey how much gratitude I own my wife Suzy and how much I love her. Suzy has been a true and great supporter, and has unconditionally loved me during my good and bad times. She has faith in me and my intellect all the time even when I didn't have faith in myself. The past four years have not been an easy ride, and I truly thank Suzy for sticking my side, even when I was moody and depressed. I married the best person out there for me. Most of all, I cannot thank enough to Suzy for giving birth to our son, Cameron

Ninghui Liu, the best outcome from the past four years. I believe after experiencing all of the four years, we both learned a lot about life and strengthened our commitment and determination to each other to live life to the fullest.

Jian Liu

June 10, 2013

Table of Contents

Abstract	ii
Co-Authorship Statement	iv
Dedication	vii
Acknowledgments	viii
Table of Contents	xii
List of Tables	xvii
List of Figures	xviii
List of Appendices	xxvi
List of Abbreviations	xxvii
Chapter 1 Introduction	1
1 Introduction	1
1.1.1 Fundamentals of LIBs.....	1
1.1.2 LIBs for automotive.....	3
1.2 Challenges in LIBs.....	4
1.3 The solutions with nanomaterials	5
1.3.1 Development of novel nanostructured anode materials.....	6
1.3.2 Development of surface-modification materials.....	13
1.4 Thesis objectives.....	25
1.5 Thesis organization	26
References	29
Chapter 2 Experimental Apparatus and Characterization Techniques	37
2.1 Experimental apparatus.....	37
2.1.1 Ultrasonic spray pyrolysis.....	37
2.1.2 Floating catalyst chemical vapor deposition.....	38

2.1.3 Microwave-assisted hydrothermal method	38
2.1.4 Atomic layer deposition system	39
2.2 Characterization techniques	40
2.2.1 Physical characterizations	40
2.2.1 Electrochemical characterizations	43
References	44
Chapter 3 Nitrogen-Doped Carbon Nanotubes with Tunable Structure and High Yield Produced by Ultrasonic Spray Pyrolysis	45
3.1 Introduction.....	46
3.2 Experimental section.....	48
3.3 Results and discussion	49
3.3.1 Morphological investigation by SEM.....	49
3.3.2 Structural investigation by SEM.....	53
3.3.3 Content and bonding environment of N by XPS	55
3.3.4 Crystallinity of NCNTs by Raman spectra	57
3.4 Conclusions.....	59
Acknowledgements	59
References	60
Chapter 4 Synthesis and Characterization of Phosphorus-Nitrogen Doped Multiwalled Carbon Nanotubes	65
4.1 Introduction.....	66
4.2 Experimental section.....	68
4.3 Results and discussion	69
4.3.1 Structural characterization of PNCNTs	69
4.3.2 Bonding environments of P in PNCNTs.....	73
4.3.3 Crystallinity of PNCNTs.....	75
4.4 Conclusions.....	78

Acknowledgements	79
References	79
Chapter 5 Microwave-Assisted Hydrothermal Synthesis of Nanostructured Spinel Li₄Ti₅O₁₂ as Anode Materials for Lithium-Ion Batteries	83
5.1 Introduction.....	84
5.2 Experimental Section	85
5.2.1 Sample preparation and characterization	85
5.2.2 Electrochemical characterization	86
5.3 Results and Discussion	86
5.4 Conclusions.....	94
Acknowledgements	94
References	94
Chapter 6 Crystallinity-Controlled Synthesis of Zirconium Oxide Thin Films on Nitrogen-Doped Carbon Nanotubes by Atomic Layer Deposition	100
6.1 Introduction.....	101
6.2 Experimental section.....	103
6.2.1 Synthesis of NCNTs	103
6.2.2 ZrO ₂ -NCNTs by ALD.....	103
6.2.3 Characterization of ZrO ₂ -NCNTs	104
6.3 Results and Discussion	104
6.3.1 Crystalline development of ALD-ZrO ₂	106
6.3.2 Growth process of ALD-ZrO ₂	111
6.3.3 Discussion	113
6.4 Conclusions.....	118
Acknowledgements	118
References	118
Supporting Information.....	127

Chapter 7 Controlled Synthesis of Zirconium Oxide on Graphene Nanosheets by Atomic Layer Deposition and Its Growth Mechanism	132
7.1 Introduction.....	133
7.2 Experimental Section	135
7.2.1 Preparation of GNS.....	135
7.2.2 ZrO ₂ -GNS by ALD	135
7.2.3 Characterization of ZrO ₂ -GNS	136
7.3 Results and Discussion	136
7.4 Conclusions.....	145
Acknowledgements	145
References	145
Supporting Information.....	152
Chapter 8 Ultrathin Atomic Layer Deposited ZrO₂ Coating to Enhance the Electrochemical Performance of Li₄Ti₅O₁₂ as an Anode Material	155
8.1 Introduction.....	156
8.2 Experimental Section	158
8.2.1 Material preparation and characterization	158
8.2.2 Electrochemical characterization.....	158
8.3 Results and Discussion	159
8.4 Conclusions.....	169
Acknowledgements	170
References	170
Supporting Information.....	175
Chapter 9 Atomic Layer Deposited Aluminum Phosphate Thin Films on Nitrogen-Doped Carbon Nanotubes	177
9.1 Introduction.....	178
9.2 Experimental Section	179

9.2.1 Material synthesis	179
9.2.1 Material characterization	180
9.3 Results and Discussion	180
9.4 Conclusions.....	184
Acknowledgements	184
References	184
Supporting Information.....	187
Chapter 10 Atomic Layer Deposition of Lithium Tantalate Solid-State Electrolytes	191
10.1 Introduction.....	192
10.2 Experimental Section	195
10.3 Results and Discussion	196
10.4 Conclusions.....	206
Acknowledgements	207
References	207
Supporting Information.....	212
Chapter 11 Conclusions and Perspectives.....	214
11.1 Conclusions.....	214
11.2 Perspectives.....	216
Appendices.....	218
Curriculum Vitae	222

List of Tables

Table 1-1: Summary of ALD coating to improve the LIB performance of the cathode and anode [53-69].	24
Table 3-1: Variation of mean nanotube diameter, nanotube length, growth rate and yield of NCNTs produced from solutions with different imidazole concentrations.	50
Table 3-2: Total N content and contents of different types of N in NCNTs produced from solutions with imidazole concentration of 0 and 200 mg/ml.	56
Table 8-1: Potential differences (V) between anodic and cathodic peaks in the first five cycles.	163
Table 8-2: Values of R_{sei} and R_{ct} obtained by simulated data in Figure 8.8 .	168
Table 10-1: Comparison of lithium tantalate and $Li_2O-Al_2O_3$ solid-state electrolytes.	205

List of Figures

Figure 1.1 Configuration of a lithium-ion battery [4].....	1
Figure 1.2 Comparison of different battery technologies in terms of volumetric and gravimetric energy density [7].	2
Figure 1.3 Total lithium ion transportation battery revenue by region, world markets: 2012-2020 (source: Pike Research) [9].	3
Figure 1.4 Voltage versus capacity for anode- and cathode-electrode materials presently used or under considerations for next-generation LIBs [7].....	5
Figure 1.5 Schematic diagram of a CVD setup in its simplest form [22].....	7
Figure 1.6 Widely-accepted growth mechanisms for CNTs: (a) tip-growth model, (b) base-growth model [21].....	8
Figure 1.7 Schematic diagram of growth model of bamboo-shaped NCNTs [23].....	9
Figure 1.8 Reversible charge/discharge capacity versus cycle numbers of CNTs and NCNTs at a current density of 100 mA g ⁻¹ [29].....	10
Figure 1.9 (a) Li ₄ Ti ₅ O ₁₂ spinel structure type and (b) Li ₇ Ti ₅ O ₁₂ rock salt structure type: blue tetrahedra represent lithium, and green octahedra represent disordered lithium and titanium [34].	12
Figure 1.10 (a) The cycling-life performances for ZrO ₂ -, Al ₂ O ₃ -, TiO ₂ -, B ₂ O ₃ - coated and uncoated (bare) LiCoO ₂ (<i>n</i> : cycle number, <i>x</i> : discharge capacity); (b) Lattice constant <i>c</i> in ZrO ₂ (■), Al ₂ O ₃ (+), TiO ₂ (□), B ₂ O ₃ (Δ) coated and bare LiCoO ₂ (●) as a function of <i>x</i> in Li _{1-x} CoO ₂ during the first charge (<i>c</i> = lattice constant) [31].	13
Figure 1.11 Schematic of three types of surface coating: rough coating, core-shell structure and ultra thin film [44].	15

Figure 1.12 Schematic representation of ALD using self-limiting surface chemistry and an AB binary reaction sequence [46].....	16
Figure 1.13 Schematic of ALD deposition of Al ₂ O ₃ using TMA and water as precursors. ...	17
Figure 1.14 Growth rate per cycle vs pulse time in ALD processL (a) fast and (b) slow chemisorption reactions with no decomposition or etching, (c) chemisorption reactions followed by precursor decomposition, and (d) chemisorption reactions followed by etching reaction [48].	18
Figure 1.15 various growth rate vs temperature in ALD processes. S1: self-limiting growth with temperature-independent rate; S2: self-limiting growth with temperature-dependent rate; L1: self-limiting not reached because of slow reaction; L2: self-limiting growth rate exceeded because of multilayer adsorption or condensation; H1: self-limiting not maintained because of precursor desorption; H2: self-limiting growth rate exceeded because of precursor decomposition [48].	19
Figure 1.16 Schematic diagram of step coverage of different thin film deposition techniques: (a) sol-gel; (b) PVD; (c) CVD; (d) ALD [49].	20
Figure 1.17 Cross-sectional SEM image of an Al ₂ O ₃ ALD film with a thickness of 300 nm on a Si wafer with a trench structure [52].	21
Figure 1.18 (a) High resolution transmission electron microscopy (HRTEM) image of the Al ₂ O ₃ -coated nanosized LiCoO ₂ particles by 6 ALD cycles on the bare powders; (b) cycling performance of the bulk LiCoO ₂ electrode, nanosized LiCoO ₂ electrode without and with 2-cycle Al ₂ O ₃ coating [53].	21
Figure 1.19 Discharge capacity as a function of cycle number of the cells with (a) 0, (b) 10 Al ₂ O ₃ , (c) 50 TiO ₂ ALD cycles performed on the LiCoO ₂ electrode [57].	22
Figure 1.20 Schematic representation of the effects of volume expansion upon (a) bare particles, (b) an ALD coated nano-MoO ₃ particle and (c) a particle from an ALD coated porous electrode [69].	23
Figure 1.21 Thesis structure and interrelationships between chapters.	27

Figure 2.1 Schematic illustration of ultrasonic spray pyrolysis.....	37
Figure 2.2 Schematic illustration of floating catalyst chemical vapor deposition.....	38
Figure 2.3 Microwave-assisted hydrothermal apparatus [1].....	38
Figure 2.4 A picture of Savannah 100 ALD system.....	39
Figure 2.5 A screen snapshot showing the setup of Savannah 100 ALD system and its controlling program.	40
Figure 2.6 A picture of Hitachi S-4800 high-resolution scanning electron microscope.	41
Figure 2.7 A picture of Hitachi H-7000 transmission electron microscope.	41
Figure 2.8 A picture of HORIBA Scientific LabRAM research Raman spectroscopy.	42
Figure 2.9 A picture of VMP3 Potentiostat/Galvanostat/EIS system.....	43
Figure 2.10 A picture of Arbin BT-2000 battery test station.....	43
Figure 3.1 SEM images of NCNTs produced from solutions with different imidazole concentrations: (a) 0 mg/ml; (b) 50 mg/ml; (c) 100 mg/ml; (d) 200 mg/ml. (Solution flow rate 0.25 ml/min; amplitude 45%).	50
Figure 3.2 SEM images of NCNTs produced at different solution flow rates (a) 0.5 ml/min; (b) 0.75 ml/min. (Imidazole concentration: 200 mg/ml; amplitude 45%)......	52
Figure 3.3 Diameter distribution of NCNTs produced at different ultrasonic amplitudes. (Imidazole concentration: 200 mg/ml; solution flow rate: 0.25 ml/min).....	53
Figure 3.4 TEM images of NCNTs produced from solutions with different imidazole concentrations: (a) 0 mg/ml; (b) 50 mg/ml; (c) 100 mg/ml; (d) 200 mg/ml. (Solution flow rate 0.25 ml/min; amplitude 45%).	54
Figure 3.5 XPS N1s spectrum of NCNTs produced from solutions with different imidazole concentrations: (a) 0 mg/ml and (b) 200 mg/ml.	55

Figure 3.6 Raman spectra of NCNTs produced from solutions with different imidazole concentrations: (a) 0 mg/ml; (b) 50 mg/ml; (c) 100 mg/ml; (d) 200 mg/ml. (Solution flow rate 0.25 ml/min; amplitude 45%).	57
Figure 3.7 Integrated intensity ratio of D to G bands (I_D/I_G) and 2D and G band (I_{2D}/I_G) as a function of the imidazole concentration.	58
Figure 4.1 SEM images of NCNTs (a) and PNCNTs synthesized with 10 mg (b), 30 mg (c), and 50 mg (d) of TPP.	69
Figure 4.2 TEM images of NCNTs (a) and PNCNTs synthesized with 10 mg (b), 30 mg (c), and 50 mg (d) of TPP.	70
Figure 4.3 BSE images of NCNTs (a) and PNCNTs synthesized with 30 mg of TPP (b), and corresponding SEM images are inserted on the up-left corner of BSE images. Typical TEM images of one individual nanotube for NCNTs (c) and PNCNTs synthesized with 30 mg of TPP (d).	72
Figure 4.4 XPS survey scan spectra of PNCNTs synthesized with 50 mg of TPP and NCNTs (a), deconvolution of P2p (if applicable), O1s, Fe2p _{3/2} and N1s peaks for PNCNTs synthesized with 50 mg of TPP (b, d, f, h) and NCNTs (c, e, g).	74
Figure 4.5 HRTEM images of NCNTs (a) and PNCNTs prepared with 50 mg of TPP (b).	76
Figure 4.6 Raman spectra of NCNTs and PNCNTs synthesized with 50 mg of TPP.	77
Figure 5.1 XRD patterns of the samples synthesized at 130 °C (a, b) and 170 °C (c, d). (a, c) as-prepared, (b, d) after calcination at 550 °C for 6 h in air.	86
Figure 5.2 SEM (a, c) and TEM (b, d) images of Li ₄ Ti ₅ O ₁₂ synthesized at 130 °C (a, b) and 170 °C (c, d). SAED pattern in the inset of (b) shows reflection rings corresponding to spinel Li ₄ Ti ₅ O ₁₂ . A HRTEM image (e) of Li ₄ Ti ₅ O ₁₂ synthesized at 130 °C shows the image of the image of lattice fringes and $d_{(111)} = 0.48$ nm.	88
Figure 5.3 N ₂ adsorption-desorption isotherms for Li ₄ Ti ₅ O ₁₂ synthesized at 130 °C and 170 °C. Inset shows pore size distribution for both samples.	89

Figure 5.4 CV curves of $\text{Li}_4\text{Ti}_5\text{O}_{12}$ prepared at (a) 130 °C and (b) 170 °C in the first three cycles at a scan rate of 0.2 mV s^{-1}	90
Figure 5.5 Galvanostatic charge/discharge curves for $\text{Li}_4\text{Ti}_5\text{O}_{12}$ prepared at 130 °C and 170 °C between 1 and 2.5 V at a current density of 200 mA g^{-1}	91
Figure 5.6 Cycling performance of $\text{Li}_4\text{Ti}_5\text{O}_{12}$ prepared at 130 °C and 170 °C measured at a current rate of 200 mA g^{-1}	92
Figure 6.1 SEM images (a, b), TEM image (c) and Raman spectrum (d) of NCNTs synthesized by the CVD method.....	105
Figure 6.2 XRD patterns (a) and Raman spectra (b) of 100-cycle ZrO_2 -NCNTs deposited at 250, 200, 150, and 100 °C. (c) Deconvolution of Raman spectrum of 100-cycle ZrO_2 -NCNTs prepared at 250 °C. (d) EDS of 100-cycle ZrO_2 -NCNTs prepared at 100 °C.....	106
Figure 6.3 SEM (a, c, e, g) and TEM (b, d, f, h) images of 100-cycle ZrO_2 -NCNTs prepared at 250 °C (a, b), 200 °C (c, d), 150 °C (e, f), and 100 °C (g, h). (Inset in each TEM image corresponds to its SAED pattern).	108
Figure 6.4 HRTEM images of 100-cycle ZrO_2 -NCNTs prepared at (a) 250 °C, (b) 200 °C, (c) 150 °C and (d) 100 °C, respectively.....	110
Figure 6.5 GPC of ALD- ZrO_2 on NCNTs as a function of deposition temperature (inset shows the thickness of ZrO_2 thin film deposited at 200 °C as a function of ALD cycles)... ..	111
Figure 6.6 SEM images (a-e) of NCNTs without ZrO_2 coating (a) and with ZrO_2 coated at 200 °C after (b) 5 cycles; (c) 10 cycles; (d) 30 cycles and (e) 50 cycles. HRTEM images (f-i) of NCNTs with ZrO_2 coated at 200 °C after (f) 5 cycles; (g) 10 cycles; (h) 30 cycles and (i) 50 cycles (The scale bar in (a-e) and (f-i) represents 20 nm and 5 nm respectively).	111
Figure 6.7 Schematic diagram for growth mechanism of ALD- ZrO_2 on NCNTs at (a) 100 °C, (b) 150-200 °C and (c) 250 °C.	117
Figure 7.1 SEM image (a), TEM image (b) and FTIR spectrum (c) of the pristine GNS.	136

Figure 7.2 SEM images of 100-cycle ZrO ₂ -GNS nanocomposites prepared at (a) 150 °C, (b) 200 °C and (c) 250 °C. (d) XRD patterns of 100-cycle ZrO ₂ -GNS nanocomposites prepared at 150 °C, 200 °C and 250 °C.....	137
Figure 7.3 SEM images of ZrO ₂ -GNS nanocomposite prepared at 150 °C (a, b, c), 200 °C (d, e, f) and 250 °C (h, i, g) with 10 cycles (a, d, h), 30 cycles (b, e, i) and 50 cycles (c, f, g)..	139
Figure 7.4 TEM (a, c, e) and HRTEM (b, d, f) images of ZrO ₂ -GNS nanocomposite prepared at 150 °C (a, b), 200 °C (c, d) and 250 °C (e, f) with 10 cycles.	140
Figure 7.5 (A) Schematic diagram of one ALD cycle using Zr(NMe ₂) ₄ and H ₂ O as precursors [42]; (B) Schematic diagram of ZrO ₂ -GNS nanocomposites prepared at 150, 200 and 250 °C.	144
Figure 8.1 Schematic diagram of LTO and LTO coated with ZrO ₂ by ALD.....	159
Figure 8.2 SEM images of (a) LTO-0, (b) LTO-1, (c) LTO-2, (d) LTO-5, (e) LTO-10 and (f) LTO-50 (The scale bars in the insets of Figure 8.2a, e represent 30 nm).....	160
Figure 8.3 EDS mapping of LTO-10.	161
Figure 8.4 HRTEM image of LTO-10 (inset shows the EDS result).	161
Figure 8.5 CV curves of LTO-0, LTO-1, LTO-2, LTO-5, LTO-10 and LTO-50 during the (a) first, (b) second and (c) third cycle at a scanning rate of 0.1 mV s ⁻¹ between 0.1-2.5 V (insets show the enlarged parts below 1 V).....	162
Figure 8.6 Charge/discharge profiles of LTO-0, LTO-1, LTO-2, LTO-5, LTO-10 and LTO-50 in the 1 st and 2 nd cycles between 0.1-2.5 V at a current density of 200 mA g ⁻¹	164
Figure 8.7 (a) Cycling stability, (b) coulombic efficiency (c) rate capability and (d) discharge capacity vs. current density of LTO-0, LTO-1, LTO-2, LTO-5, LTO-10 and LTO-50 between 0.1-2.5 V (insets in Figure 8.7a and Figure 8.7c show the discharge capacity in the first cycle).....	165

Figure 8.8 Nyquist plots of LTO-0, LTO-2, LTO-5, LTO-10 and LTO 50 (solid symbols and solid lines represent experimental and simulated data respectively, and the equivalent circuit is shown in the inset).....	167
Figure 9.1 Illustration of ALD process for aluminum phosphate.	179
Figure 9.2 (a) SEM image of NCNTs; (b) SEM image, (c) TEM image, (d) HRTEM image, (e) STEM-EDS line-scanning and (f) XPS spectrum of NCNTs coated with 100-cycle $\text{Al}_x\text{P}_y\text{O}_z$ thin film deposited using sequence of $1 \times (\text{TMA} - \text{H}_2\text{O}) - 20 \times (\text{TMP} - \text{O}_3)$	181
Figure 9.3 (a) Film thickness of $\text{Al}_{1.3}\text{PO}_{5.0}$ as a function of ALD cycle number and (b) P/Al atomic ratio in $\text{Al}_x\text{P}_y\text{O}_z$ thin films deposited using $1 \times (\text{TMA} - \text{H}_2\text{O}) - n \times (\text{TMP} - \text{O}_3)$ ($n = 5, 10$ and 20).	182
Figure 9.4 XANES Al $L_{3,2}$ -edge (a) and P $L_{3,2}$ -edge (b) spectra of $\text{Al}_{1.3}\text{PO}_{5.0}$ in this work, and standard AlPO_4 , Al_2O_3 and P_2O_5	183
Figure 10.1 Growth per cycle of the lithium tantalate thin film as a function of (a) $\text{Ta}(\text{OEt})_5$ pulse time and (b) LiO^tBu pulse time using a pulsing sequence of $400 \times (1 \times \text{Li}_2\text{O} + 1 \times \text{Ta}_2\text{O}_5)$. The lines serve as guides to the eye.	196
Figure 10.2 SEM morphology of lithium tantalate thin film deposited using a pulsing sequence of $(1 \times \text{Li}_2\text{O} + 6 \times \text{Ta}_2\text{O}_5)$: (a, b) top view of 400-cycle thin film, and (c) cross-section views of the thin films deposited with different ALD cycles.	197
Figure 10.3 (a) Thickness of the lithium tantalate thin films as a function of ALD cycles and (b) the growth per cycle of the lithium tantalate thin films as a function of Ta_2O_5 subcycle number, using pulsing sequences of $1 \times \text{Li}_2\text{O} + n \times \text{Ta}_2\text{O}_5$ ($n = 1, 6$ and 10).	198
Figure 10.4 Ta L_3 -edge XANES spectra of lithium tantalate thin films deposited using pulsing sequences of $1 \times \text{Li}_2\text{O} + n \times \text{Ta}_2\text{O}_5$ where (a) $n = 1$, (b) $n = 6$, (c) $n = 10$; (d) reference crystalline LiTaO_3 , and (e) pure Ta.	201
Figure 10.5 (a) XPS survey of the lithium tantalate thin films deposited using pulsing sequences of $1 \times \text{Li}_2\text{O} + n \times \text{Ta}_2\text{O}_5$ ($n = 1, 6$ and 10); (b) Li/Ta ratio in the thin films as a function of Ta_2O_5 subcycle number (n); and (c) deconvolution of Ta 4f spectra. In (c), the	

components A and A' correspond to the Ta 4f_{5/2} lines, and the components B and B' correspond to the Ta 4f_{7/2} lines. 202

Figure 10.6 (a) Impedance plots of the Li_{5.1}TaO_z thin film measured at different temperatures (inset shows the equivalent circuit for fitting); (b) Arrhenius plot of the ionic conductivity of the Li_{5.1}TaO_z thin film..... 204

Figure 10.7 Backscattered electron (BSE) images of 100-cycle Li_{5.1}TaO_z thin film deposited in AAO template: (a, b) top-view and (c, d) cross-section view. 206

List of Appendices

Appendix A: Permission from American Chemical Society (ACS) for Published Article ..	218
Appendix B: Permission from Royal Society of Chemistry (RSC) for Published Article...	220
Appendix C: Permission from Elsevier for Published Article.....	221

List of Abbreviations

AAO: anodic aluminum oxide

ALD: atomic layer deposition

BSE: backscattered electron

CNTs: carbon nanotubes

CV: cyclic voltammetry

CVD: chemical vapor deposition

EDS: energy-dispersive X-ray spectroscopy

EIS: electrochemical impedance spectroscopy

EVs: electric vehicles

FCCVD: floating catalyst chemical vapor deposition

FWHM: full width at half maximum

GNS: graphene nanosheets

GPC: growth per cycle

HRTEM: high-resolution transmission electron microscope

LIBs: lithium-ion batteries

LTO: lithium titanate, $\text{Li}_4\text{Ti}_5\text{O}_{12}$

MH: microwave-assisted hydrothermal

PVD: physical vapor deposition

PNCNTs: phosphorus-nitrogen doped carbon nanotubes

NCNTs: nitrogen-doped carbon nanotubes

RBM: radial breathing mode

SAED: selected area electron diffraction

SEI: solid electrolyte interphase

SEM: scanning electron microscope

SWNTs: single-wall carbon nanotubes

STEM: scanning transmission electron microscopy

TEM: transmission electron microscope

TMA: trimethylaluminum

TMP: trimethylphosphite

TPP: triphenylphosphine

PHEVs: plug-in hybrid electric vehicles

PVDF: polyvinylidene fluoride binder

XANES: X-ray absorption edge structure

XPS: X-ray photoelectron spectroscopy

XRD: X-ray diffraction

Chapter 1 Introduction

1.1 Introduction to lithium-ion batteries (LIBs)

With the rapid depletion of fossil fuels, there is great demand to seek renewable and clean energy candidates, in order to enable sustainable development of human society. During the past few decades, various clean energies (such as solar, wind and hydro) have been explored as energy alternatives [1]. However, those clean energy resources are highly time or region-dependent. Therefore, it is essential to develop effective energy storage media in order to make use of those clean energies in an efficient way [2]. Lithium-ion batteries (LIBs) are one of the most competitive candidates for energy storage [3].

1.1.1 Fundamentals of LIBs

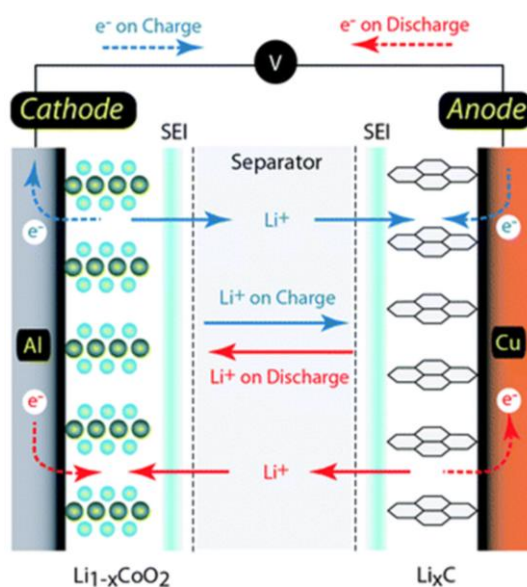


Figure 1.1 Configuration of a lithium-ion battery [4].

LIBs are electrochemical energy storage devices that can realize energy storage/release by means of charge/discharge LIB cells. LIBs are composed of three main components, the anode, cathode and electrolyte, as schematically shown in Figure 1.1. When the LIB cell is being charged, lithium ions are extracted from the cathode, transported through the

electrolyte, and inserted into the anode. During discharge process of the LIB cell, lithium ions are extracted from the anode, while diffusing through the lithium-ion conducting electrolyte, and inserted into the cathode [4-6]. LIBs are also referred to as rocking-chair batteries, as lithium ions rock back and forth between the anode and cathode electrodes when the LIB cell is charged and discharged [6].

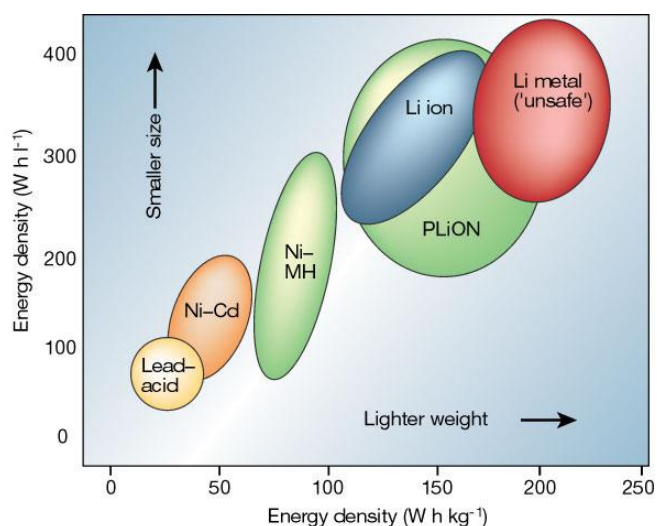
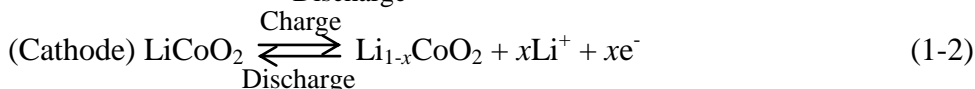
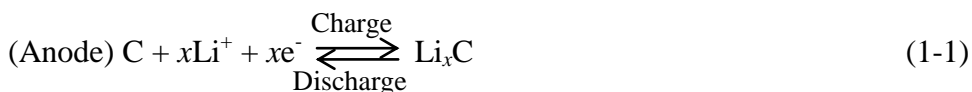


Figure 1.2 Comparison of different battery technologies in terms of volumetric and gravimetric energy density [7].

The first commercial LIBs appeared in 1991. They utilized graphite as the anode material, and lithium cobalt oxide (LiCoO_2) as the cathode material. The electrolyte typically used was 1M LiPF_6 salt in a solvent of ethylene-carbonate (EC) and dimethyl-carbonate (DMC) mixed in 1:1 volume ratio. The electrochemical reactions happened in the commercial LIBs can be expressed as follows:



The use of graphite as the anode eliminated the poor lithium metal rechargeability, and greatly increased the safety aspect of LIBs due to avoided formation of lithium dendrites, while LiCoO_2 offered good electrical performance and safety [6]. This type of LIBs still takes the majority of the current battery market, as they can deliver the highest specific

energy density among the available battery technologies, as presented in [Figure 1.2](#) [7]. Thus, LIBs have been widely applied in an increasingly diverse range of applications, including portable devices, cell phones, laptop computers and digital cameras, as well as military electronics, such as radios and mine detectors [6].

1.1.2 LIBs for automotive

During the past few years, there is growing awareness of the necessity to develop electric vehicles (EVs), a term including plug-in hybrids, extended range electric vehicles and all-electric vehicles [8], in order to reduce fossil fuel dependence and improve environmental stewardship. Interest in EVs has surged in auto industries, and manufacturers have started to develop new generations of EVs. For example, in 2010, General Motors introduced Chevrolet Volt electric vehicle into market, which can travel up to 40 miles using its LIB pack. In late 2010, Nissan introduced the Leaf, a 100-mile range EVs that are powered by an advanced LIB as its only power source. Besides auto companies, governments also initiate policies to simulate the development of EVs. Especially in 2011, US President Obama set a goal of putting one million EVs on the road by 2015 [8]. Incentives are also announced to support advance of EVs, including rebate up \$7500 for purchasing EVs, enhanced R&D investments for innovative technologies, and rewarding communities for investing EV infrastructure through competitive grants [8].

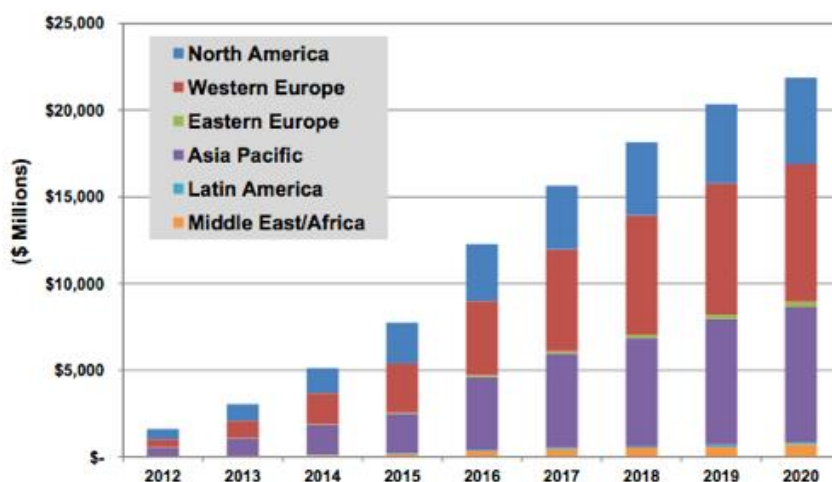


Figure 1.3 Total lithium ion transportation battery revenue by region, world markets: 2012-2020 (source: Pike Research) [9].

At the beginning of EV history, auto companies General Motors, Toyota and Honda used lead-acid batteries, later updated to nickel-metal hydride (Ni-MH), to power the electric cars [8]. In recent years, LIBs are recognized as the most promising power supply system for EV application, as they can deliver the highest energy density among available battery technologies [7]. In both Chevrolet Volt and Nissan Leaf launched in 2010, LIBs were used as the power supply system [8, 9]. As EVs are becoming the trend, the demand for LIBs has been growing explosively. As shown in [Figure 1.3](#), the worldwide LIB market for transportation is worth about \$3 billion in 2013, and the projected market value would reach over \$20 billion in 2020, according to Pike Research [9]. Therefore, it is visible that LIBs will play a more important role in the near future than ever for EVs.

1.2 Challenges in LIBs

Although being commercially available, there still exist big challenges in LIBs in order to use them as a sole energy source to power EVs, without compromising car performance, such as driving distances, speed, and safety. The limitation of current LIBs is mainly their low energy density. The energy density of LIBs is determined by their output voltage (V) and specific capacity (mAh g^{-1}), which are highly dependent on the choice of electrode materials [10, 11]. Present commercial LIBs utilize graphite anode and LiCoO_2 cathode, which have only theoretical capacities of 372 and 155 mAh g^{-1} , respectively [6]. In order to increase the energy density of LIBs, it is inevitable to develop new electrode materials with high theoretical specific capacities and appropriate working voltages. [Figure 1.4](#) summarizes a variety of anode and cathode materials presently used or considered for the next generation of rechargeable LIBs, and their working voltages and specific capacities [7]. For instance, Si anode has a theoretical capacity 4200 mAh g^{-1} , over 10 times higher than graphite anode, whereas both anodes operate at the similar voltage. Therefore, it is a general agreement that developing new electrode materials is an effective pathway to increase the energy density of LIBs dramatically.

Besides high energy density, desirable LIBs for EVs should also possess other properties, such as long cycling life, high safety, good rate capability and low cost. Especially safety is a major concern for current LIBs. Battery accidents accompanying fires and explosions have been reported in news intermittently [12]. This kind of accident is intolerable in EVs.

Additionally, long cycling life insures that LIBs can serve in EVs for years without replacement with a new battery pack. Good rate capability means LIBs in EVs can be fully charged in a very short time (a few minutes) competitive with filling gasoline. Thus, it is urgent to develop LIBs with the desirable performance mentioned above in order to realize real electrification of commercial vehicles.

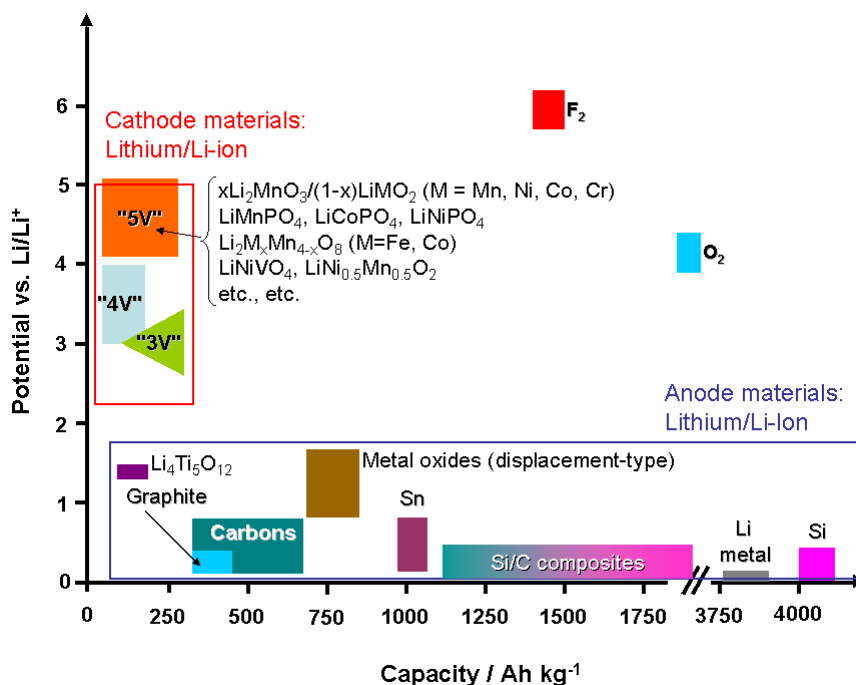


Figure 1.4 Voltage versus capacity for anode- and cathode-electrode materials presently used or under considerations for next-generation LIBs [7].

1.3 The solutions with nanomaterials

Nanomaterials have attracted great interest because of the unusual mechanical, electrical and optional properties endowed by confining the dimensions of such materials in a range of 1-100 nm [11]. Boosted development in nanomaterials have brought opportunities to a wide range of fields, of course including LIBs. As proposed by Bruce *et al.* [13], the use of nanomaterials in LIBs has many benefits: (1) they enable new electrode reactions to occur; (2) their dimensions at nanoscale increase the extraction/insertion rates of lithium ions, by shortening their transport distance within the particles, and similar enhancement in electron transport; (3) their high surface area permits a high lithium ion flux across the

electrolyte/electrode interface; (4) they possibly change the electrochemical properties of electrode materials; and (5) they can better accommodate volume change in nanoparticles associated with lithium ion intercalation/de-intercalation than their bulk counterparts [13]. Therefore, developing advanced nanomaterials is a main strategy adopted in this thesis in order to obtain high-performance LIBs. Different approaches are introduced as follows.

1.3.1 Development of novel nanostructured anode materials

Use of graphite as the anode material greatly improves the safety and cycleability of LIBs, and helps the commercialization of LIBs in 1991. However, graphite has some limitations as an electrode material for in vehicle LIBs. First of all, its theoretical capacity is too low, only 372 mAh g⁻¹. Secondly, graphite usually has a solid-electrolyte interphase (SEI) on its surface, due to its low working potential (< 0.5 V vs. Li/Li⁺) [14, 15]. SEI is a product of electrolyte decomposition on the surface of electrode materials. The formation of SEI can permanently trap some lithium ions, resulting in capacity loss during the first cycle. It has been realized that SEI could affect the battery performance, including the safety, power capability, morphology of lithium deposits and cycling life [14]. At last, graphite has 12 % volume change during charge/discharge process, which is one of the reasons for the degradation of LIB cells [16]. Therefore, developing alternatives to graphite is one of the priorities for the development of LIBs for EVs. In this thesis, efforts will be devoted to developing carbon nanotubes and lithium titanate, both of which are promising anode materials for LIB applications.

1.3.1.1 Carbon nanotubes (CNTs)

Carbon nanotubes (CNTs) are one-dimensional (1D) carbonaceous nanomaterials with cylinder structure rolled up by graphene sheets [17]. Since Ijima's report in 1991 [17], CNTs have been widely studied and found to possess many outstanding properties, including high mechanical properties, excellent electrical conductivity, and high thermal stability [18-20]. These properties promise CNTs very desirable materials for a variety of applications, such as strength composite additives, nanoscale transistors, fuel cell catalysts, and LIB electrode materials.

1.3.1.1.1 Synthesis and growth mechanisms of CNTs

There are three methods mainly used for CNT synthesis, *i.e.* arc-discharge, laser ablation and chemical vapor deposition (CVD). Arc-discharge uses electric arcs that involve very high temperatures ($\sim 4000\text{ }^{\circ}\text{C}$) to evaporate graphite electrodes [21]. The as-grown CNTs by arc-discharge are well crystallized, but contain lots of impurities, such as amorphous carbon. Laser ablation employs high-power lasers in conjunction with high-temperature furnaces to evaporate high-purity graphite target to synthesize CNTs, which have high quality and low production yield [21]. The drawbacks of arc-discharge and laser ablation restrict their wide applications for producing CNTs with suitable quality and production yield. By contrast, CVD method gets involved in catalyst-assisted thermal decomposition of hydrocarbons, and is the most popular method for producing CNTs, due to its low-cost and scalability for mass production of CNTs [21].

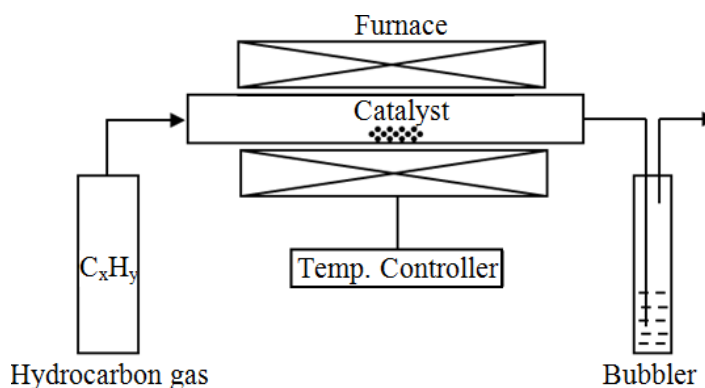


Figure 1.5 Schematic diagram of a CVD setup in its simplest form [22].

Figure 1.5 shows a schematic diagram of the simplest CVD setup [22]. In common, the CVD growth of CNTs needs three important components: hydrocarbon sources, catalysts and temperature. A typical process (see Figure 1.5) is that a hydrocarbon vapor passes through a tubular reactor heated at sufficiently high temperatures ($600\text{-}1200\text{ }^{\circ}\text{C}$), in which a catalyst is placed to decompose the hydrocarbon for the growth of CNTs [22]. The hydrocarbon sources could be gas, liquid and solid chemicals containing carbon. Most often used catalysts are Fe, Co and Ni, which have high solubility and high diffusion rate of carbon in them at high temperatures [22]. Fe, Co and Ni catalysts are commonly introduced into the tubular reactor by using solid organometallobenes, such as ferrocene,

cobaltocene and nickelocene. Depending on different applications, different types of CVD setups have been developed from Figure 1.5, such as Joule-Heating CVD, Floating catalyst CVD, Aerosol assisted CVD and Plasma enhanced CVD [23].

The widely-accepted growth mechanisms of CNTs are illustrated in Figure 1.6 [21]. In general, a hydrocarbon vapor comes in contact with a metal catalyst at high temperatures, and decomposes into carbon and hydrogen species; the carbon dissolves into the catalyst, while the hydrogen species files away; when the catalyst is saturated with the carbon, the dissolved carbon precipitates out and forms a cylindrical shape [21]. Depending on the location of the catalyst in CNTs during the growth, there are two growth models: tip-growth model and base-growth model. Tip-growth model happens in the case of that the interaction between the catalyst and substrate is weak (Figure 1.6a), while base-growth model prevails when the catalyst-substrate interaction is strong (Figure 1.6b) [21].

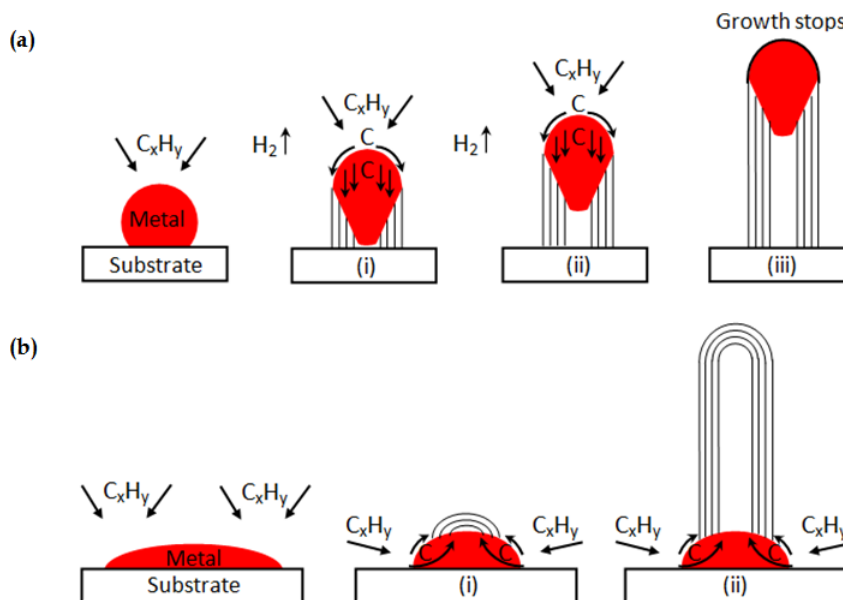


Figure 1.6 Widely-accepted growth mechanisms for CNTs: (a) tip-growth model, (b) base-growth model [21].

1.3.1.1.2 The role of element doping in CNTs

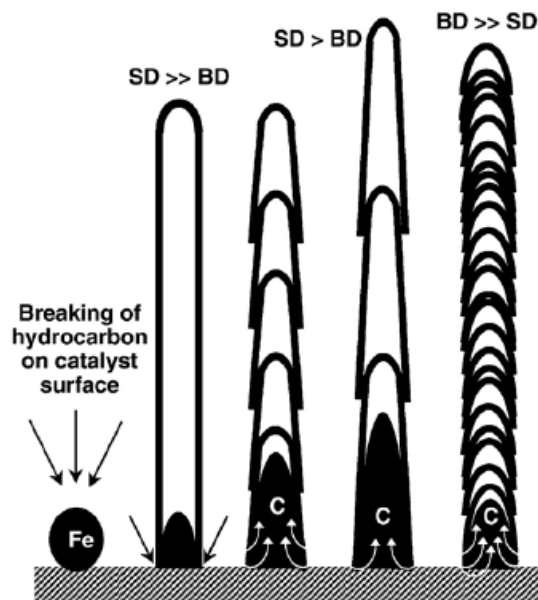


Figure 1.7 Schematic diagram of growth model of bamboo-shaped NCNTs [23].

The properties of CNTs could be improved and controlled by different functionalization methods, among which doping foreign atoms into CNTs represents an effective approach. CNTs can be doped either by electron donors or electron acceptors. Nitrogen (N), as an electron donor, is the most widely investigated doping element in CNTs, due to its close atomic size to carbon [24]. Because N contains one additional electron as compared to C, N doped CNTs exhibited better electronic conductivity than their non-doped counterparts [25]. N doping can introduce defects into CNTs, thereby greatly changing their properties. For example, N doped CNTs (NCNTs) showed less oxidation resistance than CNTs, due to the high reactivity defects along nanotubes [26]. In addition, the incorporation of N into CNTs changed their structure substantially. The NCNTs have bamboo structure, and the nanotubes look like many cups stack together oriented to the same direction [23]. It is common agreement that the growth of CNTs occurs *via* surface diffusion (SD) and/or bulk diffusion (BD) of carbon species through catalyst particles. Without N doping, carbon mainly diffuse through the catalyst surface after dissolved, thereby leading to much faster SD than BD and forming general CNTs, as seen in [Figure 1.7](#) [23]. When nitrogen precursor is used during the growth of CNTs, the dissolution of N into the catalyst

particles improves the BD of carbon species, which is responsible for the formation of compartments. At the same time, the carbon species precipitated on the catalyst surface form the other walls of CNTs. If the N content is very high, BD of carbon is much faster than SD of carbon, resulting in much denser and closer compartments, as seen in [Figure 1.7](#).

The unique structure and highly reactive sites on the surface promise NCNTs a variety of potential applications, such as in fuel cells, field emissions and LIBs. Besides N doping, investigations were also carried out on doping boron (B) and phosphours (P) into CNTs, albeit very less than N doping. Especially, P can provide more additional electron density than N, and thus is expected to change the properties of CNTs greatly. However, it is challenging to obtain P doped CNTs, partially due to its larger atomic radius than C. This thesis will introduce an easy approach to achieve high P content in CNTs.

1.3.1.2 Applications of CNTs in LIBs

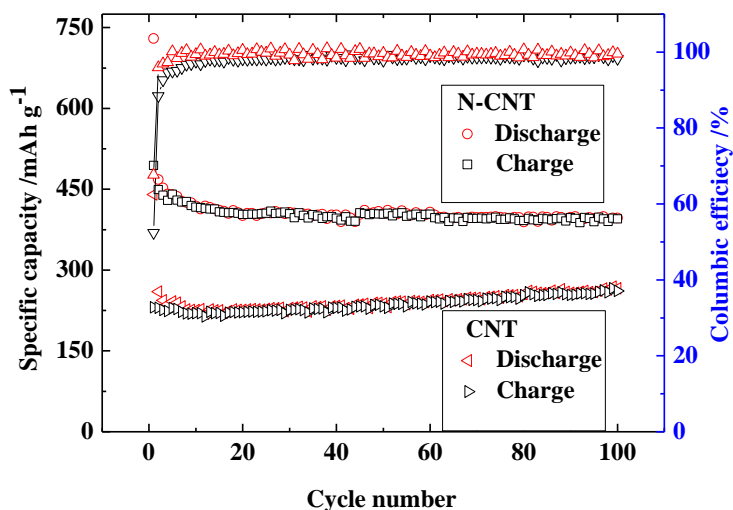


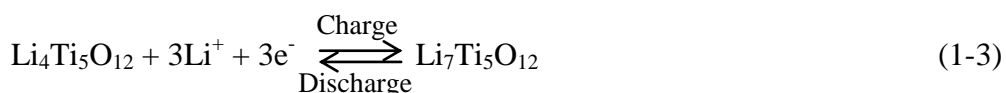
Figure 1.8 Reversible charge/discharge capacity versus cycle numbers of CNTs and NCNTs at a current density of 100 mA g^{-1} [29].

CNTs have been investigated by many researchers as lithium storage materials, and the specific capacities were usually reported to exceed the value of LiC_6 for graphite (372 mAh g^{-1}) [4, 27]. For example, the reversible capacity of single-walled carbon nanotubes (SWCNTs) synthesized by laser ablation was 600 mAh g^{-1} , significantly higher than that

the ideal value of graphite (372 mAh g^{-1}) [28]. The reasons are attributed to that lithium ions can not only be stored into stable sites located in graphitic layers, but also on the surface of nanotubes [27]. In addition, the 1D structure of CNTs can shorten the path lengths for lithium-ion diffusion, meanwhile keeping excellent electron transport along the tubes. Both factors are beneficial for the improvement of LIB performance. Recent studies also revealed that defective sites in CNTs could enable reversible lithium storage in CNTs [4]. For example, the specific capacity of SWCNTs could be increased from 600 to 1000 mAh g^{-1} by ball-milling [28]. Another approach to effectively modify CNTs is doping foreign atoms [24]. Elemental doping could not only introduce defects into CNTs [29], but also improve their electronic conductivity [25]. These factors are beneficial for the LIB performance of CNTs. [Figure 1.8](#) compares the cycling performance of NCNTs and CNTs. It can be seen that NCNTs could maintain a discharge capacity of around 400 mAh g^{-1} , which is 1 time higher than that of CNTs [29]. Therefore, systemic studies will be carried out in this thesis to incorporate different doping elements, such as N and P, into CNTs for potential LIB applications.

1.3.1.2 Lithium titanate ($\text{Li}_4\text{Ti}_5\text{O}_{12}$)

To solve the problems associated with SEI, one way is to employ an anode material with higher working voltage than graphite ($< 0.5 \text{ V vs. Li/Li}^+$) to avoid the decomposition of electrolytes. From this point of view, spinel lithium titanate ($\text{Li}_4\text{Ti}_5\text{O}_{12}$) has gained great research attention. $\text{Li}_4\text{Ti}_5\text{O}_{12}$ can accommodate three lithium ions at a working potential of about $1.55 \text{ V (vs. Li/Li}^+)$, and transform into rock salt structure $\text{Li}_7\text{Ti}_5\text{O}_{12}$ according to the following insertion reaction [30-33]:



The crystal structures of $\text{Li}_4\text{Ti}_5\text{O}_{12}$ and $\text{Li}_7\text{Ti}_5\text{O}_{12}$ are depicted in [Figure 1.9](#) [34]. The high working potential not only avoids the formation of SEI, but improves the battery safety by eliminating the formation of lithium dendrites [32]. Moreover, $\text{Li}_4\text{Ti}_5\text{O}_{12}$ has a negligible volume change of only 0.2 %, when transformed into $\text{Li}_7\text{Ti}_5\text{O}_{12}$, and as a result $\text{Li}_4\text{Ti}_5\text{O}_{12}$ is also known as a “zero strain” material [32, 35]. Combined with the low cost

and environmental friendliness, $\text{Li}_4\text{Ti}_5\text{O}_{12}$ has been becoming one of the most promising anode materials for practical LIBs.

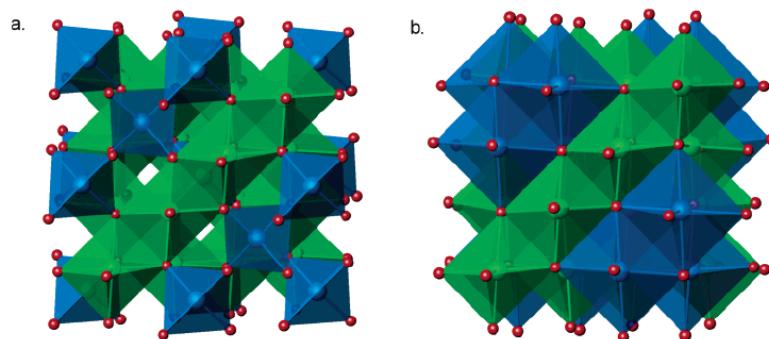


Figure 1.9 (a) $\text{Li}_4\text{Ti}_5\text{O}_{12}$ spinel structure type and (b) $\text{Li}_7\text{Ti}_5\text{O}_{12}$ rock salt structure type: blue tetrahedra represent lithium, and green octahedra represent disordered lithium and titanium [34].

To achieve high rate capability, lithium insertion materials need to have good electronic conductivity and good lithium-ion conductivity. However, $\text{Li}_4\text{Ti}_5\text{O}_{12}$ has an exceptionally low electronic conductivity ($< 10^{-13} \text{ S cm}^{-1}$ [36]), due to the empty Ti 3d state with band energy of about 2 eV [32]. To improve the rate capability of $\text{Li}_4\text{Ti}_5\text{O}_{12}$, it is essential to understand the intercalation process of lithium ions into $\text{Li}_4\text{Ti}_5\text{O}_{12}$, which involves three steps: (1) lithium ions diffuse from the bulk electrolyte solution to the electrode surface; (2) a charge-transfer reaction occurs at the surface of $\text{Li}_4\text{Ti}_5\text{O}_{12}$, accompanied by accepting electrons and lithium ions; and (3) the lithium ions diffuse into the bulk $\text{Li}_4\text{Ti}_5\text{O}_{12}$ [32]. Accordingly, two general strategies are generally adopted to improve the rate capability of $\text{Li}_4\text{Ti}_5\text{O}_{12}$: the first one is to enhance the electronic and lithium-ion conductivities *via* surface modification or ion doping, and the other is to reduce the lithium-ion diffusion distance in the bulk $\text{Li}_4\text{Ti}_5\text{O}_{12}$ by preparing nanosize $\text{Li}_4\text{Ti}_5\text{O}_{12}$ materials [32]. Carbon coating or $\text{Li}_4\text{Ti}_5\text{O}_{12}$ /carbon nanomaterial composites is proven to be effective approaches [32, 33]. Doping with cations and anions (Mg^{2+} , Ni^{3+} , Al^{3+} , Cr^{3+} , Co^{3+} , Fe^{3+} , Mn^{3+} , Ga^{3+} , Zr^{4+} , Mo^{4+} , V^{5+} , Ta^{4+} , Fe^- and Br^-) in Li, Ti or O site has been widely studied to be able to tail the conductivity of $\text{Li}_4\text{Ti}_5\text{O}_{12}$ [32, 33]. $\text{Li}_4\text{Ti}_5\text{O}_{12}$ with various morphologies, such as nanoparticles, hollow structure, nanowires and nanotubes,

have been synthesized [32, 33]. Preparing novel nanostructured $\text{Li}_4\text{Ti}_5\text{O}_{12}$ is the approach adopted in this thesis.

1.3.2 Development of surface-modification materials

1.3.2.1 The role of surface modification in LIBs

Surface modification is an effective approach to improve the LIB performance of electrode materials, such as cycling stability, rate capability and safety. It is achieved by coating the surface of electrode materials with additional materials for the purpose of preventing or alleviating undesirable side reactions between electrode materials and liquid electrolytes. During the past decades, surface modification has been widely used as an easy but effective way to enhance the LIB performance of both the anode and cathode.

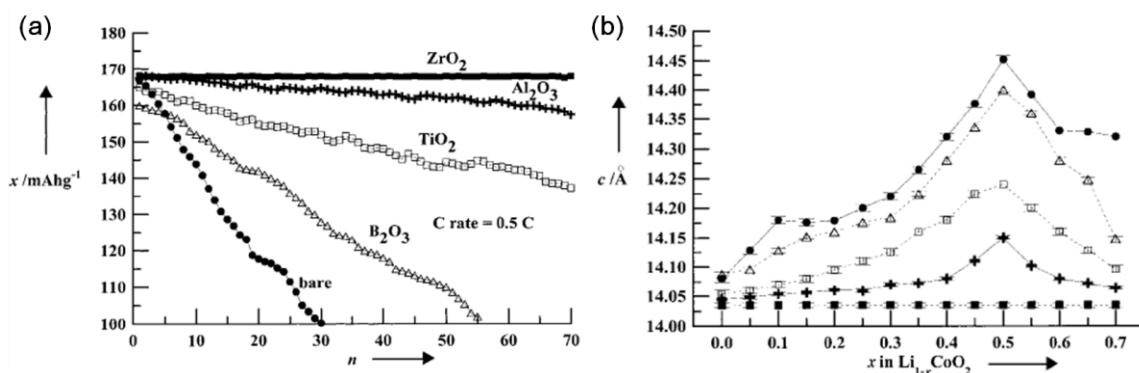


Figure 1.10 (a) The cycling-life performances for ZrO_2 -, Al_2O_3 -, TiO_2 -, B_2O_3 - coated and uncoated (bare) LiCoO_2 (n : cycle number, x : discharge capacity); (b) Lattice constant c in ZrO_2 (■), Al_2O_3 (+), TiO_2 (□), B_2O_3 (Δ) coated and bare LiCoO_2 (●) as a function of x in $\text{Li}_{1-x}\text{CoO}_2$ during the first charge (c = lattice constant) [31].

Surface coating on cathode materials has been proven to be able to prevent their direct contact with the electrolyte solution, suppress the phase transition, improve structural stability, and decrease the disorder of cations in crystal sites, therefore improving their electrochemical performance [37]. For example, the reversible amount of lithium x in $\text{Li}_{1-x}\text{CoO}_2$, the most commercialized cathode material, is general below 0.5, as lithiation of x over 0.5 at potential higher than 4.2~4.3 V (vs. Li/Li^+) leads to rapid deterioration of the stability [38]. The reason is due to the fracture of $\text{Li}_{1-x}\text{CoO}_2$ particles resulted from the

volume change and cation disorder, and the structural degradation of LiCoO_2 related to the dissolution of Co^{4+} into the electrolyte solution when $x > 0.5$ [37]. Extensive studies have shown that the above problems could be addressed by nanoscale coating layers on the LiCoO_2 powders. Different kinds of coating materials, including Al_2O_3 , ZrO_2 , TiO_2 , SnO_2 , ZnO , B_2O_3 , metal phosphates and metal fluorides [37, 39], have been explored for the purpose of surface modification. Figure 1.10a compare the cycling performance of bare LiCoO_2 and LiCoO_2 coated with ZrO_2 , Al_2O_3 , TiO_2 , and B_2O_3 [39]. It is obvious that LiCoO_2 with coating materials exhibited better cycling life than that without coating, and ZrO_2 coating had the best influence on LiCoO_2 performance among the coating materials studied [39]. More interestingly, the cycling improvement of LiCoO_2 could be associated with the suppression of non-uniform strain during delithiation by surface coatings, as indicated by the change in c lattice constant in Figure 1.10b. This strategy is applicable to other cathode materials, such as LiNiO_2 , LiMn_2O_4 and $\text{LiNi}_{1/3}\text{Co}_{1/3}\text{Mn}_{1/3}\text{O}_2$ and so on. For instance, surface coating on LiMn_2O_4 could prevent the dissolution of Mn^{4+} by HF generated from F-containing inorganic electrolyte salt, and then improve its cycling behavior, especially at elevated temperature [37]. In addition, surface coating also served to improve the electric conductivity of LiMn_2O_4 ($10^{-6} \text{ S cm}^{-1}$) for better rate capability of LIBs. $\text{Li}_2\text{O} \cdot 2\text{B}_2\text{O}_3$ glass, MgO , Al_2O_3 , $\text{Li}_{1-x}\text{CoO}_2$ ($x \geq 0$), ZnO , ZrO_2 , composite oxides, conductives and polymers have been applied as coating materials for LiMn_2O_4 [37].

Besides cathode materials, surface modification was also used in their anode counterparts. Graphite was one representative example. It is well known that the performance of graphite fades gradually during long-term cycling, mainly due to graphite exfoliation associated with co-intercalation of the electrolyte into its graphene layers during charging [40]. Moreover, the formation of SEI combined with the graphite exfoliation leads to first-cycle irreversible capacity [14, 15, 40]. Many efforts have been devoted to minimizing the side reactions, and it has been proven as an effective approach to coat graphite particles with an artificial layer. Different coating materials, including AlF_3 , ZrO_2 , Al_2O_3 and AlPO_4 , have been studied and shown to affect the LIB performance of graphite anode positively [40-43]. For example, ZrO_2 film was coated on graphite using a sol-gel method followed by thermal annealing, and the ZrO_2 coated graphite exhibited a capacity higher than the theoretical value and a pronounced stability upon cycling [42]. The reason was

attributed to the protection effect of nanocrystalline-ZrO₂ and in situ formed surface films on graphite from destruction [42]. Similarly, AlPO₄-coated graphite showed more stable cycling performance than non-coated one, due to its much smaller charge-transfer resistance than the latter [41].

1.3.2.2 The opportunity of atomic layer deposition for surface-modification materials

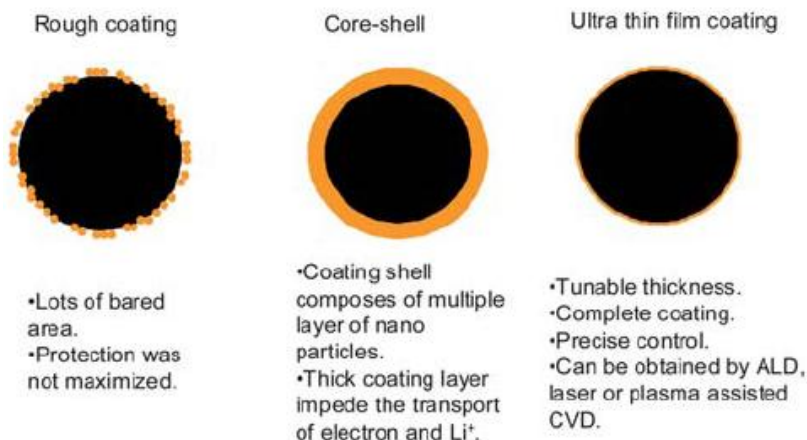


Figure 1.11 Schematic of three types of surface coating: rough coating, core-shell structure and ultra thin film [44].

The surface-modification materials were usually coated on the electrode materials by a wet-chemical method in previous studies [37-43], which lacks control on the quality of the coating layers. Recently, it has been realized that the morphology of coating layers is critical to suppress or alleviate undesired side reactions between the electrode materials and electrolyte solution. To achieve maximized surface-modification effect, the ideal coating layers on the electrode materials should be ultra thin and continuous films, as schematically shown in [Figure 1.11](#)Figure 1.10 [44]. A rough coating would leave some bared electrode materials directly exposed to the electrolyte, while a thick coating layers in core-shell type structure would impede the diffusion of electrons and lithium ions, considering the fact that most of the available coating materials, such as ZrO₂, Al₂O₃, and TiO₂, are non-conductive or poorly conductive of both electrons and lithium ions. By contrast, coating with ultra thin and continuous films could effectively prevent the undesired side reactions by forming dense layers on the electrode surface, and meanwhile

keep the fast transports of electrons and lithium ions through the thin coating layers. From this aspect, atomic layer deposition (ALD) has an exclusive advantage over other film deposition techniques, such as sol-gel method, chemical vapor deposition (CVD), physical vapor deposition (PVD).

1.3.2.2.1 Fundamentals of ALD

ALD can be defined as a film deposition technique that is based on the sequential use of self-limiting gas-solid reactions. The concept of ALD was first realized by Suntola and co-workers from Finland in 1970s [45]. Distinct from other film deposition techniques, such as CVD and PVD, in a ALD process, the chemical source vapors are introduced into the reaction chamber alternatively, one at a time, separated by purging or evacuation periods, as shown in Figure 1.12 [46]. Each precursor exposure step saturates the surface, resulting in the self-limiting film growth by ALD [46].

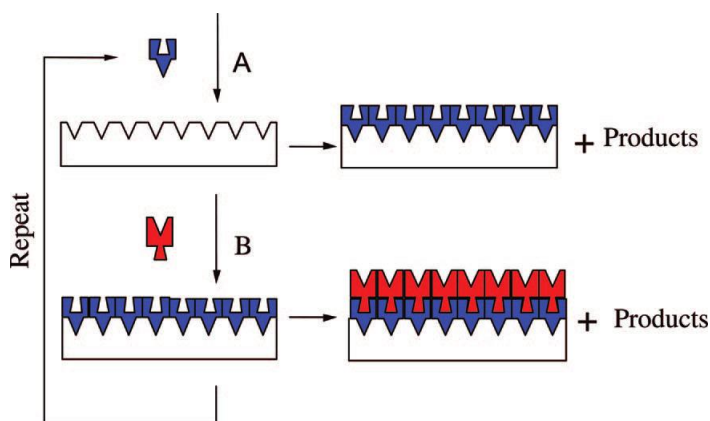
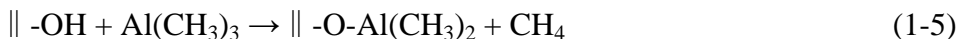


Figure 1.12 Schematic representation of ALD using self-limiting surface chemistry and an AB binary reaction sequence [46].

To demonstrate reaction mechanism of an ALD process, a model system binary Al_2O_3 deposited by ALD from trimethylaluminum (TMA) and water is taken as an example, and the process is illustrated in Figure 1.13. The overall reaction between TMA and water happened in a CVD process is described as follows [46, 47]:



The driving force for this reaction is the formation of a very strong Al-O bond, and this reaction has very high reaction enthalpy [47]. In comparison, ALD of Al_2O_3 proceeds in two half reactions suggested as follows [46, 47]:



where “ \parallel ” represents the substrate surface. The two half reactions are carried out in four steps: (i) chemisorption reaction of the TMA precursor (step 1); (ii) purge or evacuation to completely remove the unreacted TMA precursor and gaseous byproducts (step 2); (iii) chemisorption reaction of the water precursor (step 3); (iv) purge or evacuation to remove the unreacted water precursor and gaseous byproducts (step 4), as seen in [Figure 1.13](#). The four steps achieve one ALD cycle, which can be repeated as many as necessary to realize Al_2O_3 thin film with desirable thickness.

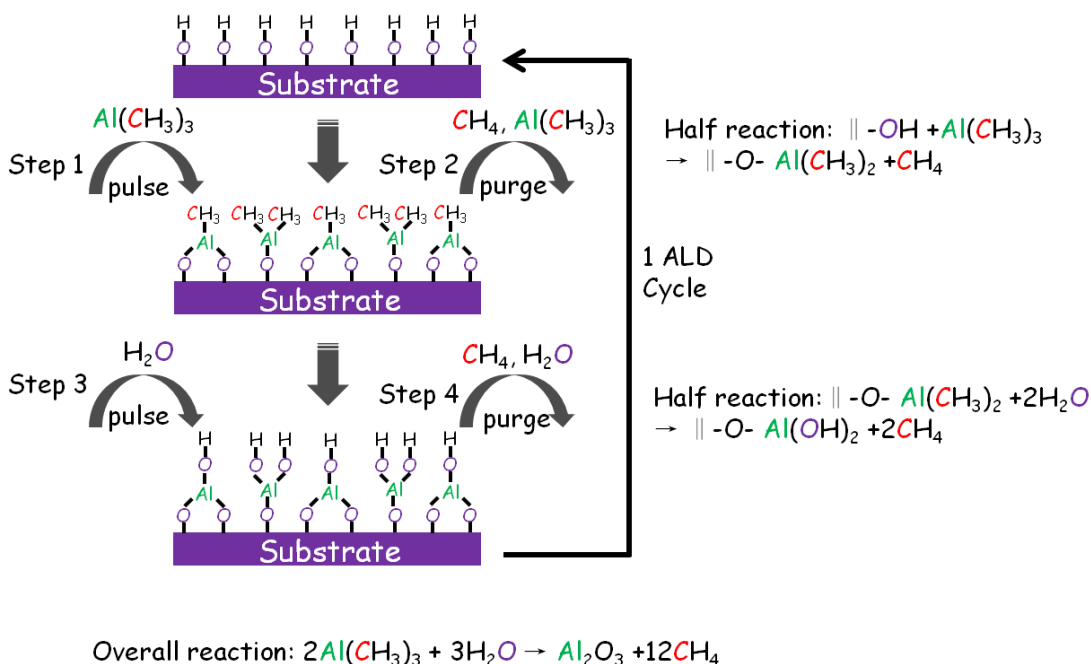


Figure 1.13 Schematic of ALD deposition of Al_2O_3 using TMA and water as precursors.

In an ALD process, there are a few important terms deserved to be emphasized as follows.

(1) **ALD cycles.** As introduced in Al_2O_3 , the film growth by ALD takes place in a cyclic manner. In the simplest binary case, one ALD cycle consists of four steps: (i) exposure of the first precursor; (ii) purge or evacuation of the reaction chamber; (iii) exposure of the second precursor; (iv) purge or evacuation of the reaction chamber [48]. The thickness of the deposited thin films is precisely controlled by repeating different ALD cycles.

(2) **Growth rate per cycle (GPC).** Growth rate of thin films deposited by ALD is usually expressed in terms of thickness increment per cycle, which is nanometer per cycle or angstroms per cycle. After obtaining thin films, its GPC can be determined by dividing the measured film thickness by the number of ALD cycles applied.

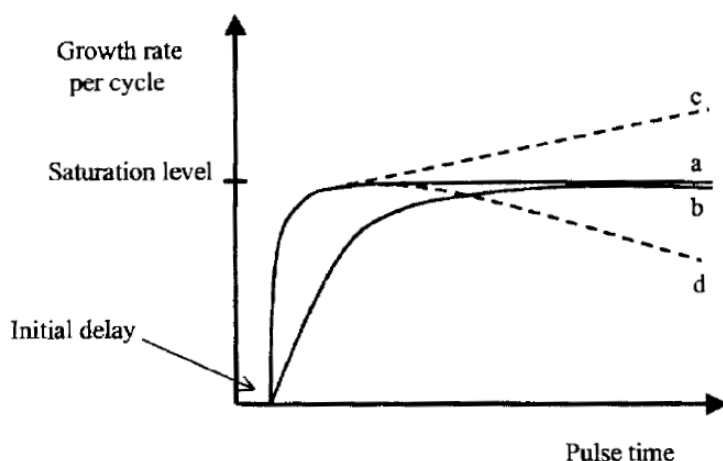


Figure 1.14 Growth rate per cycle vs pulse time in ALD process. (a) fast and (b) slow chemisorption reactions with no decomposition or etching, (c) chemisorption reactions followed by precursor decomposition, and (d) chemisorption reactions followed by etching reaction [48].

(3) **Pulse time.** Pulse time directly represents the amount of precursors introduced into the reaction chamber. In an ideal ALD process (as seen [Figure 1.14a, b](#)), the pulse time should be long enough to realize saturated growth of thin films. In this case, the GPC will remain constant with further increase of pulse time. On the other hand, if pulse time is too short, the supplied precursors are not sufficient to react all of the surface species, thus resulting in the decreased GPC and compromised film uniformity. In real cases, the GPC might increase with more pulse time with no saturation, due to the thermal decomposition

of the precursor (Figure 1.14c), or the GPC might increase and then continuously decrease with increasing pulse time, as a result of film etching from reaction byproducts (Figure 1.14d) [48].

(4) **Purge time.** In one ALD cycle, the second and fourth steps are to purge or evacuate the reaction chamber. The time for purge or evacuation should be sufficient to remove the entire remaining precursor and any byproducts, in order to prevent the appearance of two precursors in the reaction chamber at the same time.

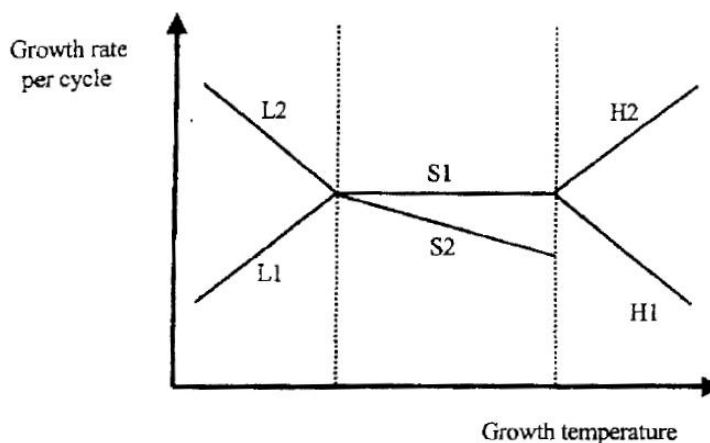


Figure 1.15 various growth rate vs temperature in ALD processes. S1: self-limiting growth with temperature-independent rate; S2: self-limiting growth with temperature-dependent rate; L1: self-limiting not reached because of slow reaction; L2: self-limiting growth rate exceeded because of multilayer adsorption or condensation; H1: self-limiting not maintained because of precursor desorption; H2: self-limiting growth rate exceeded because of precursor decomposition [48].

(5) **ALD window.** ALD window is a temperature range where self-limiting growth of thin films by ALD can be achieved (Figure 1.15). In ALD window, the GPC can be constant regardless of temperature (S1 in Figure 1.15), or can change as a function of temperature (S2 in Figure 1.15). In the latter case, the reason is usually due to the change of surface reactive sites or/and reaction mechanisms with temperature [47, 48]. Out of ALD window, the GPC might increase due to the condensation (L2 in Figure 1.15) or decomposition (H2 in Figure 1.15) of precursors, or the GPC might decrease as a result of the slow

reaction (L1 in Figure 1.15) or precursor desorption from the surface (H1 in Figure 1.15). In any of these cases, the deposition of thin films lacks of controllability and is not a real ALD process any more.

1.3.2.2.2 Benefits of ALD

The unique working mechanism enables ALD many benefits for deposition of thin films. First of all, ALD can achieve the highest step coverage of thin films among available deposition techniques. Figure 1.16 compares the step coverage of different thin film deposition techniques [49]. PVD has very poor step coverage on 3D substrates, mainly due to line-of-sight deposition, and the application of PVD is limited to planar substrates.

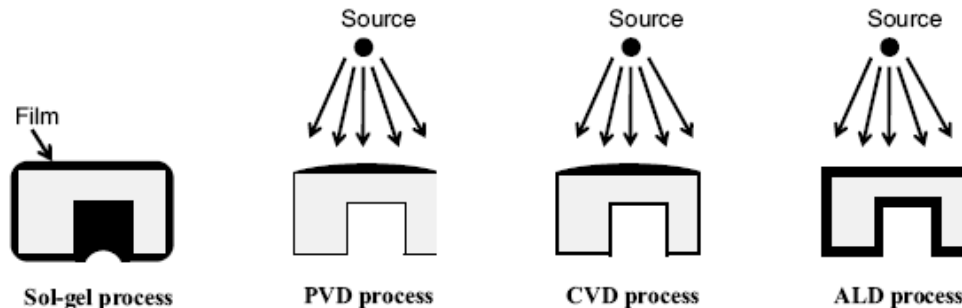


Figure 1.16 Schematic diagram of step coverage of different thin film deposition techniques: (a) sol-gel; (b) PVD; (c) CVD; (d) ALD [49].

The thin films deposited by CVD can somehow cover the surface of 3D substrates. But the film thickness varies along the flow direction, due to the presence of boundary layer and precursor concentration gradient. By contrast, ALD can achieve thin films with good step coverage in 3D substrates, even on high-aspect-ratio structures [50]. Secondly, the thickness of thin films deposited by ALD can be precisely controlled at atomic level, owing to its self-limiting nature. The growth rate of thin films is usually at the order of magnitude of angstroms. For example, the growth rate of ALD- Al_2O_3 using TMA and water as precursors was about $1.3 \text{ \AA}/\text{cycle}$ [51]. Thirdly, the thin films deposited have excellent uniformity and conformality. Figure 1.17 shows a SEM image of uniform Al_2O_3 deposited by ALD on a Si substrate with trend structure [52]. Furthermore, ALD is featured with the low temperature deposition (usually $\leq 400 \text{ }^\circ\text{C}$), even down to room

temperature (RT) in some cases. This characteristic makes ALD suitable for deposition of thin films on sensitive substrates.

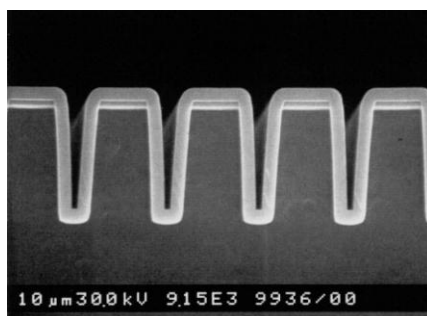


Figure 1.17 Cross-sectional SEM image of an Al_2O_3 ALD film with a thickness of 300 nm on a Si wafer with a trench structure [52].

1.3.2.2.3 Applications of ALD in surface modification for LIBs

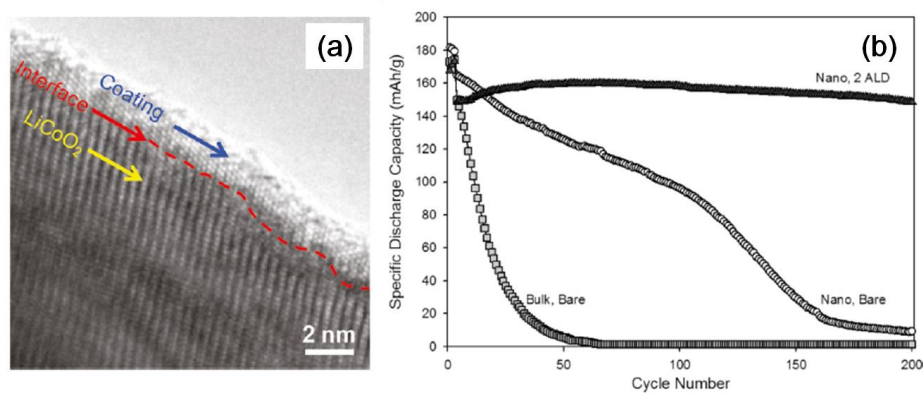


Figure 1.18 (a) High resolution transmission electron microscopy (HRTEM) image of the Al_2O_3 -coated nanosized LiCoO_2 particles by 6 ALD cycles on the bare powders; (b) cycling performance of the bulk LiCoO_2 electrode, nanosized LiCoO_2 electrode without and with 2-cycle Al_2O_3 coating [53].

Given the aforementioned advantages, ALD is an ideal technique to realize ultra thin and continuous films required for surface modification in both the cathode and anode of LIBs. It is not until last three years that the potential of ALD for surface-modification in LIBs was recognized, and up-to-date research in this field is summarized in [Table 1-1](#) [53-69]. Scott *et al.* [53] reported that nanosized LiCoO_2 electrode coated with only 2-cycle Al_2O_3

by ALD had dramatically improved cycling stability and rate capability than bare LiCoO_2 , and it could deliver a discharge capacity of 133 mAh/g at a high current density of 1400 mA/h (7.8 C), as presented in Figure 1.18. It is worth noting that Al_2O_3 deposited with 6 ALD cycles was very uniform and thin, only ~ 1 nm in thickness, as seen in Figure 1.18a. This study showed that to achieve improved LIB performance, it was critical to deposit Al_2O_3 directly on LiCoO_2 electrode, rather than on LiCoO_2 powders. In the latter case, the Al_2O_3 coating would isolate the LiCoO_2 powders, resulting in blocked diffusion pathway for lithium ions and electrons. Later on, researches by other groups confirmed the similar influence of ALD- Al_2O_3 coating on the LIB performance of LiCoO_2 electrode [54, 55, 57]. The work by Cheng *et al.* [57] compared Al_2O_3 (TMA- H_2O) and TiO_2 (TTIP- H_2O) coatings on the LIB performance of LiCoO_2 . They found that a 10-cycle Al_2O_3 coating could eliminate capacity fading effectively, while TiO_2 coating needed 50 cycles in order to achieve similar improvement, as shown in Figure 1.19. Another contribution of this work is that the authors related the LIB performance improvement to the band gap of coating materials. They pointed out that large band gap materials should be considered as ALD coating layers on cathode materials [57].

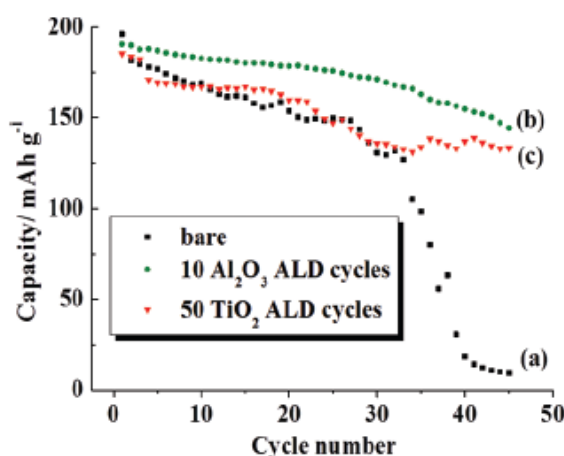


Figure 1.19 Discharge capacity as a function of cycle number of the cells with (a) 0, (b) 10 Al_2O_3 , (c) 50 TiO_2 ALD cycles performed on the LiCoO_2 electrode [57].

Besides in LiCoO_2 , ALD coating strategy has been applied in other cathode systems, including LiMn_2O_4 [56, 61, 62], $\text{LiNi}_{1/3}\text{Mn}_{1/3}\text{Co}_{1/3}\text{O}_2$ type [58-60]. In addition to ALD- Al_2O_3 , ALD- ZrO_2 and ALD- ZnO were also found to be capable of improving the cathode

performance [61, 62]. It was reported that LiMn_2O_4 coated with 2-10 cycle ZrO_2 (ZTB- H_2O) exhibited much higher capacity than the bare LiMn_2O_4 at a testing condition of 55 °C [61]. ZnO deposited from DEZ and water at 120 °C had the similar function as Al_2O_3 and ZrO_2 , in terms of improving LIB performance of LiMn_2O_4 [62]. In all cases, the improvement of cathode performance was more obvious at higher temperatures for cell cycling than at lower ones. Up to now, Al_2O_3 , ZrO_2 , ZnO and TiO_2 by ALD have been explored as coating materials in the cathode system, as summarized in [Table 1-1](#).

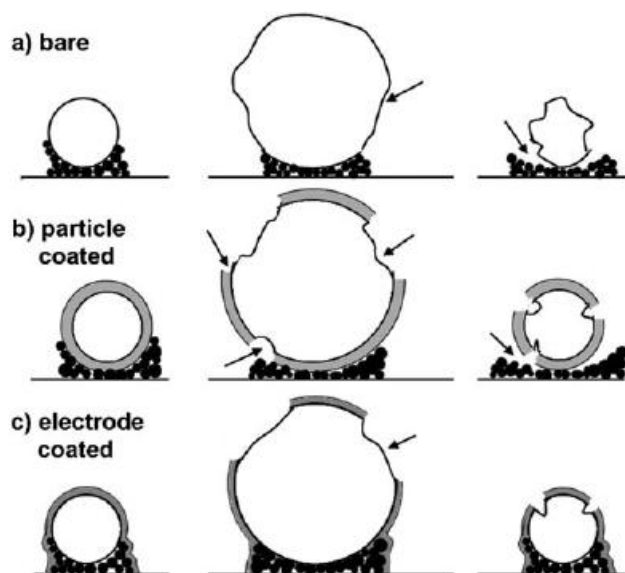


Figure 1.20 Schematic representation of the effects of volume expansion upon (a) bare particles, (b) an ALD coated nano- MoO_3 particle and (c) a particle from an ALD coated porous electrode [69].

ALD coating of metal oxides was also used in the anode materials, including graphite, Si, $\text{Li}_4\text{Ti}_5\text{O}_{12}$, MoO_3 and Fe_3O_4 [54, 63-69]. ALD coating of Al_2O_3 and TiO_2 on commercial graphite could improve its cycling stability, coulombic efficiency and thermal stability, especially at elevated temperatures (50-55 °C) [53, 63]. It was explained that the metal oxide coatings by ALD could act as artificial layers to prevent the decomposition of the electrolytes [63]. In these studies, it was revealed that the metal oxides were better coated on graphite electrode than on graphite powders, for the same reason in the cathode. For Si and MoO_3 anode materials, ALD coating of metal oxides still could enhance their cycling performance, but attributed to a different working mechanism [63, 65, 69]. [Figure 1.20](#)

Table 1-1 Summary of ALD coating to improve the LIB performance of the cathode and anode [53-69].

ALD coating material	Precursors	Temperature	Electrode materials	Ref.
Cathode				
Al ₂ O ₃	TMA, H ₂ O	180 °C	LiCoO ₂	53-55
Al ₂ O ₃	TMA, H ₂ O	120 °C	LiMn ₂ O ₄	56
Al ₂ O ₃	TMA, H ₂ O	120 °C	LiCoO ₂	57
TiO ₂	TTIP, H ₂ O	120 °C	LiCoO ₂	57
Al ₂ O ₃	TMA, H ₂ O	180 °C	LiNi _{1/3} Mn _{1/3} Co _{1/3} O ₂	58
Al ₂ O ₃	TMA, H ₂ O	80 °C	Li _{1.2} Ni _{0.15} Mn _{0.55} Co _{0.1} O ₂	59
Al ₂ O ₃	TMA, H ₂ O	180 °C	Li _{1.2} [Li _{0.20} Mn _{0.54} Ni _{0.13} Co _{0.13}]O ₂	60
ZrO ₂	ZTB, H ₂ O	120 °C	LiMn ₂ O ₄	61
ZnO	DEZ, H ₂ O	120 °C	LiMn ₂ O ₄	62
Anode				
Al ₂ O ₃	TMA, H ₂ O	180 °C	Graphite	54
Al ₂ O ₃	TMA, H ₂ O	< 150 °C	Graphite	63
TiO ₂	TiI ₄ , H ₂ O	< 150 °C	Graphite	63
Al ₂ O ₃	TMA, H ₂ O	250 °C	Si	54
Al ₂ O ₃	TMA, H ₂ O	180 °C	Si	65
Al ₂ O ₃	TMA, H ₂ O	180 °C	Li ₄ Ti ₅ O ₁₂	66
TiN	TiCl ₄ , NH ₃	500 °C	Li ₄ Ti ₅ O ₁₂	67
Al ₂ O ₃	TMA, H ₂ O	180 °C	Fe ₃ O ₄ /mesocellular carbon foam	68
Al ₂ O ₃	TMA, H ₂ O	180 °C	MoO ₃	69

Note: TTIP represents titanium isopropoxide (Ti(OCH(CH₃)₂)₄); ZTB is zirconium tert-butoxide (Zr(OC(CH₃)₃)₄); DEZ stands for diethylzinc Zn(CH₂CH₃)₂.

illustrates the evolution of a MoO₃ nanoparticle during one cycling [69]. Since MoO₃ is an electrical insulator, the carbon additive (the black small circles in Figure 1.20) and MoO₃ (the white circle in Figure 1.20) interface is critical to the overall conductivity and electrical resistance of the electrode. As shown in Figure 1.20a, the large volume change in bare MoO₃ nanoparticles during charge/discharge process leads to the pulverization of the active particles and loss of physical connection with carbon additives, which are responsible for the rapid degradation of the LIB performance. Direct coating of ALD-Al₂O₃ layer on the electrode can maintain the electrical contact of MoO₃ nanoparticles and carbon additives, thereby delaying the fading of the LIB performance, as shown in Figure 1.20c. In comparison, ALD-Al₂O₃ coating can result in worse LIB performance of

MoO₃ nanoparticles, because of the physical insulation of MoO₃ from carbon additives. Besides widely used Al₂O₃, TiO₂, and TiN prepared by ALD have been investigated in the anode [63, 67]

From above discussion, we can clearly see that ALD technique is advantageous for modifying electrode materials with ultra thin and uniform coating layers, thanks to its unique self-limiting nature. Even though some progresses have been made so far, ALD deserves to be explored further for surface modification purpose in LIBs. For instance, current research in this area was mainly focused on ALD-Al₂O₃ from TMA and water, the most successful ALD system. Many good coating materials with potentials in LIBs [29], such as AlPO₄, ZrO₂, should be developed by ALD, and then applied for surface-modification applications. Furthermore, more efforts should be devoted to understanding the underlying mechanism for performance improvement by ALD coating.

1.4 Thesis objectives

LIBs are promising on-board power supply systems for EVs and HEVs, which can reduce humankind's reliance on fossil fuels and solve related environmental problems. However, current LIBs composed of graphite/LiCoO₂ are too limited in their overall performance, especially the low energy and power density, and cannot meet the requirements in EVs and HEVs. As LIB performance is highly dependent on the choice of electrode materials (the anode and cathode), development of new electrode materials with high theoretical specific capacities becomes a key step to obtain suitable LIBs for EVs and HEVs, which should exhibit higher energy density, better rate capability and higher safety performance. Due to their unique properties, nanomaterials and nanotechnology, are expected to play a critical role in reaching the above goal, and brings EVs and HEVs into commercialization. In this content, the author will be devoted to developing a variety of advanced nanomaterials for high-performance LIBs.

Part I: To synthesize novel anode nanomaterials

(1) To develop scalable method to produce nitrogen-doped carbon nanotubes as potential anode materials and components for hybrid nanocomposites. A relation between different

experimental parameters and the quality of nitrogen-doped carbon nanotubes will be established.

(2) To explore a feasible way to incorporate phosphorus element into carbon nanotubes for potential anode application. The influence of phosphorus doping on the structure and morphology of carbon nanotubes will be investigated, and its working mechanism will be explored.

(3) To develop a fast and energy-efficient approach to synthesize $\text{Li}_4\text{Ti}_5\text{O}_{12}$ nanomaterials. Controlled synthesis of different $\text{Li}_4\text{Ti}_5\text{O}_{12}$ nanostructures will be achieved by adjusting experimental parameters, and their electrochemical performance will be evaluated.

Part II: To develop various surface-modification materials by ALD

(4) To develop different kinds of coating materials by ALD for the purpose of surface modification in LIBs. The coating materials include ZrO_2 , AlPO_4 , and LiTaO_3 solid-state electrolyte. Different substrates, including nitrogen-doped carbon nanotubes, graphene nanosheets, Si (100) and anodic aluminum oxide (AAO) template, will be used in different systems.

(5) To study the growth characteristics of different coating materials, including ZrO_2 , AlPO_4 , and LiTaO_3 solid-state electrolyte, on various substrates at different temperatures. Substrates are playing an important role for the start of ALD deposition of thin films, while temperatures have big influence on the morphology and crystallinity of deposited thin films.

(6) To investigate the effect ALD- ZrO_2 coating on the electrochemical performance of $\text{Li}_4\text{Ti}_5\text{O}_{12}$ anode material. More importantly, the underlying mechanism of ZrO_2 coating will be revealed and discussed.

1.5 Thesis organization

This thesis consists of twelve chapters (two introductory chapters, eight articles and one conclusive chapter), and are organized in an “Integrated-Article” format as outlined in the

Thesis Regulation Guide by the School of Graduate and Postdoctoral Studies (SGPS) of the University of Western Ontario. Specifically, this thesis includes the following parts.

Chapter 1 gives a general introduction to lithium-ion batteries (LIBs), challenges existed in LIBs used for electric vehicles and hybrid electric vehicles, and the solutions offered by nanomaterials and nanotechnology. Moreover, the research objectives and the thesis structure are also stated clearly.

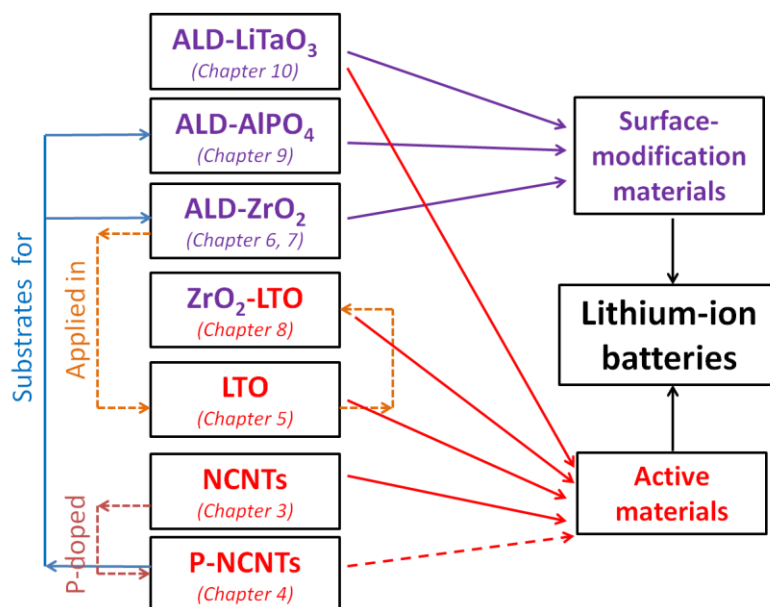


Figure 1.21 Thesis structure and interrelationships between chapters.

Chapter 2 outlines the methods used for synthesis of nanomaterials in this thesis, and the characterization techniques used to analyze their physical and electrochemical properties.

The principle research results are presented in chapters 3-10 in this thesis and their interrelationships are shown in [Figure 1.21](#).

Chapter 3 reports a new method, ultrasonic spray pyrolysis, to synthesize high-quality nitrogen-doped carbon nanotubes with tunable structure on a large scale. The effect of different experimental parameters on the morphology, structure, nitrogen-doping content and quality of nitrogen-doped carbon nanotubes was investigated in detail.

Chapter 4 presents the attempt to prepare phosphorus-nitrogen doped carbon nanotubes by a chemical vapor deposition method. It demonstrated that the structure of phosphorus-nitrogen doped carbon nanotubes changed dramatically with the amount of phosphorus precursor (triphenylphosphine) used during synthesis process. The underlying mechanism for the structure change was explored and discussed.

Chapter 5 describes synthesis of nanoflower-like and nanoparticle $\text{Li}_4\text{Ti}_5\text{O}_{12}$ prepared by a microwave-assisted hydrothermal method and their electrochemical performance as anode materials. LIB performance of the nanoflower-like and nanoparticle $\text{Li}_4\text{Ti}_5\text{O}_{12}$ was compared, and the result indicated that the nanoflower-like $\text{Li}_4\text{Ti}_5\text{O}_{12}$ exhibited much higher specific capacity than the nanoparticle $\text{Li}_4\text{Ti}_5\text{O}_{12}$, due to the larger specific surface area of the former sample.

Chapter 6 fulfills the fabrication of ZrO_2 on nitrogen-doped carbon nanotubes by atomic layer deposition technique. The study found that the as-deposited tubular ZrO_2 were well tunable in its crystallinity by simply changing deposition temperature, from amorphous at 100 °C, crystalline at 250 °C, and a mixture of the former two phases at 150-200 °C. Moreover, the thickness of ZrO_2 thin films could be simply but precisely controlled by adjusting ALD cycles. Furthermore, the growth mechanisms for ZrO_2 thin films by ALD were discussed and proposed at last.

Chapter 7 represents an extended study of atomic layer deposition of ZrO_2 on a new 2D carbon substrate, graphene nanosheets. It showed that the morphology of ZrO_2 evolved from nanoparticles to thin films with ALD cycles, and the phase of ZrO_2 trended to be more crystalline with elevating ALD deposition temperature. The growth mechanisms for ZrO_2 were proposed based on the morphological and structural evolution.

Chapter 8 gives an example of application of atomic layer deposition in anode materials. Ultrathin atomic layer deposited ZrO_2 was used to coat nanoflower-like $\text{Li}_4\text{Ti}_5\text{O}_{12}$ anode material, aiming at enhancing its LIB performance in an extended voltage range (0.1-2.5 V). The investigation revealed that ZrO_2 coating with no more than 5 ALD cycles could effectively improve the specific capacity and rate capability of $\text{Li}_4\text{Ti}_5\text{O}_{12}$. The underlying reason for the performance improvement was explored and discussed.

Chapter 9 reports development of aluminum phosphate (AlPO_4), an excellent coating material in LIBs, by atomic layer deposition method. Two ALD subcycles, Al_2O_3 (TMA- H_2O) and PO_x (TMP- O_3), were combined to obtain aluminum phosphate. The Al/P ratio in aluminum phosphate was controlled by adjusting the subcycle ratio of Al_2O_3 to PO_x . The aluminum phosphate deposited by using 1 Al_2O_3 subcycle and 10 PO_x subcycles had a composition of $\text{Al}_{1.3}\text{PO}_{5.1}$, showing thickness dependence on ALD cycles.

Chapter 10 describes atomic layer deposition of lithium tantalate (LiTaO_3) thin films, which can be used as both solid-state electrolytes and surface-modification materials. Lithium tantalate thin films were deposited by combining subcycles of Li_2O and Ta_2O_5 . The film composition varied with the subcycle ratio of Li_2O to Ta_2O_5 . Moreover, as a solid-state electrolyte, lithium tantalate with a composition of $\text{Li}_{5.1}\text{TaO}_z$ exhibited a lithium-ion conductivity of 2×10^{-8} S/cm at 299 K. Furthermore, the lithium tantalate thin films prepared by ALD showed excellent uniformity and good coverage on a 3D substrate (AAO template).

Chapter 11 summarizes the results and contributions of this thesis work. Furthermore, the author gives some personal opinions and suggestions for future work.

References

- [1] K. Tomabechi, Energy resources in the future, *Energies* **2010**, 3, 686-695.
- [2] H. Ibrahim, A. Ilinca, J. Perron, Energy storage systems-characteristics and comparisons, *Renew. Sust. Energy Rev.* **2008**, 12, 1221-1250.
- [3] C. Liu, F. Li, L. P Ma, H. M. Cheng, Advanced materials for energy storage, *Adv. Mater.* **2010**, 22, E28-E62.
- [4] B. J. Landi, M. J. Ganter, C. D. Cress, R. A. DiLeo, R. P. Raffaele, Carbon nanotubes for lithium ion batteries, *Energy Environ. Sci.* **2009**, 2, 638-654.
- [5] R. Teki, M. K. Datta, R. Krishnan, T. C. Parker, T. M. Lu, P. N. Kumta, N. Koratkar, Nanostructured Silicon Anodes for Lithium Ion Rechargeable Batteries, *Small* **2009**, 5, 2236-2242.

- [6] Lithium-ion batteries in Linden's Handbook of Batteries, T. Reddy and D. Linden, 4th Edition, **2010**, McGraw-Hill publisher.
- [7] J. -M. Tarascon, M. Armand, Issues and challenges facing rechargeable lithium batteries, *Nature* **2001**, *414*, 359-367.
- [8] "One million electric vehicles by 2015", Feb. 2011 Status Report, www.energy.gov
- [9] Pike Research Report: Electric vehicle batteries – lithium ion battery for hybrid, plug-in hybrid, and battery electric light duty vehicles: market analysis and forecasts, 2013, <http://www.navigantresearch.com/>.
- [10] A. Manthiram, Materials challenges and opportunities of lithium ion batteries, *J. Phys. Chem. Lett.* **2011**, *2*, 176-184.
- [11] A. S. Aricò, P. Bruce, B. Scrosati, J. -M. Tarascon, W. V. Schalkwijk, Nanostructured materials for advanced energy conversion and storage devices, *Nature Mater.* **2005**, *4*, 366-377.
- [12] J. Cho, Y. -W. Kim, B. Kim, J. -G. Lee, B. Park, A breakthrough in the safety of lithium secondary batteries by coating the cathode material with AlPO_4 nanoparticles, *Angew. Chem. Int. Ed.* **2003**, *42*, 1618-1621.
- [13] P. G. Bruce, B. Scrosati, J. -M. Tarascon, Nanomaterials for rechargeable lithium batteries, *Angew. Chem. Int. Ed.* **2008**, *47*, 2930-2946.
- [14] Lithium-ion batteries – solid-electrolyte interphase, P. B. Balbuena, Y. Wang, 2004, Imperial College Press publisher.
- [15] S. Flandrois, B. Simon, Carbon materials for lithium-ion rechargeable batteries, *Carbon* **1999**, *37*, 165-180.
- [16] W. -J. Zhang, A review of the electrochemical performance of alloy anodes for lithium-ion batteries, *J. Power Sources* **2011**, *196*, 13-14.
- [17] S. Iijima, Helical microtubules of graphitic carbon, *Nature* **1991**, *354*, 56-58.

- [18] M. Dresselhaus, G. Dresselhaus, R. Saito, Physics of carbon nanotubes, *Carbon* **1995**, *33*, 883-891.
- [19] N. Grobert, Carbon nanotubes-becoming clean, *Mater. Today* **2007**, *10*, 28-35.
- [20] A. Okamoto, I. Gunjishima, T. Inoue, M. Akoshima, H. Miyagawa, T. Nakano, T. Babam M. Tanenura, G. Oomi, Thermal and electrical conduction properties of vertically aligned carbon nanotubes produced by water-assisted chemical vapor deposition, *Carbon* **2011**, *49*, 294-298.
- [21] M. Kumar, Carbon nanotube synthesis and growth mechanism, in book: Carbon nanotubes-synthesis, characterization, applications, 2011, S. Yellampalli (Ed.), InTech publisher.
- [22] M. Kumar, Y. Ando, Chemical vapor deposition of carbon nanotubes: a review on growth mechanism and mass production, *J. Nanosci. Nanotechnol.* **2010**, *10*, 3739-3758.
- [23] S. K. Srivastava, V. D. Vankar, V. Kumar, Growth and microstructures of carbon nanotube films prepared by microwave plasma enhanced chemical vapor deposition process, *Thin Solid Films* **2006**, *515*, 1552-1560.
- [24] P. Ayala, R. Arenal, M. Rümeli, A. Rubio, T. Pichler, The doping of carbon nanotubes with nitrogen and their potential applications, *Carbon*, **2010**, *48*, 575-586.
- [25] M. Terrones, P. M. Ajayan, F. Banhart, X. Blas \acute{e} D. L. Carrol, J. C. Charlier, R. Czerw, B. Foley, N. Grobert, R. Kamalakaran, P. Kohler-Redlich, M. Rühle, T. Seeger, H. Terrones, N-doped and coalescence of carbon nanotubes: synthesis and electronic properties, *Appl. Phys. A* **2002**, *74*, 355-361.
- [26] A. A. Koós, F. Dillon, E. A. Obraztsova, A. Crossley, N. Grobert, Comparison of structural changes in nitrogen and boron-doped multi-walled carbon nanotubes, *Carbon* **2010**, *48*, 3033-3041.
- [27] N. A. Kaskhedikar, J. Maier, Lithium storage in carbon nanostructures, *Adv. Mater.* **2009**, *21*, 2664-2680.

- [28] B. Gao, A. Kleinhammes, X. P. Tang, C. Bower, L. Fleming, Y. Wu, O. Zhou, Electrochemical intercalation of single-walled carbon nanotubes with lithium, *Chem. Phys. Lett.* **1999**, *307*, 153-157.
- [29] X. Li, J. Liu, Y. Zhang, Y. Li, H. Liu, X. Meng, J. Yang, D. Geng, D. Wang, R. Li, X. Sun, High concentration nitrogen doped carbon nanotube anodes with superior Li^+ storage performance for lithium rechargeable battery application, *J. Power Sources* **2012**, *197*, 238-245.
- [30] H. B. Wu, J. S. Chen, H. H. Hng, W. X. Lou, Nanostructured metal oxide-based materials as advanced anodes for lithium-ion batteries, *Nanoscale* **2012**, *4*, 2526-2542.
- [31] C. -M. Park, J. -H Kim, H. Kim, H. -J. Sohn, Li-alloy based anode materials for Li secondary batteries, *Chem. Soc. Rev.* **2010**, *39*, 3115-3141.
- [32] G. -N Zhu, Y. -G. Wang, Y. -Y. Xia, Ti-based compounds as anode materials for Li-ion batteries, *Energy Environ. Sci.* **2012**, *5*, 6652-6667.
- [33] T. -F. Yi, L. -J. Jiang, J. Shu, C. -B. Yue, R. -S. Zhu, H. -B. Qiao, Recently development and application of $\text{Li}_4\text{Ti}_5\text{O}_{12}$ as anode materials of lithium ion battery, *J. Phys. Chem. Solids* **2010**, *9*, 1236-1242.
- [34] E. M. Sorensen, S. J. Barry, H. -K. Jung, J. R. Rondinelli, J. T. Vaughey, K. R. Poeppelmeier, Three-dimensionally ordered macroporous $\text{Li}_4\text{Ti}_5\text{O}_{12}$: effect of wall structure on electrochemical properties, *Chem. Mater.* **2006**, *18*, 482-489.
- [35] E. Kang, Y. S. Jung, G. -H. Kim, J. Chun, U. Wiesner, A. C. Dillon, J. K. Kim, J. Lee, Highly improved rate capability for a lithium-ion battery nano- $\text{Li}_4\text{Ti}_5\text{O}_{12}$ negative electrode via carbon-coated mesoporous uniform pores with a simple self-assembly method, *Adv. Funct. Mater.* **2011**, *21*, 4349-4357.
- [36] C. H. Chen, J. T. Vaughey, A. N. Jansen, D. W. Dees, A. J. Kahaian, T. Goacher, M. M. Thackeray, Studies of Mg-substituted $\text{Li}_{4-x}\text{Mg}_x\text{Ti}_5\text{O}_{12}$ spinel electrodes ($0 \leq x \leq 1$) for lithium batteries, *J. Electrochem. Soc.* **2001**, *148*, A102-A104.

- [37] C. Li, H. P. Zhang, L. J. Fu, H. Liu, Y. P. Wu, E. Rahm, R. Holze, H. Q. Wu, Cathode materials modified by surface coating for lithium ion batteries, *Electrochim. Acta* **2006**, *51*, 3872-3883.
- [38] J. N. Reimers, J. R. Dahn, Electrochemical and in situ X-ray diffraction studies of lithium intercalation in Li_xCoO_2 , *J. Electrochem. Soc.* **1992**, *139*, 2091-2097.
- [39] J. Cho, Y. J. Kim, T. -J. Kim, B. Park, Zero-strain intercalation cathode for rechargeable Li-ion cell, *Angew. Chem. Int. Ed.* **2001**, *40*, 3367-3369.
- [40] F. Ding, W. Xu, D. Choi, W. Wang, X. Li, M. H. Engelhard, X. Chen, Z. Yang, J. G. Zhang, Enhanced performance of graphite anode materials by AlF_3 coating for lithium-ion batteries, *J. Mater. Chem.* **2012**, *22*, 12745-12751.
- [41] S. E. Lee, E. Kim, J. Cho, Improvement of electrochemical properties of natural graphite anode materials with an ovoid morphology by AlPO_4 coating, *Electrochem. Solid-State Lett.* **2007**, *10*, A1-A4.
- [42] I. R. M. Kottegoda, Y. Kadoma, H. Ikuta, Y. Uchimoto, M. Wakihara, Enhancement of rate capability in graphite anode by surface modification with zirconia, *Electrochem. Solid-State Lett.* **2002**, *5*, A275-A278.
- [43] S. S. Kim, Y. Kadoma, H. Ikuta, Y. Uchimoto, M. Wakihara, Electrochemical performance of natural graphite by surface modification using aluminum, *Electrochem. Solid-State Lett.* **2001**, *4*, A109-A112.
- [44] Z. Chen, Y. Qin, K. Amine, Y. -K. Sun, Role of surface coating on cathode materials for lithium-ion batteries, *J. Mater. Chem.* **2010**, *20*, 7606-7612.
- [45] T. Suntola, J. Antson, Method for producing compound thin films, 1977, US patent 4058430.
- [46] S. M. George, Atomic layer deposition: an overview, *Chem. Rev.* **2010**, *110*, 111-131.

- [47] V. Miikkulainen, M. Leskelä, M. Ritala, R. L. Puurunen, Crystallinity of inorganic films grown by atomic layer deposition: overview and general trends, *J. Appl. Phys.* **2013**, *113*, 021301.
- [48] M. Ritala, M. Leskelä, Atomic layer deposition, in Handbook of Thin Film Materials, Volume 1: Deposition and Processing of Thin Films, H. S. Nalwa (Editor), **2002**, Academic Press.
- [49] S. K. Panda, H. Shin, Step coverage in ALD, in book: atomic layer deposition of nanostructured materials, N. Pinnar, M. Knez (editors), **2012**, Wiley-VCH publisher.
- [50] J. W. Elam, D. Routkevitch, P. P. Mardilovich, S. M. George, Conformal coating on ultrahigh-aspect-ratio nanopores of anodic alumina by atomic layer deposition, *Chem. Mater.* **2003**, *15*, 3507-3517.
- [51] M. D. Groner, F. H. fabreguette, J. W. Elam, S. M. George, Low-temperature Al₂O₃ atomic layer deposition, *Chem. Mater.* **2004**, *16*, 639-645.
- [52] M. Ritala, M. Leskelä, J. -P. Dekker, C. Mutsaers, P. J. Soininen, J. Skarp, Perfectly conformal TiN and Al₂O₃ films deposited by atomic layer deposition, *Chem. Vap. Deposition* **1999**, *5*, 7-9.
- [53] I. S. Scott, Y. S. Jung, A. S. Cavanagh, Y. Yan, A. C. Dillon, S. M. George, S. -H. Lee, Ultrathin coatings on nano-LiCoO₂ for Li-ion vehicular applications, *Nano Lett.* **2011**, *11*, 414-418.
- [54] Y. S. Jung, A. S. Cavanagh, L. A. Riley, S. -H. Kang, A. C. Dillon, M. D. Groner, S. M. George, S. -H. Lee, Ultrathin direct atomic layer deposition on composite electrodes for highly durable and safe Li-ion batteries, *Adv. Mater.* **2010**, *22*, 2172-2176.
- [55] Y. S. Jung, A. S. Cavanagh, A. C. Dillon, M. D. Groner, S. M. George, S. -H. Lee, Enhanced stability of LiCoO₂ cathodes in lithium-ion batteries using surface modification by atomic layer deposition, *J. Electrochem. Soc.* **2010**, *157*, A75-A81.

- [56] D. Guan, J. A. Jeevarajan, Y. Wang, Enhanced cycleability of LiMn_2O_4 cathodes by atomic layer deposition of nanosized-thin Al_2O_3 coatings, *Nanoscale* **2011**, 3, 1465-1469.
- [57] H. -M. Cheng, F. -M. Wang, J. P. Chu, R. Santhanam, J. Rick, S. -C. Lo, Enhanced cycleability in lithium ion batteries: resulting from atomic layer deposition of Al_2O_3 or TiO_2 on LiCoO_2 electrodes, *J. Phys. Chem. C* **2012**, 116, 7629-7637.
- [58] L. A. Riley, S. V. Atta, A. S. Cavanagh, Y. Yan, S. M. George, P. Liu, A. C. Dillon, S. -H. Lee, Electrochemical effects of ALD surface modification on combustion synthesized $\text{LiNi}_{1/3}\text{Mn}_{1/3}\text{Co}_{1/3}\text{O}_2$ as a layered-cathode material, *J. Power Sources* **2011**, 196, 3317-3324.
- [59] M. Bettge, Y. Li, B. Sankaran, N. D. Rago, T. Spila, R. T. Haasch, I. Petrov, D. P. Abraham, Improving high-capacity $\text{Li}_{1.2}\text{Ni}_{0.15}\text{Mn}_{0.55}\text{Co}_{0.1}\text{O}_2$ -based lithium-ion cells by modifying the positive electrode with alumina, *J. Power Sources* **2013**, 233, 346-357.
- [60] Y. S. Jung, A. S. Cavanagh, Y. Yan, S. M. George, A. Manthiram, Effects of atomic layer deposition of Al_2O_3 on the $\text{Li}_{1.2}[\text{Li}_{0.20}\text{Mn}_{0.54}\text{Ni}_{0.13}\text{Co}_{0.13}]\text{O}_2$ cathode for lithium-ion batteries, *J. Electrochem. Soc.* **2011**, 158, A1298-A1302.
- [61] J. Zhao, G. Qu, J. C. Flake, Y. Zhang, Low temperature preparation of crystalline ZrO_2 coatings for improved elevated-temperature performances of Li-ion battery cathodes, *Chem. Commun.* **2012**, 48, 8108-8110.
- [62] J. Zhao, Y. Wang, Ultrathin surface coatings for improved electrochemical performance of lithium ion battery electrodes at elevated temperature, *J. Phys. Chem. C* **2012**, 116, 11867-11876.
- [63] H. -Y. Wang, F. -M. Wang, Electrochemical investigation of an artificial solid electrolyte interface for improving the cycle-ability of lithium ion batteries using an atomic layer deposition on a graphite electrode, *J. Power Sources* **2013**, 233, 1-5.
- [64] Y. He, X. Yu, Y. Wang, H. Li, X. Huang, Alumina-coated patterned amorphous silicon as the anode for a lithium-ion battery with high coulombic efficiency, *Adv. Mater.* **2011**, 23, 4938-4941.

- [65] X. Xiao, P. Lu, D. Ahn, Ultrathin multifunctional oxide coatings for lithium ion batteries, *Adv. Mater.* **2011**, *23*, 3911-3915.
- [66] D. Ahn, X. Xiao, Extended lithium titanate cycling potential window with near zero capacity loss, *Electrochem. Commun.* **2011**, *13*, 796-799.
- [67] M. Q. Snyder, S. A. Trebukhova, B. Ravdel, M. C. Wheeler, J. DiCarlo, C. P. Tripp, W. J. DeSisto, Synthesis and characterization of atomic layer deposited titanium nitride thin films on lithium titanate spinel powder as a lithium-ion battery anode, *J. Power Sources* **2007**, *165*, 379-385.
- [68] E. Kang, Y. S. Jung, A. S. Cavanagh, G. -H. Kim, S. M. George, A. C. Dillon, J. K. Kim, J. Lee, Fe₃O₄ nanoparticles confined in mesocellular carbon foam for high performance anode materials for lithium-ion batteries, *Adv. Mater.* **2011**, *21*, 2430-2438.
- [69] L. A. Riley, A. S. Cavanagh, S. M. George, Y. S. Jung, Y. Yan, S. -H. Lee, A. C. Dillon, Conformal surface coatings to enable high volume expansion Li-ion anode materials, *ChemPhysChem* **2010**, *11*, 2124-2130.

Chapter 2 Experimental Apparatus and Characterization Techniques

2.1 Experimental apparatus

2.1.1 Ultrasonic spray pyrolysis

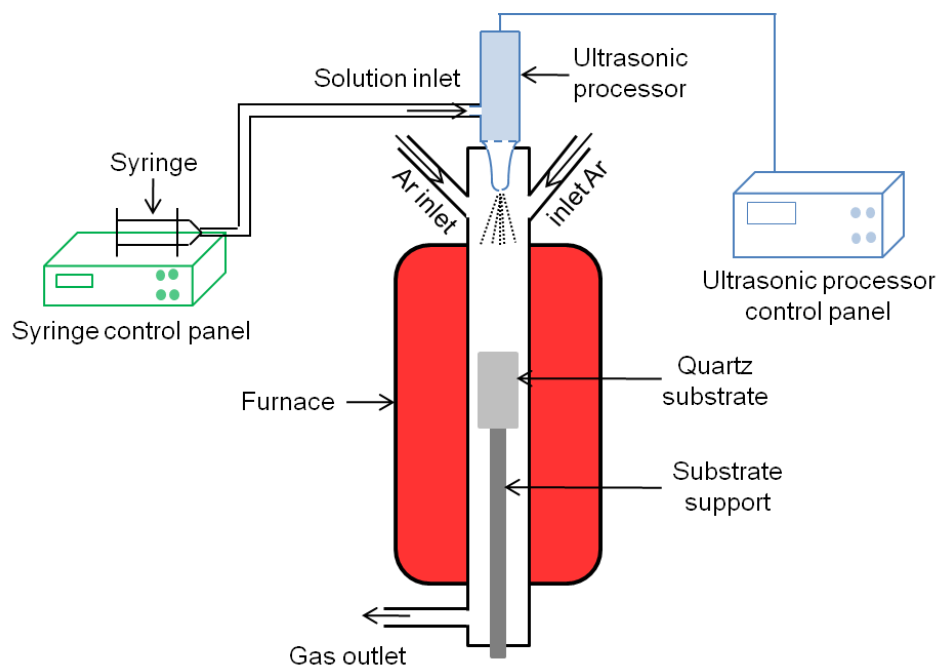


Figure 2.1 Schematic illustration of ultrasonic spray pyrolysis.

Figure 2.1 shows the schematic illustration of ultrasonic spray pyrolysis method for the growth of powder-based nitrogen-doped carbon nanotubes. This setup mainly consists of three parts called the injection part, the ultrasonic part, and the deposition chamber. In the injection part, the solution stored in a syringe is injected into the ultrasonic part at a certain feeding rate, which can be precisely controlled on the syringe control panel. In the ultrasonic part, the solution fed by the injection part is atomized in an ultrasonic processor (VCX 130 PB, Sonics & Materials Inc.), and sprayed out as tiny droplets into the deposition chamber. Ultrasonic frequency of the solution can be controlled on the control panel of the ultrasonic processor. The deposition chamber consists of a vertical

electrical furnace (50 cm length), a quartz tube ($\text{Ø}2.2 \times 70$ cm) with two gas inlets at the top and one gas outlet at the bottom, and a quartz plate ($1 \times 20 \times 90$ mm) attached on a substrate support as the substrate for the growth of nitrogen-doped carbon nanotubes. Once sprayed out by the ultrasonic processor, the solution droplets will be carried by argon (Ar) gas into the center of the furnace, where the pyrolysis occurs.

2.1.2 Floating catalyst chemical vapor deposition

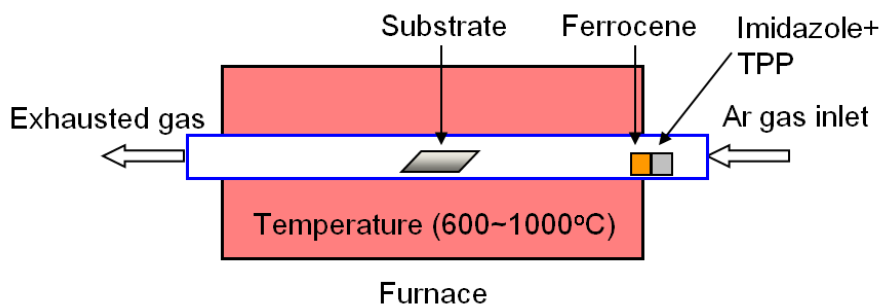


Figure 2.2 Schematic illustration of floating catalyst chemical vapor deposition.

Figure 2.2 shows the setup of floating catalyst chemical vapor deposition (FCCVD). The temperature is controlled by a tube furnace (Linderg/Blue M, Thermal Scientific). A quartz tube ($\text{Ø} 2.2$ cm) with one inlet and one outlet is put in the tube furnace. Ar gas (99.999 % in purity) is applied as the carrying and protecting gas. Substrate is placed in the center of the tube furnace, while chemicals are located at the furnace entrance.

2.1.3 Microwave-assisted hydrothermal method



Figure 2.3 Microwave-assisted hydrothermal apparatus [1].

Synthesis of materials using microwave-assisted hydrothermal method is performed in a Synthos 3000 instrument (Anton Paar), as seen in [Figure 2.3](#). This instrument can deliver 1400 W of continuous, unpulsed microwave power *via* two magnetrons, ensuring fast and effective heating rates as well as smooth reaction control [1]. This system also allows reactions under extreme conditions. For example, using XF100 model, the operating pressure can reach 60 bar, while the maximum temperature is 260 °C [1]. In addition, this apparatus enables direct scale-up of reactions from batch sizes up to liter volumes.

2.1.4 Atomic layer deposition system



Figure 2.4 A picture of Savannah 100 ALD system.

Synthesis of materials using atomic layer deposition (ALD) technique is performed in Savannah 100 ALD system (Ultratech/Cambridge Nanotech., USA). [Figure 2.4](#) shows a picture of Savannah 100 ALD system used in our laboratory. [Figure 2.5](#) illustrates the setup of the Savannah 100 ALD system and its controlling program. This ALD system consists of precursor bottles, manifold, a reaction chamber, a pressure sensor, a vacuum pump, an e-box for controlling the system and a computer. The deposition temperature in the reaction chamber varied from room temperature (RT) to 400 °C. The precursor bottles can be heated up to 200 °C to provide sufficient vapors for ALD processes. The system operating pressure is about 0.4-0.5 Torr sustained by the vacuum pump. Ar gas (99.999% in purity) is used as a carrying gas at a flowing rate of 20 sccm. All parameters for ALD

synthesis and the ALD processes are controlled by LABVIEW program installed in the computer, and an example of the program in an exposure mode is presented in Figure 2.5. In the left panel of Figure 2.5, the upper part shows the sequences of an ALD process, while the bottom part gives real-time monitoring of the system pressure.

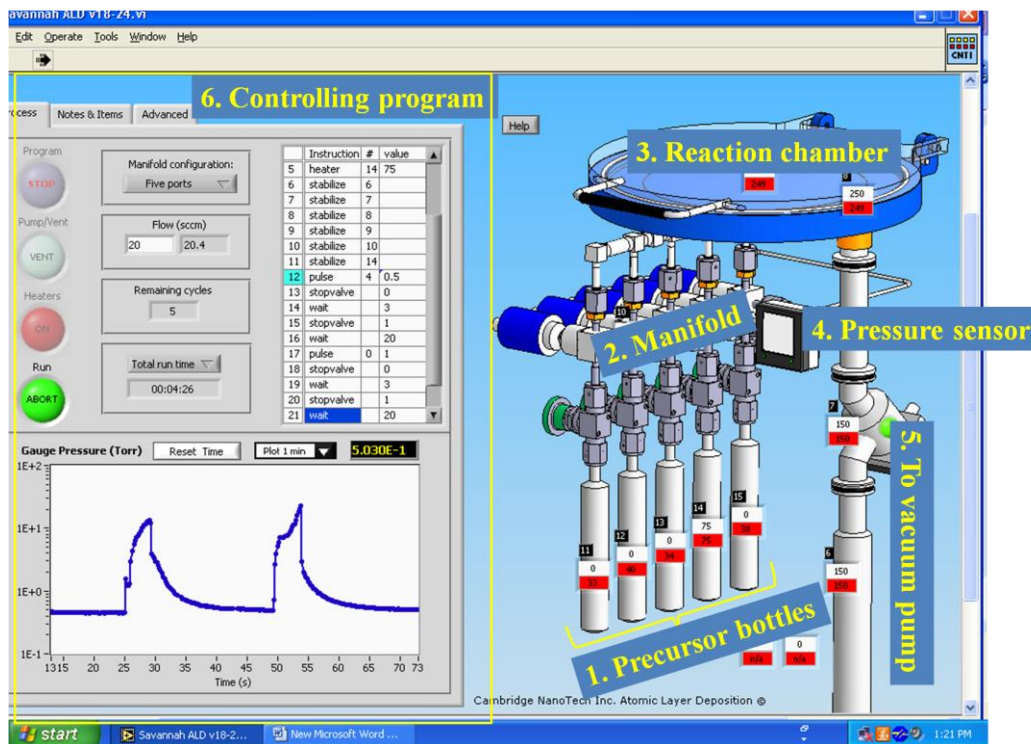


Figure 2.5 A screen snapshot showing the setup of Savannah 100 ALD system and its controlling program.

2.2 Characterization techniques

2.2.1 Physical characterizations

A variety of analytical techniques, including SEM, TEM, HRTEM, XRD, Raman, XPS and FTIR, have been used to fully characterize the physical and chemical properties of the prepared samples.

High-resolution scanning electron microscope (SEM, Hitachi S-4800) equipped with energy dispersive X-ray spectroscopy (EDS), is used to observe the morphology of the produced samples and to analyze their elemental compositions. The magnification of

Hitachi S-4800 is in a range of $\times 20$ - $\times 800,000$. The resolution of secondary electron image is 2.0 nm at 1 kV in a standard mode. The instrument is shown in [Figure 2.6](#).



Figure 2.6 A picture of Hitachi S-4800 high-resolution scanning electron microscope.



Figure 2.7 A picture of Hitachi H-7000 transmission electron microscope.

Transmission electron microscope (TEM, Hitachi H-7000) is applied to obtain structural information of the prepared samples. The resolution of Hitachi H-7000 TEM is 0.4 nm at 125 kV, higher than that of Hitachi S-4800 SEM. A picture of this instrument is given in [Figure 2.7](#). Besides conventional TEM, high-resolution TEM (HRTEM, JEOL JEM-2100) operating at 200 kV is also used to analyze the structure of the samples. JEOL JEM-2100

HRTEM is available at Canadian Center for Electron Microscopy (CCEM) located at McMaster University.

Power X-ray diffraction (XRD, Rigaku RU-200BVH) is used to gain phase information of the prepared samples. The Rigaku RU-200BVH is operated using a Co-K α source ($\lambda=1.7892 \text{ \AA}$).

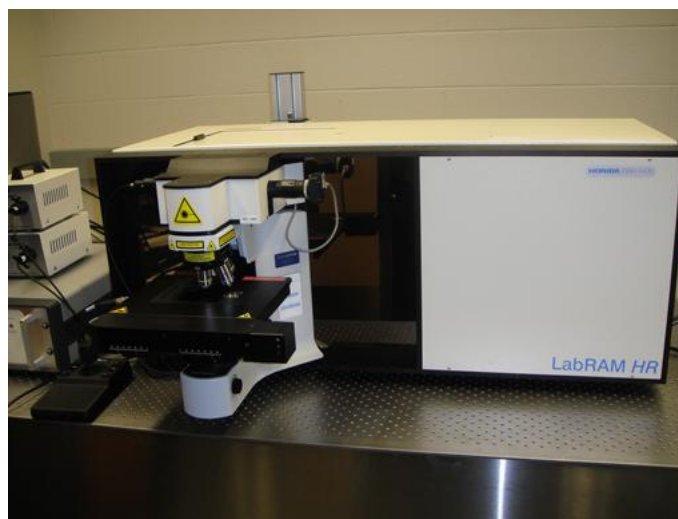


Figure 2.8 A picture of HORIBA Scientific LabRAM research Raman spectroscopy.

Raman spectroscopy (HORIBA Scientific LabRAM) is used as a supplementary tool to analyze the structure or the phase of the samples. Raman spectroscopy is operated with an incident laser beam (green light) at 532.03 nm. This instrument is available in our laboratory, and its picture is shown in [Figure 2.8](#).

X-ray photoelectron spectroscopy (XPS, Kratos AXIS Ultra Spectrometer) is used to analyze elemental composition of the prepared samples and the chemical environments of detected elements. This instrument is available at Surface Science Western.

Fourier transform-infrared spectroscopy (FTIR, Nicolet 6700 FTIR spectrometer) is used to obtain useful information about functional groups sitting at the surface of the prepared samples.

2.2.1 Electrochemical characterizations

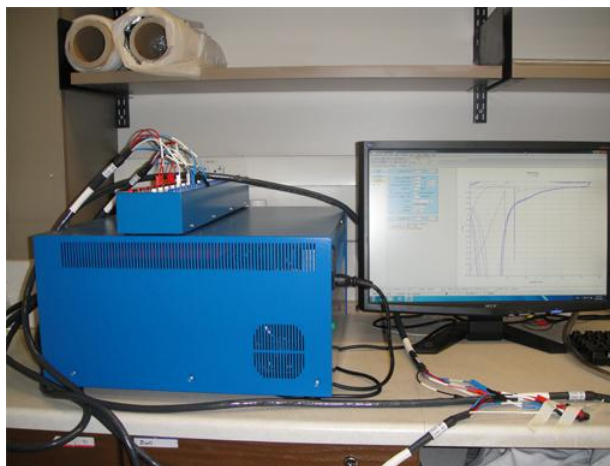


Figure 2.9 A picture of VMP3 Potentiostat/Galvanostat/EIS system.



Figure 2.10 A picture of Arbin BT-2000 battery test station.

Cyclic voltammogram (CV) performance of the anode materials is evaluated in a VMP3 Potentiostat/Galvanostat/EIS system (see [Figure 2.9](#)). Cycling stability and rate capability of the anode materials are tested in a Arbin BT-2000 battery test station (see [Figure 2.10](#)). Coin-type half-cells composed of a prepared electrode, polypropylene separator (Celgard

2400), and lithium foil as the counter electrode, are employed for electrochemical characterizations. The electrolyte consists of 1M LiPF_6 dissolved in ethylene carbonate (EC):diethyl carbonate (DEC):ethyl methyl carbonate (EMC) in a volume ratio of 1:1:1. The coin cells are assembled in a glove box (Vacuum Atmospheres Company) under a dry argon atmosphere (concentrations of moisture and oxygen are below 1 ppm).

References

- [1] www.anton-paar.com

Chapter 3 Nitrogen-Doped Carbon Nanotubes with Tunable Structure and High Yield Produced by Ultrasonic Spray Pyrolysis *

Carbon nanotubes (CNTs) are one-dimensional carbon nanomaterials, and potential alternative to current widely used graphite anode. It is widely reported that doping with foreign elements is an effective approach to modify the structure and properties of CNTs, thereby influencing their electrochemical performance as anode materials. Herein, we report a scalable method to prepare CNTs doped with nitrogen. Nitrogen-doped carbon nanotubes (NCNTs) were prepared by ultrasonic spray pyrolysis from mixtures of imidazole and acetonitrile. Imidazole, as an additive, was used to control the structure and nitrogen doping in NCNTs by adjusting its concentration in the mixtures. Scanning electron microscopy observation showed that the addition of imidazole increased the nanotube growth rate and yield, while decreased the nanotube diameter. Transmission electron microscopy study indicated that the addition of imidazole promoted the formation of a dense bamboo-like structure in NCNTs. X-ray photoelectron spectroscopy analysis demonstrated that the nitrogen content varied from 3.2 at.% to 5.2 at.% in NCNTs obtained with different imidazole concentrations. Raman spectra study showed that the intensity ratio of D to G bands gradually increased, while that of 2D to G bands decreased, due to increasing imidazole concentration. The yield of NCNTs made from mixtures of imidazole and acetonitrile can reach 192 mg in 24 min, which is fifteen times that of NCNTs prepared from only acetonitrile. The aligned NCNTs, with controlled nitrogen doping, tunable structure and high yield, may find applications in developing non-noble catalysts and novel catalyst supports for fuel cells.

Keyword: Carbon nanotubes; spray pyrolysis; nitrogen doping; chemical vapor deposition.

* Part of this chapter has been published in *Appl. Surf. Sci.* **2011**, 257, 7837-7844.

3.1 Introduction

Over the last decade, carbon nanotubes (CNTs) [1] have been widely studied due to their unique properties and potential applications in various fields, such as electronics, optics and energy conversion [2, 3]. Depending on the requirement of different applications, the properties of CNTs can be modified through different functionalization methods, of which doping foreign elements is an effective and frequently used approach [4]. Due to its similar atomic size with carbon, nitrogen (N) is widely studied as a doping element in CNTs. It is revealed that the incorporation of N could change the nanotube structure [5], chemical reactivity [6], electrical conductivity [7, 8], and mechanical properties [9] of CNTs. Due to the tunability of these properties, nitrogen-doped carbon nanotubes (NCNTs) have shown promising application potentials in various fields. For example, Dai *et al.* [10] have reported that aligned NCNTs could provide high electrocatalytic activity for oxygen reduction reactions (ORR) in fuel cells as a metal-free electrode. It has been found that the field emission property of CNTs could not only be improved by N doping [11], but also be tailored by controlling the graphitic/pyridinic N substitution [12]. In addition, uniform and dense Pt nanoparticles have been achieved by using NCNTs as substrates [13, 14]. The NCNTs supported Pt nanoparticles exhibit greatly improved stability [13] and electrocatalytic activity [14] for ORR in proton-exchange membrane fuel cells, compared with Pt nanoparticles supported on CNTs.

Recently, the doping techniques, especially in a controllable manner, have been widely studied. Various synthesis methods have been developed to produce NCNTs, including arc discharge [15], laser ablation [16], and chemical vapor deposition (CVD) [17]. The CVD method has been proven to be more controllable and more cost effective than the others. However, the practical application of NCNTs requires the production of fairly large amounts of high-quality NCNTs at a commercially viable price. Among various CVD based techniques, spray pyrolysis and aerosol assisted CVD (AACVD) seem to be suitable methods for industrial scale production of NCNTs. For example, both methods allow continuous injection of carbon and catalyst precursors, and require no additional catalyst preparation step [18, 19]. Using these two methods, it is possible to produce NCNTs without any flammable or corrosive gases such as hydrogen and ammonia [18].

Looking at these two methods, one can find that spray pyrolysis can spray solution directly into the synthesis system at controlled flow rates [18], whereas AACVD can generate solution droplets with controlled sizes [19]. Nevertheless, these desirable features have not been realized in one setup till now. Herein, by combining the advantages of spray pyrolysis and AACVD, we designed an improved spray pyrolysis method, called ultrasonic spray pyrolysis. In ultrasonic spray pyrolysis, an ultrasonic processor is used to generate fine solution droplets, which are directly sprayed into the synthesis system at controlled flow rates. Moreover, ultrasonic spray pyrolysis also features several other advantages including: (1) no need for preformed substrates; (2) possible use of mixtures of solid and liquid precursors; (3) easy scaling into an industrial scale process.

Besides the synthesis method, the controllable doping of N in CNTs also relies on the choice of precursor, catalyst, reaction temperature, reaction time and gas flow rate [20-24]. Recently, some interesting progress has been made in controlling the morphology and structure of NCNTs by using different liquid N precursors [21-23]. For example, a CNT array doped with a gradient of N concentration was achieved by gradually increasing the pyridine concentration in xylene [21]. Koś and co-authors reported that NCNTs with different structures were prepared by using the mixture of benzylamine and toluene [22, 23]. It was found that bamboo shaped nanotubes increased with the increase of benzylamine concentration, but the length and diameter of the nanotubes decreased dramatically [22, 23]. In those studies, controlled doping of N in CNTs was realized by adjusting the concentration of the N-containing precursor in the N-free precursor. However, the involvement of the N-free precursor inevitably leads to decreased N content in NCNTs [22], which is not desirable for the practical applications of NCNTs. Moreover, the addition of N-containing precursor in N-free precursor significantly suppresses the growth of NCNTs and results in a dramatically decreased yield [23, 24], which makes it difficult to produce NCNTs on a large scale.

In this work, NCNTs with controlled N doping, tunable structure and high yield have been prepared by ultrasonic spray pyrolysis. The solution used for the synthesis of NCNTs consists of a liquid N precursor (acetonitrile) and a solid N precursor (imidazole),

acting as the solvent and the solute respectively. The use of this kind of solution avoids the decrease of N content in NCNTs, because both components are N-containing precursors. And it is reported that imidazole can produce NCNTs with an N content as high as 25.7 at% [25]. Therefore, it is expected that the addition of imidazole in acetonitrile will increase the N doping in NCNTs.

3.2 Experimental section

Figure 2.1 shows the schematic illustration of ultrasonic spray pyrolysis. This setup mainly consists of three parts called the injection part, the ultrasonic part, and the deposition chamber. In the injection part, the solution stored in a syringe is injected into the ultrasonic part at a certain feeding rate, which can be precisely controlled on the syringe control panel. In the ultrasonic part, the solution fed by the injection part is atomized in an ultrasonic processor (VCX 130 PB, Sonics & Materials Inc.), and sprayed out as tiny droplets into the deposition chamber. Ultrasonic frequency of the solution can be controlled on the control panel of the ultrasonic processor. The deposition chamber consists of a vertical electrical furnace (50 cm length), a quartz tube ($\text{\O}2.2 \times 70$ cm) with two gas inlets at the top and one gas outlet at the bottom, and a quartz plate ($1 \times 20 \times 90$ mm) attached on a substrate support as the substrate for the growth of NCNTs. Once sprayed out by the ultrasonic processor, the solution droplets will be carried by argon (Ar) gas into the center of the furnace, where the pyrolysis occurs.

In a typical process, different amounts (0.5 g, 1 g and 2 g) of imidazole ($\text{C}_3\text{H}_4\text{N}_2$, Alfa Aesar 99%) and 200 mg of ferrocene ($\text{Fe}(\text{C}_5\text{H}_5)_2$, Aldrich 98%) were added into 10 ml of acetonitrile (CH_3CN , 99.5+%), and the mixture was put into an ultrasonic cleaner for 10 min to obtain a homogeneous solution. The solution was then transferred into the syringe in the injection part. The quartz plate used as the substrate for NCNTs was placed in the center of the furnace, with the help of the substrate support. Before the furnace was heated, Ar (99.999% in purity) gas was introduced into the deposition chamber from both inlets for 20 min, and the Ar gas flow rate at each inlet was maintained at 150 sccm. Then the furnace was heated to 850 °C at a rate of 60°C/min. Once the furnace reached the desirable temperature, 6 ml of the solution prepared as above was injected into the ultrasonic processor at different flow rates (0.25, 0.5 and 0.75 ml/min), and sprayed out

as tiny droplets by the ultrasonic processor at different amplitudes (45% and 85%). Then those droplets were carried into the center of the furnace, where the growth of NCNTs occurred. After 6 ml of the solution was injected, the furnace was turned off and the system cooled down to room temperature in the flowing Ar gas. NCNTs were collected from the quartz plate for future analysis.

The NCNTs were characterized by various analysis techniques including Hitachi S-4800 field-emission scanning electron microscopy (FE-SEM) operated at 5kV, Philips CM10 transmission electron microscopy (TEM) operated at 80 kV, Kratos Axis Ultra Al (alpha) X-ray photoelectron spectroscopy (XPS) operated at 14 kV, and a HORIBA Scientific LabRAM HR Raman spectrometer operated with an incident laser beam at 532.03 nm.

3.3 Results and discussion

3.3.1 Morphological investigation by SEM

3.3.1.1 Effect of imidazole concentration

The effect of imidazole concentration on the growth of NCNTs is studied in terms of the nanotube diameter, nanotube length, growth rate and yield. [Figure 3.1](#) shows the SEM images of NCNTs prepared from solutions with different imidazole concentrations. It can be seen that the nanotube diameter of NCNTs changes with the variation of the imidazole concentration. With the increase of the imidazole concentration, the nanotube diameter of NCNTs gradually decreases. The diameters of at least 150 nanotubes were measured on TEM images of each sample. Based on these data, their mean diameters are calculated and compared in [Table 3-1](#). In [Table 3-1](#), it can be found that when the imidazole concentration increases from 0 to 50, 100 and 200 mg/ml, the mean diameter of NCNTs gradually decreases from 89 to 70, 66 and 54 nm, respectively. It is noteworthy that a narrower distribution of diameters can be achieved by increasing imidazole concentration. [Koć *et al.* \[22, 23\]](#) reported that a reduction of nanotube diameter was observed by increasing benzylamine (N-containing precursor) concentration in toluene (N-free precursor). A theoretical calculation [26] shows that the reduced nanotube diameter is mainly due to the presence of N in NCNTs, which prefers to stay on the tube edge and thus induces the closure of the nanotubes. This is in accordance with our result. As shown

in section 3.3.3, the addition of imidazole into acetonitrile leads to the incorporation of more N atoms into NCNTs, which is accompanied by the reduction of nanotube diameters.

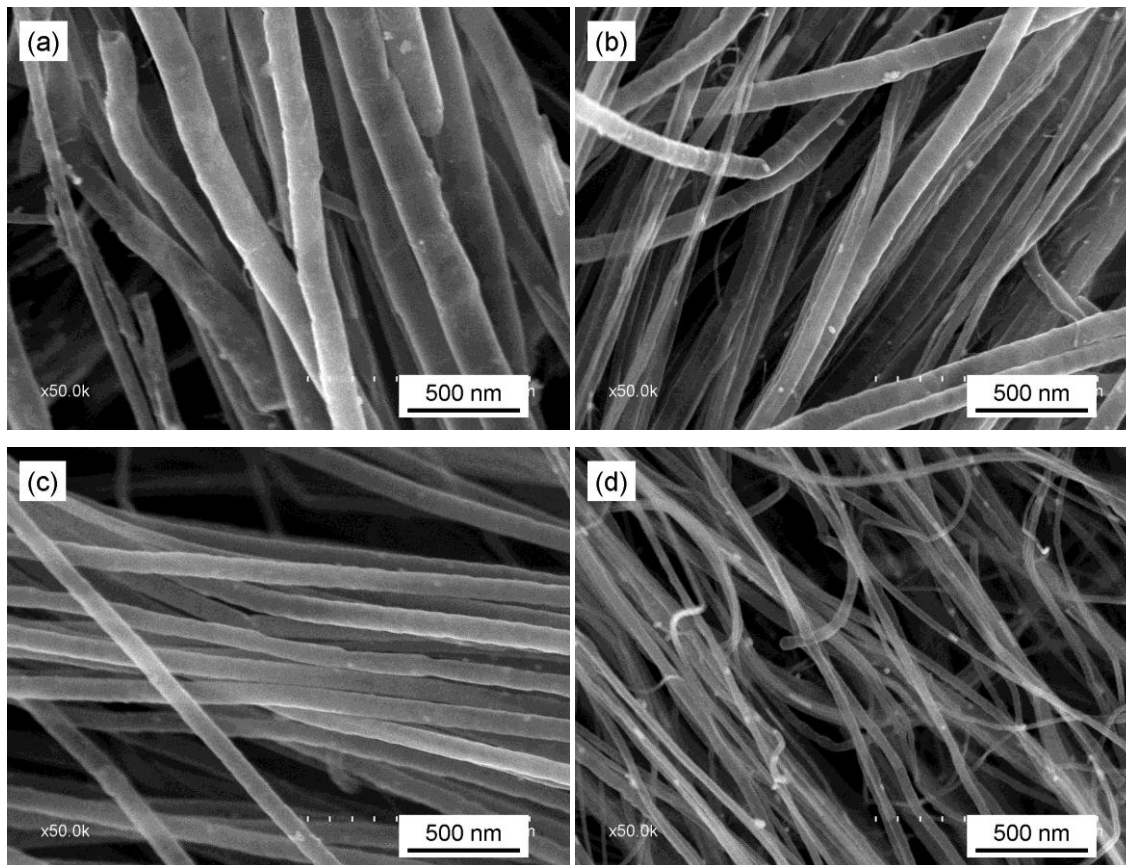


Figure 3.1 SEM images of NCNTs produced from solutions with different imidazole concentrations: (a) 0 mg/ml; (b) 50 mg/ml; (c) 100 mg/ml; (d) 200 mg/ml. (Solution flow rate 0.25 ml/min; amplitude 45%).

Table 3-1 Variation of mean nanotube diameter, nanotube length, growth rate and yield of NCNTs produced from solutions with different imidazole concentrations.

Imidazole concentration (mg/ml)	Mean nanotube diameter (nm)	Mean nanotube length (μm)	Growth rate ($\mu\text{m}/\text{min}$)	Yield (mg/6ml)
0	89 ± 5	78 ± 8	3.3	12
50	70 ± 4	112 ± 12	4.7	24
100	66 ± 4	154 ± 9	6.4	60
200	54 ± 3	397 ± 18	16.5	192

The nanotube length of each sample was measured, and the results are listed in [Table 3-1](#). In [Table 3-1](#), it can be seen that the nanotube length of NCNTs is greatly increased with the addition of imidazole. Without imidazole, the nanotube length of NCNTs produced in 24 min is measured to be $\sim 78 \mu\text{m}$. With 200 mg/ml imidazole, the length of NCNTs is found to be $\sim 397 \mu\text{m}$. Thus, the growth rate of NCNTs is increased from $3.3 \mu\text{m}/\text{min}$ for NCNTs prepared without imidazole to 4.7, 6.4, and $16.5 \mu\text{m}/\text{min}$ for NCNTs obtained with 50, 100, and 200 mg/ml imidazole, respectively. Consequently, the yield of NCNTs is increased with the addition of imidazole, as seen in [Table 3-1](#). The yield of NCNTs was obtained from the product scratched off from the quartz plate. With 200 mg/ml imidazole, 192 mg high-quality NCNTs can be easily produced in 24 min. In comparison, the yield of NCNTs prepared without imidazole in 24 min is only 12 mg, which is only one fifteenth of the former. Therefore, it can be concluded that the addition of imidazole in acetonitrile promotes the growth of nanotubes, and leads to an increased nanotube length and yield for NCNTs. Because imidazole can generate high quantities of C-N fragments at $850 \text{ }^\circ\text{C}$ [25], the solution with imidazole can provide more C-N units than that without imidazole for the growth of the nanotubes. Thus it is reasonable that the addition of imidazole in acetonitrile promotes the growth of NCNTs by providing more C-N sources. The trend of nanotube yield in our case is different from previous studies [23, 24], in which the addition of an N containing precursor in an N-free precursor led to suppressed growth of NCNTs. The difference is due to the different solvents used in the solution. The solvent used in our case is an N containing precursor (acetonitrile), while the solvents used in other studies are N-free precursor. It is suggested that pre-existing C-N bonds in the precursor play a key role for the incorporation of N atoms in NCNTs [27]. In our case, both imidazole and acetonitrile contain C-N bonds. Therefore, it is reasonable that the doping of N atoms and growth of NCNTs would be easier by using the mixture of imidazole and acetonitrile than using a mixture of one N containing precursor and one N-free precursor.

3.3.1.2 Effect of solution flow rate

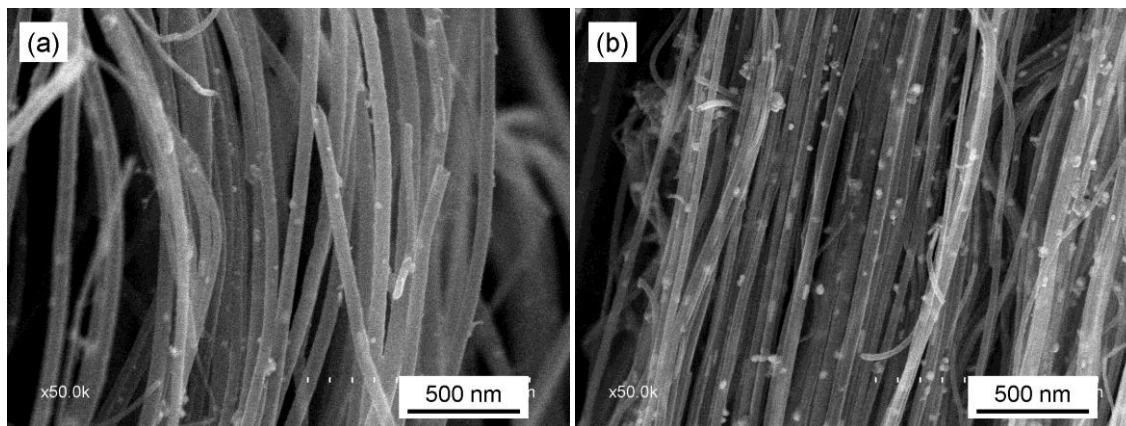


Figure 3.2 SEM images of NCNTs produced at different solution flow rates (a) 0.5 ml/min; (b) 0.75 ml/min. (Imidazole concentration: 200 mg/ml; amplitude 45%).

The effect of solution flow rate on the growth of NCNTs is studied by using a solution with imidazole concentration of 200 mg/ml, and the result is shown in Figure 3.2. In Figure 3.2, it can be seen that NCNTs prepared at solution flow rates of 0.5 and 0.75 ml/min show similarity in the nanotube diameter, which is slightly larger than that of NCNTs prepared at 0.25 ml/min, as seen in Figure 3.2d. For NCNTs prepared at a solution flow rate of 0.75 ml/min, there are many small catalyst particles attached to the surface of nanotubes. This is due to that only part of the catalyst can catalyze the growth of NCNTs at the high solution flow rate. Then the excess catalyst will deposit on the nanotube surface of NCNTs, forming small catalyst particles. Therefore, the solution flow rate mainly affects the quality of NCNTs.

3.3.1.2 Effect of amplitude

The amplitude of the ultrasonic processor is the last parameter investigated in our study. A solution with 200 mg/ml imidazole was used to grow NCNTs at amplitude 45% and 85%. The diameter distribution of each kind of NCNTs is shown in Figure 3.3. It can be seen that the nanotube diameter of NCNTs trends to decrease from 30~60 nm to 20~50 nm, as amplitude increases from 45% to 85%. The nanotube diameter is usually related to the size of the solution droplet [19]. Higher amplitude of ultrasonic processor can

generate solution droplets with smaller sizes, which lead to smaller nanotube diameters. Therefore, the amplitude has an influence on the distribution of the nanotube diameter for NCNTs prepared by ultrasonic spray pyrolysis.

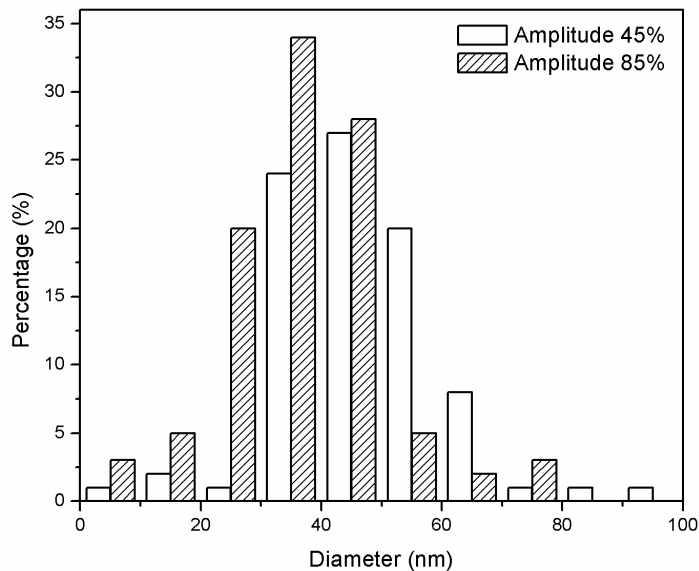


Figure 3.3 Diameter distribution of NCNTs produced at different ultrasonic amplitudes. (Imidazole concentration: 200 mg/ml; solution flow rate: 0.25 ml/min).

3.3.2 Structural investigation by SEM

The internal structures of NCNTs prepared from solutions with different imidazole concentrations are investigated by TEM, and their typical TEM images are shown in [Figure 3.4](#). In [Figure 3.4a](#), it can be seen that without imidazole, the produced NCNTs have large nanotube diameters and thin nanotube walls. There exist a few interlinks in the internal nanotubes. With the addition of 50 mg/ml imidazole, the nanotube diameter of the prepared NCNTs becomes smaller, and interlinks in the nanotubes become denser than that of NCNTs synthesized without imidazole, as seen in [Figure 3.4b](#). When the imidazole concentration is further increased to 100 mg/ml, the obtained NCNTs show similar internal structure with those prepared with 50 mg/ml imidazole. But their nanotube diameters are slightly decreased. In [Figure 3.4d](#), the nanotubes of NCNTs produced with 200 mg/ml imidazole show stacked-cone structure with periodic compartment separation, which is usually called bamboo-like structure. Comparing

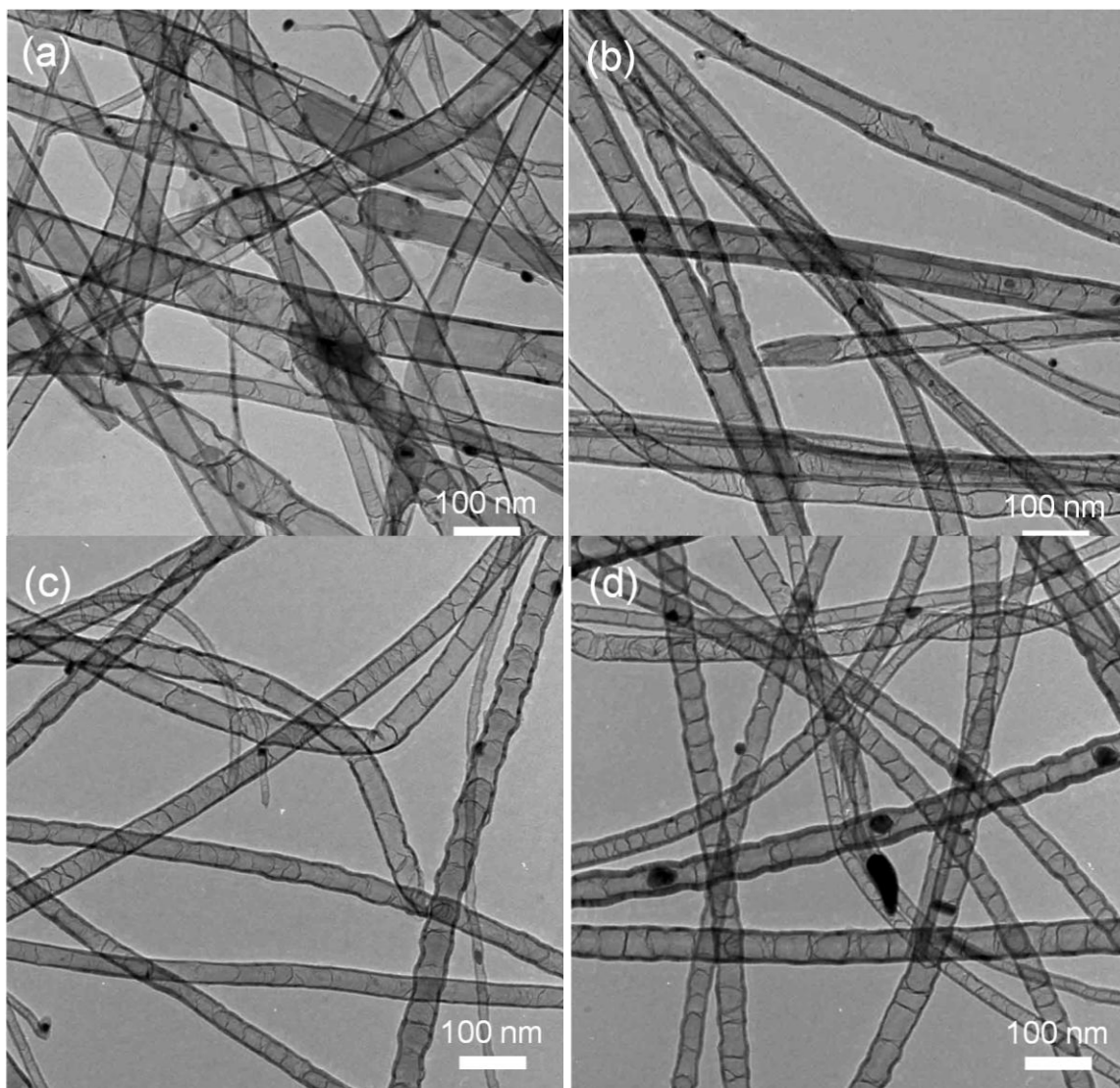


Figure 3.4 TEM images of NCNTs produced from solutions with different imidazole concentrations: (a) 0 mg/ml; (b) 50 mg/ml; (c) 100 mg/ml; (d) 200 mg/ml. (Solution flow rate 0.25 ml/min; amplitude 45%).

Figure 3.4 (a-d), it can be found that the addition of imidazole leads to the formation of a dense bamboo-like structure in the internal nanotubes of NCNTs. It is widely accepted that the formation of bamboo-like structure is caused by the presence of N in the graphitic network in NCNTs, which induces curvature of the graphitic layer [28, 29]. A higher content of N doping usually leads to a denser bamboo-like structure in the internal nanotubes of NCNTs [22, 23, 28]. In our case, the added imidazole generates many C-N

fragments during the synthesis process, which introduces more N atoms into NCNTs (proved by XPS result in section 3.3.3). The doping of more N atoms in NCNTs eventually promotes the formation of the denser bamboo-like structure in NCNTs by inducing curvature of the graphitic layer. The TEM results suggest that the inner structure of NCNTs can be controlled by simply adjusting the imidazole concentration in the solution.

3.3.3 Content and bonding environment of N by XPS

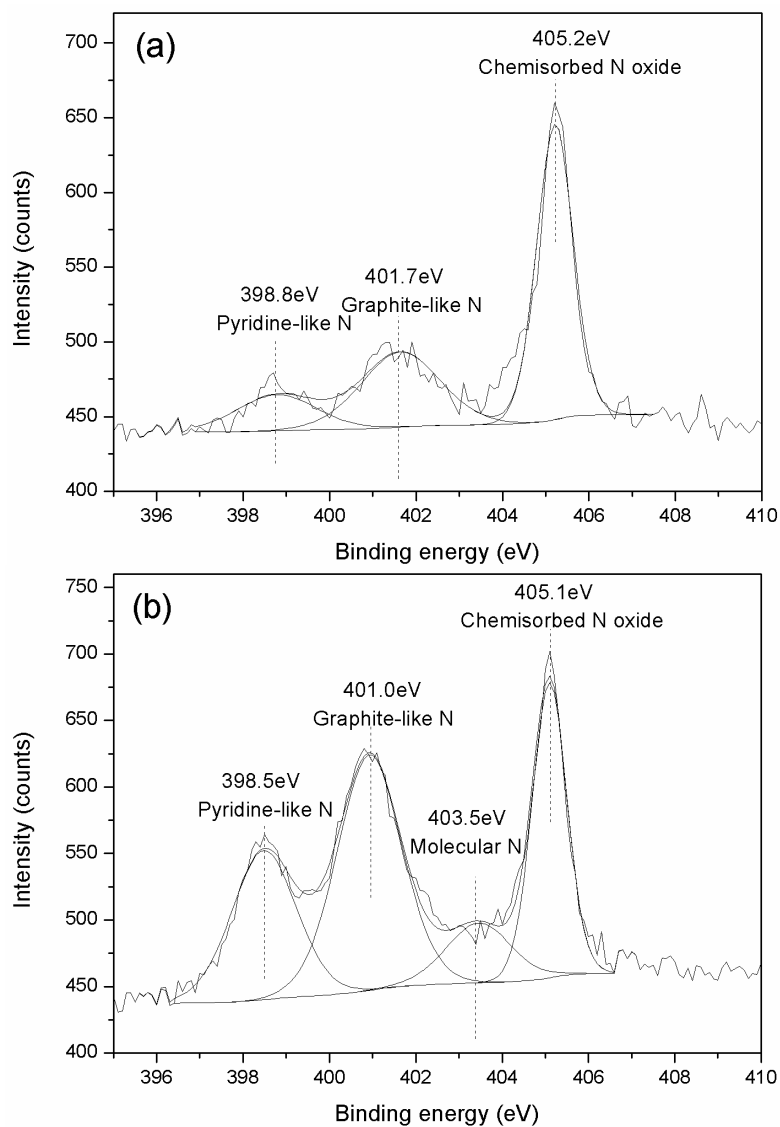


Figure 3.5 XPS N1s spectrum of NCNTs produced from solutions with different imidazole concentrations: (a) 0 mg/ml and (b) 200 mg/ml.

The content and the bonding environment of N are important factors that determine the properties of NCNTs. In order to identify the effect of imidazole on the content and the bonding environment of N doping in NCNTs, XPS analysis was carried out on NCNTs prepared without imidazole and with 200 mg/ml imidazole, and the results are compared in [Table 3-2](#) and [Figure 3.5](#). The N content, defined as atomic percent of N/(C+N), is estimated by the area ratio between the N peak and the sum of N and C peaks. As seen in [Table 3-2](#), the N content increases from 3.2 at.% for NCNTs prepared without imidazole to 5.2 at.% for NCNTs prepared with 200 mg/ml imidazole. The XPS N1s spectra of both samples are fitted into three or four components located at 398.5~398.8 eV, 401.0~401.7 eV, 403.5 eV (if applicable) and 405.1~405.2 eV, corresponding to pyridine-like N, graphite-like N, molecular N and chemisorbed N oxide, respectively [28], as seen in [Figure 3.5](#). The content of each kind of N is calculated and listed in [Table 3-2](#). In [Table 3-2](#), it can be seen that the contents of pyridine-like N and graphite-like N are obviously increased for NCNTs produced with the addition of imidazole. The intensity ratio between pyridine-like N and graphite-like N (I_{pN}/I_{gN}) is found to increase from 0.48 for NCNTs without imidazole to 0.63 for NCNTs with 200 mg/ml imidazole. It is noteworthy that molecular N appears in NCNTs obtained with 200 mg/ml imidazole. Previous studies have indicated that molecular N can be encapsulated inside the tubes [29, 30], or exist as intercalated form between the graphite layers during the growth of NCNTs [31]. The content of chemisorbed N oxide is slightly decreased for NCNTs obtained with 200 mg/ml imidazole, compared with those produced without imidazole. Therefore, the addition of imidazole not only increases the N content in NCNTs, but also alters bonding environments of N in NCNTs.

Table 3-2 Total N content and contents of different types of N in NCNTs produced from solutions with imidazole concentration of 0 and 200 mg/ml.

Imidazole concentration (mg/ml) \ N content (at.%)	Total	Pyridine-like N	Graphite-like N	Molecular N	Chemisorbed N oxide
0	3.2	0.47	0.97	-	1.76
200	5.2	1.28	2.03	0.51	1.36

3.3.4 Crystallinity of NCNTs by Raman spectra

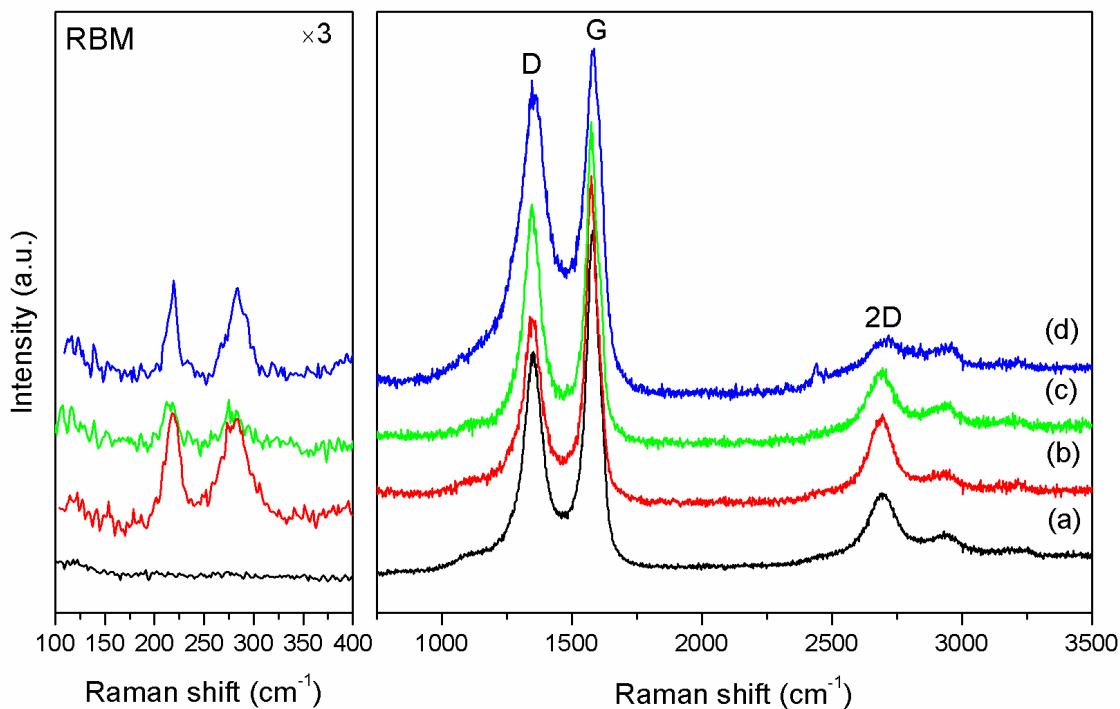


Figure 3.6 Raman spectra of NCNTs produced from solutions with different imidazole concentrations: (a) 0 mg/ml; (b) 50 mg/ml; (c) 100 mg/ml; (d) 200 mg/ml. (Solution flow rate 0.25 ml/min; amplitude 45%).

To obtain the information on the crystallinity of NCNTs, Raman spectra were carried out on NCNTs prepared with different imidazole concentrations, and their spectra are compared in Figure 3.6. From Figure 3.6, it can be seen that the Raman spectra show two main peaks around 1350 and 1590 cm^{-1} , corresponding to the D-band and the G-band respectively. The D-band is originated from atomic displacement and disorder induced features caused by lattice defect, distortion or the finite particle size [32], while the G-band indicates the formation of well-graphitized carbon nanotubes [33]. A second-order peak located at $\sim 2700 \text{ cm}^{-1}$ is also observed and usually named 2D-band, and the 2D-band is an overtone mode of the D-band [34]. Previous studies [23, 28, 34] have shown that N doping in NCNTs usually increases the intensity of D-band while decreases the intensity of 2D-band, due to increased defect density in the nanotubes. In our case, the increase of imidazole concentration in acetonitrile leads to an increase of the intensity of

D-band and a decrease of the intensity of 2D-band. The intensity ratios of D to G and 2D to G are calculated to quantitatively show this variation, as shown in Figure 3.7. As the imidazole concentration increases from 0 to 50, 100 and 200 mg/ml, the D/G ratio gradually increases from 0.57 to 0.61, 0.74 and 1, respectively. Meanwhile, 2D/G ratio decreases from 0.32 to 0.28, 0.25 and 0.13. The Raman results indicate that the addition of imidazole induces an increase in the defects and disorder in NCNTs. The reason could be attributed to the doping of more N atoms in NCNTs with the addition of imidazole.

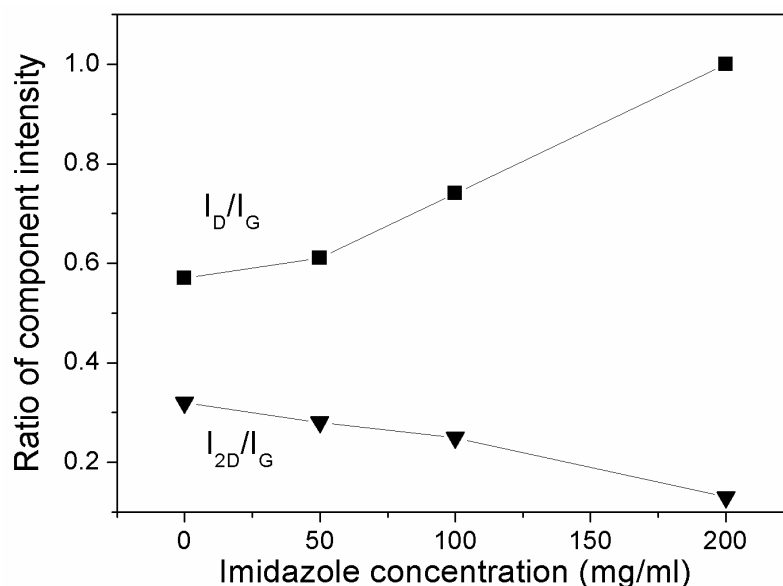


Figure 3.7 Integrated intensity ratio of D to G bands (I_D/I_G) and 2D and G band (I_{2D}/I_G) as a function of the imidazole concentration.

It is interesting to note that the Raman spectra of NCNTs prepared with imidazole show radial breathing mode (RBM) between 180 cm^{-1} and 280 cm^{-1} , which is the fingerprint of single-wall carbon nanotubes (SWNTs) [35]. The corresponding diameter of SWNTs is estimated in the range of $0.9\sim 1.1\text{ nm}$, by using the empirical relation $d\text{ (nm)} = 248/\nu\text{ (cm}^{-1}\text{)}$, where d is the SWNTs diameter and ν is Raman shift [35, 36]. The appearance of SWNTs in NCNTs is partially due to the decrease of nanotube diameters with the addition of imidazole in the solution. Another possible reason is the secondary generation of nanotubes during the synthesis process [22, 37]. During the synthesis process, the surface of the quartz plate was totally covered by nanotubes within a few minutes. Then

incoming catalyst could not reach the quartz plate, and would deposit on the nanotube surface for the growth of NCNTs [22, 37]. These new catalyst particles grown on the nanotube surface were much smaller than those grown on the surface of the quartz plate [37], and this increase the possibility of the appearance of SWNTs. Moreover, NCNTs with higher N content have more active nanotube surface, which would be easier for the deposition of catalyst particles. Thus, NCNTs with a high N content have more chance for the appearance of SWNTs than those with a low N content. This would explain why that SWNTs did not appear in NCNTs prepared without imidazole. Therefore, ultrasonic spray pyrolysis also shows the potential in the synthesis of N doped SWNTs. Large amounts of N doped SWNTs are expected when the catalyst concentration is decreased in the solution.

3.4 Conclusions

Ultrasonic spray pyrolysis was developed to synthesize nitrogen-doped carbon nanotubes (NCNTs) from mixtures of acetonitrile and imidazole. A systematic study was carried out on the effect of solution flow rate, amplitude of the ultrasonic processor and imidazole concentration on the growth of NCNTs. The results showed that the solution flow rate mainly affected the quality of NCNTs, and the amplitude had an influence on the diameter distribution of NCNTs. SEM and TEM studies indicated that the increase of imidazole concentration decreased the nanotube diameter, while increased the nanotube length and the density of bamboo-like structure in NCNTs. XPS and Raman spectra analysis showed that the addition of imidazole promoted the N doping and introduced more defects in NCNTs. These results suggest that by simply adjusting the imidazole concentration in acetonitrile, it is possible to control the nanotube diameter and length, internal structure, N content and defect density in NCNTs produced by ultrasonic spray pyrolysis.

Acknowledgements

This research was supported by Natural Sciences and Engineering Research Council of Canada (NSERC), Canada Research Chair (CRC) Program, Canada Foundation for

Innovation (CFI), Ontario Research Fund (ORF), Ontario Early Researcher Award (ERA) and University of Western Ontario.

References

- [1] S. Iijima, Helical microtubules of graphitic carbon, *Nature* **1991**, *354*, 56-58.
- [2] R. H. Baughman, A. A. Zakhidov, W. A. De Heer, Carbon nanotubes-the route toward applications, *Science* **2002**, *297*, 787-792.
- [3] D. Villers, S. H. Sun, A. M. Serventi, J. P. Dodelet, S. Desilets, Characterization of Pt nanoparticles deposited onto carbon nanotubes grown on carbon paper and evaluation of this electrode for the reduction of oxygen, *J. Phys. Chem. B* **2006**, *110*, 25916-25925.
- [4] P. Ayala, R. Arenal, M. R ümmeli, A. Rubio, T. Pichler, The doping of carbon nanotubes with nitrogen and their potential applications, *Carbon* **2010**, *48*, 575-586.
- [5] P. Nemes-incze, N. Dar áczy, Z. S árk özi, A. A. Ko ós, K. Kert ész, O. Tiprigan, Z. E. Horv áth, A. L. darabont, L. P. Bir ó, Synthesis of bamboo-structured multiwalled carbon nanotubes by spray pyrolysis method, using a mixture of benzene and pyridine, *J. Optoelectron. Adv. Mater.* **2007**, *9*, 1525-1529.
- [6] A. Nevidomskyy, G. Csanyi, M. Payne, Chemically active substitutional nitrogen impurity in carbon nanotubes, *Phys. Rev. Lett.* **2003**, *91*, 105502-105506.
- [7] C. Kaun, B. Larade, H. Mehrez, J. Taylor, H. Guo, Current-voltage characteristics of carbon nanotubes with substitutional nitrogen, *Phys. Rev. B* **2002**, *65*, 205416-205421.
- [8] E. M. M. Ibrahim, V. O. Khavrus, A. Leonhardt, S. Hampel, S. Oswald, M. H. R ümmeli, B. B üchner, Synthesis, characterization, and electrical properties of nitrogen-doped single-walled carbon nanotubes with different nitrogen content, *Diamond Relat. Mater.* **2010**, *19*, 1199-1206.
- [9] E. Hernandez, C. Goze, P. Bernier, A. Rubio, Elastic properties of single-wall nanotubes, *Appl. Phys. A Mater. Sci. Process* **1999**, *68*, 287-292.

- [10] K. Gong, F. Du, Z. Xia, M. Durstock, L. Dai, Nitrogen-doped carbon nanotube arrays with high electrocatalytic activity for oxygen reduction, *Science* **2009**, *323*, 760-764.
- [11] S. K. Srivastava, V. D. Vankar, D. V. Sridhar Rao, V. Kumar, Enhanced field emission characteristics of nitrogen-doped carbon nanotube films grown by microwave plasma enhanced chemical vapor deposition process, *Thin Solid Films* **2006**, *515*, 1851-1856.
- [12] K. Ghosh, M. Kumar, T. Maruyama, Y. Ando, Tailoring the field emission property of nitrogen-doped carbon nanotubes by controlling the graphitic/pyridinic substitution, *Carbon* **2010**, *48*, 191-200.
- [13] Y. Chen, J. Wang, H. Liu, R. Li, X. Sun, S. Ye, S. Knights, Enhanced stability of Pt electrocatalysts by nitrogen doping in CNTs for PEM fuel cells, *Electrochem. Commun.* **2009**, *11*, 2071-2076.
- [14] Y. Chen, J. Wang, H. Liu, M. N. Banis, R. Li, X. Sun, T-K. Sham, S. Ye, S. Knights, Nitrogen doping effects on carbon nanotubes and the origin of the enhanced electrocatalytic activity of supported Pt for proton-exchange membrane fuel cells, *J. Phys. Chem. C* **2011**, *115*, 3769-3776.
- [15] M. Glerup, J. Steinmetz, D. Samaille, O. Stephan, S. Enouz, A. Loiseau, S. Roth, P. Bernier, Synthesis of N-doped SWNT using the arc-discharge procedure, *Chem. Phys. Lett.* **2004**, *387*, 193-197.
- [16] H. Liu, R. Arenal, S. Enouz-Vedrenne, O. Stephan, A. Loiseau, Nitrogen configuration in individual NCNTs-SWNTs synthesized by laser vaporization technique, *J. Phys. Chem. C* **2009**, *113*, 9509-9511.
- [17] M. He, S. Zhou, J. Zhang, Z. Liu, C. Robinson, CVD growth of N-doped carbon nanotubes on silicon substrates and its mechanism, *J. Phys. Chem. B* **2005**, *109*, 9275-9279.

- [18] M. I. Ionescu, Y. Zhang, R. Li, X. Sun, H. Abou-Rachid, L.-S. Lussier, Hydrogen-free spray pyrolysis chemical vapor deposition method for the carbon nanotube growth: parametric studies, *Appl. Surf. Sci.* **2011**, *257*, 6843-6849.
- [19] A. Barreiro, D. Selbmann, T. Pichler, K. Biedermann, M. H. Rümmeli, U. Schwalke, B. Büchner, On the effects of solution and reaction parameters for the aerosol-assisted CVD growth of long carbon nanotubes, *Appl. Phys. A: Mater. Sci.* **2006**, *82*, 719-725.
- [20] C. Tang, Y. Bando, D. Golberg, D. Xu, Structure and nitrogen incorporation of carbon nanotubes synthesized by catalytic pyrolysis of dimethylformamide, *Carbon* **2004**, *42*, 2625-2633.
- [21] E. Xu, J. Wei, K. Wang, Z. Li, X. Gui, Y. Jia, H. Zhu, D. Wu, Doped carbon nanotube array with a gradient of nitrogen concentration, *Carbon* **2010**, *48*, 3097-3102.
- [22] A. A. Koós, M. Dowling, K. Jurkschat, A. Crossley, N. Grobert, Effect of the experimental parameters on the structure of nitrogen-doped carbon nanotubes produced by aerosol chemical vapor deposition, *Carbon* **2009**, *47*, 30-37.
- [23] A. A. Koós, F. Dillon, E. A. Obraztsova, A. Crossley, Nicole Grobert, Comparison of structural changes in nitrogen and boron-doped multi-walled carbon nanotubes, *Carbon* **2010**, *48*, 3033-3041.
- [24] E. N. Nxumalo, P. J. Letsoalo, L. M. Cele, N. J. Coville, The influence of nitrogen sources on nitrogen doped multi-walled carbon nanotubes, *J. Organomet. Chem.* **2010**, *695*, 2596-2602.
- [25] K. Ghosh, M. Kumar, T. Maruyama, Y. Ando, Controllable growth of highly N-doped carbon nanotubes from imidazole: structural, spectroscopic and field emission study, *J. Mater. Chem.* **2010**, *20*, 4128-4134.
- [26] B. G. Sumpter, V. Meunier, J. M. Romo-Herrera, E. Cruz-Silva, D. A. Cullen, H. Terrones, D. J. Smith, M. Terrones, Nitrogen-mediated carbon nanotube growth: diameter reduction, metallicity, bundle dispersability, and bamboo-like structure formation, *ACS Nano* **2007**, *1*, 369-375.

- [27] C. Tang, Y. Bando, D. Golberg, F. Xu, Structure and nitrogen incorporation of carbon nanotubes synthesized by catalytic pyrolysis of dimethylformamide, *Carbon* **2004**, *42*, 2625-2633.
- [28] H. Liu, Y. Zhang, R. Li, X. Sun, S. Désilets, H. Abou-Rachid, M. Jaidann, L-S. Lussier, Structural and morphological control of aligned nitrogen-doped carbon nanotubes, *Carbon* **2010**, *48*, 1498-1507.
- [29] M. Reyes-Reyes, N. Grobert, R. Kamalakaran, T. Seeger, D. Golberg, M. Rühle, Y. Bando, H. Terrones, M. Terrones, Efficient encapsulation of gaseous nitrogen inside carbon nanotubes with bamboo-like structure using aerosol thermolysis, *Chem. Phys. Lett.* **2004**, *396*, 167-173.
- [30] H. C. Choi, S. Y. Bae, W. S. Jang, J. Park, Release of N₂ from the carbon nanotubes via high-temperature annealing, *J. Phys. Chem. B* **2005**, *109*, 1683-1688.
- [31] H. C. Choi, S. Y. Bae, J. Park, Experimental and theoretical studies on the structure of N-doped carbon nanotubes: possibility of intercalated molecular N₂, *Appl. Phys. Lett.* **2004**, *85*, 5742-5744.
- [32] H. Choi, J. Park, B. Kim, Distribution and structure of N atoms in multiwalled carbon nanotubes using variable-energy X-ray photoelectron spectroscopy, *J. Phys. Chem. B* **2005**, *109*, 4333-4340.
- [33] M. S. Dresselhaus, G. Dresselhaus, R. Saito, A. Jorio, Raman spectroscopy of carbon nanotubes, *Phys. Rep.* **2005**, *409*, 47-99.
- [34] L. G. Bulusheva, A. V. Okotrub, I. A. Kinloch, I. P. Asanov, A. G. Kurennya, A. G. Kudashov, X. Chen, H. Song, Effect of nitrogen doping on Raman spectra of multi-walled carbon nanotubes, *Phys. Stat. Sol. (b)* **2008**, *245*, 1971-1974.
- [35] I. Khatri, T. Soga, T. Jimbo, S. Adhikari, H. R. Aryal, M. Umeno, Synthesis of single walled carbon nanotubes by ultrasonic spray pyrolysis method, *Diamond Relat. Mater.* **2009**, *18*, 319-323.

[36] S. Chaisitsak, J. Nukeaw, A. Tuantranont, Parametric study of atmospheric-pressure single-walled carbon nanotubes growth by ferrocene-ethanol mist CVD, *Diamond Relat. Mater.* **2007**, *16*, 1958-1966.

[37] C. Singh, M. Shaffer, A. Windle, Production of controlled architectures of aligned carbon nanotubes by an injection chemical vapor deposition method, *Carbon* **2003**, *41*, 359-368.

Chapter 4 Synthesis and Characterization of Phosphorus-Nitrogen Doped Multiwalled Carbon Nanotubes[†]

As disclosed in chapter 3, doping foreign elements is an effective way to modify the structure of CNTs. Besides the widely studied nitrogen, phosphorus is another choice of doping element to alter the structure and properties of CNTs. However, doping CNTs with phosphorus is very challenging, partially owing to the much larger atomic radius of phosphorus than carbon. Thus, investigation in doping phosphorus into CNTs is seldom.

This chapter reports our attempt to incorporate phosphorus into nitrogen-doped carbon nanotubes. Phosphorus-nitrogen doped multiwalled carbon nanotubes (PNCNTs) were prepared using a floating catalyst chemical vapor deposition method. Triphenylphosphine (TPP), as phosphorus (P) precursor, was used to control the structure of the PNCNTs. Transmission electron microscope (TEM) observation indicated that with the increase of TPP amount, the outer diameter and wall thickness of the PNCNTs gradually increased, while their inner diameter decreased. TEM and backscattered electron imaging revealed that structural changes of the nanotubes could be attributed to the shape change of the catalyst particles, from conical for NCNTs to elongated for PNCNTs, with the addition of TPP. X-ray photoelectron spectroscopy (XPS) analysis demonstrated that the P content in PNCNTs can reach as high as 1.9 at.%. Raman analysis indicated that PNCNTs had a lower crystallinity than NCNTs.

Keyword: Carbon nanotubes; phosphorus doping; chemical vapor deposition.

[†] Part of this chapter has been published in *Carbon* **2011**, *49*, 5014-5021.

4.1 Introduction

Carbon nanotubes (CNTs) [1] have been widely studied by scientists all over the world in the last two decades, due to their outstanding mechanical properties, electrical conductivity, and thermal stability [2-4]. These properties not only inspire fundamental studies on CNTs, such as band structure and chirality [5], but also make CNTs a potential candidate for a wide range of applications, such as semiconductor probes and interconnects, field emission display sources, and energy storage and conversion devices [6, 7]. Recently, there has been a great interest in controlling and improving the properties of CNTs through different functionalization methods, among which doping CNTs with foreign atoms has been proven to be an effective approach [8]. For example, nitrogen (N) atoms can donate additional electrons to the delocalized π system of the hexagonal carbon framework. Thus nitrogen-doped CNTs (NCNTs) exhibit improved electrical conductivity, compared with its non-doped counterpart [9]. The oxidation resistance of CNTs can be decreased by doping N, which introduces high-reactivity defects along nanotubes, or increased by doping boron (B), which poisons carbon active sites or forms B_2O_3 film on the surface of nanotubes protecting them from oxidation [10]. Hence, doping has been considered as a feasible strategy in a well-defined way to modify the physical and chemical properties of CNTs.

In addition to N and B, which have been intensively studied for doping in CNTs, phosphorus (P) is another doping element to modify the structure and properties of CNTs. However, studies on P doping are seldom reported. An early study on P doped diamond-like carbon (DLC) has shown that P doping could improve the electrical character of DLC by reducing the turn-on voltage and increasing the emission current density [11]. P doping in singlewalled carbon nanotubes (SWNTs) has been studied both theoretically and experimentally [12-14]. The experiment results show that P doping can significantly change the optical transition absorptions [12] and thermal conductivity of SWNTs [13]. A density functional theory (DFT) study on P doped SWNTs demonstrates that substitutional P can create localized electronic states that modify the electron transport properties of SWNTs by acting as scattering centers [14]. In addition, the substitutional P

doping also alters the mechanical strength of SWNTs, leading to a 50% reduction in the elongation upon fracture [14].

Recently, phosphorus-nitrogen doped multiwalled carbon nanotubes (PNCNTs) were synthesized by a spray pyrolysis method [15]. In this process, iron phosphide (Fe_3P) acted as the catalyst for the growth of nanotubes. Electron energy loss spectroscopy analysis demonstrated that P and N were homogeneously incorporated into the lattice of nanotubes, changing the chemical properties of PNCNTs [15]. Nevertheless, it is still challenging to synthesize high-content P doped CNTs, while high-content N or B doped CNTs have already been achieved [16, 17]. The reason is partially due to the large atomic radius difference between C (0.77 Å) and P (1.10 Å), compared with that between C and N (0.74 Å) or B (0.88 Å) [18]. This large difference would greatly increase the disorder within the hexagonal carbon framework, thus making P difficult to be doped in CNTs. However, DFT simulation demonstrated that P-N defects exhibited lower formation energy (by ca. 0.45 eV) than P defects in nanotubes [15]. In other words, by doping P and N in CNTs at the same time, it is possible to obtain a higher P content than that obtained by doping P alone. Furthermore, Kaushik et al. [16] recently reported that NCNTs with a N content of 25.7 at.% were prepared by a catalytic chemical vapor deposition method using imidazole as N precursor. Therefore, a high P content can be expected in PNCNTs, when imidazole and Triphenylphosphine (TPP), as N and P precursor respectively, are used at the same time. Meanwhile, the bonding environment of P plays a role as important as P content in determining the properties of PNCNTs. However, it has not been reported in previous literature.

In our present work, PNCNTs with a P content of 1.9 at.%, the highest reported so far, are synthesized by a floating catalyst chemical vapor deposition (FCCVD) method using ferrocene, imidazole and TPP as precursors. The effect of the amount of TPP on the structure of PNCNTs is studied. A growth mechanism of PNCNTs is proposed based on our observation. Moreover, bonding environments of P in PNCNTs are also examined, and possible bonding forms of P in PNCNTs are discussed.

4.2 Experimental section

A silicon wafer coated with an aluminum buffer layer (30 nm thickness) was used as a substrate for the growth of NCNTs and PNCNTs. The aluminum buffer layer can significantly improve the quality and growth rate of CNTs by helping the formation of uniform and well-dispersed catalyst particles on the surface of the substrate [19]. The aluminum buffer layer was coated on the surface of the silicon wafer in a sputtering system operated under a pressure of 4.0 mTorr and at a power of 300W.

FCCVD method [19, 20] was applied to synthesize NCNTs and PNCNTs in a horizontal quartz tube furnace system. 2 g of imidazole ($C_3H_4N_2$, Alfa Aesar, 99%) was thoroughly mixed with different amounts (10, 30 and 50 mg) of TPP ($P(C_6H_5)_3$, Aldrich, 99%). Then the mixture was put into a small quartz container. 10 mg of ferrocene ($Fe(C_5H_5)_2$, Aldrich, 98%) was put into a holder, which was placed over the quartz container to keep ferrocene and the mixture separate. A small piece of the substrate described above was placed in the center of the quartz tube. Before the furnace was heated, argon (Ar) gas (99.999% in purity) was introduced into the quartz tube at a flow rate of 500 sccm for 10 min in order to expel the air in the quartz tube. After that, the system was heated to 850 °C at a rate of 60°C/min. Then the quartz container was pushed into a location near the entrance of the furnace first, where the temperature was around 100 °C, suitable for the liquefaction of the mixture of imidazole and TPP. Once all the mixture was liquefied, the quartz container was pushed further into the entrance of the furnace, where the temperature was around 200 °C. At this point, ferrocene and the mixture of imidazole and TPP evaporated simultaneously. The vapor of all chemicals was brought into the high temperature region by the Ar gas where the pyrolysis and synthesis occurred at 850 °C. This step lasted for 10 min. At last, the furnace was turned off and cooled down to room temperature in the flowing Ar gas.

Morphologies of these samples were characterized by Hitachi S-4800 field-emission scanning electron microscope (SEM) operated at 5kV, Philips CM10 transmission electron microscope (TEM) operated at 80 kV, and JEOL 2010 FEG high-resolution TEM (HRTEM). Composition and element analyses of these samples were carried out by Kratos Axis Ultra Al (alpha) X-ray photoelectron spectrometer (XPS) operated at 14 kV.

Raman spectra of these samples were examined by a HORIBA Scientific LabRAM HR800 Raman spectrometer with an incident laser beam of 532.4 nm.

4.3 Results and discussion

4.3.1 Structural characterization of PNCNTs

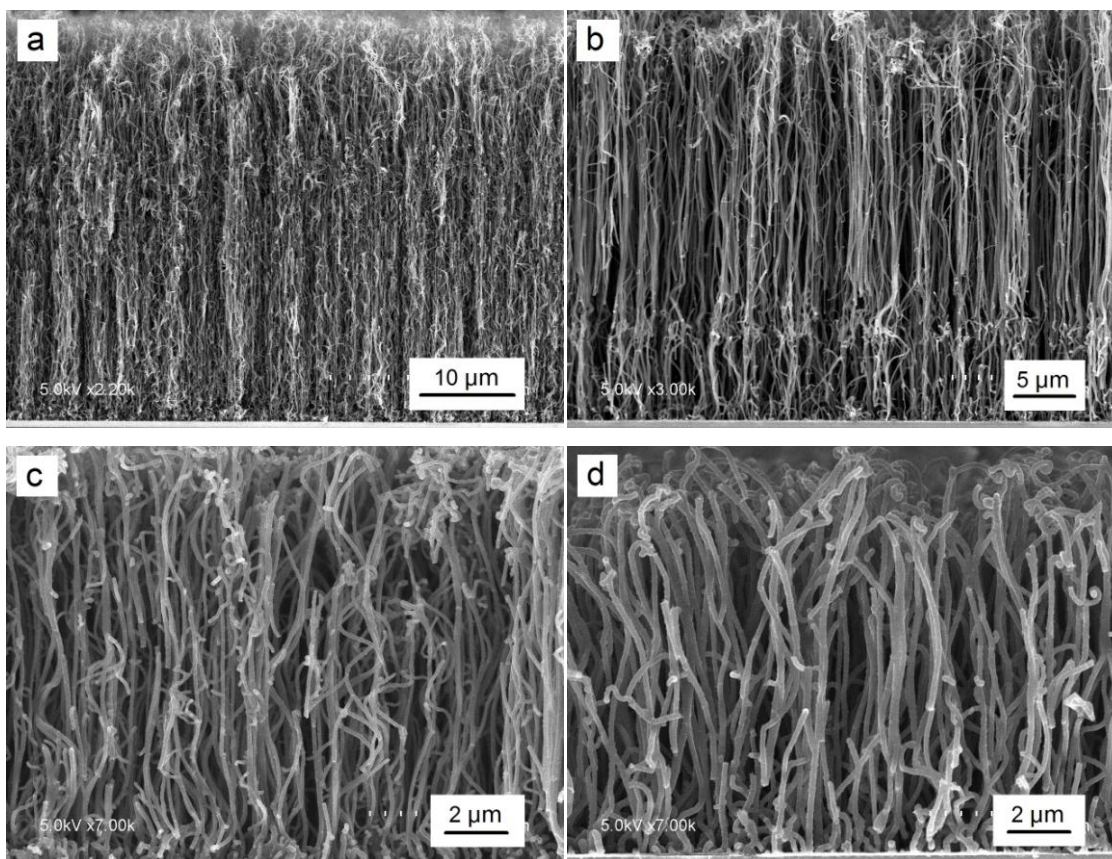


Figure 4.1 SEM images of NCNTs (a) and PNCNTs synthesized with 10 mg (b), 30 mg (c), and 50 mg (d) of TPP.

Figure 4.1 (a-d) shows typical SEM images of NCNTs and PNCNTs obtained with different amounts of TPP. It can be seen that NCNTs and PNCNTs grew perpendicularly to the silicon wafer with different densities and thicknesses of the CNT layer. As seen in Figure 4.1a, the silicon wafer is totally covered by aligned NCNTs with high density. The thickness of the CNT layer was measured to be about 42 μm for NCNTs. When TPP is used in the synthesis process, the shape of these nanotubes experiences an obvious change from curved for NCNTs to straight for PNCNTs. The thickness of the CNT layer

decreases from 42 μm for NCNTs to 29, 13 and 12 μm for PNCNTs synthesized with 10, 30 and 50 mg of TPP respectively, as seen in Figure 4.1 (b-d). And the density of these nanotubes also experiences a decrease with the increase of TPP amount. These results indicate that the growth of nanotubes is greatly suppressed by the addition of TPP. This phenomenon was also observed previously [15], in which the catalyst activity gradually deteriorated due to the increasing ratio of Fe_2P to Fe_3P in the catalyst with the addition of TPP and finally hampered the growth of PNCNTs.

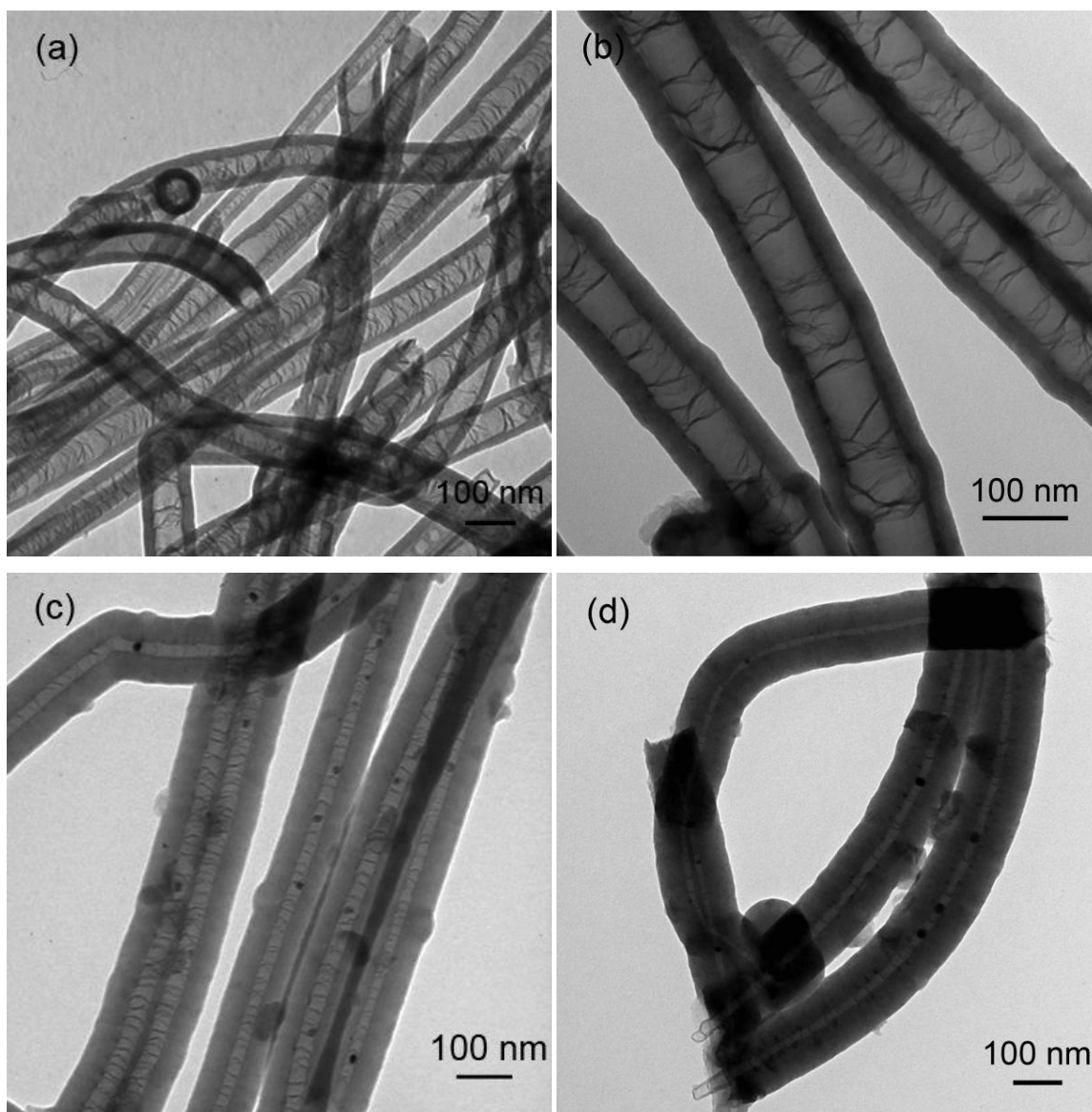


Figure 4.2 TEM images of NCNTs (a) and PNCNTs synthesized with 10 mg (b), 30 mg (c), and 50 mg (d) of TPP.

In order to investigate the relationship between the structure of PNCNTs and the amount of TPP used, TEM characterization was carried out, and the result is presented in [Figure 4.2](#). [Figure 4.2a](#) shows a typical TEM image of NCNTs synthesized without TPP. It can be seen that NCNTs exhibit an irregular and inter-linked corrugated structure, which is typical for NCNTs. With the addition of TPP, all PNCNTs show similarities in the inner structure to NCNTs, which looks like many cones stacked together. But great differences can be observed between NCNTs and PNCNTs in their outer diameters and wall thicknesses. The ratio between the inner and the outer diameter (D_i/D_o) of NCNTs or PNCNTs is used to show the variation of wall thickness. At least 100 nanotubes were measured to calculate the average value of D_i/D_o of NCNTs and each kind of PNCNTs. The outer diameter of NCNTs is around 70-90 nm, and the wall thickness is around 15-35 nm, as seen in [Figure 4.2a](#). So D_i/D_o is around 0.68 for NCNTs. When 10 mg of TPP is added to the reaction, the outer diameter and the wall thickness of PNCNTs increase to 110-130 nm and 60-70 nm respectively, while D_i/D_o decreases to around 0.48, as shown in [Figure 4.2b](#). With 30 mg of TPP, the outer diameter of PNCNTs stays almost unchanged, whereas the wall thickness increases to 80-100 nm. D_i/D_o drops to 0.23. When the amount of TPP is further increased to 50 mg, the outer diameter and the wall thickness of PNCNTs increase to 150-160 nm and 120-140nm respectively. D_i/D_o stays almost unchanged at around 0.22. These results suggest that the structure of PNCNTs can be controlled by changing the amount of TPP used in the reaction. With the increasing amount of TPP, the outer diameter and the wall thickness of PNCNTs increase, while the inner diameter decreases greatly. Interestingly, it is found that a few small catalyst particles with a spherical shape are trapped in the inner nanotubes of PNCNTs synthesized with 30 and 50 mg of TPP.

In order to understand the effect of TPP on the structural changes of PNCNTs, backscattered electron (BSE) imaging and TEM were performed on NCNTs and PNCNTs synthesized with 30 mg of TPP, focusing on their catalyst particles. From BSE images, [Figure 4.3 \(a\)](#) and [\(b\)](#), it can be clearly seen that catalyst particles are located at the bottom of nanotubes for both NCNTs and PNCNTs. This phenomenon suggests that the growth of NCNTs and PNCNTs follow a base-growth mechanism. This is consistent with the root growth model for PNCNTs as reported by Sumpter *et al.* [21]. In [Figure 4.3](#),

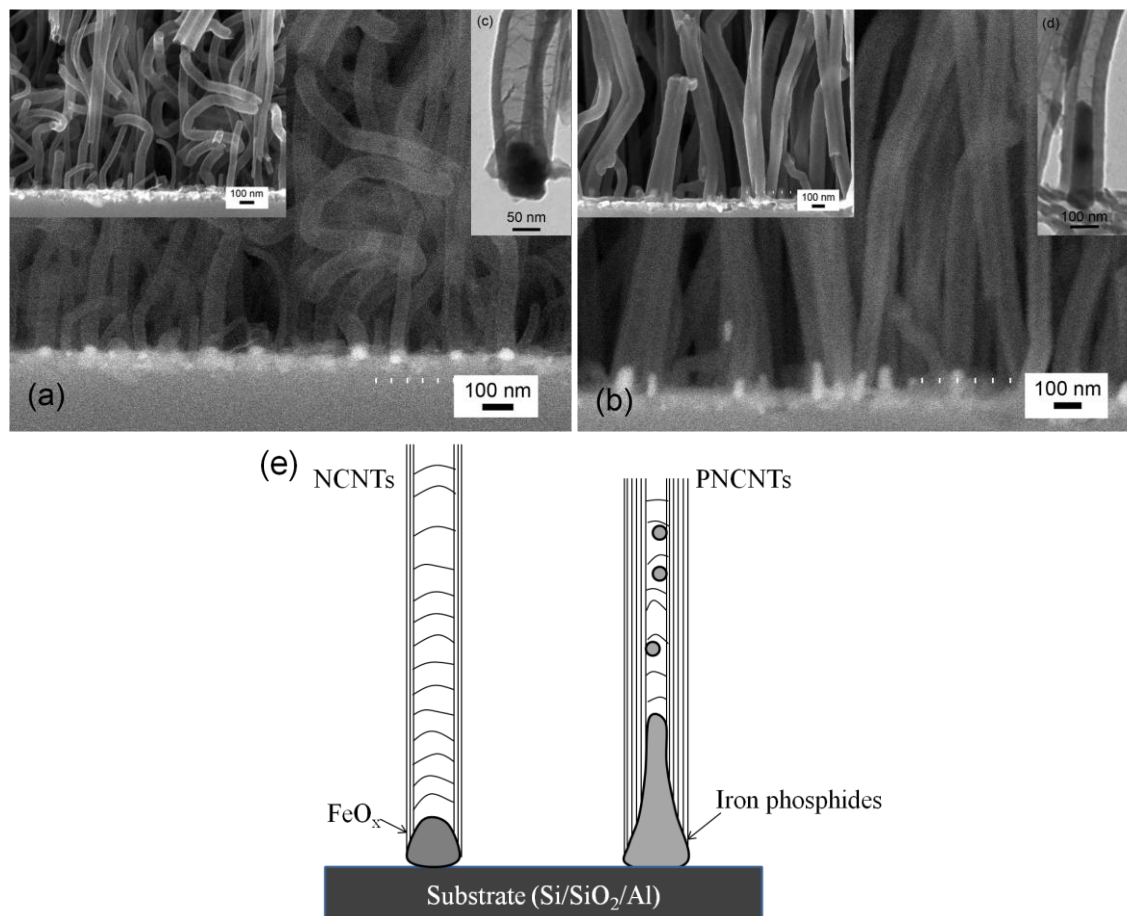


Figure 4.3 BSE images of NCNTs (a) and PNCNTs synthesized with 30 mg of TPP (b), and corresponding SEM images are inserted on the up-left corner of BSE images. Typical TEM images of one individual nanotube for NCNTs (c) and PNCNTs synthesized with 30 mg of TPP (d).

it can also be found that there are great differences between NCNTs and PNCNTs in the shape and the size of catalyst particles. The catalyst particles of NCNTs have a conical shape, and their sizes are around 50-60 nm. In comparison, the catalyst particles of PNCNTs are elongated, and the sizes of their top and bottom are about 20-40 nm and 70-90 nm respectively. These results are further confirmed by TEM observations, as shown in Figure 4.3 (c) and (d). In Figure 4.3 (a-d), it can be found that for both NCNTs and PNCNTs, the inner diameter of nanotubes is related to the size of the catalyst top. Previous studies have shown that the inner layer of NCNTs or PNCNTs is formed from the top surface of the catalysts through bulk diffusion, while the outer layer of NCNTs or

PNCNTs is nucleated from the side of the catalyst mainly through surface diffusion [22, 23]. Therefore, the inner diameter of nanotubes depends on the size of the catalyst top. Hence, in our case, the smaller inner diameter of PNCNTs than NCNTs could be attributed to the smaller top surface of the elongated catalyst than the conical one. The shape and size difference between the catalyst of NCNTs and that of PNCNTs is probably due to their different melting points. The Fe_2P or Fe_3P catalysts for PNCNTs has a lower melting point (MP) (1166 °C for Fe_3P , 1370 °C for Fe_2P) than pure Fe (1538 °C) for NCNTs [15, 24]. During the process of nanotube growth, catalyst particles with a low MP would be easily deformed and elongated along the direction of nanotube growth due to the extrusion force caused by nanotube precipitation [22]. Thus it is reasonable to believe that the top of elongated catalyst particles can be separated by the extrusion force occasionally, forming small particles trapped in the inner nanotubes observed in [Figure 4.2 \(c, d\)](#). It is noticed that similar sequential trapping of catalyst particles in CNTs was also previously observed by Jourdain *et al.*, and it was due to the inclusion of P into the catalyst particles [25]. The growth mechanisms for NCNTs and PNCNTs are shown in [Figure 4.3f](#).

4.3.2 Bonding environments of P in PNCNTs

In order to determine P content and its bonding environments in PNCNTs, XPS was performed on PNCNTs synthesized with 50 mg of TPP, and the result is shown in [Figure 4.4](#). For comparison, the XPS result of NCNTs is also given out. [Figure 4.4a](#) shows full-range XPS spectra of NCNTs and PNCNTs synthesized with 50 mg of TPP. For NCNTs, the main peaks are distinguished at 280.9 eV, 396.35 eV, 528.7 eV and 705.8 eV, corresponding to C1s, N1s, O1s, and Fe2p, respectively. For PNCNTs, besides the elements above, the existence of P is indicated by the two peaks located at 131.1 eV and 188.9 eV, which are P2p and P2s respectively. The content of P, defined as atomic percent of P with respect to the sum of C and P, is estimated by the area ratio of P peak and the sum of P and C peaks ($P/(C+P)$). The P content of PNCNTs is calculated to be 1.9 at.%. Because the catalyst particles of PNCNTs are P-rich [15], their contribution to total P content should also be considered. The deconvolution of $\text{Fe}2p_{3/2}$ peaks for NCNTs and PNCNTs are shown in [Figure 4.4 \(e\)](#) and [\(f\)](#), respectively. For NCNTs, the $\text{Fe}2p_{3/2}$

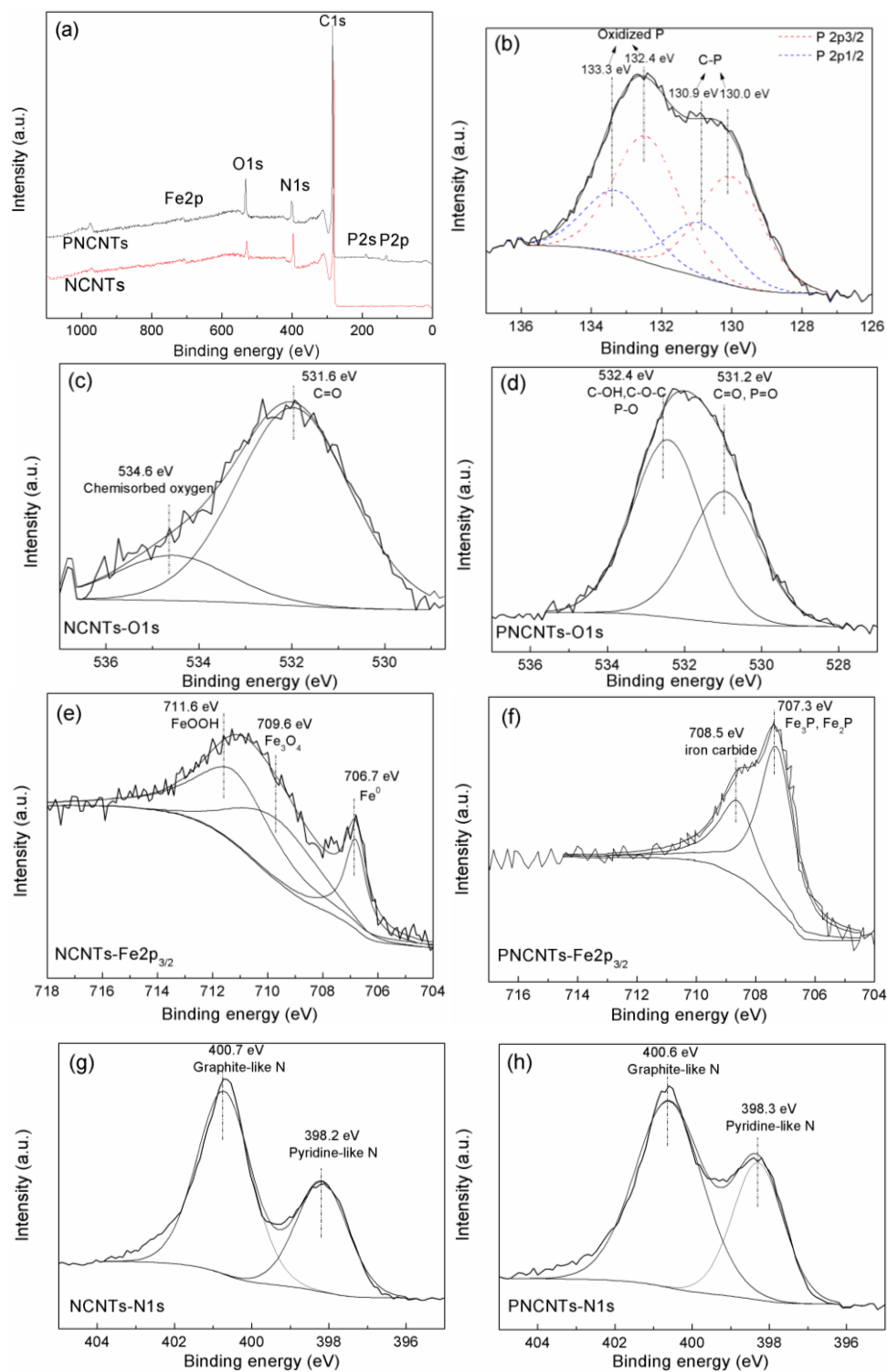


Figure 4.4 XPS survey scan spectra of PNCNTs synthesized with 50 mg of TPP and NCNTs (a), deconvolution of P2p (if applicable), O1s, Fe2p_{3/2} and N1s peaks for PNCNTs synthesized with 50 mg of TPP (b, d, f, h) and NCNTs (c, e, g).

peak is fitted into Fe^0 , Fe_3O_4 and FeOOH , located at 706.7, 709.6 and 711.6 eV respectively [19]. For PNCNTs, the $\text{Fe}2p_{3/2}$ peak is fitted into two components 707.3 and 708.5 eV respectively. The first component corresponds to Fe_2P or Fe_3P [26], and the second one is for iron carbide [27], with their respective contributions of 64.3% and 35.7%. Fe/P ratio of PNCNTs is determined to be 0.19. Therefore, Fe_2P or Fe_3P in catalyst particles contributes 4-6% to the total P content of PNCNTs. The asymmetric $\text{P}2p$ peak is fitted into two double peaks, as seen in [Figure 4.4b](#). The first two peaks near 130.0 eV indicate the presence of C-P bonds [28], and the second two ones around 133.0 eV are associated with oxidized P [28, 29]. It is reasonable to think that a fraction of P at the nanotube surface was oxidized during the synthesis process because of the presence of oxygen, which can be attributed to several reasons, such as the oxygen released from solid precursors and the oxygen adsorbed on the surface of the substrate [30]. However, the O/P ratio is as high as 4.3 for PNCNTs, implying that oxidized P only contribute a small fraction to the $\text{O}1s$ peak. The oxidized P probably exists as P-O or P=O bonds [28, 29], as seen in [Figure 4.4d](#).

N doping is an important factor to determine the properties of CNTs. Therefore, the effect of TPP addition on the N content and N bonding environments in PNCNTs is studied. The N content, defined as atomic percent of N with respect to the sum of C and N, is estimated by the area ratio of N peak and the sum of C and N peaks ($N/(C+N)$). With the addition of TPP, the N content decreases from 10.2 at.% for NCNTs to 7.1 at.% for PNCNTs. The deconvolution of $\text{N}1s$ peaks for NCNTs and PNCNTs is shown in [Figure 4.4 \(g\)](#) and [\(h\)](#) respectively. It can be seen that, for both samples, $\text{N}1s$ peak is fitted into two peaks at 400.6 eV and 398.3 eV, which correspond to graphite-like N and pyridine-like N respectively [20]. The intensity ratio between graphite-like N and pyridine-like N (I_{gN}/I_{pN}) is 1.7 for PNCNTs and 1.8 for NCNTs. These results indicate that the addition of TPP may suppress the doping of N into PNCNTs, but has little effect on the types of N.

4.3.3 Crystallinity of PNCNTs

To obtain information about the effect of TPP addition on the crystallinity of PNCNTs, HRTEM and Raman spectra were performed on NCNTs and PNCNTs synthesized with 50 mg of TPP. The HRTEM images of NCNTs and PNCNTs are shown in [Figure 4.5](#).

PNCNTs have very thick nanotube walls (as seen in [Figure 4.2d](#)), which make it difficult to obtain information about the inner nanotubes by HRTEM. Thus we only compare the features of the outer surfaces of NCNTs and PNCNTs. In [Figure 4.5](#), it can be seen that both NCNTs and PNCNTs have rough surfaces with a thin amorphous layer. Compared with NCNTs, PNCNTs exhibit a slight decrease in the degree of long-range ordered crystallinity.

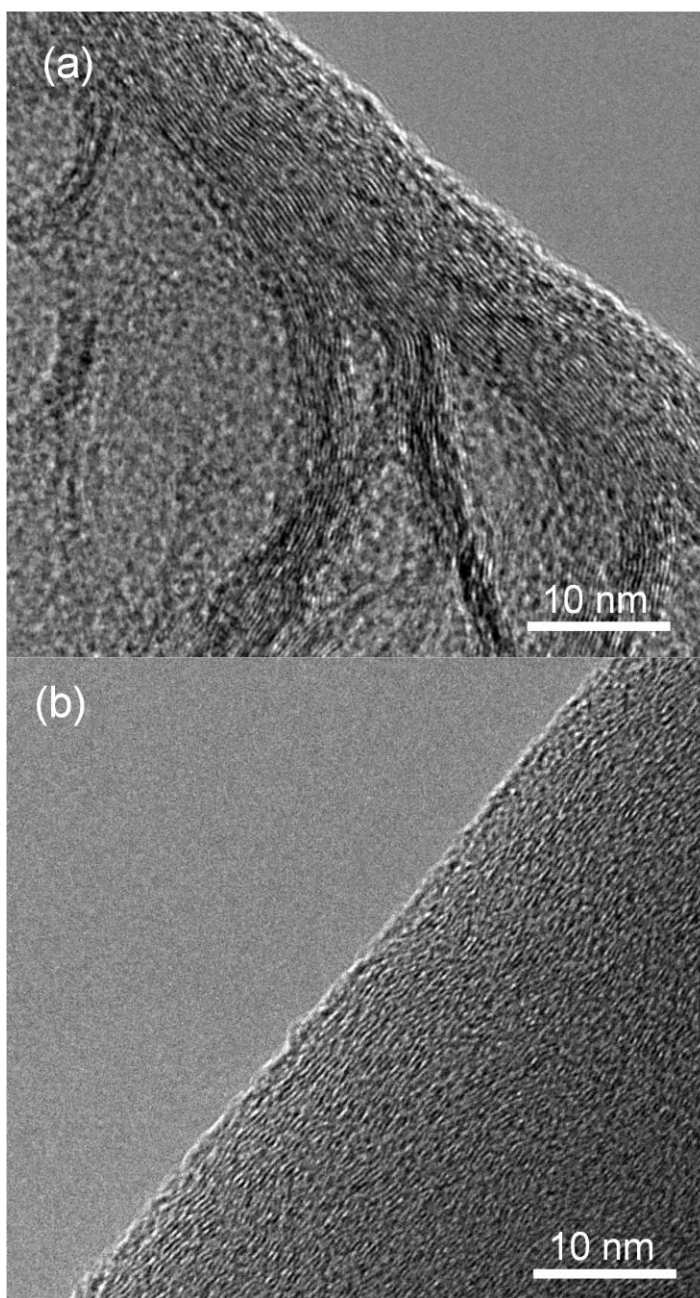


Figure 4.5 HRTEM images of NCNTs (a) and PNCNTs prepared with 50 mg of TPP (b).

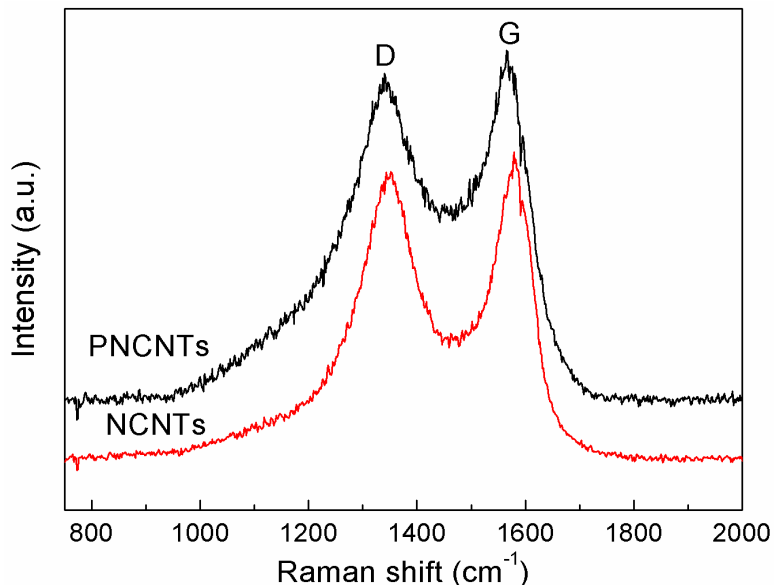


Figure 4.6 Raman spectra of NCNTs and PNCNTs synthesized with 50 mg of TPP.

Two first-order Raman spectra of PNCNTs synthesized with 50mg of TPP and NCNTs were plotted in [Figure 4.6](#). The band located at $\sim 1342 \text{ cm}^{-1}$ (D-band) is originated from atomic displacement and disorder induced features caused by lattice defect, distortion, or the finite particle size [31]. The band at $\sim 1568\text{-}1582 \text{ cm}^{-1}$ (G-band) indicates the formation of well-graphitized carbon nanotubes [32]. The intensity ratio between D-band and G-band (I_D/I_G) or the variation of the full width at half-maximum (FWHM) is usually used to represent the crystalline order in CNTs [20, 33, 34]. In our case, I_D/I_G is calculated to be 0.94 for both NCNTs and PNCNTs. The FWHMs of D-band and G-band increase from 146.3 and 83.6 cm^{-1} for NCNTs to 161.2 and 101.5 cm^{-1} for PNCNTs respectively. Narrowing of the Raman modes indicates a better crystallization of the nanotubes or a larger crystal planer domain size in graphite sheets and consequently a lower degree of disorder [34]. In our case, the broadening of D-band and G-band of PNCNTs shows that they have a lower crystalline order than NCNTs. This is in accordance with the HRTEM result. Therefore, it can be concluded that the addition of TPP during synthesis process leads to a lower crystallinity of PNCNTs than NCNTs. It is well known that the decrease of N content in NCNTs usually leads to an increase of crystalline order [20, 33]. However, In our case, PNCNTs still exhibit a lower crystalline order than NCNTs, although the N content of the former (7.1 at.%) is lower than that of

the latter (10.2 at.%). The reason is probably due to the P doping into PNCNTs by introducing TPP. A previous study has shown that the incorporation of P into SWNTs can cause a substantial increase in D-band intensity [12], which suggests an increase in defects and disorder. Therefore, it can be considered that P doping contribute to an increase in defects and disorder in PNCNTs. The P and N doping result in a lower crystalline order of PNCNTs than that of NCNTs. Moreover, it is noticed that G-band undergoes a down-shift from 1582 cm^{-1} for NCNTs to 1568 cm^{-1} for PNCNTs. The G-band represents the tangential mode vibration of carbon atoms in graphene sheets, and shifts of the G-band are interpreted in terms of C-C expansion (or contraction) and the changes of electronic structure [32]. The down-shift of G-band could also be attributed to the P doping in PNCNTs. P atoms can provide more free electrons than N atoms do. Both N and P in PNCNTs can act as electron donors, and improve electron transfer between valance and conduction bands.

4.4 Conclusions

Aligned phosphorus-nitrogen doped multiwalled carbon nanotubes (PNCNTs) with tunable structure have been synthesized on a silicon wafer by a simple FCCVD method. SEM analysis showed that the length and yield of PNCNTs decreased dramatically with an increase in the amount of TPP. TEM observations indicated that with an increasing amount of TPP, the outer diameter and the wall thickness of PNCNTs gradually increased, while the inner diameter decreased, represented by the decrease of D_I/D_O from 0.68 for NCNTs, to 0.68, 0.23 and 0.22 for PNCNTs with TPP amount of 10, 30 and 50 mg, respectively. TEM and BSE imaging studies revealed that the shape changes of catalyst particles, from conical for NCNTs to elongated for PNCNTs, was responsible for these structural changes. XPS result revealed that PNCNTs had a P content of 1.9 at.%, with 4-6% contribution from the P-rich catalyst particles. The P in PNCNTs existed in C-P bonds, and part of P at the nanotube surface was oxidized. Raman analysis showed PNCNTs exhibited broader FWHM for both the G-band and D-band, and a lower position of the G-band than for NCNTs due to P doping. Both XPS and HRTEM results indicate that PNCNTs was less crystalline than NCNTs.

Acknowledgements

This research was supported by Natural Sciences and Engineering Research Council of Canada (NSERC), Phostech Lithium Inc., Canada Research Chair (CRC) Program, Canada Foundation for Innovation (CFI), Ontario Research Fund (ORF), Ontario Early Researcher Award (ERA) and University of Western Ontario. We are in debt to David Tweddell, Fred Pearson, Ronald Smith and Mark Biesinger for their kind help and fruitful discussions.

References

- [1] S. Iijima, Helical microtubules of graphitic carbon, *Nature* **1991**, 354, 56-58.
- [2] M. Dresselhaus, G. Dresselhaus, R. Saito, Physics of carbon nanotubes, *Carbon* **1995**, 33, 883-891.
- [3] N. Grobert, Carbon nanotubes-becoming clean, *Mater. Today* **2007**, 10, 28-35.
- [4] A. Okamoto, I. Gunjishima, T. Inoue, M. Akoshima, H. Miyagawa, T. Nakano, T. Baba, M. Tanenura, G. Oomi, Thermal and electrical conduction properties of vertically aligned carbon nanotubes produced by water-assisted chemical vapor deposition, *Carbon* **2011**, 49, 294-298.
- [5] M. P. Antram, F. Léonard, Physics of carbon nanotube electronic devices, *Rep. Prog. Phys.* **2006**, 69, 507-561.
- [6] R. H. Baughman, A. A. Zakhidov, W. A. De Heer, Carbon nanotubes-the route toward applications, *Science* **2002**, 297,787-792.
- [7] K. Gong, F. Du, Z. Xia, M. Durstock, L. Dai, Nitrogen-doped carbon nanotube array with high electrocatalytic activity for oxygen reduction, *Science* **2009**, 323, 760-764.
- [8] P. Ayala, R. Arenal, M. Rümeli, A. Rudio, T. Pichler, The doping of carbon nanotubes with nitrogen and their potential applications, *Carbon* **2010**, 48, 575-586.

- [9] M. Terrones, P. M. Ajayan, F. Banhart, X. Blas \acute{e} D. L. Carrol, J. C. Charlier, R. Czerw, B. Foley, N. Grobert, R. Kamalakaran, P. Kohler-Redlich, M. R \ddot{u} hle, T. Seeger, H. Terrones, N-doped and coalescence of carbon nanotubes: synthesis and electronic properties. *Appl. Phys. A* **2002**, *74*, 355-361.
- [10] A. A. Ko \acute{o} s, F. Dillon, E. A. Obraztsova, A. Crossley, N. Grobert, Comparison of structural changes in nitrogen and boron-doped multi-walled carbon nanotubes, *Carbon* **2010**, *48*, 3033-3041.
- [11] C.-F. Chen, C.-L. Tsai, C.-L. Lin, Electronic properties of phosphorus-doped triode-type diamond field emission arrays, *Mater. Chem. Phys.* **2001**, *72*, 210-213.
- [12] J. Xu, L. Guan, diameter-selective band structure modification of single-walled carbon nanotubes by encapsulated phosphorus chains, *J. Phys. Chem. C* **2009**, *113*, 15099-15101.
- [13] I. O. Maciel, J. Campos-Delgado, E. Cruz-Silva, M. A. Pimenta, B. G. Sumpter, V. Meunier, F. L \acute{o} pez-Ur \acute{a} s, E. Munoz-Sandoval, H. Terrones, M. Terrones, A. Jorio, Synthesis, electronic structure, and Raman scattering of phosphorus-doped single-wall carbon nanotubes, *Nano Lett.* **2009**, *9*, 2267-2272.
- [14] E. Cruz-Silva, F. L \acute{o} pez-Uias, E. Munoz-Sandoval, B. G. Sumpter, H. Terrones, J.-C. Charlier, V. Meunier, M. Terrones, Electronic transport and mechanical properties of phosphorus- and phosphorus-nitrogen-doped carbon nanotubes, *ACS Nano* **2009**, *3*, 1913-1921.
- [15] E. Cruz-Silva, D. A. Cullen, L. Gu, J. M. Romo-Herrera, E. Munoz-Sandoval, F. L \acute{o} pez-Uias, B. G. Sumpter, V. Meunier, J.-C. Charlier, D. J. Smith, H. Terrones, M. Terrones, Heterodoped nanotubes: theory, synthesis, and characterization of phosphorus-nitrogen doped multiwalled carbon nanotubes, *ACS Nano* **2008**, *2*, 441-448.
- [16] K. Ghosh, M. Kumar, T. Maruyama, Y. Ando, Controllable growth of highly N-doped carbon nanotubes from imidazole: structural, spectroscopic and field emission study, *J Mater. Chem.* **2010**, *20*, 4128-4134.

- [17] P. H. Redlich, J. Loeffler, P. M. Ajayan, J. Bill, F. Aldinger, M. Rühle, B-C-N nanotubes and boron doping of carbon nanotubes, *Chem. Phys. Lett.* **1996**, *260*, 465-470.
- [18] H. Rossotti, *Diverse atoms: profiles of the chemical elements*, New York: Oxford University Press, **1998**, 62-158.
- [19] H. Liu, D. Arato, R. Li, Y. Zhang, P. Merel, X. Sun, Aligned multi-walled carbon nanotubes synthesized by floating catalyst CVD: effects of buffer layer and substrates, *Surf. Coating Tech.* **2008**, *202*, 4114-4120.
- [20] H. Liu, Y. Zhang, R. Li, X. Sun, S. Désilets, H. Abou-Rachid, M. Jaidann, L.-S. Lussier, Structural and morphological control of aligned nitrogen-doped carbon nanotubes, *Carbon* **2010**, *48*, 1498-1507.
- [21] B. G. Sumpter, J. Huang, V. Meunier, J. M. Romo-Herrera, E. Cruz-Silva, H. Terrones, M. Terrones, A theoretical and experimental study on manipulating the structure and properties of carbon nanotubes using substitutional dopants, *Int. J. Quantum Chem.* **2009**, *109*, 97-118.
- [22] M. Reyes-Reyes, N. Grobert, R. Kamalakaran, T. Seeger, D. Golberg, M. Rühle, Y. Bando, H. Terrones, M. Terrones, Efficient encapsulation of gaseous nitrogen inside carbon nanotubes with bamboo-like structure using aerosol thermolysis, *Chem. Phys. Lett.* **2004**, *396*, 167-173.
- [23] C. J. Lee, Growth model of bamboo-shaped carbon nanotubes by thermal chemical vapor deposition, *Appl. Phys. Lett.* **2000**, *77*, 3397-3399.
- [24] F. Benissad-Aissani, H. Aït-Amar, M.-C. Schouler, P. Gadelle, The role of phosphorus in the growth of vapour-grown carbon fibres obtained by catalytic decomposition of hydrocarbons, *Carbon* **2004**, *32*, 2163-2168.
- [25] V. Jourdain, E. T. Simpson, M. Paillet, T. Kasama, R. E. Dunin-Borkowski, P. Poncharal, A. Zahab, A. Loiseau, J. Robertson, P. Bernier, Periodic inclusion of room-temperature-ferromagnetic metal phosphides nanoparticles in carbon nanotubes, *J. Phys. Chem. B* **2006**, *110*, 9759-9763.

- [26] M. Godec, D. J. Mandrino, B. Šuštaršič, D. Nolan, M. Jenko, Characterization of rapidly solidified nanocrystalline soft magnetic ribbons based on Fe-Si-B with P and Ga additions, *Surf. Interface Anal.* **2008**, *40*, 498-502.
- [27] F. Bonnet, F. Ropital, Y. Berthier, P. Marcus, Filamentous carbon formation caused by catalytic metal particles from iron oxide, *Material and Corrosion* **2003**, *54*, 870-880.
- [28] J. Gorham, J. Torres, G. Wolfe, A. d'Agostino, D. H. Fairbrother, Surface reactions of molecular and atomic oxygen with carbon phosphide films, *J. Phys. Chem. B* **2005**, *109*, 20379-20386.
- [29] A. M. Puziy, O. I. Poddubnaya, R. P. Socha, J. Gulgul, M. Wisniewski, XPS and NMR studies of phosphoric acid activated carbons, *Carbon* **2008**, *46*, 2113-2123.
- [30] M. He, S. Zhou, J. Zhang, Z. Liu, C. Robinson, CVD growth of N-doped carbon nanotubes on silicon substrates and its mechanism, *J. Phys. Chem. B* **2005**, *109*, 1808-1820.
- [31] H. Choi, J. Park, B. Kim, Distribution and structure of N atoms in multiwalled carbon nanotubes using variable-energy X-ray photoelectron spectroscopy, *J. Phys. Chem. B* **2005**, *109*, 4333-4340.
- [32] M. S. Dresselhaus, G. Dresselhaus, R. Saito, A. Jorio, Raman spectroscopy of carbon nanotubes, *Phys. Rep.* **2005**, *409*, 47-99.
- [33] A. A. Koós, F. Dillon, E. A. Obraztsova, A. Crossley, N. Grobert, Comparison of structural changes in nitrogen and boron-doped multi-walled carbon nanotubes, *Carbon* **2010**, *48*, 3033-3041.
- [34] R. M. Yadav, P. S. Dobal, T. Shripathi, R. S. Katiyar, O. N. Srivastava, Effect of growth temperature on bamboo-shaped carbon-nitrogen (C-N) nanotubes synthesized using ferrocene acetonitrile precursor, *Nanoscale Res. Lett.* **2009**, *4*, 197-203.

Chapter 5 Microwave-Assisted Hydrothermal Synthesis of Nanostructured Spinel $\text{Li}_4\text{Ti}_5\text{O}_{12}$ as Anode Materials for Lithium-Ion Batteries ‡

NCNTs and PNCNTs synthesized in chapter 3 and 4 are very promising anode materials for LIBs. However, due to their low working voltage below 0.5 V, carbon materials suffer from the formation of solid-electrolyte interphase (SEI), which could result in low battery efficiency and bring safety problems. To avoid these problems, one way is to find another anode material with higher working voltages. Lithium titanate ($\text{Li}_4\text{Ti}_5\text{O}_{12}$), with voltage potential at 1.55 V (vs. Li/Li^+), is free the formation of SEI, and thereby one alternative to carbon materials.

In this chapter, we report the synthesis of nanoflower-like and nanoparticle spinel $\text{Li}_4\text{Ti}_5\text{O}_{12}$ by a microwave-assisted hydrothermal (MH) method following calcination. As-prepared $\text{Li}_4\text{Ti}_5\text{O}_{12}$ was characterized by scanning electron microscopy, transmission electron microscopy, X-ray powder diffraction and cyclic voltammetry. The nanoflower-like and nanoparticle $\text{Li}_4\text{Ti}_5\text{O}_{12}$ exhibited discharge capacities of 176.7 and 109.8 mAh g^{-1} respectively, for the first cycle, and maintained reversible capacities of 138.4 and 91.7 mAh g^{-1} respectively, at a 1.1 C-rate (200 mA g^{-1}) after 100 cycles. The better performance of nanoflower-like $\text{Li}_4\text{Ti}_5\text{O}_{12}$ relative to nanoparticle $\text{Li}_4\text{Ti}_5\text{O}_{12}$ is attributed to the larger specific surface area and shorter Li^+ diffusion path of the former relative to the latter. The MH preparation process is straightforward and fast; thus it shows promise for widespread lithium ion battery applications.

Keyword: $\text{Li}_4\text{Ti}_5\text{O}_{12}$; microwave-assisted hydrothermal method; lithium ion batteries; anode material.

‡ Part of this chapter has been published in *Electrochim. Acta* **2012**, 63, 100-104.

5.1 Introduction

Lithium ion batteries (LIBs) are the most developed energy storage system for portable devices, electric vehicles (EVs) and hybrid electric vehicles (HEVs) due in large part to their high energy density and long cycling life [1-4]. At present, graphite is widely used in commercial LIBs as the anode material, but it suffers from poor abuse tolerance for EV and HEV applications [5]. Recently, spinel $\text{Li}_4\text{Ti}_5\text{O}_{12}$ has attracted much interest as a promising anode (negative electrode) material for LIBs due to its unique advantages [4-20]. The potential for unusually high-power cells has spurred much of this research [21-24]. The working voltage of spinel $\text{Li}_4\text{Ti}_5\text{O}_{12}$ is approximately at 1.55 V (*vs.* Li/Li^+), which avoids the formation of a conventional solid electrolyte interphase (e.g. as seen over graphite), as the electrolyte is not exposed to strongly reducing potentials; thus, high coulombic efficiencies result [18]. In addition, the zero-strain of spinel $\text{Li}_4\text{Ti}_5\text{O}_{12}$ upon lithiation and delithiation yields excellent structural stability and reversibility during charge and discharge processes [19]. Moreover, the high lithium ion mobility in $\text{Li}_4\text{Ti}_5\text{O}_{12}$ provides good rate capability in LIBs, which is desirable for traction applications [20].

In recent years, much effort has been devoted to developing nanoscaled spinel $\text{Li}_4\text{Ti}_5\text{O}_{12}$, which can improve the charge/discharge rate by shorting diffusion path of electrons and lithium ions. Spinel $\text{Li}_4\text{Ti}_5\text{O}_{12}$ nanomaterials with different morphologies, such as nanotubes and nanowires [25, 26], nanosheets [27, 28] and porous microspheres [29], have been successfully synthesized by solvothermal [25] and hydrothermal [26-29] methods. Recently, microwave-assisted hydrothermal (MH) methods have been employed and found to be efficient for the synthesis of nanomaterials [30-37]. MH methods rely on the interactions of dielectric materials, be the liquid or solid, with microwave radiation that causes direct dielectric heating [30]; the process yields very rapid heating relative to less direct conventional hydrothermal (CH) methods [31]. In general, it takes only 1 to 3 minutes to heat water up to 100 to 150 °C by MH methods, while 60 to 100 minutes are often required using CH methods [31]. In addition, MH methods have several advantages over CH methods: (1) short reaction time and low-temperature processing [32, 33], (2) extremely rapid kinetics of crystallization [34], and

(3) low energy consumption [32-34]. Up to now, MH methods have been used successfully to synthesize nanomaterials of MnO_2 [30], WO_3 [31], Co_3O_4 [35] and LiFePO_4 [36, 37].

Herein, we report the synthesis of nanostructured $\text{Li}_4\text{Ti}_5\text{O}_{12}$ by a MH method and following heat treatment. Nanoflower-like and nanoparticle $\text{Li}_4\text{Ti}_5\text{O}_{12}$ were obtained at different temperatures. The electrochemical properties of the nanoflower-like and nanoparticle $\text{Li}_4\text{Ti}_5\text{O}_{12}$ were investigated as anode materials for LIBs. The effect of morphology on the LIB performance of $\text{Li}_4\text{Ti}_5\text{O}_{12}$ is discussed.

5.2 Experimental Section

5.2.1 Sample preparation and characterization

In a typical process, 191.6 mg LiOH and 1 mL 30% H_2O_2 was dissolved into 20 mL deionized water, and the mixture was stirred for several minutes until a clear solution was obtained. Then 0.59 mL titanium tetraisopropoxide (TTIP) was dropwise added into the clear solution with stirring. After stirring for 30 min, 15 mL of the obtained solution was transferred to an 80 mL Teflon-lined PTFE autoclave vessel, which was sealed and heated to desired temperatures (130 and 170 °C), with a holding time of 20 minutes in a microwave-assisted hydrothermal synthesis system (Anton Paar Synthos 3000). After the autoclave was cooled to room temperature, products were collected by centrifugation, washed with deionized water thoroughly, and dried in an oven at 80 °C for 12 h. Last, the as-prepared products were calcined in a quartz tube furnace at 550 °C for 6 h in air.

The materials were characterized by X-ray diffraction (XRD, Rigaku RU-200BVH with a $\text{Co-K}\alpha$ source, with $\lambda=1.7892 \text{ \AA}$), field emission scanning electron microscopy (SEM, Hitachi S4800), transmission electron microscopy (TEM, Hitachi H-7000), and high resolution TEM (HRTEM, JEOL 2010 FEG microscope). N_2 adsorption/desorption isotherms were obtained using a Folio Micromeritics TriStar II Surface Area and Pore Size Analyzer.

5.2.2 Electrochemical characterization

Electrochemical measurements were performed by using coin-type half cells assembled in an argon-filled glove box ($[O_2] < 1$ ppm, $[H_2O] < 1$ ppm). The electrolyte was 1M $LiPF_6$ solution in ethylene carbonate and dimethyl carbonate with a volume ratio of 1:1. To prepare the electrode, the active material powder, acetylene black and polyvinylidene fluoride binder, with a weight ratio of 80:10:10 were mixed until substantially homogeneous, and pasted onto a copper foil. Each electrode foil has a surface area of 1.6 cm^2 and contains active material of ~ 5 mg. Then the electrode was dried under vacuum at $110 \text{ }^\circ\text{C}$ for 12 h. The coin cells were cycled at a current density of 200 mA g^{-1} with cutoff voltages of 1.0 and 2.5 V by using an Arbin BT-2000 Battery Test System.

5.3 Results and Discussion

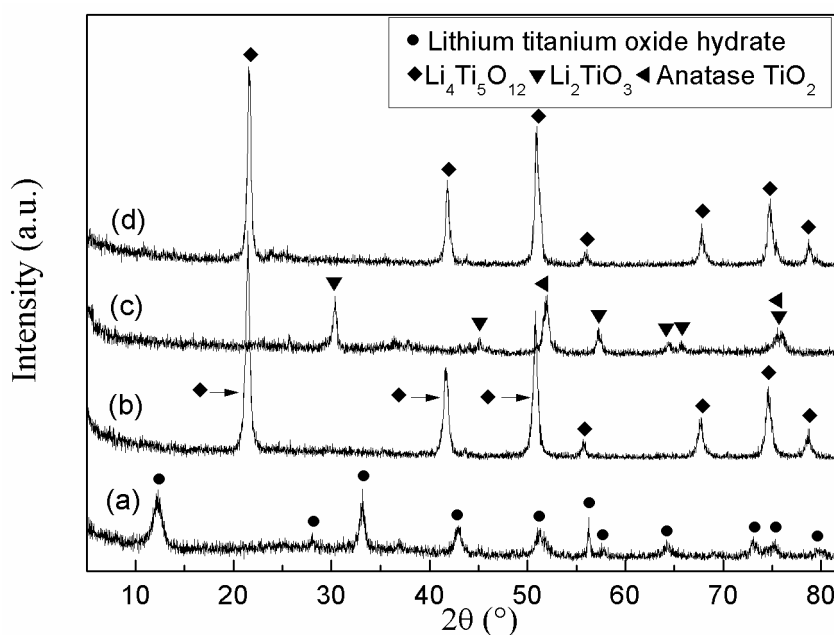


Figure 5.1 XRD patterns of the samples synthesized at $130 \text{ }^\circ\text{C}$ (a, b) and $170 \text{ }^\circ\text{C}$ (c, d). (a, c) as-prepared, (b, d) after calcination at $550 \text{ }^\circ\text{C}$ for 6 h in air.

[Figure 5.1](#) shows XRD patterns of the products as-prepared at 130 and $170 \text{ }^\circ\text{C}$, and after calcination at $550 \text{ }^\circ\text{C}$ for 6 h in air. In [Figure 5.1a](#), it can be seen that the product as-prepared at $130 \text{ }^\circ\text{C}$ is in agreement with lithium titanium oxide hydrate (JCPDS Card No.

47-0123). It is reported that lithium titanium oxide hydrate can be transformed into spinel $\text{Li}_4\text{Ti}_5\text{O}_{12}$ by heat treatment above 350°C [38]. For the sample as-prepared at 170°C , it is composed of Li_2TiO_3 (JCPDS Card No. 33-0831) and anatase TiO_2 (JCPDS Card No. 89-4921), as shown in Figure 5.1c. Li_2TiO_3 and anatase TiO_2 are two precursors widely used for the synthesis of spinel $\text{Li}_4\text{Ti}_5\text{O}_{12}$ by solid-state methods, as they can react with each other to form spinel $\text{Li}_4\text{Ti}_5\text{O}_{12}$ at elevated temperatures [39]. After calcined at 550°C for 6 h, both samples can be indexed as spinel lithium titanate, in accordance with spinel $\text{Li}_4\text{Ti}_5\text{O}_{12}$ (JCPDS Card No. 49-0207), as seen in Figure 5.1 (b, d). In the two XRD patterns, no other phases are found, implying high purity of the two samples.

Figure 5.2 presents morphologies of $\text{Li}_4\text{Ti}_5\text{O}_{12}$ synthesized at 130 and 170°C . In Figure 5.2a, it can be seen that the $\text{Li}_4\text{Ti}_5\text{O}_{12}$ prepared at 130°C possesses nanoflower-like spheres with diameters ranging from 500 to 900 nm. Each nanoflower-like sphere comprises many vertical nanosheets. The thickness of the nanosheets is on the order of 10 nm (Figure 5.2 (b, e)). Selected area electron diffraction (SAED) pattern (inset in Figure 5.2b) shows the highly crystalline features of spinel $\text{Li}_4\text{Ti}_5\text{O}_{12}$. An HRTEM image of one nanosheet is shown in Figure 5.2e. The lattice distance is measured to be 0.48 nm, which is well in accordance with the $d_{(111)}$ spacing of spinel $\text{Li}_4\text{Ti}_5\text{O}_{12}$. The morphology of the $\text{Li}_4\text{Ti}_5\text{O}_{12}$ produced at 170°C is shown in Figure 5.2 (c, d). This kind of $\text{Li}_4\text{Ti}_5\text{O}_{12}$ consists of numerous nanoparticles, the size of which varies from tens of nanometers to hundreds of nanometers, as seen in Figure 5.2d. Those nanoparticles agglomerate and form micro-size particles, as shown in Figure 5.2c. Based on the above results, it can be concluded that nanoflower-like and nanoparticle $\text{Li}_4\text{Ti}_5\text{O}_{12}$ with high purity and high crystallinity are successfully synthesized by the MH method and following heat treatment.

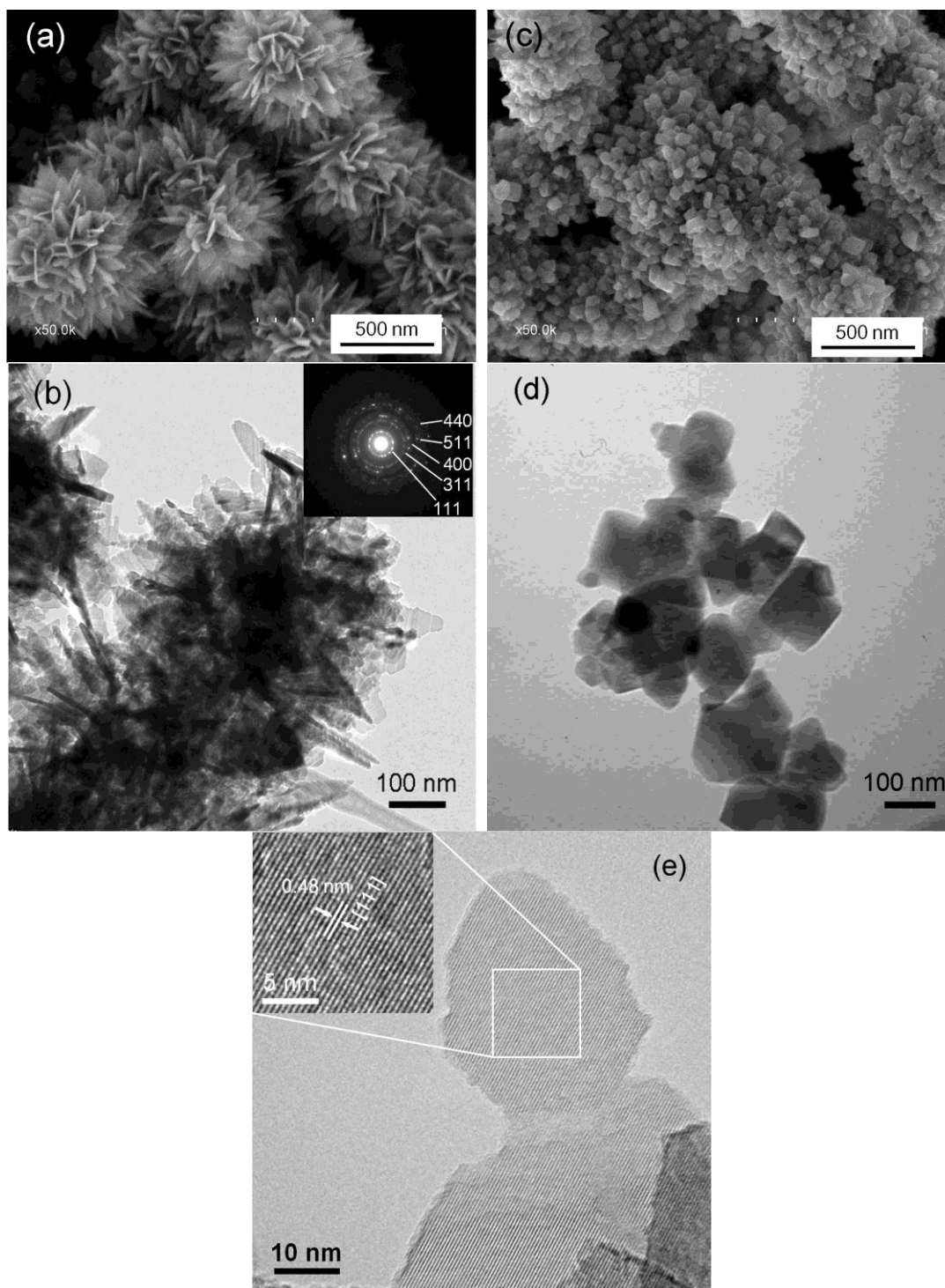


Figure 5.2 SEM (a, c) and TEM (b, d) images of $\text{Li}_4\text{Ti}_5\text{O}_{12}$ synthesized at 130 °C (a, b) and 170 °C (c, d). SAED pattern in the inset of (b) shows reflection rings corresponding to spinel $\text{Li}_4\text{Ti}_5\text{O}_{12}$. A HRTEM image (e) of $\text{Li}_4\text{Ti}_5\text{O}_{12}$ synthesized at 130 °C shows the image of lattice fringes and $d_{(111)} = 0.48$ nm.

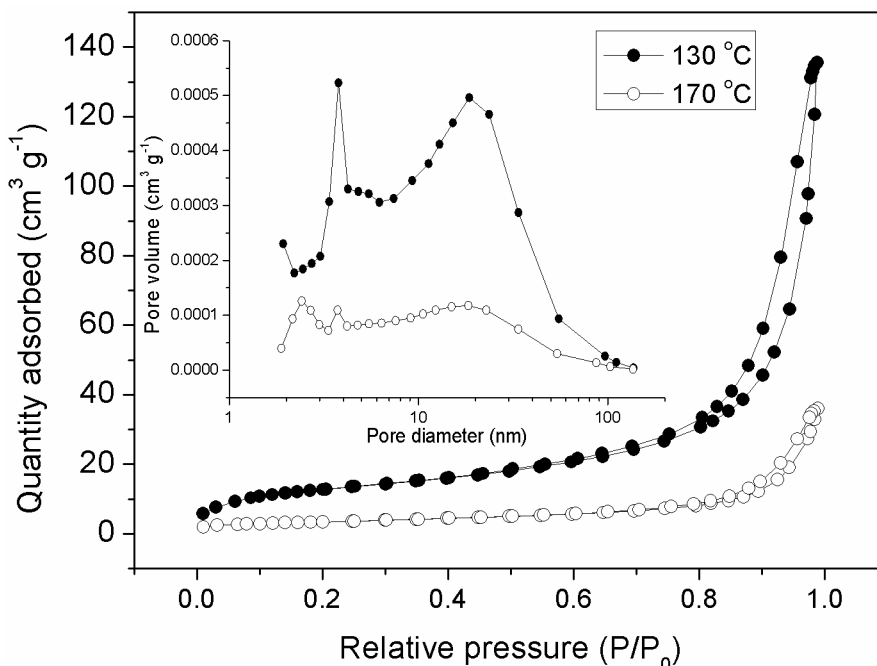


Figure 5.3 N₂ adsorption-desorption isotherms for Li₄Ti₅O₁₂ synthesized at 130 °C and 170 °C. Inset shows pore size distribution for both samples.

Figure 5.3 shows the N₂ adsorption/desorption isotherms and pore size distribution (inset) for the nanoflower-like and nanoparticle Li₄Ti₅O₁₂. The N₂ adsorption/desorption isotherms of both samples show type IV isotherms (IUPAC classification) with distinct hysteresis loops at high partial pressures, indicating the presence of mesopores and macropores [38]. Nanoflower-like and nanoparticle Li₄Ti₅O₁₂ show similar pore size distributions, with a narrow peak at about 3 nm and a broad peak centered at 19 nm. Brunauer-Emmett-Teller (BET) analysis shows that nanoflower-like Li₄Ti₅O₁₂ has a specific surface area of 46.8 m² g⁻¹, which is much larger than that of the similarly measured 12.1 m² g⁻¹ for the nanoparticle Li₄Ti₅O₁₂. The pore volumes of nanoflower-like and nanoparticle Li₄Ti₅O₁₂ are 0.21 cm³ g⁻¹ and 0.06 cm³ g⁻¹, respectively.

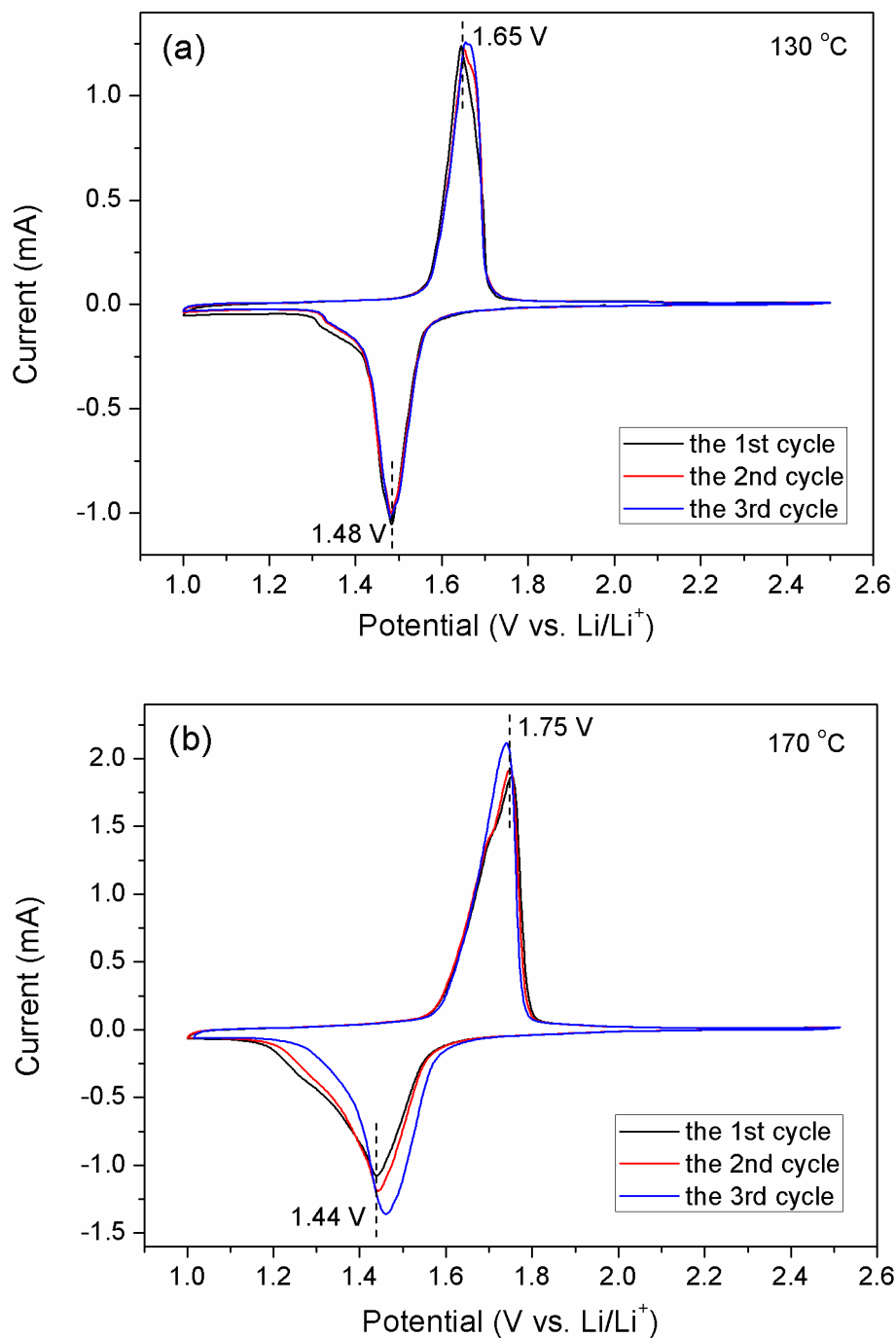


Figure 5.4 CV curves of $\text{Li}_4\text{Ti}_5\text{O}_{12}$ prepared at (a) 130 °C and (b) 170 °C in the first three cycles at a scan rate of 0.2 mV s^{-1} .

Figure 5.4 (a, b) show the cyclic voltammograms (CVs) of nanoflower-like and nanoparticle $\text{Li}_4\text{Ti}_5\text{O}_{12}$ respectively, for the first three cycles. In the first cycle, one pair of redox peaks appears at 1.48 (reduction) and 1.65 (oxidation) V in nanoflower-like

$\text{Li}_4\text{Ti}_5\text{O}_{12}$, and 1.44 (reduction) and 1.75 (oxidation) V in nanoparticle $\text{Li}_4\text{Ti}_5\text{O}_{12}$. Those two peaks correspond to the Li^+ insertion (reduction) and extraction (oxidation) processes [27-29]. The potential differences between anodic and cathodic peaks for nanoflower-like $\text{Li}_4\text{Ti}_5\text{O}_{12}$ and nanoparticle $\text{Li}_4\text{Ti}_5\text{O}_{12}$ are 0.17 and 0.33 V, respectively, suggesting a lower electrode polarization for the former [40]. Comparing Figure 5.4a with Figure 5.4b, we can see that the peak currents of anodic and cathodic reactions are comparable for nanoflower-like $\text{Li}_4\text{Ti}_5\text{O}_{12}$, while they are asymmetric for nanoparticle $\text{Li}_4\text{Ti}_5\text{O}_{12}$. The asymmetric peak currents have been observed in CVs of bulk spinel $\text{Li}_4\text{Ti}_5\text{O}_{12}$ and can be attributed to the slow lithium ion diffusivity in bulk spinel $\text{Li}_4\text{Ti}_5\text{O}_{12}$ [26]. It is believed that the agglomeration of nanoparticle $\text{Li}_4\text{Ti}_5\text{O}_{12}$ after heat treatment is responsible for its asymmetric peak currents in the CVs and less reversible behavior. For nanoflower-like $\text{Li}_4\text{Ti}_5\text{O}_{12}$, the thin nanosheets keep their shapes after calcination, and symmetric peak currents in CVs result, along with less polarization. Further supporting this observation, in Figure 5.4, it is shown that the initial three cycles almost overlap for nanoflower-like $\text{Li}_4\text{Ti}_5\text{O}_{12}$, while slight mismatch is observed for nanoparticle $\text{Li}_4\text{Ti}_5\text{O}_{12}$. This difference suggests that nanoflower $\text{Li}_4\text{Ti}_5\text{O}_{12}$ has better reversibility than nanoparticle $\text{Li}_4\text{Ti}_5\text{O}_{12}$ during the insertion/extraction processes of Li^+ into/from $\text{Li}_4\text{Ti}_5\text{O}_{12}$ [41].

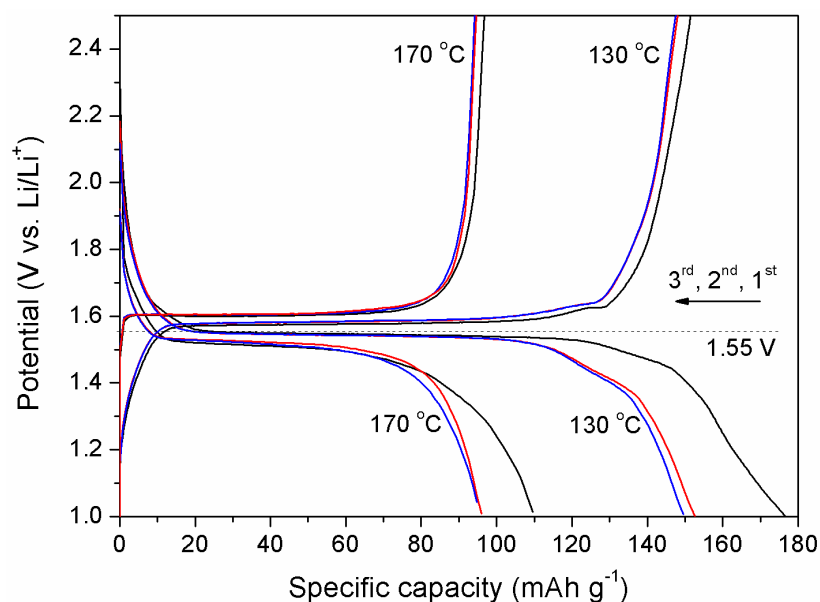


Figure 5.5 Galvanostatic charge/discharge curves for $\text{Li}_4\text{Ti}_5\text{O}_{12}$ prepared at 130 °C and 170 °C between 1 and 2.5 V at a current density of 200 mA g^{-1} .

Figure 5.5 shows the initial three charge/discharge curves for nanoflower-like and nanoparticle $\text{Li}_4\text{Ti}_5\text{O}_{12}$ samples. It can be seen that both samples exhibit flat plateaus around 1.5-1.6 V (vs. Li/Li^+), which corresponds to the reversible two phase transition between $\text{Li}_4\text{Ti}_5\text{O}_{12}$ and $\text{Li}_7\text{Ti}_5\text{O}_{12}$ [25, 26]. For nanoflower-like $\text{Li}_4\text{Ti}_5\text{O}_{12}$, the first discharge capacity reaches as high as 176.7 mAh g^{-1} , and an irreversible capacity of 14% is obtained at the first cycle. Nanoparticle $\text{Li}_4\text{Ti}_5\text{O}_{12}$ delivers a capacity of 109.8 mAh g^{-1} , and shows an irreversible capacity of 12 % for the first cycle. A similar irreversible capacity during the first charge/discharge cycle has been reported [39, 41]. It is usually attributed to the dissolution of surface impurities, such as adsorbed trace water, from the electrodes into the liquid electrolyte [29, 31]. From Figure 5.5, it can also be seen that nanoflower-like $\text{Li}_4\text{Ti}_5\text{O}_{12}$ has a smaller difference between charge and discharge plateau potentials than nanoparticle $\text{Li}_4\text{Ti}_5\text{O}_{12}$. This result is consistent with the CVs and suggests faster overall kinetics for the nanoflower-like $\text{Li}_4\text{Ti}_5\text{O}_{12}$ relative to the nanoparticle $\text{Li}_4\text{Ti}_5\text{O}_{12}$. The reason could be attributed to the shorter diffusion path of Li^+ in nanoflower-like $\text{Li}_4\text{Ti}_5\text{O}_{12}$. The larger specific surface area of nanoflower-like $\text{Li}_4\text{Ti}_5\text{O}_{12}$, relative to the nanoparticle $\text{Li}_4\text{Ti}_5\text{O}_{12}$ also insures a larger contact area between electrode and electrolyte, which is beneficial for the Li^+ exchange.

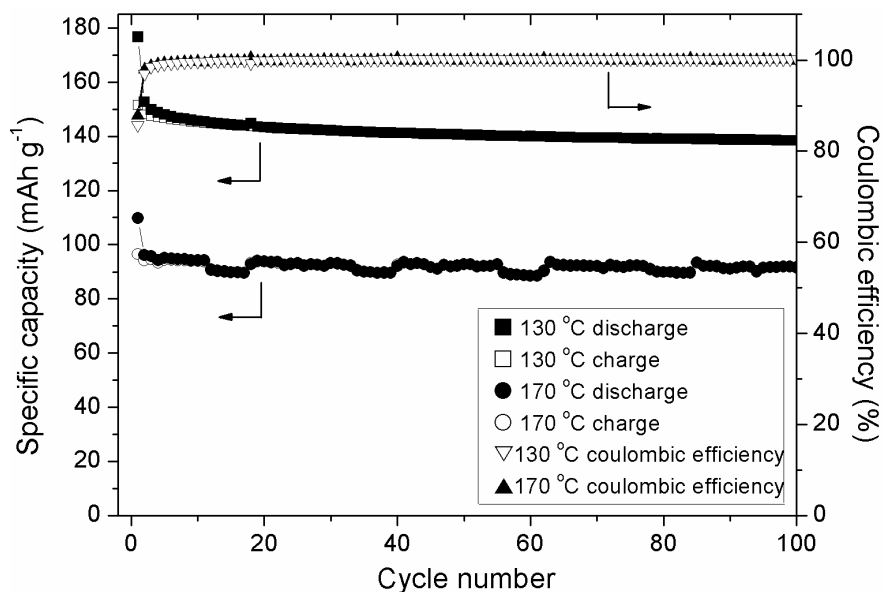


Figure 5.6 Cycling performance of $\text{Li}_4\text{Ti}_5\text{O}_{12}$ prepared at 130 °C and 170 °C measured at a current rate of 200 mA g^{-1} .

The cyclic stabilities of nanoflower-like and nanoparticle $\text{Li}_4\text{Ti}_5\text{O}_{12}$ are studied at a rate of 200 mA g^{-1} , and the results are shown in [Figure 5.6](#). It can be seen that the specific capacity of nanoparticle $\text{Li}_4\text{Ti}_5\text{O}_{12}$ remains stable after the first cycle. For nanoflower-like $\text{Li}_4\text{Ti}_5\text{O}_{12}$, the irreversible capacity rapidly decreases with upon cycling, and the specific capacity stabilizes after *ca.* 10 cycles. Both samples exhibit high coulombic efficiencies after the first cycle, effectively 100% for the measurement employed. After 100 cycles, the specific capacities of nanoflower-like and nanoparticle $\text{Li}_4\text{Ti}_5\text{O}_{12}$ are determined to be 138.4 mAh g^{-1} and 91.7 mAh g^{-1} , respectively. It has been widely reported that excellent electrochemical performance could be achieved in high surface area anodes due to short diffusion distance of Li^+ in solid body [25, 26, 31]. In addition, provided deleterious side reactions are not a concern, smaller particles are beneficial in that they provide increased surface area for electrochemical reaction and reduced overall reaction resistance. Therefore, the larger specific capacity of nanoflower-like $\text{Li}_4\text{Ti}_5\text{O}_{12}$ than nanoparticle $\text{Li}_4\text{Ti}_5\text{O}_{12}$ could be attributed to the larger specific surface area and shorter Li^+ diffusion path of the former relative to the latter. In [Figure 5.6](#), the capacity retention after 100 cycles is calculated to be 78% and 82% for nanoflower-like and nanoparticle $\text{Li}_4\text{Ti}_5\text{O}_{12}$, respectively. It should be noted that the capacity retentions in our case are slightly lower than those reported in some literatures [42, 43]. Nonetheless, similar capacity retention of $\text{Li}_4\text{Ti}_5\text{O}_{12}$ was observed previously [39, 41], and the large capacity loss could be attributed to several reasons. One reason is that the annealing temperature of $\text{Li}_4\text{Ti}_5\text{O}_{12}$ in our case ($550 \text{ }^\circ\text{C}$) is relatively lower than those ($700\text{-}800 \text{ }^\circ\text{C}$) in Ref. [42, 43]. Higher annealing temperature can lead to better crystallinity of $\text{Li}_4\text{Ti}_5\text{O}_{12}$ and then a reduced initial capacity loss [44]. However, it can also easily result in the agglomeration of $\text{Li}_4\text{Ti}_5\text{O}_{12}$, which would make its performance worse. Another reason could be the adsorbed trace water, surface defects such as surface vacancies or voids, which are common for nanomaterials but will lead to irreversible capacity [28, 29, 31]. It should be mentioned that nanoflower-like $\text{Li}_4\text{Ti}_5\text{O}_{12}$ synthesized by MH method exhibits comparable performance to $\text{Li}_4\text{Ti}_5\text{O}_{12}$ prepared by CH method, whereas MH process takes much shorter time (20 minutes) than CH process (12-36 h) [26, 28, 31].

5.4 Conclusions

Spinel $\text{Li}_4\text{Ti}_5\text{O}_{12}$ with nanoflower-like and nanoparticle morphologies were successfully synthesized by a microwave-assisted hydrothermal method and following heat treatment. The nanoflower-like $\text{Li}_4\text{Ti}_5\text{O}_{12}$ exhibits a layered structure of high specific surface area and provides good reversibility and cycling performance. The nanoflower-like $\text{Li}_4\text{Ti}_5\text{O}_{12}$ delivered a specific capacity of 176.7 mAh g^{-1} during the first cycle, and maintained 138.4 mAh g^{-1} after 100 cycles.

Acknowledgements

This research was supported by General Motors of Canada, Natural Sciences and Engineering Research Council of Canada (NSERC), Canada Research Chair (CRC) Program, Canada Foundation for Innovation (CFI), Ontario Research Fund (ORF), Ontario Early Researcher Award (ERA) and University of Western Ontario.

References

- [1] J. -M. Tarascon, M. Armand, Issues and challenges facing rechargeable lithium batteries, *Nature* **2001**, *414*, 359-367.
- [2] K. Kang, Y. S. Meng, J. Br éger, C. P. Grey, G. Ceder, Electrodes with high power and high capacity for rechargeable lithium batteries, *Science* **2006**, *311*, 977-980.
- [3] M. Winter, J. O. Besenhard, M. E. Spahr, P. Nov ák, Insertion electrode materials for rechargeable lithium batteries, *Adv. Mater.* **1998**, *10*, 725-763.
- [4] M. Armand, J. -M. Tarascon, Building better batteries, *Nature* **2008**, *451*, 652-657.
- [5] N. A. Kaskhedikar, J. Maier, Lithium storage in carbon nanostructures, *Adv. Mater.* **2009**, *21*, 2664-2680.
- [6] K. M. Colbow, J. R. Dahn, R. R. Haering, Structure and electrochemistry of the spinel oxides LiTi_2O_4 and $\text{Li}_{4/3}\text{Ti}_{5/3}\text{O}_4$, *J. Power Sources* **1989**, *26*, 397-402.

- [7] T. Ohzuku, A. Ueda, Why transition metal (di) oxides are the most attractive materials for batteries, *Solid State Ionics* **1994**, *69*, 201-211.
- [8] E. Ferg, R. J. Gummow, A. de Kock, M. M. Thackeray, Spinel anodes for lithium-ion batteries, *J. Electrochem. Soc.* **1994**, *141*, L147-L150.
- [9] T. Ohzuku, A. Ueda, N. Yamamoto, Zero-strain insertion material of $\text{Li}[\text{Li}_{1/3}\text{Ti}_{5/3}]\text{O}_4$ for rechargeable lithium cells, *J. Electrochem. Soc.* **1995**, *142*, 1431-1435.
- [10] K. Zaghib, M. Armand, M. Gauthier, Electrochemistry of anodes in solid-state Li-ion polymer batteries, *J. Electrochem. Soc.* **1998**, *145*, 3135-3140.
- [11] S. Scharner, W. Weppner, P. Schmid-Baurmann, Evidence of two-phase formation upon lithium insertion into the $\text{Li}_{1.33}\text{Ti}_{1.67}\text{O}_4$ spinel, *J. Electrochem. Soc.* **1999**, *146*, 857-861.
- [12] F. Ronci, P. Reale, B. Scrosati, S. Panero, V.R. Albertini, P. Perfetti, M. di Michiel, J.M. Merino, High-resolution in-situ structural measurements of the $\text{Li}_{4/3}\text{Ti}_{5/3}\text{O}_4$ “zero-strain” insertion material, *J. Phys. Chem. B* **2002**, *106*, 3082-3086.
- [13] A. Gotcher, Nanostructured electrodes: experts have recognized for years the advantages of lithium ion technology over traditional power batteries, particularly those based on lead acid chemistry, *Adv. Mater. Processes* **2005**, *163*, 32-33.
- [14] I. Plitz, A. Dupasquier, F. Badway, J. Gural, N. Pereira, A. Gmitter, G. G. Amatucci, The design of alternative nonaqueous high power chemistries, *Appl. Phys. A: Mater. Sci. Process.* **2006**, *82*, 615-626.
- [15] S. Stewart, P. Albertus, V. Srinivasan, I. Plitz, N. Pereira, G. Amatucci, J. Newman, Evidence of two-phase formation upon lithium insertion into the $\text{Li}_{1.33}\text{Ti}_{1.67}\text{O}_4$ spinel, *J. Electrochem. Soc.* **2008**, *155*, A253-A261.
- [16] P. Liu, E. Sherman, M. Verbrugge, Electrochemical and structural characterization of lithium titanate electrodes, *J. Solid State Electrochem.* **2010**, *14*, 585-591.

- [17] J. S. Wang, M. W. Verbrugge, P. Liu, Composite titanate-graphite negative electrode for improved state-of-charge estimation of lithium-ion batteries, *J. Electrochem. Soc.* **2010**, *157*, A185-A189.
- [18] J. Shu, Study of the interface between $\text{Li}_4\text{Ti}_5\text{O}_{12}$ electrodes and standard electrolyte solutions in 0.0-5.0V, *Electrochem. Solid-State Lett.* **2008**, *11*, A238-A240.
- [19] H. Ge, N. Li, D. Li, C. Dai, D. Wang, Electrochemical characteristics of spinel $\text{Li}_4\text{Ti}_5\text{O}_{12}$ discharged to 0.01V, *Electrochem. Comm.* **2008**, *10*, 719-722.
- [20] S. Takai, M. Kamata, S. Fujine, K. Yoneda, K. Kanda, T. Esaka, Diffusion coefficient measurement of lithium ion in sintered $\text{Li}_{1.33}\text{Ti}_{1.67}\text{O}_4$ by means of neutron radiography, *Solid State Ionics* **1999**, *123*, 165-172.
- [21] M. W. Verbrugge, P. Liu, Electrochemical characterization of high-power lithium ion batteries using triangular voltage and current excitation sources, *J. Power Sources* **2007**, *174*, 2-8.
- [22] M. Imazaki, K. Ariyoshi, T. Ohzuku, An approach to 12 V “lead-free” batteries: tolerance toward overcharge of 2.5 V battery consisting of LTO and LAMO, *J. Electrochem. Soc.* **2009**, *156*, A780-A786.
- [23] N. Takami, H. Inagaki, T. Kishi, Y. Harada, Y. Fujita, K. Hoshina, Electrochemical kinetics and safety of 2-volt class Li-ion battery system using lithium titanium oxide anode, *J. Electrochem. Soc.* **2009**, *156*, A128-A132.
- [24] K. Zaghib, M. Dontigny, A. Guerfi, P. Charest, I. Rodrigues, A. Mauger, C. M. Julien, Safe and fast-charging Li-ion battery with long shelf life for power applications, *J. Power Sources* **2011**, *196*, 3949–3954.
- [25] D. K. Lee, H. -W. Shim, J. S. An, C. M. Cho, I. -S. Cho, K. S. Hong, D. W. Kim, Synthesis of heterogeneous $\text{Li}_4\text{Ti}_5\text{O}_{12}$ nanostructured anodes with long-term cycle stability, *Nanoscale Res. Lett.* **2010**, *5*, 1585-1589.

- [26] J. Li, Z. Tang, Z. Zhang, Controllable formation and electrochemical properties of one-dimensional nanostructured spinel $\text{Li}_4\text{Ti}_5\text{O}_{12}$, *Electrochem. Comm.* **2005**, 7, 894-899.
- [27] C. Lai, Y. Y. Dou, X. Li, X. P. Gao, Improvement of the high rate capability of hierarchical structured $\text{Li}_4\text{Ti}_5\text{O}_{12}$ induced by the pseudocapacitive effect, *J. Power Sources* **2010**, 195, 3676-3679.
- [28] J. Chen, L. Yang, S. Fang, Y. Tang, Synthesis of sawtooth-like $\text{Li}_4\text{Ti}_5\text{O}_{12}$ nanosheets as anode materials for Li-ion batteries, *Electrochim. Acta* **2010**, 55, 6596-6600.
- [29] L. Shen, C. Yuan, H. Luo, X. Zhang, K. Xu, Y. Xia, Facile synthesis of hierarchically porous $\text{Li}_4\text{Ti}_5\text{O}_{12}$ microspheres for high rate lithium ion batteries, *J. Mater. Chem.* **2010**, 20, 6998-7004.
- [30] E. K. Nyutu, C. -H. Chen, S. Sithambaram, V. M. B. Crisostomo, S. L. Suib, Systematic control of particle size in rapid open-vessel microwave synthesis of K-OMS-2 nanofibers, *J. Phys. Chem. C* **2008**, 112, 6786-6793.
- [31] A. Phuruangrat, D. J. Ham, S. J. Hong, S. Thongtem, J. S. Lee, Synthesis of hexagonal WO_3 nanowires by microwave-assisted hydrothermal method and their electrocatalytic activities for hydrogen evolution reaction, *J. Mater. Chem.* **2010**, 20, 1683-1690.
- [32] J. Zhang, Y. Wang, J. Yang, J. Chen, Z. Zhang, Microwave-assisted synthesis of potassium titanate nanowires, *Mater. Lett.* **2006**, 60, 3015-3017.
- [33] W. Li, Synthesis and characterization of bismuth sulfide nanowires through microwave solvothermal technique, *Mater. Lett.* **2008**, 62, 243-245.
- [34] L. Ma, W. Chen, J. Zhao, Y. Zheng, X. Li, Z. Xu, Microwave-assisted synthesis of praseodymium hydroxide nanorods and thermal conversion to oxide nanorod, *Mater. Lett.* **2007**, 61, 1711-1714.

- [35] S. Q. Chen, Y. Wang, Microwave-assisted synthesis of a Co_3O_4 -graphene sheet-on-sheet nanocomposites as a superior anode material for Li-ion batteries, *J. Mater. Chem.* **2010**, *20*, 9735-9739.
- [36] A. V. Murugan, T. Muraliganth, A. Manthiram, Comparison of microwave assisted solvothermal and hydrothermal synthesis of LiFePO_4/C nanocomposite cathodes for lithium ion batteries, *J. Phys. Chem. C* **2008**, *112*, 14665-14671.
- [37] Y. Zhang, H. Feng, X. Wu, L. Wang, A. Zhang, T. Xia, H. Dong, M. Liu, One-step microwave synthesis and characterization of carbon-modified nanocrystalline LiFePO_4 , *Electrochim. Acta* **2009**, *54*, 3206-3210.
- [38] Y. Tang, L. Yang, S. Fang, Z. Qiu, $\text{Li}_4\text{Ti}_5\text{O}_{12}$ hollow microspheres assembled by nanosheets as an anode material for high-rate lithium ion batteries, *Electrochim. Acta* **2009**, *54*, 6244-6249.
- [39] T. Yuan, R. Cai, Z. Shao, Different effect of the atmospheres on the phase formation and performance of $\text{Li}_4\text{Ti}_5\text{O}_{12}$ prepared from ball-milling-assisted solid-phase reaction with pristine and carbon-precoated TiO_2 as starting materials, *J. Phys. Chem. C* **2011**, *115*, 4943-4952.
- [40] B. Zhang, H. Du, B. Li, F. Kang, Structure and electrochemical properties of Zn-doped $\text{Li}_4\text{Ti}_5\text{O}_{12}$ as anode materials in Li-ion battery, *Electrochem. Solid-State Lett.* **2010**, *13*, A36-A38.
- [41] Y. F. Tang, L. Yang, Z. Qiu, J. S. Huang, Preparation and electrochemical lithium storage of flower-like spinel $\text{Li}_4\text{Ti}_5\text{O}_{12}$ consisting of nanosheets, *Electrochem. Commun.* **2008**, *10*, 1513-1516.
- [42] C. Jiang, E. Hosono, M. Ichihara, I. Honma, H. Zhou, Synthesis of nanocrystalline $\text{Li}_4\text{Ti}_5\text{O}_{12}$ by chemical lithiation of anatase nanocrystals and postannealing, *J. Electrochem. Soc.* **2008**, *115*, A553-A556.

- [43] A. S. Prakash, P. Manikandan, K. Ramesha, M. Sathiya, J-M. Tarascon, A. K. Shukla, Solution-combustion synthesized nanocrystalline $\text{Li}_4\text{Ti}_5\text{O}_{12}$ as high-rate performance Li-ion battery anode, *Chem. Mater.* **2010**, 22, 2857-2863.
- [44] J. Deng, Z. Lu, I. Belharouak, K. Amine, C. Y. Chung, Preparation and electrochemical properties of $\text{Li}_4\text{Ti}_5\text{O}_{12}$ thin film electrodes by pulsed laser deposition, *J. Power Sources* **2009**, 193, 816-821.

Chapter 6 Crystallinity-Controlled Synthesis of Zirconium Oxide Thin Films on Nitrogen-Doped Carbon Nanotubes by Atomic Layer Deposition [§]

In LIBs, one main reason for the performance degradation is the side reactions happening at the interface of electrode materials and liquid electrolytes. For example, in the LiCoO₂ cathode, HF acid generated from the electrolytes during the cycling can dissolve the Co element in LiCoO₂, thereby leading to rapid fading of the LIB performance. One way to prevent or alleviate the dissolution of Co is coating LiCoO₂ cathode with an artificial thin layer, which is inert to HF acid. Zirconium oxide (ZrO₂) is one typical coating material.

In this chapter, ZrO₂ thin film was deposited on nitrogen-doped carbon nanotubes (NCNTs) by atomic layer deposition (ALD) using tetrakis(dimethylamido)zirconium (IV) and water as precursors. The observation using scanning electron microscope and transmission electron microscope (TEM) revealed that the tubular films of 100-cycle ZrO₂ were very uniform and conformal on NCNTs. Further characterization, using X-ray diffraction, Raman spectroscopy, selected area electron diffraction and high-resolution TEM disclosed that the crystallinity of the deposited ZrO₂ films was controllable with deposition temperatures in the range of 100 - 250 °C. In contrast to the pure amorphous ZrO₂ film deposited at 100 °C, tetragonal crystalline ZrO₂ film was prepared at 250 °C, while a mixture of the former two phases was found between 150 °C and 200 °C. In all cases, the growth of ZrO₂ tubular films on NCNTs showed a transformation from an “island growth” mode to a “layer-by-layer growth” mode with increasing ALD cycles.

Keyword: Zirconium oxide, carbon nanomaterials; nanocomposites; nitrogen doping; growth mode.

[§] Part of this chapter has been published in *J. Phys. Chem. C* **2012**, *116*, 14656-14664.

6.1 Introduction

Since the work by Iijima in 1991[1], carbon nanotubes (CNTs) have been drawing much attention from various areas due to their unique properties [2, 3]. Up to now, CNTs have been involved in a wide range of potential applications, such as reinforced materials, nanoelectronic devices, field emission display sources, and energy storage and conversion devices [4, 5]. Recently, great interest has been raised to make one-dimensional nanocomposites by using CNTs as supports for the deposition of various materials [6-9]. In particular, CNTs have been considered as the most promising templates for fabricating metal oxide-CNT nanocomposites, which possess exceptional chemical, mechanical, and physical properties [10-15]. These advanced nanocomposites are likely to become key components in the next generation of magnetic, optical, and electronic devices.

Zirconium oxide (ZrO_2) is an attractive material in many fields because of its excellent mechanical, thermal, optical and electrical characteristics [16, 17]. ZrO_2 can present three polymorphic crystalline structures, *i.e.*, monoclinic (below 1170 °C), tetragonal (1170-2370 °C), and cubic (above 2370 °C) [17]. Recently, there were many efforts devoted to fabricate ZrO_2 -CNT nanocomposites in hopes of broadening the applications of ZrO_2 [18-23]. For example, ZrO_2 -CNT nanocomposite prepared by a hydrothermal method was found to be a good biocompatible matrix for protein immobilization [18]. In addition, it was also found that the Pt catalyst supported by ZrO_2 -CNT nanocomposites exhibited significantly improved catalytic activity towards methanol and ethanol oxidation in direct methanol and ethanol fuel cells, compared with that supported by either CNTs or commercial C [19, 20]. Moreover, CNT transistors integrated with high-k ZrO_2 were applied as advanced gate dielectrics, which will be crucial for future molecular electronics [21]. Thus, ZrO_2 -CNT nanocomposites are promising for applications in fuel cells, batteries, electronics devices, and chemical sensors.

To fulfill these applications, it is of great importance to controllably synthesize ZrO_2 -CNT nanocomposites. In previous studies, the fabrication of ZrO_2 -CNT nanocomposites was mainly achieved by solution-based methods [16, 17, 23-25]. For example, Sun *et al.* [23] synthesized ZrO_2 -CNT nanocomposites *via* decomposition of $Zr(NO_3)_4 \cdot 8H_2O$ in

supercritical carbon dioxide-ethanol solution with dispersed CNTs at relatively low temperatures. Shan *et al.* [24] prepared ZrO₂-CNT nanocomposites with phase-controlled ZrO₂ by hydrothermal treatment of CNTs in ZrOCl₂·8H₂O aqueous solution at 150 °C. Most of these studies were focused on controlling the phase [17, 24, 25] or morphology [16] of ZrO₂ coated on CNTs, and the CNTs used in these studies required a pretreatment process by either covalent [26] or non-covalent [14, 27] methods to functionalize their inert surface. The pretreatment might adversely affect the inherent properties of the CNTs.

Herein, we developed an alternative approach to synthesize ZrO₂-CNT nanocomposites. This approach features crystallinity-controlled deposition of ZrO₂ tubular films directly on nitrogen doped carbon nanotubes (NCNTs) using atomic layer deposition (ALD), which has been our research interest both in synthesizing [28, 32] and applications [33, 34]. ALD is a unique technique which allows the deposition of conformal and uniform thin films via sequential and self-terminating gas-solid reactions with controlled film thickness at atomic level [35, 36]. The coating of ZrO₂ on CNTs was previously achieved with the use of ZrCl₄ and H₂O as precursors, whereas detailed studies are still lacking [21]. Moreover, the use of ZrCl₄ as Zr precursor may constrain the application of ZrO₂, because ZrCl₄ suffers from serious processing problems including the corrosion of deposition system caused by HCl generated during the reaction, high risk of small particles being transported into substrates, and high evaporation temperature (165 °C) due to its low volatility [37]. In comparison, tetrakis(dimethylamido)zirconium (IV) (Zr(NMe₂)₄) as an ALD precursor has several advantages over ZrCl₄, such as sufficient volatility, thermal stability, and high reactivity to a hydroxylated surface [38-40]. Using Zr(NMe₂)₄ and H₂O as ALD precursors, for example, ZrO₂ films were successfully deposited on Si and glassy carbon substrates, with a growth per cycle (GPC) of 0.096 ± 0.002 nm in the range of 50 - 250 °C [38, 39]. It was reported that the ALD of ZrO₂ (ALD-ZrO₂) using these two precursors consists of two half reactions [38]:



where “||” represents substrate surface and “(g)” denotes vapor species. Therefore, in this work, $\text{Zr}(\text{NMe}_2)_4$ and H_2O were employed as precursors for ALD- ZrO_2 . The NCNTs were homemade and suitable for ALD processes without any additional pretreatment steps [29, 31]. In summary, this work describes the uniform deposition of ALD- ZrO_2 films on NCNTs, with not only precisely controlled thickness at nanoscale level, but also highly tunable crystallinity, from amorphous to crystalline. In addition, the growth process of ALD- ZrO_2 on NCNTs was explored, and the growth mechanisms of ALD- ZrO_2 on NCNTs were proposed. This kind of ZrO_2 -NCNT nanocomposites synthesized by ALD may find many potential applications, such as fuel cells, batteries, electronics and gas sensors.

6.2 Experimental section

6.2.1 Synthesis of NCNTs

NCNTs were prepared by a chemical vapor deposition (CVD) method, using melamine ($\text{C}_3\text{H}_6\text{N}_6$, 99+%, Aldrich) as the only source for both carbon and nitrogen. The substrate used for the growth of NCNTs was a carbon paper, which had been sequentially coated by an aluminum film (30 nm in thickness) and an iron film (5 nm in thickness) in a sputtering system. The aluminum film as a buffer layer could improve the quality and growth rate of NCNTs, while the iron film could catalyze the growth of NCNTs [41]. In a typical process, NCNTs were grown by the pyrolysis of melamine at 800 °C using argon (99.999% in purity) as a protective and carrier gas. More details could be found in our previous work [42].

6.2.2 ZrO_2 -NCNTs by ALD

The deposition of ZrO_2 on NCNTs was achieved by alternatively supplying $\text{Zr}(\text{NMe}_2)_4$ (99%, STREM) and deionized water (H_2O) into a commercial ALD reactor (Savannah 100, Cambridge Nanotech Inc., USA). $\text{Zr}(\text{NMe}_2)_4$ was heated to 75 °C, while water was kept at room temperature. In that case, sufficient precursor vapors could be supplied for the deposition of ZrO_2 . Additionally, the delivery lines were heated to 100 °C to prevent the precursors from condensation. Nitrogen gas (99.999% in purity) was used as a carrier gas with a flow rate of 20 sccm, and the ALD reactor was maintained at a low level of

base pressure (typically 0.3 - 0.4 Torr) by a vacuum pump (Pascal 2005 I, Adixen). One ALD cycle was executed with the following six steps: (1) a supply of $\text{Zr}(\text{NMe}_2)_4$ with a t_1 pulse time; (2) a 3.0 s extended exposure of $\text{Zr}(\text{NMe}_2)_4$ to NCNTs; (3) a purging of oversupplied $\text{Zr}(\text{NMe}_2)_4$ and any byproducts with a t_2 purge time; (4) a supply of H_2O with a t_3 pulse time; (5) a 3.0 s extended exposure of H_2O to NCNTs; (6) a purging of excess H_2O and any byproducts a t_4 purge time. In short, the deposition procedure can be described as $t_1 - t_2 - t_3 - t_4$. ZrO_2 was deposited on NCNTs by repeating the above ALD cycle at 250, 200, 150 and 100 °C, respectively.

6.2.3 Characterization of ZrO_2 -NCNTs

The morphology and structure of as-synthesized ZrO_2 -NCNT nanocomposites were characterized by a field-emission scanning electron microscope (SEM, Hitachi S4800) equipped with energy dispersive X-ray spectroscopy (EDS), transmission electron microscope (TEM, Hitachi H - 7000), high-resolution TEM (HRTEM, JEOL 2010 FEG), micro X-ray diffraction (XRD, Bruker D8, Co - $K\alpha$ source, $\lambda=1.7892 \text{ \AA}$), and Raman spectrometer (HORIBA Scientific LabRAW HR800) with an incident laser beam of 532.4 nm.

6.3 Results and Discussion

Figure 6.1 (a-c) shows the morphology and structure of NCNTs prepared by the CVD method. From Figure 6.1 (a, b), it can be seen that the carbon paper was totally covered by high-density NCNTs with diameters in a range of 20 - 35 nm. TEM image in Figure 6.1c indicates that the synthesized NCNTs possess a typical bamboo-like structure, which is induced by nitrogen doping in the hexagonal framework of carbon layers [42, 43]. Raman spectrum of the NCNTs shows two first-order Raman peaks centered at $\sim 1342 \text{ cm}^{-1}$ and $\sim 1582 \text{ cm}^{-1}$, which are so-called D-band and G-band respectively, as seen in Figure 6.1d. The intensity ratio between D-band and G-band (I_D/I_G) is calculated to be 0.94 for the NCNTs, revealing its high degree of disorder due to nitrogen doping [43].

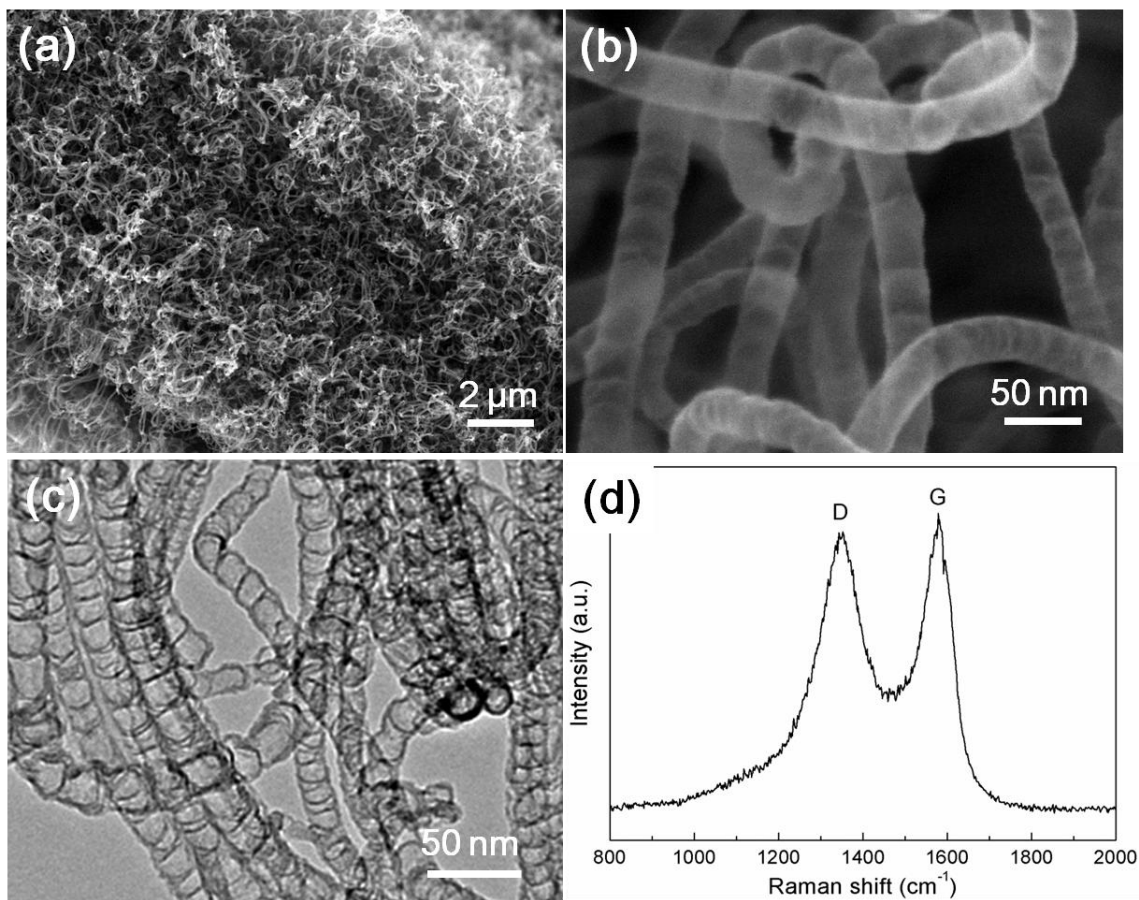


Figure 6.1 SEM images (a, b), TEM image (c) and Raman spectrum (d) of NCNTs synthesized by the CVD method.

In order to find out the conditions for saturated growth of ALD-ZrO₂, the pulse time and purge time for both precursors were optimized. The deposition temperature was chosen to be 200 °C using Zr(NMe₂)₄ and H₂O as precursors [38]. The optimization was carried out by changing one parameter at a time while keeping the others constant. The results indicated that a 0.5 s pulse of Zr(NMe₂)₄ and a 1.0 s pulse of H₂O are sufficient to realize saturated growth of ALD-ZrO₂ thin film on NCNTs (Figure SI-6.1). The purge time is required at least 30 s in order to avoid CVD-like growth of ZrO₂ (Figure SI-6.2 (a, b)) and to achieve uniform deposition of ALD-ZrO₂ thin film (Figure SI-6.2 (c, d)). A prolonged purge time had no obvious effect on the thickness and uniformity of ALD-ZrO₂ thin film (Figure SI-6.2 (e, f)). Therefore, all the ALD-ZrO₂ was conducted with the procedure of 0.5 s - 30 s - 1 s - 30 s.

6.3.1 Crystalline development of ALD-ZrO₂

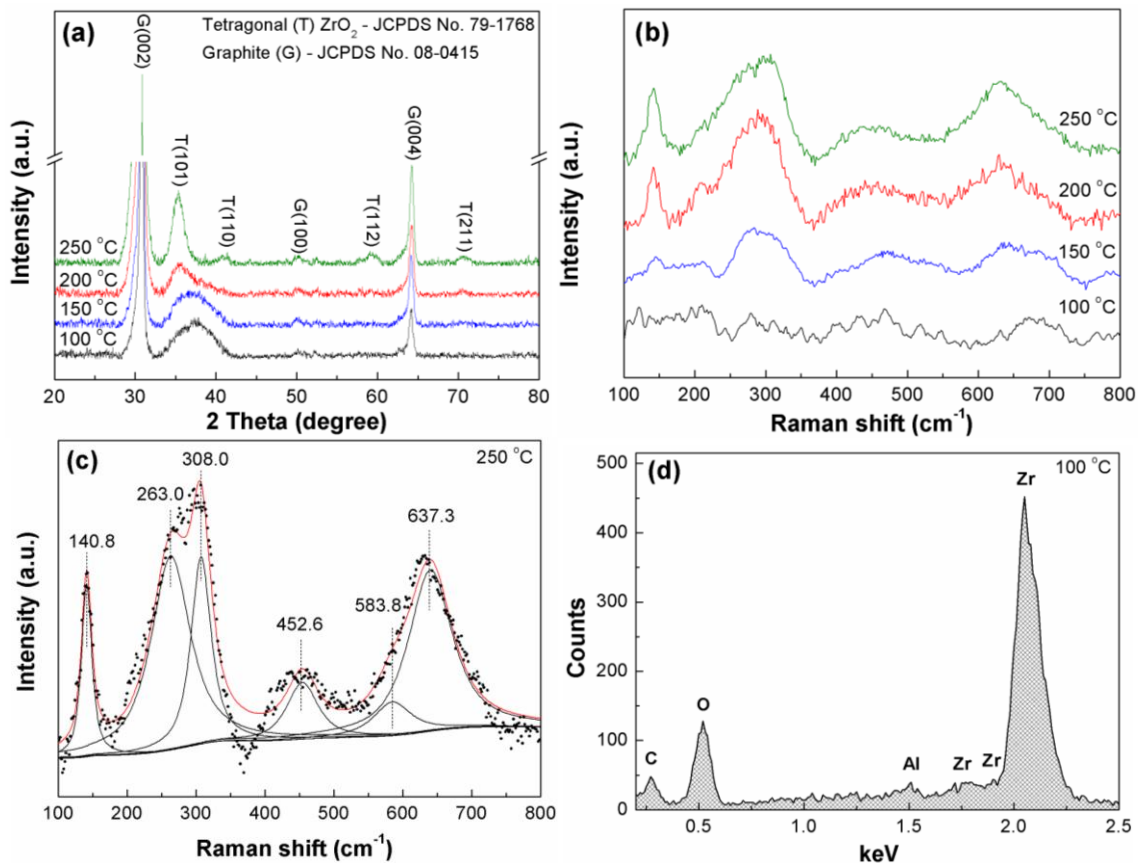


Figure 6.2 XRD patterns (a) and Raman spectra (b) of 100-cycle ZrO₂-NCNTs deposited at 250, 200, 150, and 100 °C. (c) Deconvolution of Raman spectrum of 100-cycle ZrO₂-NCNTs prepared at 250 °C. (d) EDS of 100-cycle ZrO₂-NCNTs prepared at 100 °C.

The structural phases of 100-cycle ALD-ZrO₂ prepared at 250, 200, 150 and 100 °C were identified by XRD and Raman techniques, and the results are presented in Figure 6.2. Figure 6.2a shows the XRD patterns of 100-cycle ZrO₂-NCNTs prepared at 250, 200, 150 and 100 °C. It can be seen that all samples exhibit two strong peaks at 30 ° and 64 °, and a weak one at 50 °, which are indexed as (002), (004) and (100) planes of graphite (JCPDS PDF No. 08-0415), respectively. They are apparently induced by the carbon paper and NCNTs grown on it. For the ZrO₂-NCNTs prepared at 250 °C, the other peaks located at 36 °, 41 °, 59 °, and 71 ° are well consistent with the planes of (101), (110), (112) and (211) of tetragonal ZrO₂ (JCPDS PDF No. 79-1768), respectively. The four peaks could be also assigned to cubic ZrO₂, however, the existence of which is excluded later by Raman

examination. With a decrease in deposition temperature, the peak of (101) plane of tetragonal ZrO_2 shifts to higher degrees and becomes broader in terms of half-width. In the meantime, the other peaks belonging to tetragonal ZrO_2 become weaker in intensity. They totally disappear in the ZrO_2 -NCNTs prepared at 100 °C. The XRD results indicate that the ALD- ZrO_2 experienced a gradual decrease in its crystallinity when decreasing the deposition temperature. Raman spectroscopy was carried out on the above samples in a region of 100-800 cm^{-1} , and the results are presented in Figure 6.2 (b, c). From Figure 6.2b, it can be seen that Raman spectra are approximately the same for ZrO_2 -NCNTs prepared at 250, 200 and 150 °C. Deconvolution of the Raman spectrum for ZrO_2 -NCNTs prepared at 250 °C reveals six peaks located at 140.8, 263.0, 308.0, 452.6, 538.8 and 637.3 cm^{-1} (Figure 6.2c), which can be clearly assigned to the six Raman active modes ($A_{1g} + 2B_{1g} + 3E_g$) of tetragonal ZrO_2 [44,45]. The similar results were also obtained for ZrO_2 -NCNTs prepared at 200 and 150 °C. For the ZrO_2 -NCNTs prepared at 100 °C, however, broad peaks with weak intensities are observed in its Raman spectrum (Figure 6.2b), from which it is hard to identify the phase of the deposited ZrO_2 . This kind of Raman spectrum is probably due to the extremely limited long-range periodicity of ZrO_2 prepared at such a low temperature [45]. Nonetheless, EDS analysis verified the presence of Zr and O elements in the ZrO_2 -NCNTs prepared at 100 °C, as seen in Figure 6.2d.

It should be noted that tetragonal ZrO_2 is generally stable at high temperatures (1170 - 2370 °C) [17], while in our case it was not only prepared at temperatures below 250 °C but also stable at room temperature. The occurrence of tetragonal ZrO_2 at low temperatures has been reported previously [46-49]. Earlier studies believed that the low-temperature tetragonal ZrO_2 should be ascribed to grain size effect, *i.e.* ZrO_2 with small size and high surface area can provide high surface energy to stabilize metastable tetragonal ZrO_2 at low temperatures [48,49]. In this work, NCNTs acted as promising ALD- ZrO_2 substrate with high surface area and high surface energy, which in return help the stabilization of tetragonal ZrO_2 at temperatures below 250 °C.

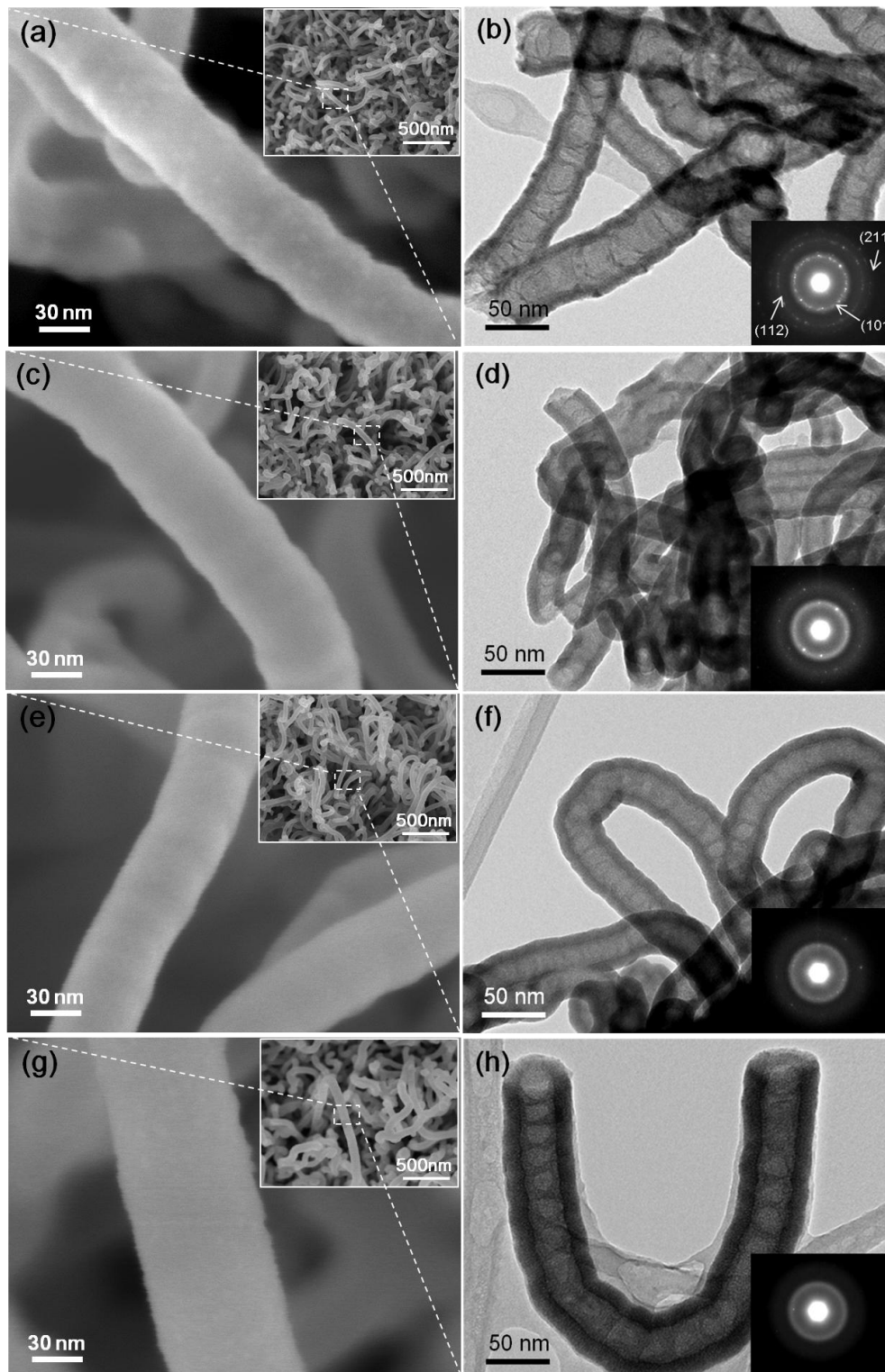


Figure 6.3 SEM (a, c, e, g) and TEM (b, d, f, h) images of 100-cycle ZrO_2 -NCNTs prepared at 250 °C (a, b), 200 °C (c, d), 150 °C (e, f), and 100 °C (g, h). (Inset in each TEM image corresponds to its SAED pattern).

The morphologies of 100-cycle ALD-ZrO₂ on NCNTs prepared at 250, 200, 150 and 100 °C were observed by SEM and TEM, and the results are presented in Figure 6.3. From Figure 6.3 (a, c, e, g), it can be clearly seen that NCNTs are homogeneously coated with ZrO₂ tubular thin films at deposition temperatures of 250, 200, 150, and 100 °C. TEM observation reveals that these ZrO₂ thin films are extremely uniform and conformal on NCNTs in all the cases, as shown in Figure 6.3 (b, d, f, h). Furthermore, selected area electron diffraction (SAED) was employed and the crystallinity of ALD-ZrO₂ was revealed, as shown by the insets in Figure 6.3 (b, d, f, h). For the ZrO₂-NCNTs prepared at 250 °C, the SAED diffraction rings can be indexed as (101), (112) and (211) planes of tetragonal ZrO₂, indicating its polycrystalline feature (see the inset in Figure 6.3b). From Figure 6.3 (d) and (f), it can be clearly seen that the diffraction rings become more diffusive with the decreasing deposition temperature. In the case of 100 °C, only diffusive rings are observed, as shown by the inset in Figure 6.3h, manifesting that the ALD-ZrO₂ consists of only amorphous phase. The SAED results indicate that ALD-ZrO₂ on NCNTs is temperature-dependent in the crystallinity. In particular, the information extracted from SAED and XRD results (see Figure 6.2a) are consistent on the crystallinity of the ALD-ZrO₂ prepared at different deposition temperatures.

The microstructures of 100-cycle ALD-ZrO₂ were further investigated using HRTEM, as shown in Figure 6.4. Figure 6.4a reveals that ALD-ZrO₂ thin film is fully crystalline at 250 °C, and the interplanar spacing of 0.298 nm (as marked in Figure 6.4a) is consistent with the spacing distance between (101) planes of tetragonal ZrO₂. In the case of 200 °C, the ZrO₂ thin film is composed of both crystalline nanoparticles and amorphous layers. These nanoparticles, with tetragonal ZrO₂ phase, randomly distribute in the “matrix” of the amorphous ZrO₂, as shown in Figure 6.4b. At the lower deposition temperature of 150 °C, as shown in Figure 6.4c, it is found that these nanoparticles become sparse, and the “matrix” of amorphous ZrO₂ layers takes the dominance. At the lowest deposition temperature of 100 °C, as shown in Figure 6.4d, only amorphous ZrO₂ thin film can be identified. Based on the above results, it can be concluded that the crystallinity of ALD-ZrO₂ is temperature-dependent, *i.e.*, the deposited ZrO₂ shows crystalline tetragonal phase at 250 °C, amorphous phase at 100 °C, and a mixture of the former two in the range of 200 - 150 °C.

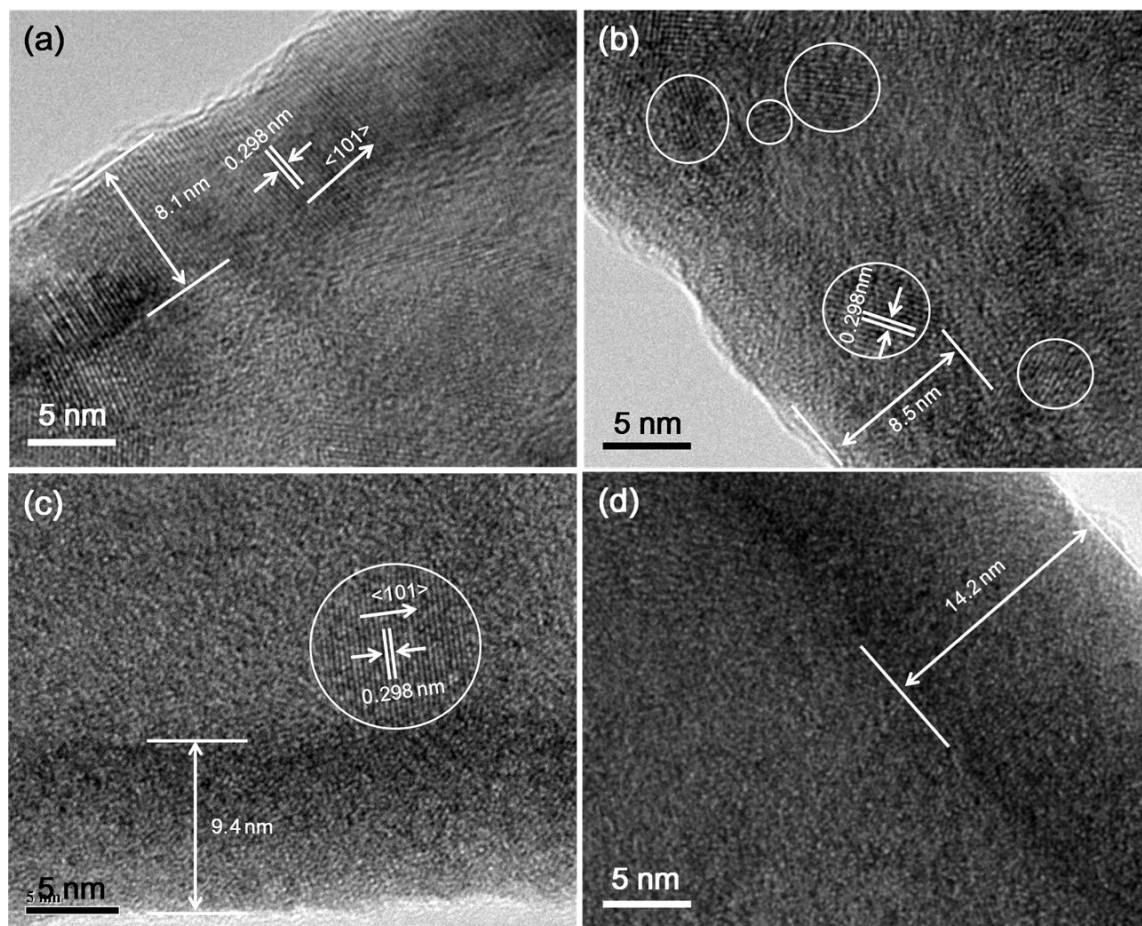


Figure 6.4 HRTEM images of 100-cycle ZrO_2 -NCNTs prepared at (a) 250 °C, (b) 200 °C, (c) 150 °C and (d) 100 °C, respectively.

During ALD processes, growth per cycle (GPC) is an important measure to evaluate the growth ability of desirable materials. In this work, the GPC of ALD- ZrO_2 is calculated based on the thickness of 100-cycle ALD- ZrO_2 thin films, as shown in [Figure 6.4](#). The GPC turns out to be 0.081, 0.085, 0.094 and 0.142 nm, at 250, 200, 150 and 100 °C, respectively (as plotted in [Figure 6.5](#)). It can be seen that the GPC of ZrO_2 keeps almost the same (around 0.085 nm) from 250 °C to 150 °C. One can also find that the GPC of ZrO_2 at 100 °C (0.142 nm) is apparently higher than those at the other temperatures.

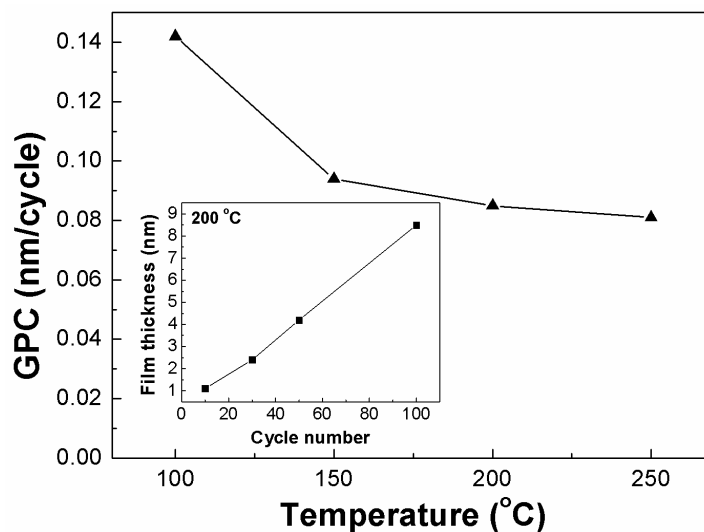


Figure 6.5 GPC of ALD-ZrO₂ on NCNTs as a function of deposition temperature (inset shows the thickness of ZrO₂ thin film deposited at 200 °C as a function of ALD cycles).

6.3.2 Growth process of ALD-ZrO₂

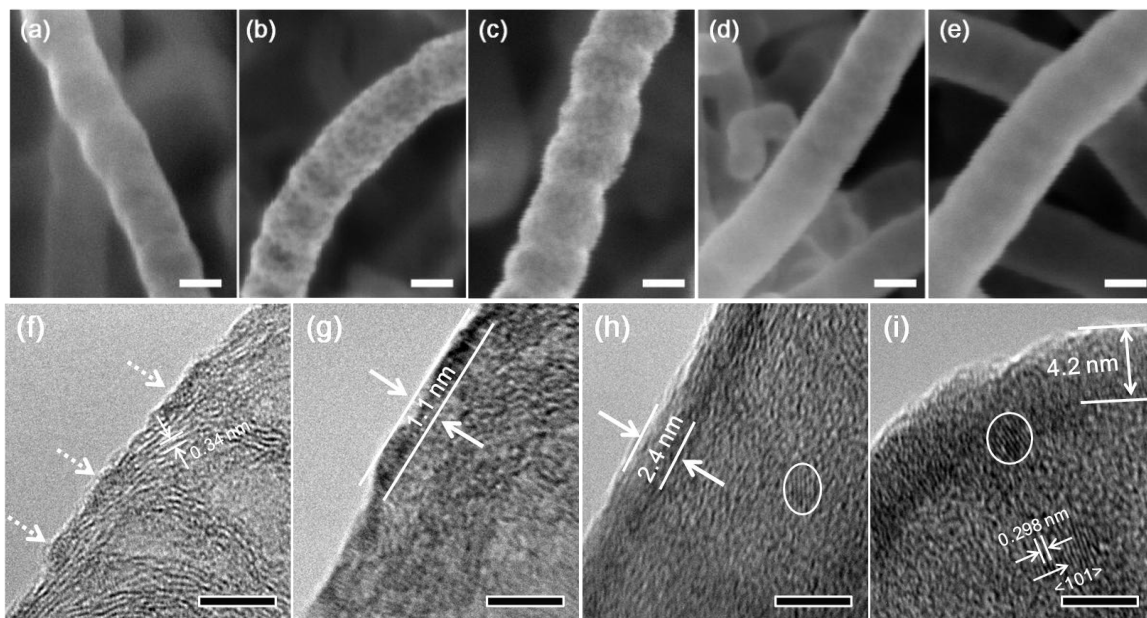


Figure 6.6 SEM images (a-e) of NCNTs without ZrO₂ coating (a) and with ZrO₂ coated at 200 °C after (b) 5 cycles; (c) 10 cycles; (d) 30 cycles and (e) 50 cycles. HRTEM images (f-i) of NCNTs with ZrO₂ coated at 200 °C after (f) 5 cycles; (g) 10 cycles; (h) 30 cycles and (i) 50 cycles (The scale bar in (a-e) and (f-i) represents 20 nm and 5 nm respectively).

The morphological evolution of ALD-ZrO₂ with ALD cycle was explored by SEM and HRTEM on the ZrO₂-NCNTs prepared at 200 °C, and shown in Figure 6.6. Comparing Figure 6.6 (a) with (b), it is obvious that the surface of NCNTs is coated with many nanoparticles after only 5 ALD cycles. With the increase of ALD cycle, those nanoparticles start to coalesce (Figure 6.6c), and eventually close into a uniform thin film after 30 cycles (Figure 6.6d). Further increasing ALD cycle leads to a thicker thin film, with its uniformity maintained, as shown in Figure 6.6e and Figure 6.3c. The morphological development of ALD-ZrO₂ was confirmed by HRTEM in Figure 6.6 (f-i). SEM observation on the ZrO₂-NCNTs prepared at 250, 150 and 100 °C indicates the similar growth process of ALD-ZrO₂ (Figure SI-(6.4-6.6)). This phenomenon implies that the growth of ALD-ZrO₂ on NCNTs follows an “island growth” mode at the very early stage and a “layer-by-layer growth” mode afterward.

HRTEM images of the ZrO₂-NCNTs prepared at 200 °C after different ALD cycles also disclose the crystalline development of ALD-ZrO₂ with ALD cycles, as displayed in Figure 6.6 (f-i). Before 10 cycles, the ALD-ZrO₂ exhibits amorphous state, as seen in Figure 6.6 (f, g). After 30 cycles, the ALD-ZrO₂ thin film is still dominated by amorphous phase, in the “matrix” of which some crystalline tetragonal ZrO₂ nanoparticles (diameter around 1.5 nm) can be found (Figure 6.6h). With increasing ALD cycle, those crystalline ZrO₂ nanoparticles grow into bigger sizes, while the amorphous ZrO₂ thin film becomes thicker, as shown in Figure 6.6i and Figure 6.3d. Thus, at 200 °C, the growth of amorphous ZrO₂ continues during the whole ALD process, while nucleation and growth of crystalline ZrO₂ start in the “matrix” of amorphous ZrO₂ at the intermediate stage. The thicknesses of ZrO₂ thin films after different ALD cycles at 200 °C are measured in Figure 6.6 (g-i), and plotted as a function of ALD cycle number (see the inset in Figure 6.5). In Figure 6.5, it can be clearly seen that the film thickness of ALD-ZrO₂ shows an almost linear relationship with ALD cycles, indicating the self-limiting growth of ALD-ZrO₂ on NCNTs.

6.3.3 Discussion

From the results in sections 6.3.1 and 6.3.2, one can easily see that ALD is distinguished as an innovative approach to synthesize ZrO₂-NCNT nanocomposites in a well-controlled manner. The deposited ZrO₂ thin films not only have highly tunable crystallinity, from amorphous to crystalline, but also have precisely controlled thickness at atomic level. The first feature is mainly ascribed to temperature-dependence of ALD-ZrO₂, whereas the second one is resulted from the self-terminating nature of ALD process. To better understand the characteristic of ALD-ZrO₂, it is essentially important to clarify the influence of ALD process parameters, *i.e.* the temperatures, substrates and precursors [36], on the growth process, the GPC and the crystallinity of ALD-ZrO₂ on NCNTs.

As disclosed in section 6.3.2, the growth of ALD-ZrO₂ on NCNTs follows an “island growth” mode at the very early stage and a “layer-by-layer growth” mode after coalescence of these islands into a thin film, in a temperature range of 100 - 250 °C. Interestingly, island growth of ALD-ZrO₂ was also previously observed on the substrate of hydrogen-terminated silicon using ZrCl₄ and H₂O as precursors [50-52]. The reason for this undesired ALD process was attributed to the lack of functional OH adsorption sites on the hydrogen passivated surfaces, and the island growth of ZrO₂ started most likely at reactive defect sites of the substrate [50]. Another study reported that ZnO nanoparticles could be grown on single-walled carbon nanotubes (SWCNTs) by ALD, due to the sparse amount of defective sites on SWCNTs [53]. Thus, the NCNT substrate in our case is believed to play a crucial role in determining the special growth process of ALD-ZrO₂. As well-known, NCNTs are rich of surface defects induced by nitrogen doping [43]. These N-induced defects make the surface of NCNTs more reactive than that of CNTs, thereby suitable for the direct growth of metal nanoparticles or nanowires on it [54-55]. In our previous work, NCNTs were also employed as substrates for ALD-SnO₂, and it was found that the surface defect sites, especially induced by pyridine-like N and graphite-like N, were preferable sites for the nucleation of ALD-SnO₂ [29]. Therefore, in this work, it is reasonable to believe that N-induced defect sites at the surface of NCNTs are responsible for the island growth of ALD-ZrO₂ at the very early stage. During the first cycle, Zr(NMe₂)₄ would chemically bond with these N-induced

defect sites, and then H₂O introduced would react with the chemisorbed Zr(NMe₂)₄ via Reaction (2), generating –OH group terminated surface [38]. The following ALD cycles would happen preferably on the existing ZrO₂ surface *via* Reaction (6-1) and Reaction (6-2) sequentially, leading to the “island growth” of ALD-ZrO₂ on NCNTs (see Figure 6.6 (b, f)). With further increase of ALD cycle, those ALD-ZrO₂ islands would grow in both vertical and lateral directions, and finally coalesce into a film (Figure 6.6 (c, d, g, h)). From this point on, the deposition of ZrO₂ would occur on the film following a “layer-by-layer growth” mode (Figure 6.6 (e, i) and Figure 6.3 (c, d)). The thickness of ZrO₂ thin film can be simply but accurately controlled by means of the number of ALD cycle (see Figure 6.5). In addition, it was demonstrated that chemically bonded N in NCNTs were thermally stable up to 800 °C [56], and thus the N-induced defects on NCNTs in our case could be considered to remain unaffected by the temperature change from 100 °C to 250 °C. Moreover, theoretical calculation [57] showed that for Zr(NMe₂)₄, scission of metal-ligand bonds was more feasible than scission of N-C bonds, and experiment study [38] also indicated that the reaction of Zr(NMe₂)₄ and H₂O in ALD would follow Reaction (6-1) and (6-2) in the temperature range of 100 - 250 °C. Therefore, in our case, it can be considered that the temperature change do not affect the substrate and the reaction mechanism of precursors. At all deposition temperatures, ALD-ZrO₂ followed the similar growth process, *i.e.* “island growth” mode at the very early stage and “layer-by-layer growth” mode after the close of these islands into a thin film, as presented in Figure 6.6 and Figure SI-(6.4-6.6).

GPC is an important factor to measure the growth of ALD materials. In this work, the GPC of ALD-ZrO₂ experienced an increase with decreasing temperature (see Figure 6.5). In particular, the GPC of ALD-ZrO₂ at 100 °C (0.142 nm) is obviously higher than those at the other temperatures (around 0.085 nm). Earlier studies have shown that the temperature could affect the GPC of ALD materials by having effect on the number and types of reactive sites on the substrates, and/or the preferred reaction mechanisms [36]. As discussed above, the temperature change from 100 - 250 °C seemed not to affect the reaction mechanism of Zr(NMe₂)₄ and H₂O in the ALD process [38,57]. However, temperature does have influence on the -OH groups, which were reactive sites for ALD process and generated via Reaction (1). Many previous studies [58-60] have indicated

that the number and types of hydroxyl groups were temperature-dependent, and high temperature could lead to dehydroxylation. During ALD-ZrO₂, the dehydroxylation of hydroxyl groups was described as follows [59]:



Undoubtedly, this dehydroxylation would reduce the number of -OH groups and thereby lead to a lower GPC at higher temperatures. Besides hydroxyl groups, physisorbed Zr(NMe₂)₄ and H₂O are probably accountable for the higher GPC at 100 °C. Ritala *et al.* [61] have shown that even at 500 °C, the desorption of water from the hydroxyl-terminated surface could be slow enough, and long purge periods were needed. Hausmann *et al.* [38] have proved that it took much longer time to purge all surface-physisorbed Zr(NMe₂)₄ and H₂O at lower temperatures. Therefore, given the same purge time in our case, there would be more surface-physisorbed Zr(NMe₂)₄ and H₂O at lower temperatures, which would in return contribute to the growth of ZrO₂. Surprisingly, the ZrO₂ thin film at lower temperatures still maintained its uniformity, as shown in [Figure 6.3](#) and [Figure 6.4](#). A prolonged purge time (60 s) for both precursors did not obviously affect the thickness of ZrO₂ thin film ([Figure SI-6.3](#)). Probably longer purge time than 60s is required in order to avoid the surface-physisorbed precursors, but it will inevitably increase the preparation time of ALD-ZrO₂.

Besides growth mode and GPC, it is of great interest to explain the temperature dependence of the crystallinity of ALD-ZrO₂. In section 6.3.2, one can find that the deposition temperature is the only parameter that distinguishes the four samples in this work. Apparently, it plays a crucial role in determining the crystallinity of ALD-ZrO₂. Similar trend of crystallinity as a function of temperature was also previously reported in ALD-grown ZrO₂ [38, 62, 63], TiO₂ [28, 64], HfO₂ [65], and SnO₂ [29, 30]. It was demonstrated that the temperature had strong effects on surface mobility of absorbed species [64, 66], reaction mechanisms [29, 30, 63], and surface reactive sites [29, 63], thereby influencing the crystallinity of ALD-grown materials. High temperatures could enhance the surface mobility of absorbed species and promote the ordering of the structure with minimum energy, thus leading to the growth of crystallites [64, 66]. Meng

et al. [29,30] prepared phase-controlled ALD-SnO₂ using SnCl₄ and H₂O as precursors, and proposed that the change of reaction mechanism from ligand exchange and chlorination with increasing temperatures was responsible for the phase transition from amorphous to crystalline. In addition, Scarel *et al.* [63] suggested that the reaction mechanism between -OH species and ZrCl₄ could be changed by the decreased density of -OH species with increasing temperatures, thus affecting the crystallinity of deposited ZrO₂. In our case, a higher temperature could help the mobilization of absorbed species, and enable the Zr and/or O ions to occupy the positions corresponding to the lowest free energy of the crystal [64], resulting in the crystalline phase of ALD-ZrO₂. XRD (Figure 6.2a) and HRTEM (Figure 6.4) results indicated that the ZrO₂ was preferentially oriented in the [101] direction, which seems to have the lowest free energy. Until now, there is no evidence showing that the reaction mechanism between Zr(NMe₂)₄ and H₂O is temperature-dependent in the temperature range we employed, as discussed previously. Nonetheless, the increase of temperature can modify the surface reactive sites *via* dehydroxylation process described in Reaction (6-3), leading to reduced hydroxyl groups at the surface. This might be a reason accountable for the increased crystallinity of ALD-ZrO₂ with elevating temperatures. Unfortunately, there is to date little knowledge about the effect of decreased hydroxyl groups on the reaction mechanism and the crystallinity of ALD-ZrO₂ using Zr(NMe₂)₄ and H₂O as precursors, and further investigations are needed. Another potential reason for ZrO₂ being amorphous at lower temperatures is the residual dimethylamido ligand in the film, which could possibly prevent the crystallization of ZrO₂. From above discussion, one can clearly see the critical effect of temperature on the crystallinity of ZrO₂ at given ALD cycle. On the other hand, it should be noticed that at a given temperature, the crystallinity of ZrO₂ would be mainly related to the film thickness, and more crystalline ZrO₂ could be found in the thicker film, as disclosed in Figure 6.6. This phenomenon was also observed in previous studies, and could be explained as follows [39, 67]. At a given temperature, the nucleation events of crystalline ZrO₂ distributed randomly over the surface of the substrate during each ALD cycle. The increase of ALD cycle could lead to the nucleation of more crystalline ZrO₂ nuclei in the thicker film. Once crystalline ZrO₂ nuclei formed, the following ALD cycle would contribute further mass to the nuclei resulting in the growth of crystalline ZrO₂.

Therefore, the thicker film induced by more ALD cycle contained more crystalline ZrO_2 than the thinner film did. It should be emphasized that the ALD of ZrO_2 was done no more than 100 ALD cycles in this work. Further increase of ALD cycles could lead to the change of ZrO_2 in its crystallinity (amorphous or crystalline) [33, 67], its phase (tetragonal, cubic or monoclinic) [67], or/and even its surface roughness [33].

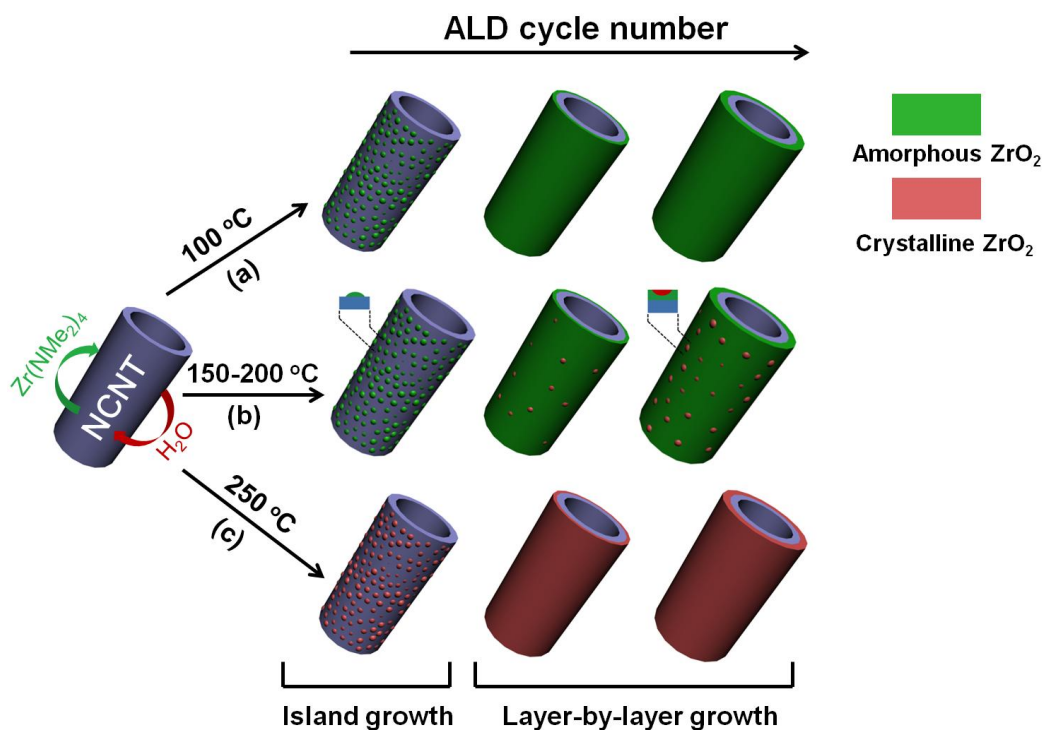


Figure 6.7 Schematic diagram for growth mechanism of ALD-ZrO₂ on NCNTs at (a) 100 °C, (b) 150-200 °C and (c) 250 °C.

Figure 6.7 presents a schematic diagram to summarize the crystallite and morphological developments of ALD-ZrO₂ at temperatures between 100 °C and 250 °C. It can be seen that ZrO₂ exhibits only amorphous phase at 100 °C, whereas only crystalline phase at 250 °C. At intermediate temperature (150 - 200 °C), the growth of amorphous ZrO₂ starts at the very beginning and continues during the whole process, while crystalline ZrO₂ nucleated and grew only during the intermediate process. It should be noted that crystalline ZrO₂ was embedded in the “matrix” of amorphous ZrO₂, not affecting the uniformity of the ZrO₂ thin film. At all temperatures, the growth of ALD-ZrO₂ follows an

“island growth” mode at the very early stage and a “layer-by-layer growth” mode after the coalescence of those “islands” into a film.

6.4 Conclusions

In this work, ZrO₂-NCNT nanocomposites were successfully prepared by ALD at deposition temperatures from 100 °C to 250 °C. The results showed that the crystallinity of ZrO₂ thin film experienced a gradual decrease with the decrease of temperature. Deposition temperature of 250 °C resulted in pure crystalline ZrO₂, while 100 °C led to pure amorphous ZrO₂. Mixed phases of crystalline and amorphous ZrO₂ appeared in ZrO₂-NCNTs between 150 °C to 200 °C. The ZrO₂ thin film was very uniform and conformal. The GPC of ZrO₂ was 0.081, 0.085, 0.094 and 0.142 nm, at 250, 200, 150 and 100 °C, respectively. At all deposition temperatures, the growth of ZrO₂ followed “island-growth” mode during the early stage and “layer-by-layer growth” mode after the coalescence of those “islands” into a film. It is expected that such ZrO₂-NCNT nanocomposites have great potential for various applications in fuel cells, batteries, electronics devices, and chemical sensors.

Acknowledgements

This research was supported by General Motors of Canada, Natural Sciences and Engineering Research Council of Canada (NSERC), Canada Foundation for Innovation (CFI), Ontario Research Fund (ORF), Ontario Early Researcher Award (ERA) and University of Western Ontario. The authors also would like to thank Fred Pearson at McMaster University for his help on HRTEM.

References

- [1] S. Iijima, Helical microtubules of graphitic carbon, *Nature* **1991**, 354, 56-58.
- [2] M. Dresselhaus, G. Dresselhaus, R. Saito, Physics of carbon nanotubes, *Carbon* **1995**, 33, 883-891.

- [3] A. Okamoto, I. Gunjishima, T. Inoue, M. Akoshima, H. Miyagawa, T. Nakano, T. Baba, M. Tanemura, G. Oomi, Thermal and electrical conduction properties of vertically aligned carbon nanotubes produced by water-assisted chemical vapor deposition, *Carbon* **2011**, *49*, 294-298.
- [4] R. H. Baughman, A. A. Zakhidov, W. A. De Heer, Carbon nanotubes-the route toward applications, *Science* **2002**, *297*, 787-792.
- [5] K. Gong, F. Du, Z. Xia, M. Durstock, L. Dai, Nitrogen-doped carbon nanotube array with high electrocatalytic activity for oxygen reduction, *Science* **2009**, *323*, 760-764.
- [6] D. J. Guo, H. L. Li, Highly dispersed Ag nanocomposites on functional MWNT surfaces for methanol oxidation in alkaline solution, *Carbon* **2005**, *43*, 1259-1264.
- [7] Y. H. Wang, Y. N. Li, J. B. Zang, H. Huang, Microstructure and thermal characteristic of Si-coated multi-walled carbon nanotubes, *Nanotechnology* **2006**, *17*, 3817.
- [8] Y. Morisada, Y. Miyamoto, SiC-coated carbon nanotubes and their application as reinforcements for cemented carbides, *Mater. Sci. Eng. A* **2004**, *381*, 57-61.
- [9] L. Fu, Z. M. Liu, Y. Q. Liu, B. X. Han, J. Q. Wang, P. A. Hu, L. C. Cao, D. B. Zhu, Coating carbon nanotubes with rare earth oxide multiwalled nanotubes, *Adv. Mater.* **2004**, *16*, 350-352.
- [10] G. Korneva, H. Ye, Y. Gogotsi, D. Halverson, G. Friedman, J. C. Bradley, K. G. Kornev, Carbon nanotubes loaded with magnetic particles, *Nano Lett.* **2005**, *5*, 879-884.
- [11] A. Jitianu, T. Cacciaguerra, R. Benoit, S. Delpeux, F. Béguin, S. Bonnamy, Synthesis and characterization of carbon nanotubes-TiO₂ nanocomposites, *Carbon* **2004**, *42*, 1147-1151.
- [12] L. Jiang, L. Gao, Fabrication and characterization of ZnO-coated multi-walled carbon nanotubes with enhanced photocatalytic activity, *Mater. Chem. Phys.* **2005**, *91*, 313-316.

- [13] Y. X. Liang, Y. J. Chen, T. H. Wang, Low-resistance gas sensors fabricated from multiwalled carbon nanotubes coated with a thin tin oxide layer, *Appl. Phys. Lett.* **2004**, *85*, 666-668.
- [14] D. B. Farmer, R. G. Gordon, Atomic layer deposition on suspended single-walled carbon nanotubes via gas-phase noncovalent functionalization, *Nano Lett.* **2006**, *6*, 699-703.
- [15] R. M. Piticescu, R. R. Piticescu, D. Taloi, V. Badilita, Hydrothermal synthesis of ceramic nanomaterials for functional applications, *Nanotechnology* **2003**, *14*, 312.
- [16] J. Lu, J. B. Zang, S. X. Shan, H. Huang, Y. H. Wang, Synthesis and characterization of core-shell structural MWNT-zirconia nanocomposites, *Nano Lett.* **2008**, *8*, 4070-4074.
- [17] T. Y. Luo, T. X. Liang, C. S. Li, Stabilization of cubic zirconia by carbon nanotubes, *Mater. Sci. Eng. A* **2004**, *366*, 206-209.
- [18] R. Liang, M. Deng, S. Cui, H. Chen, J. Qiu, Direct electrochemistry and electrocatalysis of myoglobin immobilized on zirconia/multi-walled carbon nanotube nanocomposite, *Mater. Res. Bull.* **2010**, *45*, 1855-1860.
- [19] H. Song, X. Qiu, F. Li, Promotion of carbon nanotube-supported Pt catalyst for methanol and ethanol electro-oxidation by ZrO₂ in acidic media, *Appl. Catal. A* **2009**, *364*, 1-7.
- [20] D. Guo, X. Qiu, W. Zhu, L. Chen, Synthesis of sulfated ZrO₂/MWCNT composites as new supports of Pt catalysts for direct methanol fuel cell application, *Appl. Catal. B* **2009**, *89*, 597-601.
- [21] A. Javey, H. Kim, M. Brink, Q. Wang, A. Ural, J. Guo, P. Mcintype, P. Mceuen, M. Lundstrom, H. Dai, High-k dielectrics for advanced carbon-nanotube transistors and logic gates, *Nature* **2002**, *1*, 241-246.

- [22] K. Pal, D. J. Kang, Z. X. Zhang, J. K. Kim, Synergistic effects of zirconia-coated carbon nanotubes on crystalline structure of polyvinylidene fluoride nanocomposites: electrical properties and flame-retardant behavior, *Langmuir* **2010**, *26*, 3609-3614.
- [23] Z. Sun, X. Zhang, N. Na, Z. Liu, B. Han, G. An, Synthesis of ZrO₂-carbon nanotube composites and their application as chemiluminescent sensor material for ethanol, *J. Phys. Chem. B* **2006**, *110*, 13410-13414.
- [24] Y. Shan, L. Gao, Synthesis and characterization of phase controllable ZrO₂-carbon nanotube nanocomposites, *Nanotechnology* **2005**, *16*, 625-630.
- [25] F. Lupo, R. Kamalakaran, C. Scheu, N. Grobert, M. Rühle, Microstructural investigations on zirconium oxide-carbon nanotube composites synthesized by hydrothermal crystallization, *Carbon* **2004**, *42*, 1995-1999.
- [26] S. Banerjee, T. Hemraj-Benny, S. S. Wong, Covalent surface chemistry of single-walled carbon nanotubes, *Adv. Mater.* **2005**, *17*, 17-29.
- [27] Y. Lu, S. Bangsaruntip, X. Wang, L. Zhang, Y. Nishi, H. Dai, DNA functionalization of carbon nanotubes for ultrathin atomic layer deposition of high k dielectrics for nanotube transistors with 60 mV/decade switching, *J. Am. Chem. Soc.* **2006**, *128*, 3518-3519.
- [28] X. Meng, D. Geng, J. Liu, R. Li, X. Sun, Controllable synthesis of graphene-based titanium dioxide nanocomposites by atomic layer deposition, *Nanotechnology* **2011**, *22*, 165602.
- [29] X. Meng, Y. Zhong, Y. Sun, M. N. Banis, R. Li, X. Sun, Nitrogen-doped carbon nanotubes coated by atomic layer deposited SnO₂ with controlled morphology and phase, *Carbon* **2011**, *49*, 1133-1144.
- [30] X. Meng, Y. Zhang, S. Sun, R. Li, X. Sun, Three growth modes and mechanisms for highly structure-tunable SnO₂ nanotube arrays of template-directed atomic layer deposition, *J. Mater. Chem.* **2011**, *21*, 12321-12330.

- [31] X. Meng, M. Ionescu, M. Banis, Y. Zhong, H. Liu, Y. Zhang, S. Sun, R. Li, X. Sun, Heterostructural coaxial nanotubes of CNT@Fe₂O₃ via atomic layer deposition: effects of surface functionalization and nitrogen-doping, *J. Nanopart. Res.* **2011**, *13*, 1207-1218.
- [32] X. Meng, D. Geng, J. Liu, M. Banis, Y. Zhang, R. Li, X. Sun, Non-aqueous approach to synthesize amorphous/crystalline metal oxide-graphene nanosheet hybrid composites, *J. Phys. Chem. C* **2010**, *114*, 18330-18337.
- [33] Y. Chen, J. Wang, X. Meng, Y. Zhong, R. Li, X. Sun, S. Ye, S. Knights, Atomic layer deposition assisted Pt-SnO₂ hybrid catalysts on nitrogen-doped CNTs with enhanced electrocatalytic activities for low temperature fuel cells, *Int. J. Hydrogen Energy* **2011**, *36*, 11085-11092.
- [34] X. Li, X. Meng, J. Liu, D. Geng, Y. Zhang, M. Banis, Y. Li, R. Li, X. Sun, M. Cai, M. Verbrugge, Tin oxide with controlled morphology and crystallinity by atomic layer deposition onto graphene nanosheets for enhanced lithium storage, *Adv. Funct. Mater.* **2012**, *22*, 1647-1654.
- [35] S. M. George, Atomic layer deposition: an overview, *Chem. Rev.* **2010**, *110*, 111-131.
- [36] R. L. Puurunen, Surface chemistry of atomic layer deposition: a case study for the trimethylaluminum/water process, *J. Appl. Phys.* **2005**, *97*, 121301-121352.
- [37] W. H. Nam, S. W. Rhee, Atomic layer deposition of ZrO₂ thin films using dichlorobis[bis-(trimethylsilyl)amido] zirconium and water, *Chem. Vap. Deposition* **2004**, *10*, 201-205.
- [38] D. M. Hausmann, E. Kim, J. Becker, R. G. Gordon, Atomic layer deposition of hafnium and zirconium oxides using metal amide precursors, *Chem. Mater.* **2002**, *14*, 4350-4358.
- [39] D. M. Hausmann, R. G. Gordon, Surface morphology and crystallinity control in the atomic layer deposition (ALD) of hafnium and zirconium oxide thin films, *J. Cryst. Growth* **2003**, *249*, 251-261.

- [40] J. S. Becker, E. Kim, R. G. Gordon, Atomic layer deposition of insulating hafnium and zirconium nitrides, *Chem. Mater.* **2004**, *16*, 3497-3501.
- [41] H. Liu, D. Arato, R. Li, Y. Zhang, P. Merel, X. Sun, Aligned multi-walled carbon nanotubes synthesized by floating catalyst CVD: Effects of buffer layer and substrates, *Surf. Coating Tech.* **2008**, *202*, 4114-4120.
- [42] Y. Zhong, M. Jaidann, Y. Zhang, G. Zhang, H. Liu, M. I. Ionescu, R. Li, X. Sun, H. Abou-Rachid, L. S. Lussier, Synthesis of high nitrogen doping of carbon nanotubes and modeling the stabilization of filled DAATO@CNTs (10,10) for nanoenergetic materials, *J. Phys. Chem. Solids* **2010**, *71*, 134-139.
- [43] H. Liu, Y. Zhang, R. Li, X. Sun, S. Désilets, H. Abou-Rachid, M. Jaidan, L. S. Lussier, Structural and morphological control of aligned nitrogen-doped carbon nanotubes, *Carbon* **2010**, *48*, 1498-1507.
- [44] T. Hirata, E. Asari, M. Kitajima, Infrared and Raman spectroscopic studies of ZrO₂ polymorphs doped with Y₂O₃ or CeO₂, *J. Solid State Chem.* **1994**, *110*, 201-217.
- [45] V. G. Keramidas, W. B. White. Raman scattering study of the crystallization and phase transformations of ZrO₂, *J. Am. Ceram. Soc.* **1974**, *57*, 22-24.
- [46] S. Ferrari, D. T. Dekadjevi, S. Spiga, G. Tallarida, C. Wiemer, M. Fanciulli, Structural and electrical characterization of ALCVD ZrO₂ thin films on silicon, *J. Non-Cryst. Solids* **2002**, *303*, 29-34.
- [47] L. Chen, T. Mashimo, E. Omurzak, H. Okudera, C. Iwamoto, A. Yoshiasa, Pure tetragonal ZrO₂ nanoparticles synthesized by pulsed plasma in liquid, *J. Phys. Chem. C* **2011**, *115*, 9370-9375.
- [48] M. W. Pitcher, S. V. Ushakov, A. Navrotsky, B. F. Woodfield, G. Li, J. Boerio-Goates, B. M. Tissue, Energy crossovers in nanocrystalline zirconia, *J. Am. Ceram. Soc.* **2005**, *88*, 160-167.

- [49] R. C. Garvie, The occurrence of metastable tetragonal zirconia as a crystallite size effect, *J. Phys. Chem.* **1965**, *69*, 1238-1243.
- [50] R. L. Puurunen, W. Vandervorst, W. F. A. Besling, O. Richard, H. Bender, T. Conard, C. Zhao, A. Delabie, M. Caymax, S. D. Gendt, M. Heyns, M. M. Viitanen, M. Ridder, H. H. Brongersma, Y. Tamminga, T. Dao, T. Win, M. Verheijen, M. Kaiser, M. Tuominen, Island growth in the atomic layer deposition of zirconium oxide and aluminum oxide on hydrogen-terminated silicon: Growth mode modeling and transmission electron microscopy. *J. Appl. Phys.* **2004**, *86*, 4878-4889.
- [51] M. Copel, M. Gribelyuk, E. Gusev, Structure and stability of ultrathin zirconium oxide layer on Si(001), *Appl. Phys. Lett.* **2000**, *76*, 436-438.
- [52] W. F. A. Besling, E. Young, T. Conard, C. Zhao, R. Carter, W. Vandervorst, M. Caymax, S. De Gendt, M. Heyns, J. Maes, M. Tuominen, S. Haukka, Characterization of ALCVD Al₂O₃-ZrO₂ nanolaminates, link between electrical and structural properties, *J. Non-Cryst. Solid* **2002**, *303*, 123-133.
- [53] Y. S. Min, H. Lee, Y. H. Lee, C. S. Hwang, Botryoidal growth of crystalline ZnO nanoparticles on a forest of single-walled carbon nanotubes by atomic layer deposition, *CrystEngComm* **2011**, *13*, 3451-3454.
- [54] C. L. Sun, L. C. Chen, M. C. Su, L. S. Hong, O. Chyan, C. Y. Hsu, K. H. Chen, T. F. Chang, L. Chang, Ultrafine platinum nanoparticles uniformly dispersed on arrayed NCNTs nanotubes with high electrochemical activity, *Chem. Mater.* **2005**, *17*, 3749-3753.
- [55] S. Sun, G. Zhang, Y. Zhong, H. Liu, R. Li, X. Zhou, X. Sun, Ultrathin single crystal Pt nanowires grown on N-doped carbon nanotubes, *Chem. Commun.* **2009**, *45*, 7048-7050.
- [56] H. C. Choi, S. Y. Bae, W.-S. Jang, J. Park, H. J. Song, H.-J. Shin, H. Jung, J.-P. Ahn, Release of N₂ from the carbon nanotubes via high-temperature annealing, *J. Phys. Chem. B* **2005**, *109*, 1683-1688.

- [57] J. C. F. Rodríguez-Reyes, A. V. Teplyakov, Mechanisms of adsorption and decomposition of metal alkylamide precursors for ultrathin film growth, *J. Appl. Phys.* **2008**, *104*, 084907.
- [58] R. Matero, A. Rahtu, M. Ritala, M. Leskelä T. Sajavaara, Effect of water dose on the atomic layer deposition rate of oxide thin films, *Thin Solid Films* **2000**, *368*, 1-7.
- [59] M. Cassir, F. Goubin, C. Bernay, P. Vernoux, D. Lincot, Synthesis of ZrO₂ thin films by atomic layer deposition: growth kinetics, structural and electrical properties, *Appl. Surf. Sci.* **2002**, *193*, 120-128.
- [60] J. Aarik, A. Aidla, V. Sammelselg, H. Siimon, T. Uustare, Control of thin film structure by reactant pressure in atomic layer deposition of TiO₂, *J. Cryst. Growth* **1996**, *169*, 496-502.
- [61] M. Ritala, M. Leskelä Zirconium dioxide thin films deposited by ALE using zirconium tetrachloride as precursor, *Appl. Surf. Sci.* **1994**, *75*, 333-340.
- [62] K. Kukli, M. Ritala, J. Aarik, T. Uustare, Influence of growth temperature on properties of zirconium dioxide films grown by atomic layer deposition, *J. Appl. Phys.* **2002**, *92*, 1833-1840.
- [63] G. Scarel, S. Ferrari, S. Spiga, C. Wiemer, G. Tallarida, M. Fanciulli, Effects of growth temperature on the properties of atomic layer deposition grown ZrO₂ films, *J. Vac. Sci. Technol. A* **2003**, *21*, 1359-1365.
- [64] J. Aarik, A. Aidla, T. Uustare, V. Sammelselg, Morphology and structure of TiO₂ thin films grown by atomic layer deposition, *J. Cryst. Growth* **1995**, *148*, 268-275.
- [65] M. Ritala, M. Leskelä L. Niinistö, T. Prohaska, G. Friedbacher, M. Grasserbauer, Development of crystallinity and morphology in hafnium dioxide thin films grown by atomic layer epitaxy, *Thin Solid Films* **1994**, *250*, 72-80.
- [66] C. H. L. Goodman, M. V. Pessa, Atomic layer epitaxy, *J. Appl. Phys.* **1986**, *60*, R65-R81.

[67] J. Aarik, A. Aidla, H. Mändar, T. Uustare, V. Sammelselg, Growth kinetics and structure formation of ZrO_2 thin films in chloride-based atomic layer deposition process, *Thin Solid Films* **2002**, 408, 97-103.

Supporting Information

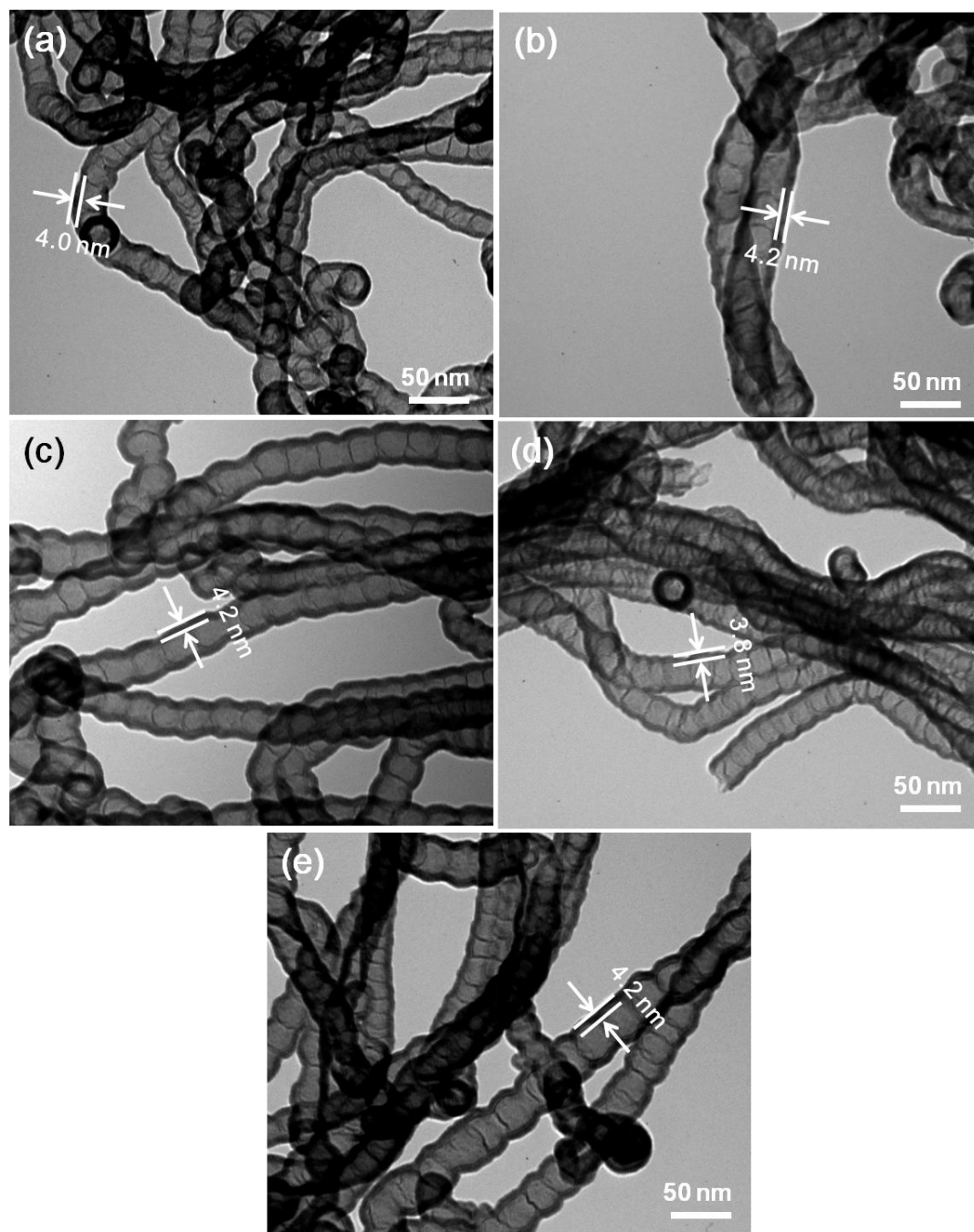


Figure SI-6.1 TEM images of 50-cycle ZrO₂-NCNTs prepared at 200 °C using recipe of (a) 0.2 s - 30 s - 1.0 s - 30 s; (b) 0.5 s - 30 s - 1.0 s - 30 s; (c) 0.8 s - 30 s - 1.0 s - 30 s; (d) 0.5 s - 30 s - 0.5 s - 30 s and (e) 0.5 s - 30 s - 1.5 s - 30 s (the error of the thickness measurement in TEM images is about 0.5 nm).

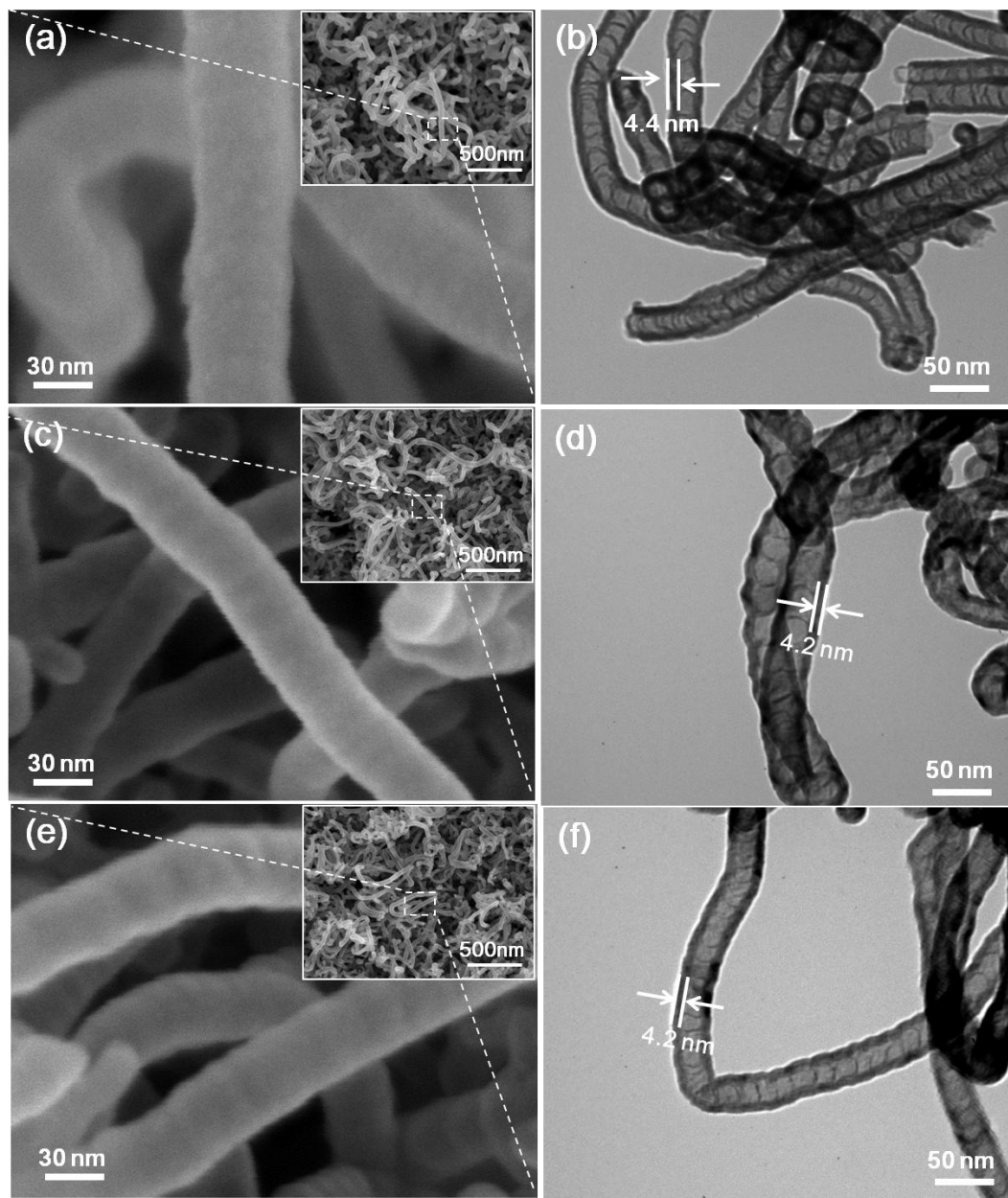


Figure SI-6.2 SEM (a, c, e) and TEM (b, d, f) images of 50-cycle ZrO₂-NCNTs prepared at 200 °C using recipe of (a, b) 0.5 s - 15 s - 1.0 s - 15 s; (c, d) 0.5 s - 30 s - 1.0 s - 30 s and (e, f) 0.5 s - 60 s - 1.0 s - 60 s (the error of the thickness measurement in TEM images is about 0.5 nm).

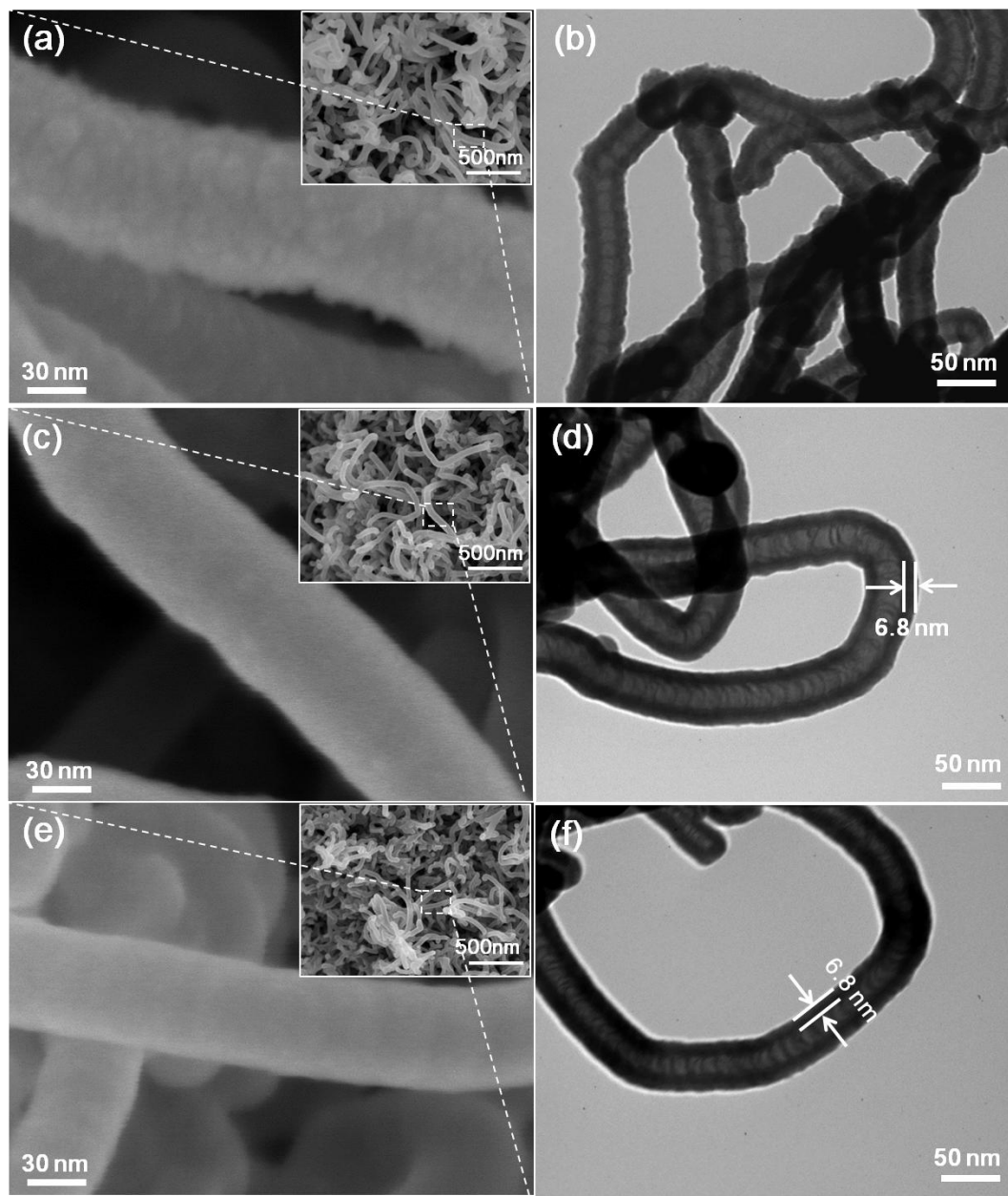


Figure SI-6.3 SEM (a, c, e) and TEM (b, d, f) images of 50-cycle ZrO_2 -NCNTs prepared at 100°C using recipe of (a, b) 0.5 s - 15 s - 1.0 s - 15 s; (c, d) 0.5 s - 30 s - 1.0 s - 30 s and (e, f) 0.5 s - 60 s - 1.0 s - 60 s (the error of the thickness measurement in TEM images is about 0.5 nm).

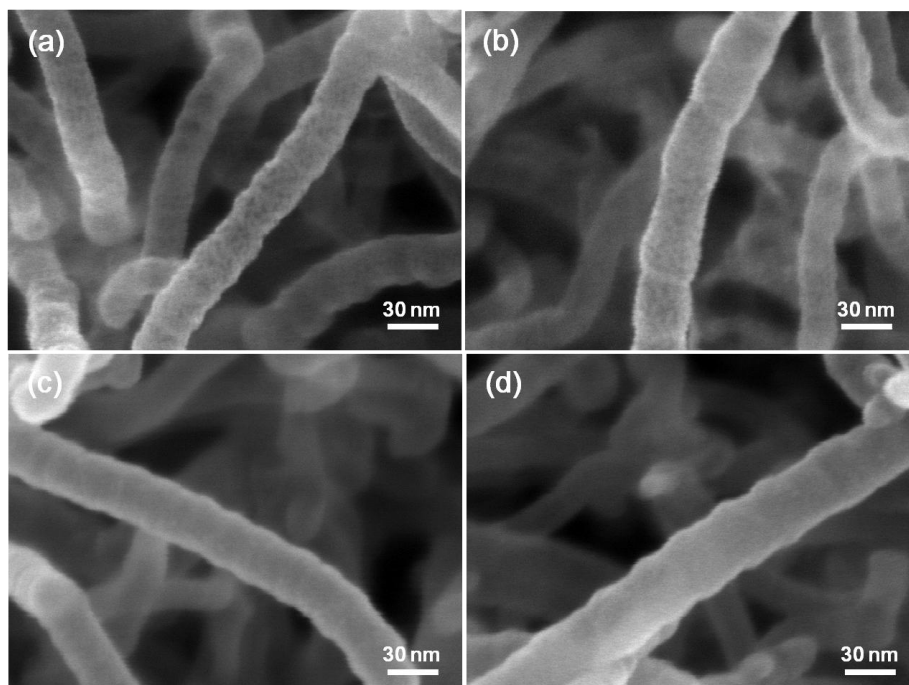


Figure SI-6.4 SEM images of ZrO_2 -NCNTs prepared at 250 °C after (a) 5 cycles; (b) 10 cycles; (c) 30 cycles and (d) 50 cycles.

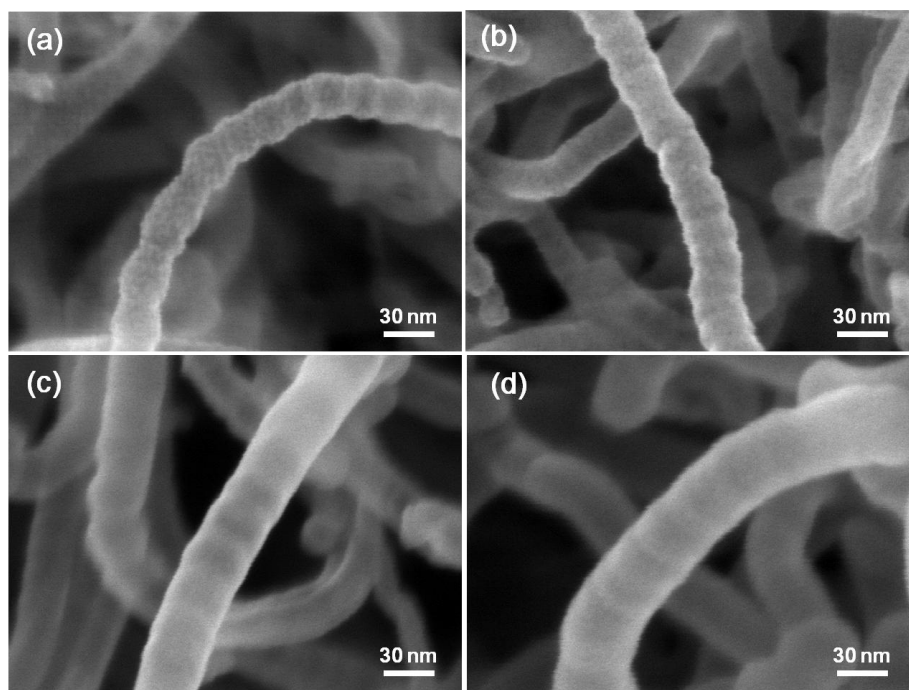


Figure SI-6.5 SEM images of ZrO_2 -NCNTs prepared at 150 °C after (a) 5 cycles; (b) 10 cycles; (c) 30 cycles and (d) 50 cycles.

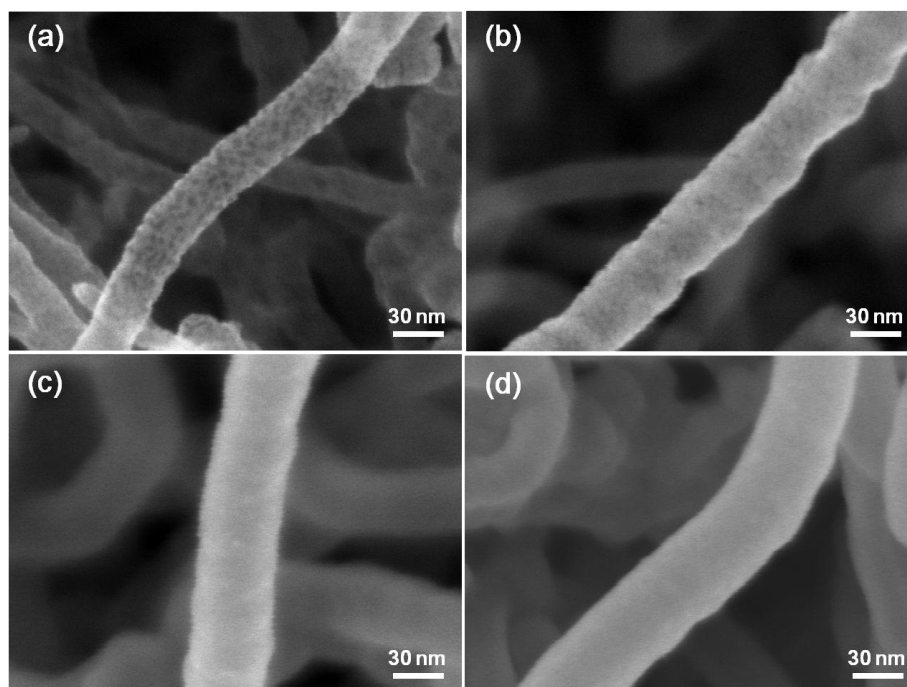


Figure SI-6.6 SEM images of ZrO_2 -NCNTs prepared at 100°C after (a) 5 cycles; (b) 10 cycles; (c) 30 cycles and (d) 50 cycles.

Chapter 7 Controlled Synthesis of Zirconium Oxide on Graphene Nanosheets by Atomic Layer Deposition and Its Growth Mechanism **

This chapter was an extended study of ALD-ZrO₂ in chapter 6, and the substrate was changed from nitrogen-doped carbon nanotubes (NCNTs) to graphene nanosheets (GNS) in order to investigate the substrate effect and obtain better understanding on the growth behavior of ZrO₂.

Herein, ZrO₂ was deposited on GNS by ALD using tetrakis(dimethylamido)zirconium (IV) and water as precursors. The results indicated that both morphology and crystallinity of the deposited ZrO₂ were controllable in a temperature range of 150 - 250 °C. At all the temperatures studied, ZrO₂ nanoparticles were formed with lower number of ALD cycles (< 10 cycles at 150 °C and < 30 cycles at 200 and 250 °C), while ZrO₂ thin films were achieved uniformly with higher number of ALD cycles (> 10 cycles at 150 °C and > 30 cycles at 200 and 250 °C). The crystallinity of the deposited ZrO₂ was highly dependent on the deposition temperature. The ZrO₂ deposited at 150 °C exhibited mainly amorphous nature, whereas that prepared at 250 °C consisted of crystalline phase. At 200 °C, a mixture of amorphous and crystalline ZrO₂ appeared in the ZrO₂-GNS nanocomposite. In all cases, the growth of ZrO₂ on GNS showed a transformation from an “island growth” mode to a “layer-by-layer growth” mode with increasing ALD cycle.

Keyword: Atomic layer deposition; zirconium oxide, graphene; island growth; layer-by-layer growth.

** Part of this chapter has been published in *Carbon* **2012**, 52, 74-82.

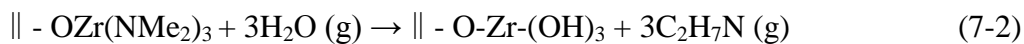
7.1 Introduction

As a two-dimensional (2D) nanostructure composed of sp^2 hybridized carbon, graphene has been drawing worldwide attention since its discovery in 2004 [1]. It possesses high thermal conductivity ($\sim 5000 \text{ W m}^{-1} \text{ K}^{-1}$) [2], excellent electric conductivity ($200\,000 \text{ cm}^2 \text{ V}^{-1} \text{ s}^{-1}$) [3], large surface area (theoretical value, $2630 \text{ m}^2 \text{ g}^{-1}$) [4], and strong mechanical strength [5]. These outstanding properties promise graphene in a wide range of potential applications, such as electronics [6], supercapacitors [4], lithium ion batteries [7, 8], fuel cells [9], solar cells [10, 11] and bioscience/ biotechnologies [12]. Recently, there is increasing interest in using graphene as a building block to fabricate multifunctional nanocomposites, which combine desired properties of each component. So far, polymer, metal, or metal oxides have been incorporated into graphene for various applications [13-20]. In particular, metal oxides supported by graphene represent one kind of nanocomposites with unique mechanical, catalytic, and electrochemical properties [15-23]. For example, TiO_2 -graphene nanocomposites were used for hydrogen evolution from water photocatalytic splitting [16]. SnO_2 -graphene nanocomposites showed enhanced cyclic performance and lithium storage capacity [18]. In addition, Co_3O_4 grown on graphene exhibited surprisingly high catalytic activity toward oxygen reduction reaction and oxygen evolution reaction due to synergetic chemical coupling effects between Co_3O_4 and graphene [20]. Thus, metal oxide-graphene nanocomposites have great potential for applications in fuel cells, lithium ion batteries, solar cells, supercapacitors, *etc.*

Zirconium Oxide (ZrO_2) is an attractive material in various industrial applications due to its excellent mechanical, thermal, optical and electrical characteristics [24, 25]. Up to now, there have been lots of studies on depositing ZrO_2 onto one-dimensional (1D) carbon nanotubes (CNTs) [24, 25], and applying ZrO_2 -CNT nanocomposites for various applications, such as catalyst supports for fuel cells [26, 27], biocompatible matrix for protein immobilization [28], and transistors as advanced gate dielectrics [29]. As a young carbon nanomaterial, graphene holds several advantages over CNTs as supports for metal oxides, such as free of metallic impurities, cheap and accessible production from graphite [30]. Unfortunately, there are few efforts on developing ZrO_2 -graphene nanocomposites

until now. It was only recently that two literatures reported the synthesis of ZrO₂-graphene nanocomposites by an electrodeposition method, and their use for detection of organophosphorus agents and biosensor application [30, 31]. Inspired by the wide applications of ZrO₂-CNTs, ZrO₂-graphene nanocomposites can also be very promising for many potential applications, which need to be fully explored. To fulfill this, it is of great importance to synthesize ZrO₂-graphene nanocomposites, especially in a controllable fashion.

In previous studies, the synthesis of ZrO₂-graphene nanocomposites was mainly achieved by electrodeposition method [30, 31]. It can also be synthesized by solution-based methods, which have been widely used for the production of metal oxide-graphene nanocomposites [16-20]. Even though these methods offer the advantages of low cost and suitability for large-scale production, they are still suffering from the limitation of controlled synthesis with desired material properties. In recent years, atomic layer deposition (ALD) emerged as a powerful approach to engineering various nanostructures [32-39]. ALD is one kind of chemical vapor deposition (CVD) technique, and proceeds in a layer-by-layer manner by two sequential and self-terminating gas-solid reactions [40-41]. Compared with other kinds of CVD methods (such as plasma-enhanced CVD, conventional thermal CVD), ALD has advantages of achieving deposition of thin films with highly conformity and uniformity and precisely controlled thickness at Angstrom or monolayer level [40, 41]. Moreover, the deposition temperature of ALD is usually lower than that of other CVD methods (usually < 400 °C), and in some cases it can be even down to room temperature, which is beneficial for sensitive substrates [40, 41]. In this study, therefore, ALD was employed to prepare ZrO₂-graphene nanocomposites, using tetrakis(dimethylamido)zirconium (IV) (Zr(NMe₂)₄) and H₂O as precursors, which was reported to consist of two half reactions [42]:



where “||” represents substrate surface and “(g)” denotes vapor species. Homemade graphene nanosheets (GNS) were employed as substrates for ALD-ZrO₂. To our best knowledge, it is the first time of reporting the ZrO₂-GNS nanocomposites synthesized by ALD in open literatures. The deposited ZrO₂ was not only controllable in its morphology, either nanoparticles or nanofilms, but also tunable in its crystallinity, from crystalline to amorphous phase. This kind of ZrO₂-GNS nanocomposites prepared by ALD might find potential applications in many fields, such as supercapacitors, fuel cells, sensors and electronics.

7.2 Experimental Section

7.2.1 Preparation of GNS

GNS was prepared by thermal reduction of graphite oxide (GO) [43]. Briefly, GO was first produced by oxidizing natural graphite using a modified Hummers method [44]; then the as-synthesized GO was heated at 1050 °C for 30 s under argon gas to obtain GNS. More details about the preparation process of GNS can be found in our previous work [33,45].

7.2.2 ZrO₂-GNS by ALD

In a typical process, GNS powders were firstly loaded into a commercial ALD reactor (Savannah 100, Cambridge Nanotech Inc., USA) preheated to a desired temperature. A schematic diagram of the ALD reactor can be found in Figure SI-1. Then, Zr(NMe₂)₄ (99%, STREM) and deionized water (H₂O) were alternatively introduced into the ALD reactor for ALD-ZrO₂. Zr(NMe₂)₄ was heated to 75 °C while H₂O was kept at room temperature, in order to provide sufficient vapors for ALD-ZrO₂. Delivery lines were heated to 100 °C to prevent the precursors from condensation. Nitrogen gas (99.999% in purity) was used as a carrier gas at a flow rate of 20 sccm, and the ALD reactor was maintained at a low level of base pressure (typically 0.3-0.4 Torr) by a vacuum pump (Pascal 2005 I, Adixen). One ALD cycle was executed with the completion of following six steps: (1) a 0.5 s supply of Zr(NMe₂)₄; (2) a 3.0 s extended exposure of Zr(NMe₂)₄ in the ALD reactor; (3) a 30 s purge of excess Zr(NMe₂)₄ and any byproducts; (4) a 1.0 s supply of H₂O (5) a 3.0 s extended exposure of H₂O in the ALD reactor; (6) a 30 s purge

of excess H₂O and any byproducts. ZrO₂-GNS nanocomposites were prepared by repeating above ALD cycle at different deposition temperatures. In this study, three deposition temperatures were employed for ALD-ZrO₂ on GNS: 150, 200 and 250 °C.

7.2.3 Characterization of ZrO₂-GNS

The as-synthesized ZrO₂-GNS nanocomposites were characterized using a field-emission scanning electron microscope (SEM, Hitachi S4800) equipped with energy dispersive X-ray spectroscopy (EDS), transmission electron microscope (TEM, Hitachi H-7000), high-resolution TEM (HRTEM, JEOL 2010 FEG), micro X-ray diffraction (XRD, Bruker D8, Co-K α source, $\lambda=1.7892$ Å), and Fourier transform-infrared (FTIR, Nicolet 6700 FTIR spectrometer).

Electrochemical behaviors of the samples were evaluated with 0.5 M H₂SO₄ at room temperature using an Autolab potentiostat/galvanostat (PGSTAT-30) scanned from -0.66 to 0.24 V versus a saturated calomel reference electrode (SCE) at a scan rate of 50 mVs⁻¹.

7.3 Results and Discussion

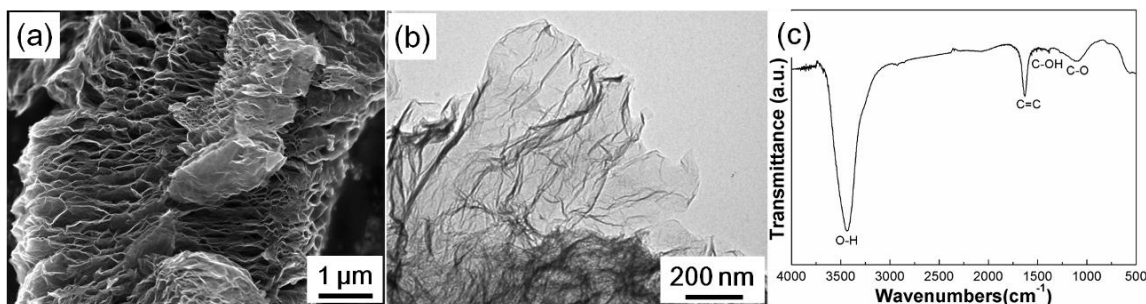


Figure 7.1 SEM image (a), TEM image (b) and FTIR spectrum (c) of the pristine GNS.

The pristine GNS were characterized by SEM, TEM, and FTIR, and the results are presented in [Figure 7.1](#). [Figure 7.1a](#) show that the pristine GNS have an accordion-like porous structure, which is composed of many thin graphene wrinkles. TEM observation reveals that these graphene wrinkles are transparent, as seen in [Figure 7.1b](#). From FTIR spectrum in [Figure 7.1c](#), it can be seen that the pristine GNS exhibit two strong peaks located at 3450 cm⁻¹ and 1635 cm⁻¹, which correspond to stretching vibrations of hydroxyl group (-OH) and skeletal vibration of graphitic domains (C=C), respectively

[45,46]. There are other two peaks observed at 1384 cm^{-1} and 1100 cm^{-1} , which are assigned to C-OH and C-O stretching vibrations, respectively [45, 46].

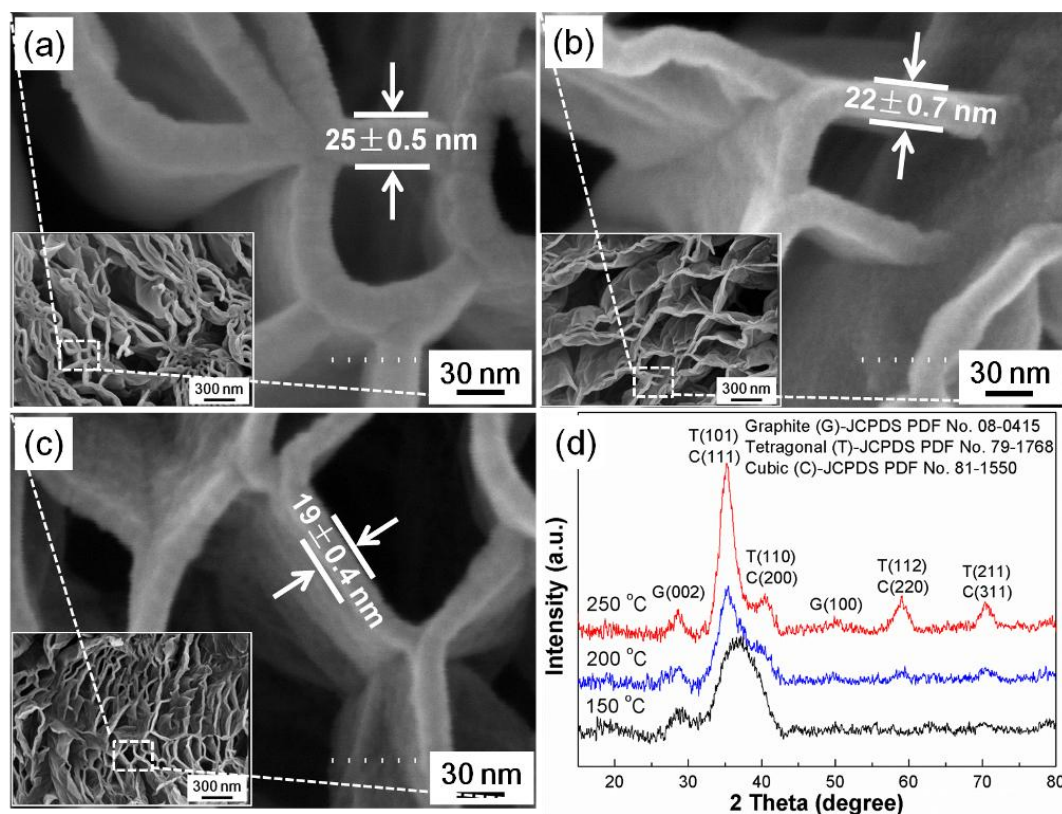


Figure 7.2 SEM images of 100-cycle ZrO_2 -GNS nanocomposites prepared at (a) $150\text{ }^\circ\text{C}$, (b) $200\text{ }^\circ\text{C}$ and (c) $250\text{ }^\circ\text{C}$. (d) XRD patterns of 100-cycle ZrO_2 -GNS nanocomposites prepared at $150\text{ }^\circ\text{C}$, $200\text{ }^\circ\text{C}$ and $250\text{ }^\circ\text{C}$.

ZrO_2 -GNS nanocomposites were prepared at 150 , 200 and $250\text{ }^\circ\text{C}$ with different numbers of ALD cycles. 100-cycle ZrO_2 -GNS nanocomposites were characterized by SEM and XRD, and the results are shown in Figure 7.2. In Figure 7.2 (a-c), it can be clearly seen that after 100-cycle ALD- ZrO_2 , the graphene wrinkles of GNS are totally coated with smooth thin films at all three deposition temperatures. Low-magnification SEM images (Insets in Figure 7.2 (a-c)) indicate that these thin films are very uniformly deposited onto the whole GNS powders. The thickness of the coated wrinkles is measured to be 25 ± 0.5 , 22 ± 0.7 and $19\pm 0.4\text{ nm}$, for 100-cycle ZrO_2 -GNS nanocomposites prepared at 150 , 200 and $250\text{ }^\circ\text{C}$, respectively (Figure 7.2 (a-c)). Furthermore, if we suppose the pristine

graphene wrinkles are about 4 nm in the thickness with a conservative estimate (as indicated in Figure SI-7.1 of the Supporting Information), the growth per cycle (GPC) of ALD-ZrO₂ would be roughly evaluated as 1.05, 0.90, and 0.75 Å, at 150, 200 and 250 °C, respectively. The GPC is calculated by the following equation: $GPC = (\text{thickness of coated wrinkles} - \text{thickness of pristine wrinkles}) / (2 \times \text{cycle numbers})$ [33]. Figure 7.2d shows the XRD results of 100-cycle ZrO₂-GNS nanocomposites prepared at 150, 200 and 250 °C. It can be seen that all samples exhibit one strong peak at 29 ° and one weak one at 50 °, which correspond to the (022) and (100) planes of graphite (JCPDS PDF No. 08-0415), respectively. Apparently, those two peaks were induced by GNS powders. For the ZrO₂-GNS nanocomposite prepared at 250 °C, there also appear several strong peaks located at 35 °, 40 °, 59 ° and 70 ° in its XRD, which can be assigned to the planes of (101), (110), (112) and (211) of tetragonal ZrO₂ (JCPDS PDF No. 79-1768), respectively, or/and (111), (200), (220) and (311) of cubic ZrO₂ (JCPDS PDF No. 81-1550), respectively. These strong sharp peaks in XRD reveal the crystalline state of deposited ZrO₂ at 250 °C. With a decrease of deposition temperature, the peaks of ZrO₂ become weaker in the intensity and boarder in the half-width. Except T(101) or/and C(111) peak, the others of ZrO₂ becomes almost invisible for the ZrO₂-GNS nanocomposite prepared at 150 °C. The XRD results indicate that the crystallinity of deposited ZrO₂ experienced a gradual decrease with the decrease of deposition temperature. Based on the above results, it can be concluded that ZrO₂ thin films were successfully deposited on GNS at 150, 200 and 250 °C with 100 ALD cycles, and the GPC and crystallinity were temperature dependent.

To further understand the characteristics of ALD-ZrO₂, the morphological evolution of ALD-ZrO₂ on GNS with increasing cycle numbers was explored, and Figure 7.3 presents the development of ALD-ZrO₂ on GNS after 10, 30 and 50 cycles at 150, 200 and 250 °C. At 150 °C, the graphene wrinkles are coated with dense ZrO₂ nanoparticles after 10 cycles (Figure 7.3a). After 30 cycles, the ZrO₂ coating on the graphene wrinkles becomes very smooth thin films, and the thickness of the coated wrinkles is measured to be around 12±0.5 nm, as seen in Figure 7.3b. Figure 7.3c indicates that 50-cycle ZrO₂ coating leads to thickness increase of the coated wrinkles to about 14±0.7 nm, with the uniformity of ZrO₂ thin films maintained. The growth of ALD-ZrO₂ on GNS at 200 and 250 °C exhibits

the similar trend of morphological evolution as that at 150 °C, as shown in [Figure 7.3 \(d-g\)](#). The deposited ZrO_2 on GNS are nanoparticles with lower ALD cycles (<10 at 150 °C and <30 at 200 and 250 °C), while thin films with higher ALD cycles (>10 at 150 °C and >30 at 200 and 250 °C). This phenomenon suggests the growth of ALD- ZrO_2 on GNS follows an “island growth” mode at the very beginning, and a “layer-by-layer growth” mode after those “islands” coalesce into thin films. From [Figure 7.3](#), one can also find that the GPC of ZrO_2 on GNS increases with the elevating temperature at the same ALD cycles. For example, with 10 cycles, the size and density of ZrO_2 nanoparticles obviously increase with the decreasing temperatures, as revealed in [Figure 7.3 \(a, d, h\)](#). Low-magnification SEM images of 10-, 30-, and 50-cycle ZrO_2 -GNS nanocomposites at 150, 200 and 250 °C can be found in [Figure SI-\(7.2-7.4\)](#).

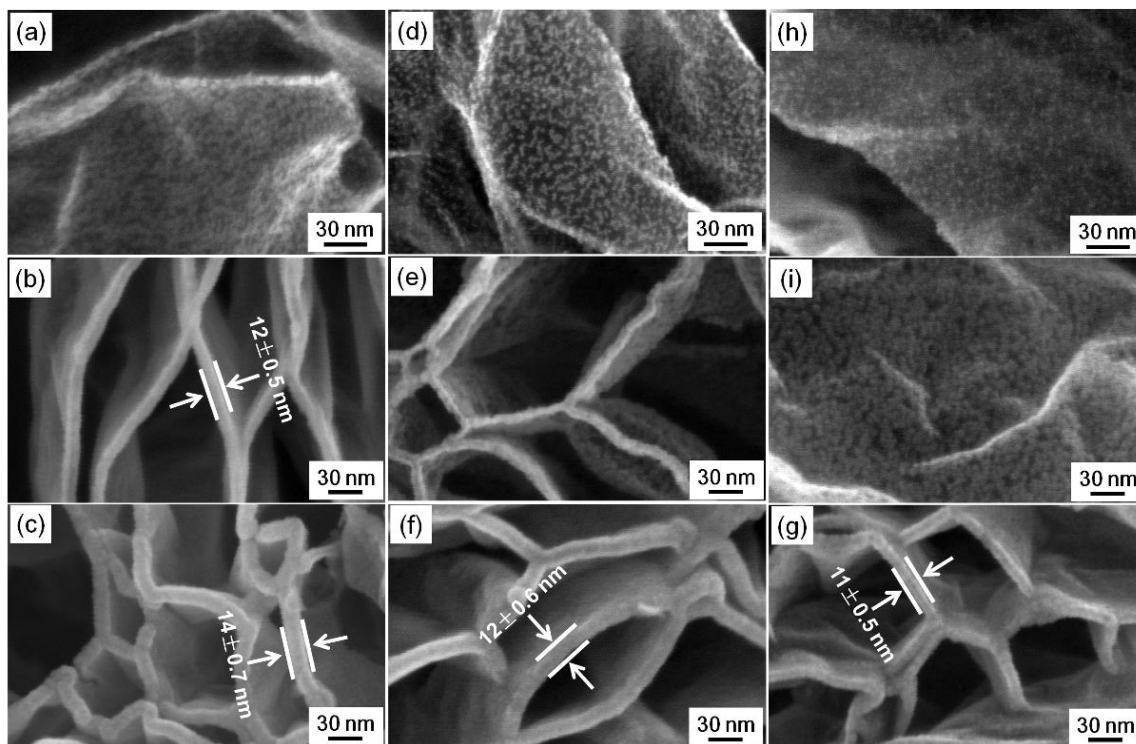


Figure 7.3 SEM images of ZrO_2 -GNS nanocomposite prepared at 150 °C (a, b, c), 200 °C (d, e, f) and 250 °C (h, i, g) with 10 cycles (a, d, h), 30 cycles (b, e, i) and 50 cycles (c, f, g).

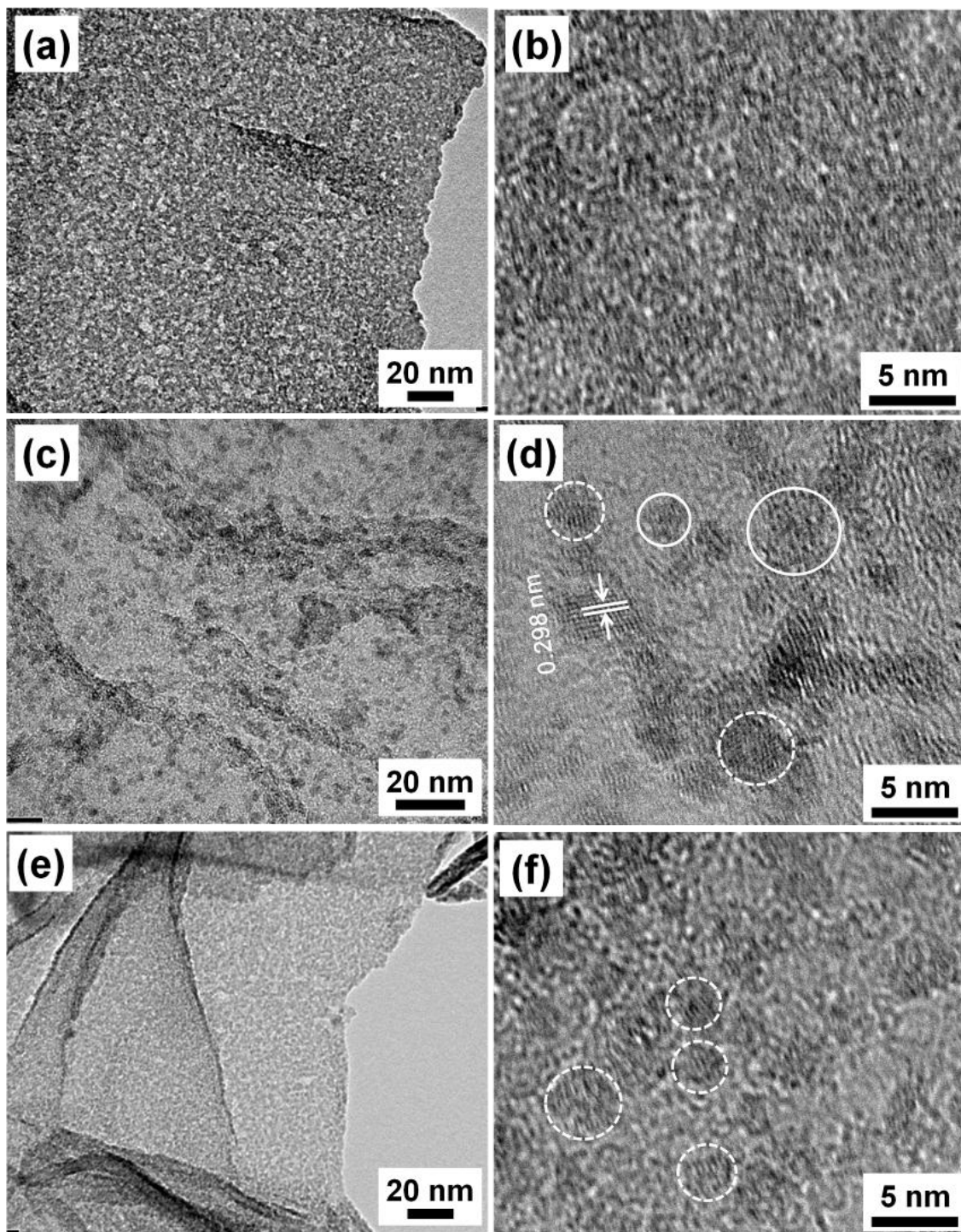


Figure 7.4 TEM (a, c, e) and HRTEM (b, d, f) images of ZrO_2 -GNS nanocomposite prepared at 150 °C (a, b), 200 °C (c, d) and 250 °C (e, f) with 10 cycles.

The morphology and structure of 10-cycle ZrO_2 -GNS nanocomposites prepared at 150, 200 and 250 °C were further studied by TEM and HRTEM, and the results are presented

in Figure 7.4. In Figure 7.4 (a, c, e), one can easily find that the GNS after 10 cycles at 150, 200 and 250 °C become opaque in a large part, compared with the initial transparent GNS (Figure 7.1c), indicating the deposition of dense ZrO₂ nanoparticles. The structural difference of the ZrO₂ nanoparticles among those three samples is disclosed by the HRTEM result. HRTEM image in Figure 7.4b reveals the disordered nature of the deposited ZrO₂ nanoparticles at 150 °C, implying the dominance of amorphous phase in this sample. The EDS result confirms the presence of Zr and O elements in 10-cycle ZrO₂-GNS nanocomposite prepared at 150 °C (see Figure SI-7.4 of the Supporting Information). For the sample prepared at 200 °C, the HRTEM image (Figure 7.4d) indicates the coexistence of single crystalline nanoparticles (as indicated by dash circles) and amorphous ones (as marked by solid circles). The interplanar spacing of one of the single crystalline nanoparticles is measured to be 0.298 nm, agreeing well with the lattice distance between (101) planes of tetragonal ZrO₂, as seen in Figure 7.4d. Figure 7.4f shows the HRTEM image of 10-cycle ZrO₂-GNS nanocomposite prepared at 250 °C. Clear interplanar spaces can be observed in most of the nanoparticles in this sample (dash-circled in Figure 7.4f), even though their sizes are really small (down to 1 nm), and crystalline ZrO₂ is suggested to dominate in this sample. By comparing Figure 7.4b, Figure 7.4d, and Figure 7.4f, it can be found that the crystallinity of the deposited ZrO₂ increases with the elevating temperature. The HRTEM result is well consistent with XRD result in Figure 7.2d. Based on the above studies, it can be concluded that the deposited ZrO₂ was dominated by amorphous phase at 150 °C and crystalline phase at 250 °C, and amorphous and crystalline ZrO₂ coexisted in the ZrO₂-GNS nanocomposite prepared at 200 °C.

In the following part, we will discuss the reasons responsible for the controlled morphology and crystallinity of ALD-ZrO₂ on GNS, the role of GNS as substrates for the growth of ALD materials, and propose the growth mechanism of ALD-ZrO₂ on GNS.

From the above results, it has been evidenced that the ALD-ZrO₂ on GNS were not only controllable in its morphology, either nanoparticles or thin films, but also tunable in its crystallinity, from amorphous to crystalline. The morphology of the ALD-ZrO₂ was dependent on the ALD cycles at a given temperature, *i.e.* ZrO₂ nanoparticles were

obtained with low ALD cycles, while ZrO₂ thin films were achieved with high ALD cycles. This phenomenon indicates that ZrO₂ followed an “island growth” mode at the early stage, while a “layer-by-layer growth” mode after the coalescence of those ZrO₂ “islands”. During an ALD process, a prerequisite is the substrate surface terminated with hydroxyl groups, which serve as reactive sites for the nucleation and growth of ALD materials [40, 41]. Previous studies have shown that island-growth of ALD-ZrO₂ happened on hydrogen-terminated silicon, which was lack of functional OH adsorption sites [47-49]. A recent study showed that ZnO nanoparticles could be grown on single-walled carbon nanotubes, which had a sparse amount of reactive sites for precursor chemisorptions [50]. In this work, the substrates for ALD-ZrO₂ are GNS produced by thermal reduction of GO, which usually have hydroxyl groups bonded to the carbon network [51, 52]. The FTIR spectrum in [Figure 7.1c](#) confirms the existence of a significant amount of hydroxyl groups on GNS, as illustrated in [Figure 7.5 \(A1\)](#). During the first half-cycle, Zr(NMe₂)₄ would preferably react with –OH groups on GNS *via* Reaction (7-1), as schematically shown in [Figure 7.5 \(A2, A3\)](#). After that, H₂O introduced in the second half-cycle would react with Zr(NMe₂)₄ chemically bonded on GNS through Reaction (7-2), generating –OH groups at the outer surface of GNS (see [Figure 7.5 \(A4, A5\)](#)). Then the deposition of ZrO₂ would be achieved by repeating the above ALD cycle. Therefore, those hydroxyl groups dispersed on GNS would account for the island growth of ZrO₂ with low ALD cycles. With further increasing ALD cycles, those ZrO₂ ‘islands’ would coalesce and finally close into thin films, as observed in [Figure 7.3](#). From this point on, the growth of ZrO₂ would happen in a layer-by-layer way, leading to deposition of uniform thin films. From [Figure 7.2](#) and [Figure 7.3](#), it is also obvious that with a given ALD cycle, the size of ZrO₂ particles or the thickness of ZrO₂ thin films varies with the deposition temperature. Higher deposition temperature would lead to smaller ZrO₂ particles or thinner ZrO₂ thin films. It can be explained by the temperature-dependent nature of hydroxyl groups, and high temperature could lead to dehydroxylation, as described as follows [53]:



Obviously, the dehydroxylation would reduce the density of hydroxyl groups, thereby leading to the smaller ZrO_2 particles or thinner ZrO_2 thin films of ALD- ZrO_2 at a higher temperature. Besides hydroxyl groups, physisorbed $\text{Zr}(\text{NMe}_2)_4$ and H_2O are probably another reason for the higher GPC at 150 °C. Hausmann *et al.* [42] have proved that it took much longer time to purge all surface-physisorbed $\text{Zr}(\text{NMe}_2)_4$ and H_2O at lower temperatures. Therefore, given the same purge time in our case, there would be more surface-physisorbed $\text{Zr}(\text{NMe}_2)_4$ and H_2O at lower temperatures, which would in return contribute to the growth of ZrO_2 . As to the crystallinity of ALD materials, previous studies have demonstrated that the temperature could affect the crystallinity of ALD materials by having influence on the reaction mechanisms [37, 56], and surface mobility of absorbed species [53, 55]. For $\text{Zr}(\text{NMe}_2)_4$, theoretical calculation showed that scission of metal-ligand bonds was more feasible than scission of N-C bonds [57]. Moreover, experiment study has revealed that the reaction of $\text{Zr}(\text{NMe}_2)_4$ and H_2O in ALD would follow Reaction (7-1) and (7-2) in the temperature range of 150 - 250 °C [42]. Therefore, it can be considered that the reaction mechanism of $\text{Zr}(\text{NMe}_2)_4$ and H_2O was not affected by the temperature change in this study. During an ALD process, high temperatures could improve the surface mobility of absorbed species and promote the ordering of the structure with minimum energy, thus leading to the growth of crystallites [54, 55]. In our case, a higher temperature could enhance the mobility of absorbed species, and enable the Zr and/or O ions to occupy the positions corresponding to the lowest free energy of the crystal [55], thus resulting in the crystalline phase of ALD- ZrO_2 at 250 °C. At a given temperature, the crystallinity of ALD- ZrO_2 could be also related to the film thickness, and more crystalline ZrO_2 could be found in the thicker film [58]. The nucleation events of crystalline ZrO_2 were even during each ALD cycles. The increase of ALD cycles could result in the nucleation of more crystalline ZrO_2 and thicker film. Therefore, the thicker film might contain more crystalline ZrO_2 than the thinner film does.

From above discussion, one can see that the surface nature of GNS plays a critical role in the nucleation and growth of ALD- ZrO_2 , and GNS with hydroxyl groups are desirable for this ALD process. Previous study by Dai *et al.* indicated that ALD- Al_2O_3 could hardly grow on pristine graphene prepared by peel-off method, due to the lack of surface functional groups [59]. Ozone pretreatment [60] and wet chemistry pretreatment [61]

have been shown as effective methods to render the graphene surface more suitable to oxide precursor bonding. In this work, it is demonstrated that the as-prepared GNS by thermal reduction of GO could be directly used for the uniform deposition of ALD-ZrO₂. The functionalized GNS (Figure 7.1c) could be resulted from the uncompleted reduction of GO at 1050 °C during the preparation process [45].

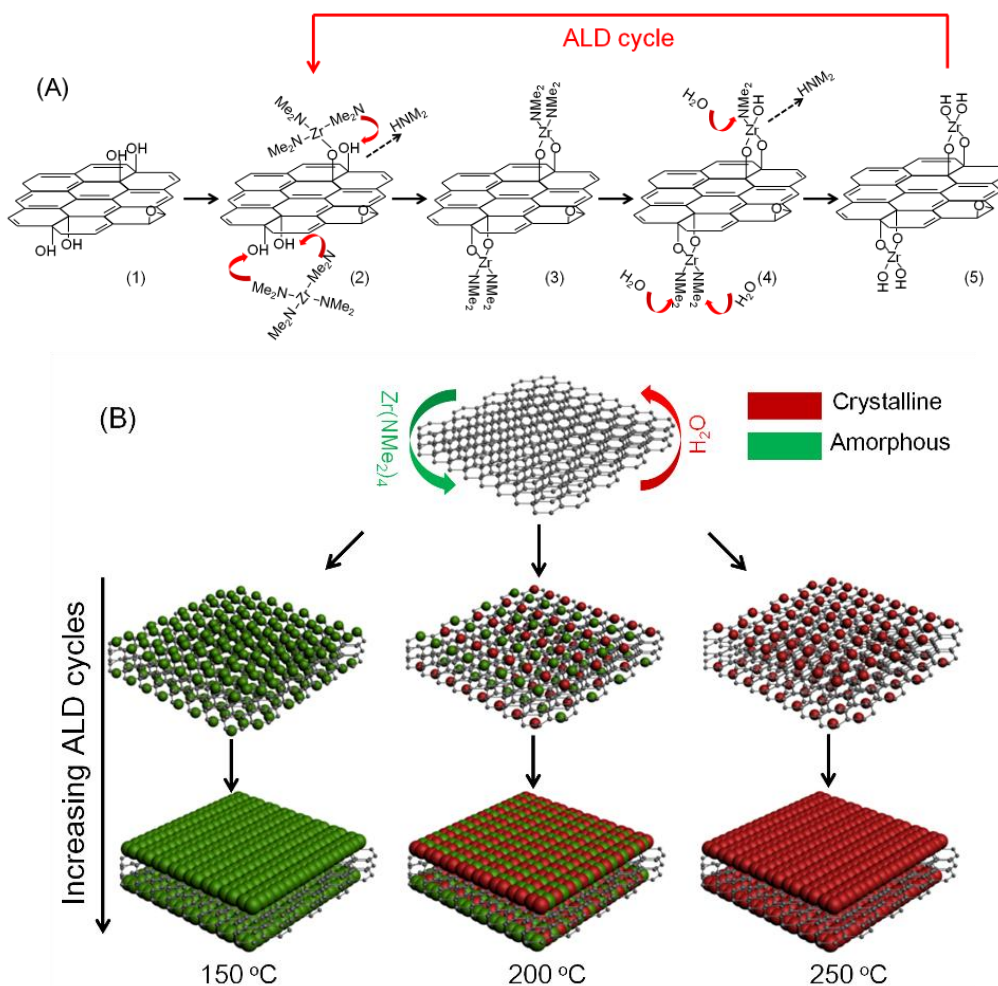


Figure 7.5 (A) Schematic diagram of one ALD cycle using Zr(NMe₂)₄ and H₂O as precursors [42]; (B) Schematic diagram of ZrO₂-GNS nanocomposites prepared at 150, 200 and 250 °C.

Figure 7.5B presents a schematic diagram to summarize the ZrO₂-GNS nanocomposites prepared at different deposition temperatures. At all temperatures, ALD-ZrO₂ on GNS are nanoparticles with low ALD cycles, while thin films with high ALD cycles. The

phase of deposited ZrO_2 is dominated by amorphous at 150 °C, and crystalline at 250 °C. The former two phases coexist in the ZrO_2 -GNS nanocomposite prepared at 200 °C.

7.4 Conclusions

In this work, ZrO_2 -GNS nanocomposites were prepared by ALD at deposition temperatures from 150 °C to 250 °C. The results showed that the crystallinity of the deposited ZrO_2 experienced a gradual decrease with the decrease of temperature. The dominant phase of the deposited ZrO_2 was crystalline at 250 °C and amorphous at 150 °C. Mixed phases of crystalline and amorphous ZrO_2 were found in the ZrO_2 -GNS nanocomposite prepared at 200 °C. At all the temperatures, the ZrO_2 deposited with lower number of ALD cycles showed nanoparticle morphology, while that produced with higher number of ALD cycles exhibited as uniform thin films. In all cases, the growth of ZrO_2 on GNS followed an “island growth” mode at the early stage, and a “layer-by-layer growth” mode after the coalescence of those ZrO_2 “islands”. It is expected that this kind of ZrO_2 -GNS nanocomposites, with controlled morphology and crystallinity of ZrO_2 , will find potential applications in various fields, such as supercapacitors, fuel cells, batteries and electronics.

Acknowledgements

This research was supported by General Motors of Canada, Natural Sciences and Engineering Research Council of Canada (NSERC), Canada Foundation for Innovation (CFI), Ontario Research Fund (ORF), Ontario Early Researcher Award (ERA) and University of Western Ontario. The authors also would like to thank Fred Pearson at McMaster University for his help on HRTEM.

References

- [1] K. S. Novoselov, A. K. Geim, S. V. Morozov, D. Jiang, Y. Zhang, S. V. Dobonos, I. V. Grigorieva, A. A. Firsov, Electric field effect in atomically thin carbon films, *Science* **2004**, *306*, 666-669.

- [2] A. A. Balandin, S. Ghosh, W. Bao, I. Calizo, D. Teweldebrhan, F. Miao, C. N. Lau, Superior thermal conductivity of single-layer graphene, *Nano Lett.* **2008**, *8*, 902-907.
- [3] K. I. Nolotin, K. J. Sikes, Z. Jiang, M. Klima, G. Fudenberg, J. Hone, P. Kim, H. L. Stormer, Ultrahigh electron mobility in suspended graphene, *Solid State Commun.* **2008**, *146*, 351-355.
- [4] M. D. Stoller, S. Park, Y. Zhu, J. An, R. S. Ruoff, Graphene-based ultracapacitors, *Nano Lett.* **2008**, *8*, 3498-3502.
- [5] C. Lee, X. Wei, J. W. Kysar, J. Hone, Measurement of the elastic properties and intrinsic strength of monolayer graphene, *Science* **2008**, *321*, 385-388.
- [6] J. Hass, W. A. Heer, E. H. Conrad, The growth and morphology of epitaxial multilayer graphene, *J Phys: Condens Matter* **2008**, *20*, 323202.
- [7] E. Yoo, J. Kim, E. Hosono, H. Zhou, T. Kudo, I. Honma, Large reversible Li storage of graphene nanosheet families for use in rechargeable lithium ion batteries, *Nano Lett.* **2008**, *8*, 2277-2282.
- [8] X. Li, D. Geng, Y. Zhang, X. Meng, R. Li, X. Sun, Superior cycle stability of nitrogen-doped graphene nanosheets as anodes for lithium ion batteries, *Electrochem. Commun.* **2011**, *13*, 822-825.
- [9] D. Geng, Y. Chen, Y. Chen, Y. Li, R. Li, X. Sun, S. Ye, S. Knights, High oxygen-reduction activity and durability of nitrogen-doped graphene, *Energy Environ Sci.* **2011**, *4*, 760-764.
- [10] X. Wang, L. Zhi, N. Tsao, Ž. Tomović, J. Li, K. Müllen, Transparent carbon films as electrodes in organic solar cells, *Angew. Chem. Int. Ed.* **2008**, *47*, 2990-2992.
- [11] J. Wu, H. A. Becerril, Z. Bao, Z. Liu, Y. Chen, P. Peumans, Organic solar cells with solution-processed graphene transparent electrodes, *Appl. Phys. Lett.* **2008**, *92*, 263302.

- [12] Z. Liu, J. T. Robinson, X. Sun, H. Dai, PEGylated nanographene oxide for delivery of water-insoluble cancer drugs, *J. Am. Chem. Soc.* **2008**, *130*, 10876-10877.
- [13] Y. Li, W. Gao, L. Ci, C. Wang, P. M. Ajayan, Catalytic performance of Pt nanoparticles on reduced graphene oxide for methanol electro-oxidation, *Carbon* **2010**, *48*, 1124-1130.
- [14] S. Guo, S. Dong, E. Wang, Three-dimensional Pt-on-Pd bimetallic nanodendrites supported on graphene nanosheet: facile synthesis and used as an advanced nanoelectrocatalyst for methanol oxidation, *ACS Nano* **2010**, *4*, 547-555.
- [15] S. Stankovich, D. A. Dikin, G. H. B. Dommett, K. M. Kohlhaas, E. J. Zimney, E. A. Stach, R. D. Piner, S. T. Nguyen, R. S. Ruoff, Graphene-based composite materials, *Nature* **2006**, *442*, 282-286.
- [16] X. Zhang, H. Li, X. Cui, Y. Lin, Graphene/TiO₂ nanocomposites: synthesis, characterization and application in hydrogen evolution from water photocatalytic splitting, *J. Mater. Chem.* **2010**, *20*, 2801-2806.
- [17] D. Wang, D. Choi, J. Li, Z. Yang, Z. Nie, R. Kou, D. Hu, C. Wang, L. V. Saraf, J. Zhang, I. A. Aksay, J. Liu, Self-assembled TiO₂-graphene hybrid nanostructures for enhanced Li-ion insertion, *ACS Nano* **2009**, *3*, 907-914.
- [18] S. M. Paek, E. Yoo, I. Honma, Enhanced cyclic performance and lithium storage capacity of SnO₂/graphene nanoporous electrodes with three-dimensionally delaminated flexible structure, *Nano Lett.* **2009**, *9*, 72-75.
- [19] D. Wang, R. Kou, D. Choi, Z. Yang, Z. Nie, J. Li, L. V. Saraf, D. Hu, J. Zhang, G. L. Graff, J. Liu, M. A. Pope, I. A. Aksay, Ternary self-assembly of ordered metal oxide-graphene nanocomposites for electrochemical energy storage, *ACS Nano* **2010**, *4*, 1587-1595.
- [20] Y. Liang, Y. Li, H. Wang, J. Zhou, J. Wang, T. Regier, H. Dai, Co₃O₄ nanocrystals on graphene as a synergistic catalyst for oxygen reduction reaction, *Nature Mater.* **2011**, *10*, 780-786.

- [21] Y. Huang, J. Liang, Y. Chen, An overview of the applications of graphene-based materials in supercapacitors, *Small* **2012**, *8*, 1805-1834.
- [22] G. Yu, L. Hu, N. Liu, H. Wang, M. Vosgueritchian, Y. Yang, Y. Cui, Z. Bao, Enhancing the supercapacitor performance of graphene/MnO₂ nanostructured electrodes by conductive wrapping, *Nano Lett.* **2011**, *11*, 4438-4442.
- [23] S. Chen, J. Zhu, X. Wu, Q. Han, X. Wang, Graphene oxide-MnO₂ nanocomposites for supercapacitors, *ACS Nano* **2010**, *4*, 2822-2830.
- [24] J. Lu, J. B. Zang, S. X. Shan, H. Huang, Y. H. Wang, Synthesis and characterization of core-shell structural MWNT-zirconia nanocomposites, *Nano Lett.* **2008**, *8*, 4070-4074.
- [25] Y. Shan, L. Gao, Synthesis and characterization of phase controllable ZrO₂-carbon nanotube nanocomposites, *Nanotechnology* **2005**, *16*, 625-630.
- [26] H. Song, X. Qiu, F. Li, Promotion of carbon nanotube-supported Pt catalyst for methanol and ethanol electro-oxidation by ZrO₂ in acidic media, *Appl. Catal. A* **2009**, *364*, 1-7.
- [27] D. Guo, X. Qiu, W. Zhu, L. Chen, Synthesis of sulfated ZrO₂/MWCNT composites as new supports of Pt catalysts for direct methanol fuel cell application, *Appl. Catal. B* **2009**, *89*, 597-601.
- [28] R. Liang, M. Deng, S. Cui, H. Chen, J. Qiu, Direct electrochemistry and electrocatalysis of myoglobin immobilized on zirconia/multi-walled carbon nanotube nanocomposite, *Mater. Res. Bull.* **2010**, *45*, 1855-1860.
- [29] A. Javey, H. Kim, M. Brink, Q. Wang, A. Ural, J. Guo, P. McIntyre, P. Mceuen, M. Lundstrom, H. Dai, High-k dielectrics for advanced carbon-nanotube transistors and logic gates, *Nature* **2002**, *1*, 241-246.
- [30] D. Du, J. Liu, X. Zhang, X. Cui, Y. Lin, One-step electrochemical deposition of a graphene-ZrO₂ nanocomposite: preparation, characterization and application for detection of organophosphorus agents, *J. Mater. Chem.* **2011**, *21*, 8032-8037.

- [31] J. Gong, X. Miao, H. Wan, D. Song, Facile synthesis of zirconia nanoparticles-decorated graphene hybrid nanosheets for an enzymeless methyl parathion sensor, *Sens. Actuators B: Chem.* **2012**, *162*, 341-347.
- [32] M. Knez, K. Nielsch, L. Niinistö, Synthesis and surface engineering of complex nanostructures by atomic layer deposition, *Adv. Mater.* **2007**, *19*, 3425-3438.
- [33] X. Meng, D. Geng, J. Liu, R. Li, X. Sun, Controllable synthesis of graphene-based titanium dioxide nanocomposites by atomic layer deposition, *Nanotechnology* **2011**, *22*, 165602.
- [34] J. W. Elam, N. P. Dasgupta, F. B. Prinz, ALD for clean energy conversion, utilization, and storage, *MRS Bulletin* **2011**, *36*, 899-906.
- [35] M. Leskelä, M. Ritala, O. Nilsen, Novel materials by atomic layer deposition and molecular layer deposition, *MRS Bulletin* **2011**, *36*, 877-884.
- [36] H. C. M. Knoop, M. E. Donders, M. C. M. van de Sanden, P. H. L. Notten, W. M. M. Kessels, Atomic layer deposition for nanostructured Li-ion batteries, *J. Vac. Sci. Technol. A* **2012**, *30*, 010801.
- [37] X. Meng, D. Geng, J. Liu, M. Banis, Y. Zhang, R. Li, X. Sun, Non-aqueous approach to synthesize amorphous/crystalline metal oxide-graphene nanosheet hybrid composites, *J. Phys. Chem. C* **2010**, *114*, 18330-18337.
- [38] S. D. Elliott, Mechanism, products, and growth rate of atomic layer deposition of noble metals, *Langmuir* **2010**, *26*, 9179-9182.
- [39] C. Bae, H. Shin, K. Nielsch, Surface modification and fabrication of 3D nanostructures by atomic layer deposition, *MRS Bulletin* **2011**, *36*, 887-897.
- [40] R. L. Puurunen, Surface chemistry of atomic layer deposition: a case study for the trimethylaluminum/water process, *J. Appl. Phys.* **2005**, *97*, 121301-121352.

- [41] S. M. George, Atomic layer deposition: an overview, *Chem. Rev.* **2010**, *110*, 111-131.
- [42] D. M. Hausmann, E. Kim, J. Becker, R. G. Gordon, Atomic layer deposition of hafnium and zirconium oxides using metal amide precursors, *Chem. Mater.* **2002**, *14*, 4350-4358.
- [43] H. C. Schniepp, J. L. Li, M. J. McAllister, H. Sai, M. Herrera-Alonso, D. H. Adamson, R. K. Prud'homme, R. Car, D. A. Saville, I. A. Aksay, Functionalized single graphene sheets derived from splitting graphene oxide, *J. Phys. Chem. B* **2006**, *110*, 8535-8539.
- [44] W. S. Hummers, J. R. Offeman, Preparation of graphitic oxide, *J. Am. Chem. Soc.* **1958**, *80*, 1339.
- [45] D. Geng, S. Yang, Y. Zhang, J. Yang, J. Liu, R. Li, T. K. Sham, X. Sun, S. Ye, S. Knights, Nitrogen doping effects on the structure of graphene, *Appl. Surf. Sci.* **2011**, *257*, 9193-9198.
- [46] S. Stankovich, R. D. Piner, S. T. Nguyen, R. S. Ruoff, Synthesis and exfoliation of isocyanate-treated graphene oxide nanoplatelets, *Carbon* **2006**, *44*, 3342-3347.
- [47] R. L. Puurunen, W. Vandervorst, W. F. A. Besling, O. Richard, H. Bender, T. Conard, C. Zhao, A. Delabie, M. Caymax, S. D. Gendt, M. Heyns, M. M. Viitanen, M. Ridder, H. H. Brongersma, Y. Tamminga, T. Dao, T. Win, M. Verheijen, M. Kaiser, M. Tuominen, Island growth in the atomic layer deposition of zirconium oxide and aluminum oxide on hydrogen-terminated silicon: Growth mode modeling and transmission electron microscopy. *J. Appl. Phys.* **2004**, *86*, 4878-4889.
- [48] M. Copel, M. Gribelyuk, E. Gusev, Structure and stability of ultrathin zirconium oxide layer on Si(001), *Appl. Phys. Lett.* **2000**, *76*, 436-438.
- [49] W. F. A. Besling, E. Young, T. Conard, C. Zhao, R. Carter, W. Vandervorst, M. Caymax, S. D. Gendt, M. Heyns, J. Maes, M. Tominen, S. Haukka, Characterization of

ALCVD Al₂O₃-ZrO₂ nanolaminates, link between electrical and structural properties, *J. Non-Cryst. Solid* **2002**, *303*,123-133.

[50] Y. S. Min, P.H. Lee, Y. H. Lee, C. S. Hwang, Botryoidal growth of crystalline ZnO nanoparticles on a forest of single-walled carbon nanotubes by atomic layer deposition, *CrystEngComm* **2011**, *13*, 3451-3454.

[51] S. Park, R. S. Ruoff, Chemical methods for the production of graphenes, *Nature Nanotech.* **2009**, *4*, 217-224.

[52] D. Li, M. B. Müller, S. Gilje, R. B. Kaner, G. G. Wallace, Processable aqueous dispersions of graphene nanosheets, *Nature nanotech.* **2008**, *13*, 101-105.

[53] M. Cassir, F. Goubin, C. Bernay, P. Vernoux, D. Lincot, Synthesis of ZrO₂ thin films by atomic layer deposition: growth kinetics, structural and electrical properties, *Appl. Surf. Sci.* **2002**, *193*, 120-128.

[54] J. Aarik, A. Aidla, T. Uustare, V. Sammelselg, Morphology and structure of TiO₂ thin films grown by atomic layer deposition, *J. Cryst. Growth* **1995**, *148*, 268-675.

[55] C. H. L. Goodman, M. V. Pessa, Atomic layer epitaxy, *J. Appl. Phys.* **1986**, *60*, R65-81.

[56] X. Meng, Y. Zhang, S. Sun, R. Li, X. Sun, Three growth modes and mechanisms for highly structure-tunable SnO₂ nanotube arrays of template-directed atomic layer deposition, *J. Mater. Chem.* **2011**, *21*, 12321-12330.

[57] J. C. F. Rodríguez-Reyes, A. V. Teplyakov, Mechanisms of adsorption and decomposition of metal alkylamide precursors for ultrathin film growth, *J. Appl. Phys.* **2008**, *104*, 084907.

[58] D. M. Hausmann, R. G. Gordon, Surface morphology and crystallinity control in the atomic layer deposition (ALD) of hafnium and zirconium oxide thin films, *J. Cryst. Growth* **2003**, *249*, 251-261.

[59] X. Wang, S. M. Tabakman, H. Dai, Atomic layer deposition of metal oxides on pristine and functionalized graphene, *J. Am. Chem. Soc.* **2008**, *130*, 8152-8153.

[60] B. Lee, G. Mordì, M. J. Kim, Y. J. Chabal, E. M. Vogel, R. M. Wallace, K. J. Cho, L. Colombo, J. Kim, Characteristics of high-k Al₂O₃ dielectric using ozone-based atomic layer deposition for dual-gated graphene devices, *Appl. Phys. Lett.* **2010**, *97*, 043107.

[61] N. Y. Garces, V. D. Wheeler, J. K. Hite, G. G. Jernigan, J. L. Tedesco, N. Nepal, et al. Epitaxial graphene surface preparation for atomic layer deposition of Al₂O₃. *J. Appl. Phys.* **2011**, *109*, 124304.

Supporting Information

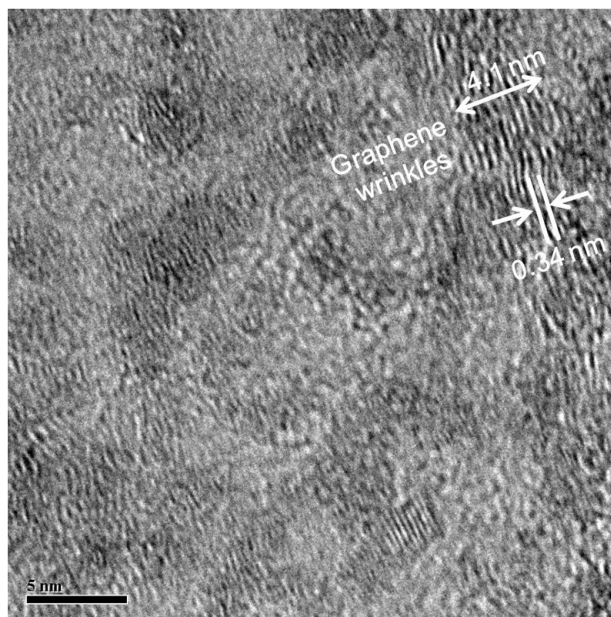


Figure SI-7.1 HRTEM image of ZrO₂-GNS nanocomposite prepared at 200 °C with 10 cycles showing the thickness of graphene wrinkles.

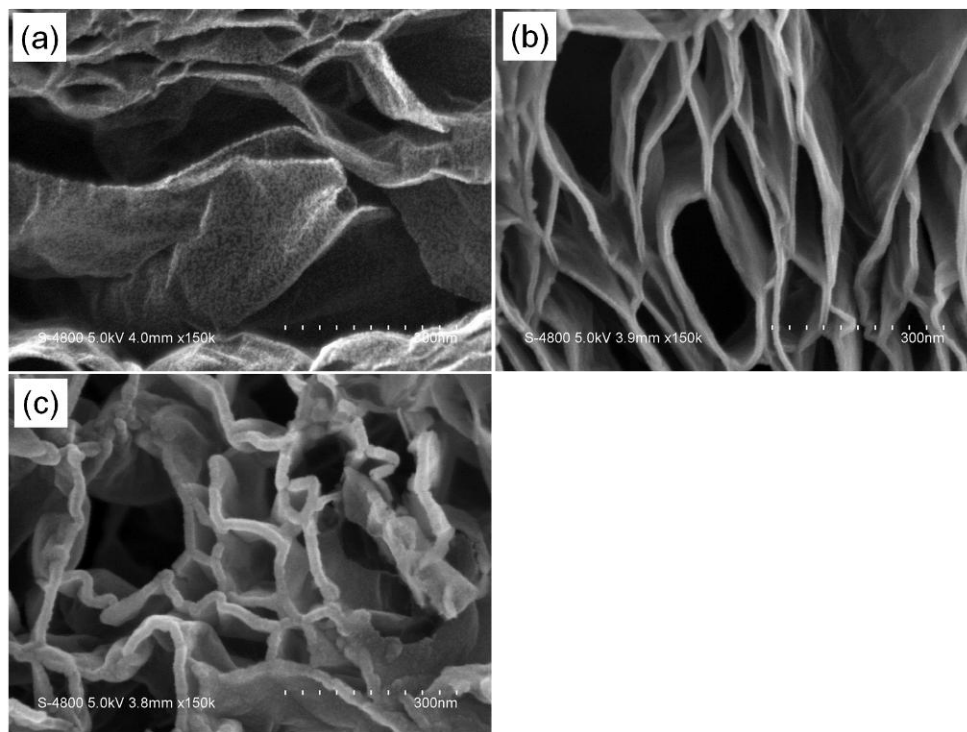


Figure SI-7.2 Low-magnification SEM images of ZrO_2 -GNS nanocomposites prepared at 150°C with (a) 10 cycles, (b) 30 cycles and (c) 50 cycles.

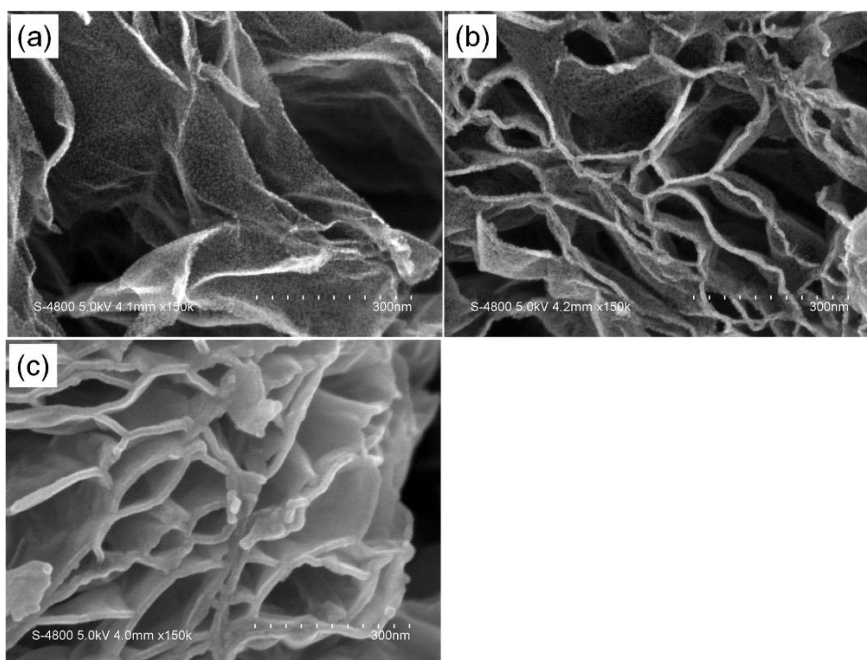


Figure SI-7.3 Low-magnification SEM images of ZrO_2 -GNS nanocomposites prepared at 200°C with (a) 10 cycles, (b) 30 cycles and (c) 50 cycles.

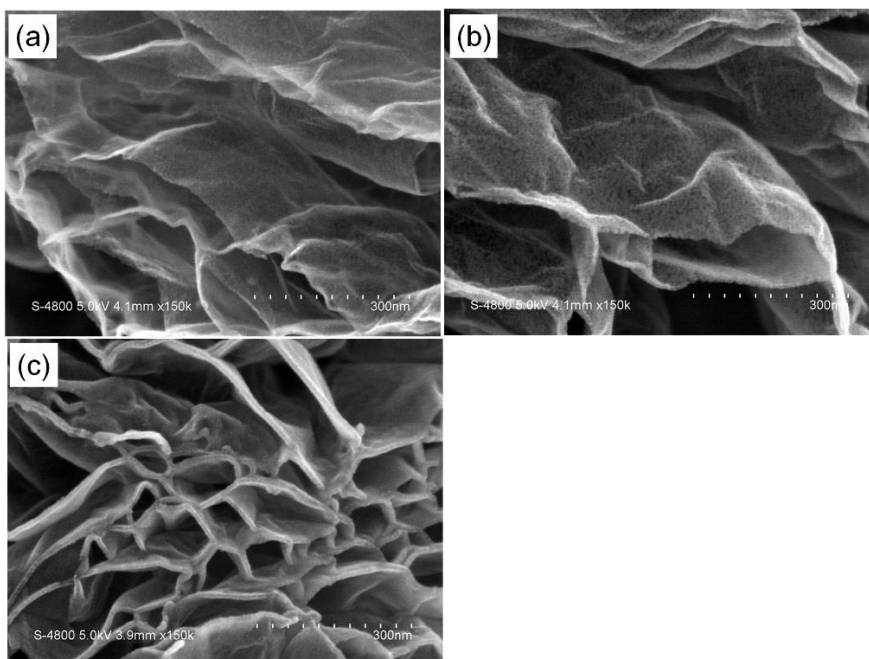


Figure SI-7.4 Low-magnification SEM images of ZrO_2 -GNS nanocomposites prepared at 250 °C with (a) 10 cycles, (b) 30 cycles and (c) 50 cycles.

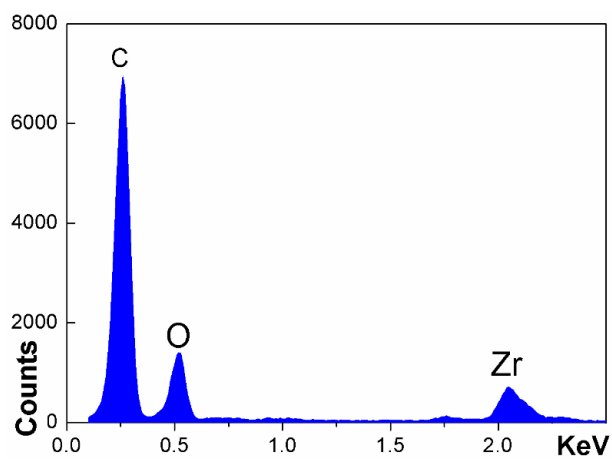


Figure SI-7.5 EDS result of ZrO_2 -GNS nanocomposite prepared at 150 °C with 10 cycles.

Chapter 8 Ultrathin Atomic Layer Deposited ZrO₂ Coating to Enhance the Electrochemical Performance of Li₄Ti₅O₁₂ as an Anode Material^{††}

Solid-electrolyte interphase (SEI) is a product of the decomposition of liquid electrolytes on the surface of anode materials. To solve the problems associated with SEI, one way to prevent or alleviate the SEI formation is coating anode materials with an artificial layer, such as ALD-ZrO₂ developed in chapter 6 and 7.

In this chapter, Li₄Ti₅O₁₂ synthesized in chapter 5 is used as a model to investigate the influence of ALD-ZrO₂ coating on the SEI formation and thereby the electrochemical performance of Li₄Ti₅O₁₂. ALD was used to deposit ZrO₂ directly on Li₄Ti₅O₁₂ electrode. The thickness of the deposited ZrO₂ was controlled by adjusting ALD cycles from 0 to 1, 2, 5, 10 and 50. The electrochemical performances of the Li₄Ti₅O₁₂ electrodes with and without ZrO₂ coating were compared. The cyclic voltammetry result indicated that ZrO₂ coating with 2, 5 and 10 ALD cycles could effectively reduce the electrochemical polarization of the Li₄Ti₅O₁₂ electrode. Charge-discharge test revealed that the Li₄Ti₅O₁₂ electrodes with 1-, 2- and 5-cycle ZrO₂ coating exhibited higher specific capacity, better cycling performance and rate capability than the pristine Li₄Ti₅O₁₂ in a voltage range of 0.1-2.5 V. However, ZrO₂ coating with more than 5 ALD cycles could lead to degraded performance of Li₄Ti₅O₁₂. Mechanism for the enhanced electrochemical performance of Li₄Ti₅O₁₂ was explored by electrochemical impedance spectroscopy, and the reason was attributed to the suppressed formation of solid electrolyte interphase and the improved electron transport by ultrathin ZrO₂ coating.

Keyword: Zirconium oxide; atomic layer deposition; lithium-ion battery; lithium titanate.

^{††} Part of this chapter has been published in *Electrochim. Acta* **2013**, 93, 195-201.

8.1 Introduction

Recently, considerable efforts have been made to developing high performance Li-ion batteries (LIBs) in the applications of power plug-in hybrid electric vehicles (PHEVs) and electric vehicles (EVs) [1, 2]. As the electrochemical performance of LIBs strongly depends on the electrode materials, it is of great importance to select proper anode and cathode materials. At present, graphite is widely used in commercial LIBs as the anode material, but it suffers from poor abuse tolerance for PHEV and EV applications [3]. Spinel $\text{Li}_4\text{Ti}_5\text{O}_{12}$ (LTO) has attracted increasing attention as an alternative to graphite due to its high working potential of the redox couple $\text{Ti}^{4+}/\text{Ti}^{3+}$ (*ca.* 1.55 V vs. Li/Li^+) [4]. One advantage of LTO over other anode materials is the negligible volume change during charge/discharge process, because of which LTO is known as a “zero-strain” material [5, 6]. Beside the structural stability, LTO is also found to exhibit good thermodynamic stability due to its compatibility with electrolyte, promising LIBs a good safety for PHEV and EV applications [7]. However, LTO exhibits an inherently insulating property owing to the empty Ti 3d-sates with band gap energy of ~ 2 eV, which seriously hinders its high-rate performance [6, 8]. To solve this problem, two strategies are generally adopted, *i.e.* reducing the physical diffusion length of electrons and Li-ions by preparing nanosized LTO materials [9-14], or/and enhancing the Li-ion diffusion and electronic conductivity *via* surface modification or ion doping [9, 10, 15-18]. By means of these methods, the drawback of LTO has been overcome to a great extent, and its high rate performance has been improved greatly [9-18]. Currently, LTO has been considered as one of the most promising anode materials in practical energy applications [19].

In most previous studies, the electrochemical performance of LTO was evaluated in a voltage window of higher than 1 V, because the redox couple $\text{Ti}^{4+}/\text{Ti}^{3+}$ operates at 1.55 V (*vs.* Li/Li^+) [4]. Recently, there is increasing awareness that it is necessary to study the LIB performance of LTO at a lower voltage than 1 V, in view of the following aspects: (1) It is important to study the over-charge behaviours of LTO for safety concern, as uneven electrodes will result in local polarization and local overcharge during lithium uptake process [20, 21]; (2) LTO electrodes operate at a lower voltage could offer a higher discharge capacity and a higher cell voltage, thereby resulting in higher energy density of

LIBs [22-26]. It was widely reported that the discharge capacity of LTO could exceed its theoretical capacity of 175 mAh g^{-1} (based on $\text{Li}_4\text{Ti}_5\text{O}_{12}/\text{Li}_7\text{Ti}_5\text{O}_{12}$ transition), when the voltage window extended down to 0 V [22-26]. For example, LTO powders prepared by a solid state method exhibited a discharge capacity of 155 mAh g^{-1} after 50 cycles between 1-2 V, while a higher specific capacity of 190 mAh g^{-1} after 50 cycles could be achieved in a voltage range of 0.1-2 V [24]. The extra discharge capacity resulted from the further reduction of Ti^{4+} between 0.6 and 0.1 V, which was repeatable in the subsequent cycles [22-27]. However, the increased capacity of LTO by extended voltage window was accompanied by the decomposition of electrolyte between 0.5-1 V, which would lead to the formation of solid electrolyte interphase (SEI) [21]. Therefore, suppressing the formation of SEI becomes important in order to enhance the cycling performance and coulombic efficiency of LTO in an extended voltage window [28, 29].

Recently, atomic layer deposition (ALD) technique has attracted increasing attention in the field of LIBs [30, 31], for its capability to realize excellent coverage and conformal deposition of thin films with precisely controlled thickness at nanoscale level [32]. As to the application in anodes, ALD- Al_2O_3 is the most studied coating material, and Al_2O_3 coating has been found to be able to alleviate the cracking of the anodes during charge-discharge process [33, 34], suppress the side reactions between anodes and electrolyte [33-36], mitigate the decomposition of SEI, especially at elevated temperatures [34, 37], and preserving mechanical integrity of the electrodes by “knitting” the active materials to the conductive additive [37, 38], thereby improving the LIB performance. Besides Al_2O_3 , ZrO_2 is another excellent coating material for both anodes [39] and cathodes [40, 41] in LIBs. To our best knowledge, ALD coating of ZrO_2 has not been demonstrated in the application of LIB anodes so far. In the present work, therefore, we use ALD- ZrO_2 coating to modify the LTO electrode in order to improve its LIB performance in an extended voltage window (0.1-2.5 V). The effect of ZrO_2 coating with different thicknesses on the LIB performance of the LTO electrode was investigated in details, and it was demonstrated that only ZrO_2 coating with no more than 5 ALD cycles can enhance the electrochemical performance of the LTO. Underlying mechanism for the improvement was explored and discussed.

8.2 Experimental Section

8.2.1 Material preparation and characterization

Nanoflower-like LTO powders were synthesized by a microwave assisted hydrothermal method and following heat treatment, and the detailed process was described in our previous work [42]. To prepare the electrode, the LTO powders, acetylene black and polyvinylidene fluoride binder (PVDF), with a weight ratio of 80:10:10, were mixed homogeneously, and then the slurry was pasted onto a copper foil. The obtained electrode was dried under vacuum at 110 °C for 12 h. ALD-ZrO₂ was achieved using tetrakis(dimethylamido)zirconium (IV) and water as precursors at a deposition temperature of 100 °C. Detailed procedure of ALD-ZrO₂ was reported in our previous study [44]. Coating of ALD-ZrO₂ was conducted directly on the as-prepared LTO electrode, with different ALD cycles (0, 1, 2, 5, 10 and 50). In the following section, the LTO electrode coated with 0, 1, 2, 5, 10 and 50-cycle ZrO₂ is referred as LTO-0, LTO-1, LTO-2, LTO-5, LTO-10 and LTO-50, respectively. The loading of active materials (including ZrO₂ if applicable) is ~ 2.23, 2.32, 2.39, 2.41, 2.46 and 2.71 mg for LTO-0, LTO-1, LTO-2, LTO-5, LTO-10 and LTO-50, respectively.

The morphology and structure of the above samples were characterized by a field-emission scanning electron microscope (SEM, Hitachi S4800) equipped with energy dispersive X-ray spectroscopy (EDS) and high-resolution transmission electron microscope (HRTEM, JEOL 2010 FEG).

8.2.2 Electrochemical characterization

Electrochemical measurements were performed by using coin-type half cells assembled in an argon-filled glove box ([O₂] < 1 ppm, [H₂O] < 1 ppm). The coin-type half-cell consisted of the LTO electrodes prepared above, polypropylene separator (Celgard 2400), and lithium foil as the counter electrode. The electrolyte was 1M LiPF₆ solution in ethylene carbonate (EC): diethyl carbonate (DEC): ethyl methyl carbonate (EMC) with a volume ratio of 1:1:1. The electrochemical performance of the coin-type half cells was tested in an Arbit BT-2000 Battery Test System.

8.3 Results and Discussion

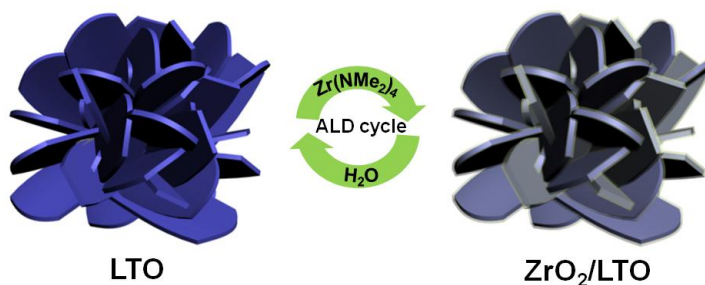


Figure 8.1 Schematic diagram of LTO and LTO coated with ZrO_2 by ALD.

It was reported that ZrO_2 could be deposited by ALD using $\text{Zr}(\text{NMe}_2)_4$ and H_2O as precursors in a wide temperature range of 50-300 °C [43, 44]. In this work, the same precursor combination was adopted for ALD- ZrO_2 , which was directly applied on the LTO electrode at 100 °C. Typically the first ALD- ZrO_2 reaction requires a hydroxyl-terminated surface, which is present on metal oxides [35]. According to published work [43, 44], each ALD cycle should deposit a uniform ZrO_2 layer of approximately 0.096-0.142 nm in thickness. After different ALD cycles, the surface of LTO was covered by uniform ZrO_2 film, as schematically shown in [Figure 8.1](#).

[Figure 8.2](#) displays the morphologies of the LTO electrodes with and without ZrO_2 coating. The initial LTO consists of many nanosheets with wall thickness of ~ 18 nm, as seen in [Figure 8.2a](#). For LTO-1 and LTO-2, there is no visible change in the morphology, as indicated in [Figure 8.2 \(b, c\)](#). For LTO-5, the edges of nanosheets are lighter than the central parts, which might be induced by the ZrO_2 coating, as presented in [Figure 8.2d](#). In [Figure 8.2e](#), it is obvious that LTO-10 has thicker nanosheets and slightly rougher surface than LTO-0, due to the ZrO_2 coating. 50-cycle ALD leads to the growth of ZrO_2 film on the surface of nanosheets, the thickness of which is measured to be ~ 35 nm for LTO-50. The higher growth per cycle of ZrO_2 in this case is due to the large surface area of nanoflower-like LTO ($46.8 \text{ m}^2 \text{ g}^{-1}$) [42], which makes completely purge of H_2O from reactor difficult. During the pulse of $\text{Zr}(\text{NMe}_2)_4$, the presence of H_2O in the reactor leads to slightly enhanced growth per cycle resulting from some chemical vapour deposition. SEM images of the above samples at low magnification are included in [Figure SI-8.1](#) of

the Supporting Information. EDS analysis confirms the existence of Zr and O elements in the ALD-ZrO₂ coated samples, and the intensity of Zr element increases with ALD cycles (Figure SI-8.2 of the Supporting Information). Furthermore, the EDS mapping reveals the uniform distribution of Zr and O elements on the LTO, and [Figure 8.3](#) shows the EDS mapping result of LTO-10 as an example.

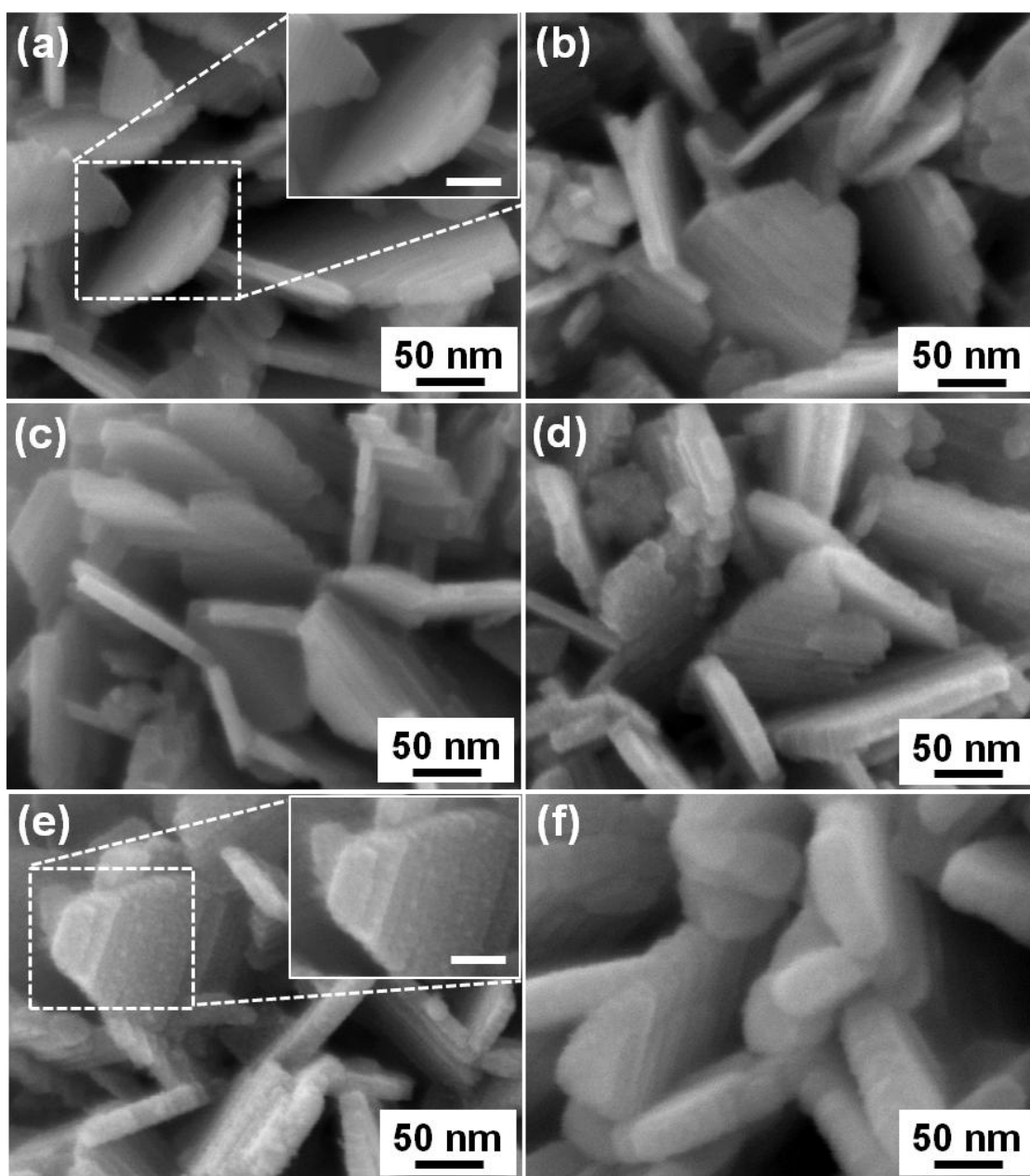


Figure 8.2 SEM images of (a) LTO-0, (b) LTO-1, (c) LTO-2, (d) LTO-5, (e) LTO-10 and (f) LTO-50 (The scale bars in the insets of [Figure 8.2a, e](#) represent 30 nm).

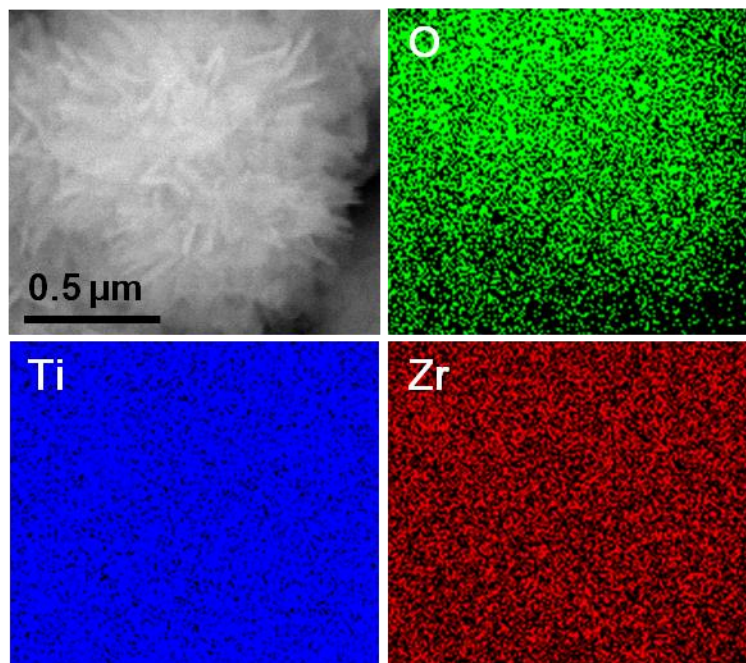


Figure 8.3 EDS mapping of LTO-10.

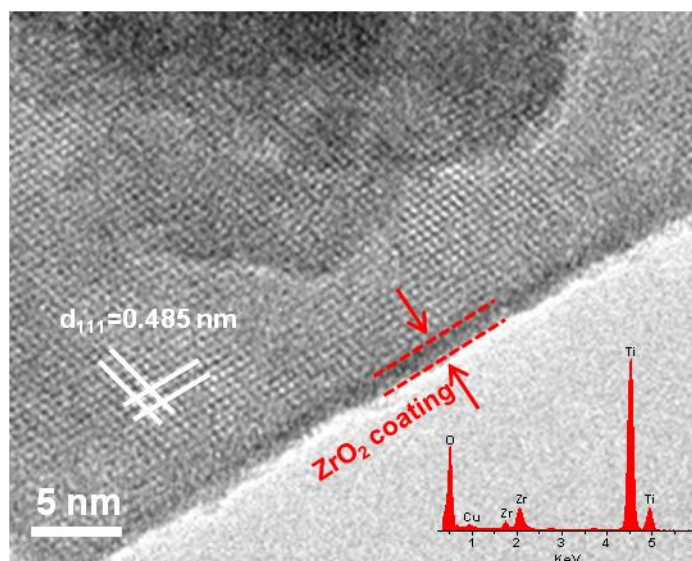


Figure 8.4 HRTEM image of LTO-10 (inset shows the EDS result).

To further study the ZrO_2 coating on the LTO, HRTEM was performed on LTO-10, and the result is shown in Figure 8.4. The lattice distance of LTO-10 is measured to be 0.485 nm, in agreement well with $d_{(111)}$ spacing of spinel $\text{Li}_4\text{Ti}_5\text{O}_{12}$ (JCPDS PDF No. 49-0270). In Figure 8.4, it is evident that the surface of LTO-10 is covered by a dense and uniform

thin film, as marked by the red dash lines. EDS of HRTEM further verifies the presence of Zr and O elements in LTO-10. The ZrO_2 coating layer is determined to be ~ 2 nm in thickness. Based on the results of SEM, EDS and HRTEM, it can be concluded that uniform ZrO_2 films with different thicknesses were successfully coated on the LTO electrode by ALD.

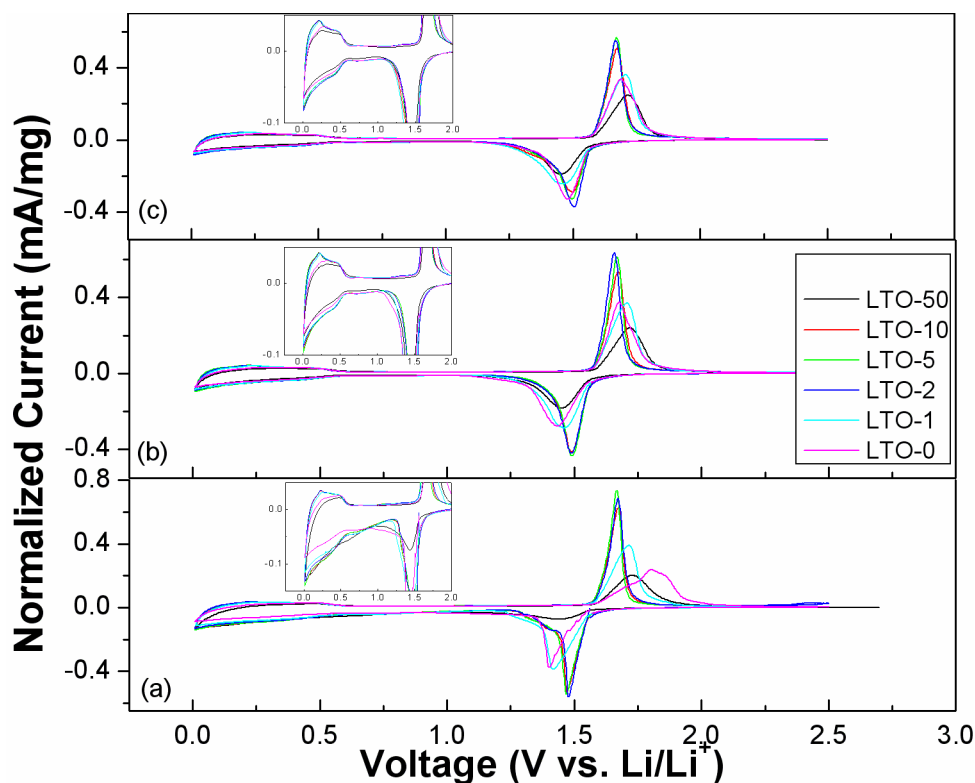


Figure 8.5 CV curves of LTO-0, LTO-1, LTO-2, LTO-5, LTO-10 and LTO-50 during the (a) first, (b) second and (c) third cycle at a scanning rate of 0.1 mV s^{-1} between 0.1-2.5 V (insets show the enlarged parts below 1 V).

The electrochemical performance of the LTO electrodes with and without ZrO_2 coating was evaluated in order to study the ZrO_2 coating effect systematically. [Figure 8.5](#) shows the cyclic voltammograms (CVs) of different samples in the first three cycles. In [Figure 8.5](#), one can see that between 1-2.5 V, one pair of redox peaks appears at about 1.70 V (anodic) and 1.47 V (cathodic) for all the samples, which are correlated to the spinel/rock-salt phase transition ($\text{Li}_4\text{Ti}_5\text{O}_{12}/\text{Li}_7\text{Ti}_5\text{O}_{12}$) [12-15]. It is obvious that even at such a low scanning rate (0.1 mV s^{-1}), the degree of the electrochemical polarization is

different among the samples. [Table 8-1](#) compares the potential differences between the anodic and cathodic peaks in the first five cycles (anodic and cathodic peak potentials are included in Table SI-8-1 of the Supporting Information). It can be found that the potential difference gradually decreases with ZrO₂ coating up to 10 ALD cycles, and then experiences an increase with 50-cycle ZrO₂ coating. For example, the potential difference in the fifth cycle is 0.315, 0.281, 0.171, 0.178, 0.178 and 0.321 V for LTO-0, LTO-1, LTO-2, LTO-5, LTO-10 and LTO-50, respectively. The narrowed potential differences of LTO-2, LTO-5 and LTO-10 indicate reduced polarization and enhanced electrochemical kinetics of the LTO electrodes by ZrO₂ coating with no more than 10 ALD cycles. Insets of [Figure 8.5](#) show the enlarged CVs below 1 V, and one can find another couple of reduction and oxidation peaks located between 0.1-0.6 V. Those two peaks are observed to be repeatable in the subsequent cycles, and therefore enlarging the potential window can increase the reversible capacity of the LTO electrode. The reduction peak below 0.6 V could be attributed to the further reduction of Ti⁴⁺ [27]. When Li₄Ti₅O₁₂ is charged to Li₇Ti₅O₁₂, only one Ti⁴⁺ is reduced and there are still 2/3 Ti⁴⁺ remaining in the reduction production of Li₇Ti₅O₁₂ to accept electrons [27, 45]. Further intercalation of lithium ions into Li₇Ti₅O₁₂ below 0.6 V could occupy the tetrahedral (8a) sites, leading to the increased reversible capacity of spinel Li₄Ti₅O₁₂ [45].

Table 8-1 Potential differences (V) between anodic and cathodic peaks in the first five cycles.

	1 st cycle	2 nd cycle	3 rd cycle	4 th cycle	5 th cycle
LTO-0	0.398	0.243	0.213	0.250	0.315
LTO-1	0.297	0.247	0.253	0.268	0.281
LTO-2	0.196	0.167	0.165	0.152	0.171
LTO-5	0.197	0.176	0.176	0.175	0.178
LTO-10	0.201	0.184	0.175	0.184	0.178
LTO-50	0.289	0.268	0.264	0.271	0.321

[Figure 8.6](#) displays the charge/discharge profiles of the LTO electrodes with and without ZrO₂ coating during the first two cycles. It can be seen that all the samples except LTO-50 exhibit flat plateaus near 1.55 V and inclined curves between 0.1 to 0.6 V (vs. Li/Li⁺), which agree well with the two pairs of redox peaks in the CVs ([Figure 8.5](#)). LTO-50 shows continuously decreased potential with the intercalation of lithium ions in the LTO

during the first cycle, which is probably due to the inhibited lithium ion diffusion by thick insulating ZrO_2 layer. In Figure 8.6, it is apparent that the discharge/charge capacities of LTO-0 are lower than those of LTO-1, LTO-2, LTO-5 and LTO-10, but higher than LTO-50. For example, the discharge capacity in the second cycle is 216, 226, 230, 224, 222 and 180 mAh g^{-1} for LTO-0, LTO-1, LTO-2, LTO-5, LTO-10 and LTO-50, respectively. This result suggests that appropriate ZrO_2 coating can improve the discharge/charge capacities of the LTO. For all the samples, there are obvious capacity losses after the first cycle, which could be attributed to the SEI formation below 1 V [28, 29].

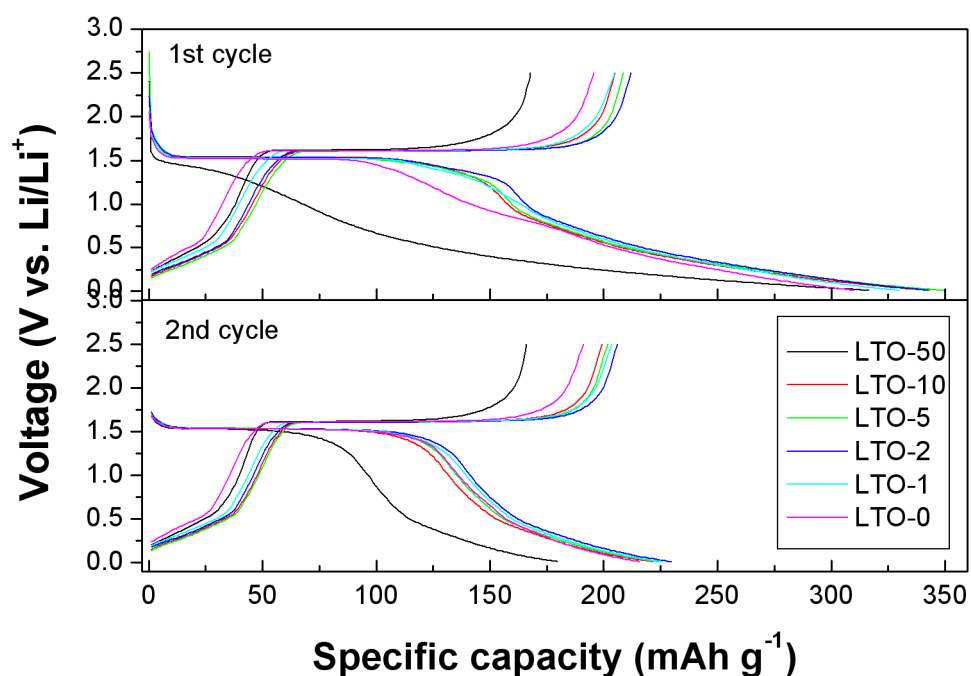


Figure 8.6 Charge/discharge profiles of LTO-0, LTO-1, LTO-2, LTO-5, LTO-10 and LTO-50 in the 1st and 2nd cycles between 0.1-2.5 V at a current density of 200 mA g^{-1} .

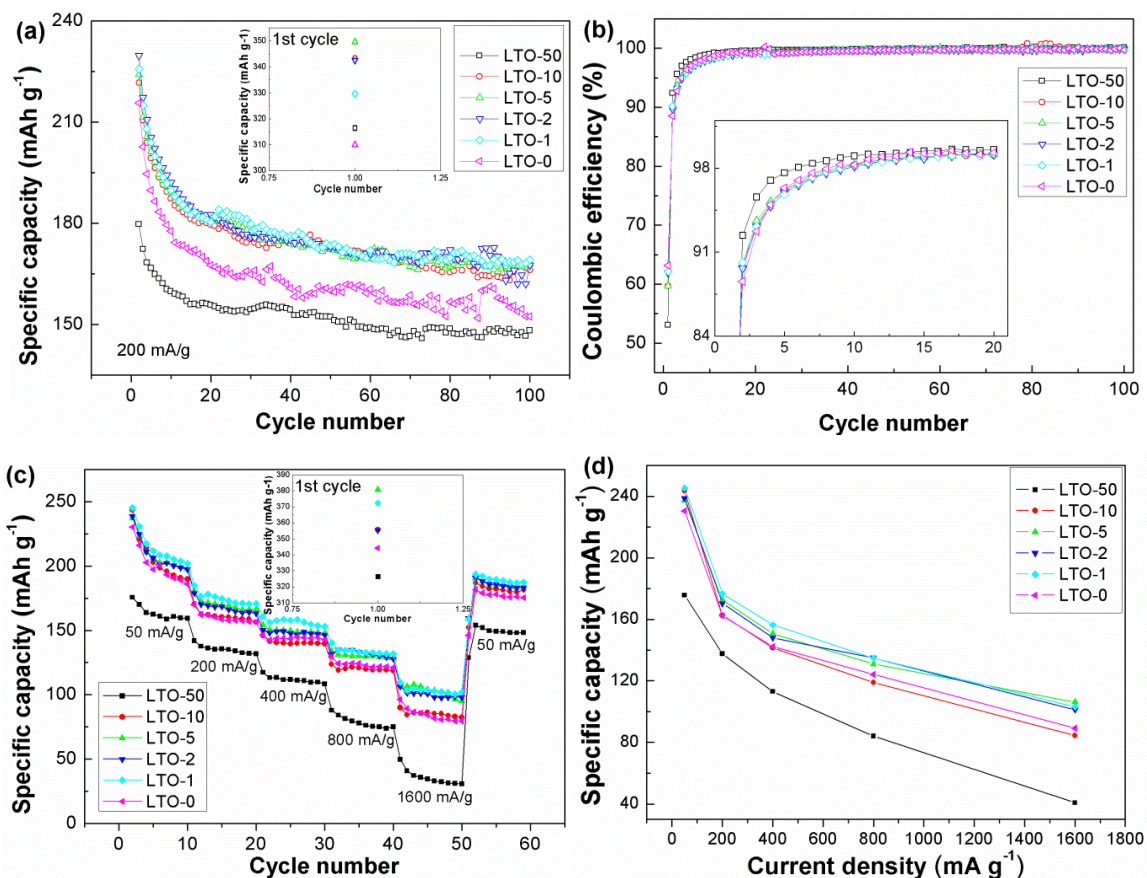


Figure 8.7 (a) Cycling stability, (b) coulombic efficiency (c) rate capability and (d) discharge capacity vs. current density of LTO-0, LTO-1, LTO-2, LTO-5, LTO-10 and LTO-50 between 0.1-2.5 V (insets in Figure 8.7a and Figure 8.7c show the discharge capacity in the first cycle).

Figure 8.7 presents the cycling stabilities and rate capabilities of the LTO electrodes with and without ZrO₂ coating between 0.1-2.5 V. The cycling stabilities in Figure 8.7a indicates that LTO-1, LTO-2, LTO-5 and LTO-10 exhibit higher specific capacity and better cycling performance than LTO-0 and LTO-50 at a current density of 200 mA g⁻¹. The initial discharge capacity is 310, 330, 343, 350, 343 and 216 mAh g⁻¹ for LTO-0, LTO-1, LTO-2, LTO-5, LTO-10 and LTO-50, respectively. All the samples show obvious capacity losses in the second cycle, due to the irreversible lithium ions trapped in the SEI [28, 29]. Then the irreversible capacity rapidly decreases upon cycling, and the reversible capacity stabilizes after *ca.* 20 cycles. After 100 cycles, LTO-0, LTO-1, LTO-2, LTO-5, LTO-10 and LTO-50 can maintain a specific capacity of 152, 169, 168, 168, 166

and 148 mAh g^{-1} , respectively. The coulombic efficiency (CE) of each sample is compared in Figure 8.7b. The CE in the first cycle is determined to be 63%, 62%, 62%, 60%, 60% and 53% for LTO-0, LTO-1, LTO-2, LTO-5, LTO-10 and LTO-50, respectively. In the following cycles, the CE increases greatly for all the samples, and keeps at $\sim 100\%$ after 20 cycles. In the inset of Figure 8.7b, one can easily find that LTO-50 has much higher CE than the others after the first cycle, suggesting that ZrO_2 coating can effectively suppress further decomposition of electrolyte and the formation of SEI after the first cycle. Figure 8.7c presents the rate capabilities of all the samples at various current densities ($50\text{-}1600 \text{ mA g}^{-1}$), and the second-cycle discharge capacity at each current density is compared in Figure 8.7d. In Figure 8.7c, it can be found that the rate capabilities of LTO-1, LTO-2 and LTO-5 are obviously better than that of LTO-0, especially at a high current density of 1600 mA g^{-1} , while LTO-50 shows worse rate capability than LTO-0. The rate capability of LTO-10 is comparable with that of LTO-0. With the increase of the current density, the discharge capacity gradually decreases for all the samples, as seen in Figure 8.7d. At a current density of 1600 mA g^{-1} , the discharge capacity is 90, 103, 101, 106, 86 and 41 mAh g^{-1} for LTO-0, LTO-1, LTO-2, LTO-5, LTO-10 and LTO-50, respectively. Moreover, all the samples can recover the initial reversible capacity at 50 mA g^{-1} . Based on the CV and charge-discharge tests, it can be concluded that ZrO_2 coating with no more than 5 ALD cycles can improve the specific capacity, cycling performance and rate capability of the LTO electrode.

To find out the reason for the improved electrochemical performance, electrochemical impedance spectroscopy (EIS) measurement of the LTO electrodes with and without ZrO_2 coating was carried out at about 1.5 V in a frequency range from 0.1 to 10^4 Hz, and typical Nyquist plots are given in Figure 8.8. It can be seen the Nyquist plots of LTO-0, LTO-2, LTO-5, LTO-10 and LTO-50 are composed of two partially overlapped and depressed semicircles in the high-frequency and middle-frequency ranges, and one inclined line at low frequency (except LTO-50). The EIS curves are simulated using the equivalent circuit in the inset of Figure 8.8, and one can find that the experimental and simulated data are almost coincident. Accordingly, the depressed semicircles at high frequency can be attributed to the resistance of SEI film (R_{sei}), those at middle frequency are caused by charge-transfer resistance (R_{ct}) at the interface of electrolyte and electrode,

and the sloped lines at low frequency can be considered to be the Warburg impedance (W) [25, 28, 29]. R_s is the solution resistance, and CPE1 and CPE2 are placed to represent the double layer capacitance and passivation film capacitance [18]. The values of R_s , R_{sei} and R_{ct} are obtained from the simulated data of EIS in Figure 8.8, and listed in Table 8-2. In Table 8-2, it can be seen that the R_{sei} of LTO-2, LTO-5, LTO-10 and LTO-50 are obviously lower than that of LTO-0, implying thinner SEI film formed on the former ones than the latter one [28]. one can also see that the R_{ct} of LTO-0 (32.35 Ω) is higher than that of LTO-2 (14.77 Ω) and LTO-5 (16.94 Ω), but lower than that of LTO-10 (44.25 Ω) and LTO-50 (657.80 Ω), indicating that only ZrO_2 coating with appropriate thickness (no more than 5 ALD cycles) can increase the charge-transfer reaction at the interface of electrolyte and electrode. Combining EIS with electrochemical performance results, it can be found that LTO electrodes with lower R_{sei} and R_{ct} values (LTO-2 and LTO-5) exhibit better LIB performance than those with higher R_{sei} or/and R_{ct} (LTO-0, LTO-10 and LTO-50). Furthermore, it should be noted that LTO-2, LTO-5 and LTO-10 exhibit lower R_s value than LTO-0 does, suggesting the decreased overall internal resistance with less than 10-cycle ZrO_2 coatings. This also partially accounts for the enhanced LIB performance of LTO-2 and LTO-5. The reason is attributable to improved mechanical adhesion of electrode materials to the current collectors by appropriate ZrO_2 coatings [38].

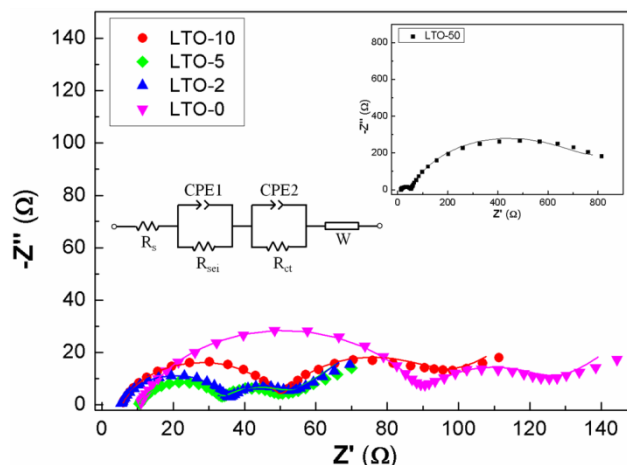
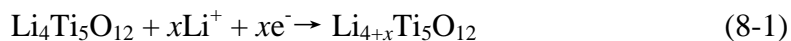


Figure 8.8 Nyquist plots of LTO-0, LTO-2, LTO-5, LTO-10 and LTO 50 (solid symbols and solid lines represent experimental and simulated data respectively, and the equivalent circuit is shown in the inset).

Table 8-2 Values of R_{sei} and R_{ct} obtained by simulated data in [Figure 8.8](#).

Sample \ Resistance	R_{sei} (Ω)	R_{ct} (Ω)
LTO-0	79.43	32.35
LTO-2	30.57	14.77
LTO-5	23.16	16.94
LTO-10	41.84	44.25
LTO-50	38.64	657.8

For the interpretation of the impedance response measured with LTO electrodes, no general consensus has yet been reached, and the results and explanations vary in literatures. For example, Ahn and Xiao [29] claimed that Al_2O_3 coating on LTO electrode could act a barrier restraining the SEI formation, thereby improving the cycling stability and coulombic efficiency of LTO electrode. In another study, carbon coating was found being able to improve the LIB performance of LTO electrode, by promoting formation of thick and successive SEI film on its surface [28]. In the following part, we will try to explain the effect of ZrO_2 coating on the LIB performance of LTO electrode based on the EIS results and electrochemical reaction:



The Li-ion insertion into $Li_4Ti_5O_{12}$ consists of three processes: (1) the solvated Li ions diffuse from electrolyte solution to the surface of $Li_4Ti_5O_{12}$; (2) a charge-transfer reaction occurs at the interface between $Li_4Ti_5O_{12}$ and the electrolyte, accompanied by accepting electrons coming from current collector and Li ions from the electrolyte; (3) Li ions diffuse into the bulk $Li_4Ti_5O_{12}$ [9]. Obviously, ZrO_2 coating could mainly affects the charge transfer reaction happened at the interface between $Li_4Ti_5O_{12}$ and the electrolyte, and the working mechanism could be explained by the influence of ZrO_2 coating on the transport of electrons or/and Li ions. (1) On the Li-ion transport. On one hand, EIS result indicates that ZrO_2 coating could effectively accelerate the diffusion of Li ions through SEI film, by reducing the SEI resistance ([Table 8-2](#)). The reason is most likely due to the fact that ZrO_2 coating could prevent the direct contact between LTO and electrolyte, and cover the catalytic sites on the LTO surface for the decomposition of electrolyte, thereby restraining SEI formation and reducing SEI resistance. On the other hand, the artificial

ZrO₂ coating layer could also hinder the diffusion of Li ions, because it is not Li-ion conductive. Thus, ZrO₂ coating is a double-sided sword for Li-ion diffusion. The thickness of ZrO₂ coating becomes critically important: it has to be thick enough to reduce SEI resistance, while also has to be thin enough to avoid blocking Li-ion diffusion through it. Our study indicates that ZrO₂ coating with no more than 5 ALD cycles is the optimized parameter. (2) On the electron transport. Previous studies have shown that direct metal oxide coating on electrode could not only maintain the electron pathways between active materials and carbon additives [35], but also improve the adhesion of electrode materials to the current collector [38], thereby improving the electron transport among them. In our case, therefore, it can be considered that direct ZrO₂ coating on LTO electrode acts as the similar way to improve electron transport (as disclosed by the reduced R_s in Table 8-2) and contribute to the reduced charge-transfer resistance of LTO-2 and LTO-5 compared with that of LTO-0 (Table 8-2). It is worthy to mention that the increased charge-transfer resistance of LTO-10 and LTO-50 results from the blocked Li-ion diffusion due to thicker ZrO₂ coating with low electronic conductivity. In those cases, the improvement from electron transport becomes neglected.

In summary, ZrO₂ coating with less than 10 ALD cycles can enhance the specific capacity, cycling performance and rate capability of the LTO between 0.1-2.5 V. The reason could be attributed to the suppressed SEI formation and the improved electron transport by coating ultrathin ZrO₂ film directly on the LTO electrode. ZrO₂ coating with more than 10 ALD cycles would worsen the electrochemical performance of the LTO, probably due to the blocking effect of thick ZrO₂ coating on the lithium ion diffusion. Moreover, ZrO₂ coating can decrease the specific capacity of the LTO by adding extra weight to the electrode materials, without contributing any capacity to lithium ion storage. This situation becomes more and more non-negligible with increasing ALD cycles. As a result, LTO-50 has obvious higher weight of the electrode materials than the others due to the thick ZrO₂ coating. Therefore, the additional weight of ZrO₂ coating is another reason for the lowered specific capacity of LTO-50 than LTO-0 (Figure 8.7).

8.4 Conclusions

ZrO₂ coating was conducted directly on the Li₄Ti₅O₁₂ electrode by atomic layer

deposition with different cycles (0, 1, 2, 5, 10 and 50). The results indicated that ZrO_2 coating with less than 10 ALD cycles could enhance the specific capacity, cycling stability and rate capability of the $\text{Li}_4\text{Ti}_5\text{O}_{12}$ electrode in a voltage range of 0.1-2.5 V. The mechanism study by EIS revealed that the reason for the enhance LIB performance was mainly due to the suppressed SEI formation and the improved electron transport by ultrathin ZrO_2 coating. This work provides a novel and effective approach to improve the electrochemical performance of anode materials *via* surface-modification by atomic layer deposition. It is believed that this work will be inspirable for other researchers and beneficial for the development of lithium ion batteries used in PHEVs and EVs.

Acknowledgements

This research was supported by General Motors of Canada, Natural Sciences and Engineering Research Council of Canada (NSERC), Canada Research Chair (CRC) Program, Canada Foundation for Innovation (CFI), Ontario Research Fund (ORF), Ontario Early Researcher Award (ERA) and University of Western Ontario.

References

- [1] M. Armand, J. -M. Tarascon, Building better batteries, *Nature* **2008**, *451*, 652-657.
- [2] J. -M. Tarascon, Key challenges in future Li-battery research, *Phil. Trans. R. Soc. A* **2010**, *368*, 3227-3241.
- [3] N. A. Kaskhedikar, J. Maier, The effect of the charging protocol on the cycle life of a Li-ion battery, *Adv. Mater.* **2009**, *21*, 2664-2680.
- [4] E. Ferg, R. J. Gummow, A. de Kock, M. M. Thackeray, Spinel anodes for lithium-ion batteries, *J. Electrochem. Soc.* **1994**, *141*, L147-L150.
- [5] P. Liu, E. Sherman, M. Verbrugge, Electrochemical and structural characterization of lithium titanate electrodes, *J. Solid State Electrochem.* **2010**, *14*, 585-591.

- [6] C. Y. Ouyang, Z. Y. Zhong, M. S. Lei, Ab initio studies of structural and electronic properties of $\text{Li}_4\text{Ti}_5\text{O}_{12}$ spinel, *Electrochem. Commun.* **2007**, *9*, 1107-1112.
- [7] T. F. Yi, Y. Xie, Y. R. Zhu, R. S. Zhu, H. Shen, Structural and thermodynamic stability of $\text{Li}_4\text{Ti}_5\text{O}_{12}$ anode material for lithium-ion batteries, *J. Power Sources* **2013**, *222*, 448-454.
- [8] C. H. Chen, J. T. Vaughey, A. N. Jansen, D. W. Dees, A. J. Kahaian, T. Goacher, M. M. Thackeray, Studies of Mg-substituted $\text{Li}_{4-x}\text{Mg}_x\text{Ti}_5\text{O}_{12}$ spinel electrodes ($0 \leq x \leq 1$) for lithium batteries, *J. Electrochem. Soc.* **2001**, *148*, A102-A104.
- [9] G. N. Zhu, Y. G. Wang, Y. Y. Xia, Ti-based compounds as anode materials for Li-ion batteries, *Energy Environ. Sci.* **2012**, *5*, 6652-6667.
- [10] T. F. Yi, L. J. Jiang, J. Shu, C. B. Yue, R. S. Zhu, H. B. Qiao, Recent development and application of $\text{Li}_4\text{Ti}_5\text{O}_{12}$ as anode material of lithium ion battery, *J. Phys. Chem. Solids* **2010**, *71*, 1236-1242.
- [11] J. Li, Z. Tang, Z. Zhang, Controllable formation and electrochemical properties of one-dimensional nanostructured spinel $\text{Li}_4\text{Ti}_5\text{O}_{12}$, *Electrochem. Comm.* **2005**, *7*, 894-899.
- [12] C. Lai, Y. Y. Dou, X. Li, X. P. Gao, Improvement of the high rate capability of hierarchical structured $\text{Li}_4\text{Ti}_5\text{O}_{12}$ induced by the pseudocapacitive effect, *J. Power Sources* **2010**, *195*, 3676-3679.
- [13] E. M. Sorensen, S. J. Barry, H. K. Jung, J. M. Rondinelli, J. T. Vaughey, K. R. Poeppelmeier, Three-dimensionally ordered macroporous $\text{Li}_4\text{Ti}_5\text{O}_{12}$: Effect of wall structure on electrochemical properties, *Chem. Mater.* **2006**, *18*, 482-489.
- [14] J. Haetge, P. Hartmann, K. Brezesinski, J. Janek, T. Brezesinski, Ordered large-pore mesoporous $\text{Li}_4\text{Ti}_5\text{O}_{12}$ spinel thin film electrodes with nanocrystalline framework for high rate rechargeable lithium batteries: relationships among charge storage, electrical conductivity, and nanoscale structure, *Chem. Mater.* **2011**, *23*, 4384-4393.

- [15] L. Cheng, J. Yan, G. N. Zhu, J. Y. Luo, C. X. Wang, Y. Y. Xia, General synthesis of carbon-coated nanostructure $\text{Li}_4\text{Ti}_5\text{O}_{12}$ as a high rate electrode material for Li-ion intercalation, *J. Mater. Chem.* **2010**, *20*, 595-602.
- [16] L. Zhao, Y. S. Hu, H. Li, Z. Wang, L. Chen, Porous $\text{Li}_4\text{Ti}_5\text{O}_{12}$ coated with N-doped carbon from ionic liquids for Li-Ion batteries, *Adv. Mater.* **2011**, *23*, 1385-1388.
- [17] S. Huang, Z. Wen, X. Zhu, Z. Gu, Preparation and electrochemical performance of Ag doped $\text{Li}_4\text{Ti}_5\text{O}_{12}$, *Electrochem. Commun.* **2004**, *6*, 1093-1097.
- [18] L. Shen, C. Yuan, H. Luo, X. Zhang, K. Xu, F. Zhang, In situ growth of $\text{Li}_4\text{Ti}_5\text{O}_{12}$ on multi-walled carbon nanotubes: Novel coaxial nanocables for high rate lithium ion batteries, *J. Mater. Chem.* **2011**, *21*, 761-767.
- [19] H. G. Jung, M. W. Jang, J. Hassoun, Y. K. Sun, B. Scrosati, A high-rate long-life $\text{Li}_4\text{Ti}_5\text{O}_{12}/\text{Li}[\text{Ni}_{0.45}\text{Co}_{0.1}\text{Mn}_{1.45}]\text{O}_4$ lithium-ion battery, *Nature Commun.* **2011**, *2*, 516.
- [20] T. F. Yi, Y. Xie, J. Shu, Z. Wang, C. B. Yue, R. S. Zhu, H. B. Qiao, Structure and electrochemical performance of niobium-substituted spinel lithium titanium oxide synthesized by solid-state method, *J. Electrochem. Soc.* **2011**, *158*, A266-A274.
- [21] J. Shu, Study of the interface between $\text{Li}_4\text{Ti}_5\text{O}_{12}$ electrodes and standard electrolyte solutions in 0.0-5.0 V, *Electrochem. Solid-State Lett.* **2008**, *11*, A238-A240.
- [22] H. Ge, N. Li, D. Li, C. Dai, D. Wang, Electrochemical characteristics of spinel $\text{Li}_4\text{Ti}_5\text{O}_{12}$ discharge to 0.01 V, *Electrochem. Commun.* **2008**, *10*, 719-722.
- [23] X. L. Yao, S. Xie, H. Q. Nian, C. H. Chen, Spinel $\text{Li}_4\text{Ti}_5\text{O}_{12}$ as a reversible anode material down to 0 V, *J. Alloys Compds.* **2008**, *465*, 375-379.
- [24] T. F. Yi, J. Shu, Y. R. Zhu, X. D. Zhu, C. B. Yue, A. N. Zhou, R. S. Zhu, High-performance $\text{Li}_4\text{Ti}_{5-x}\text{V}_x\text{O}_{12}$ ($0 \leq x \leq 0.3$) as an anode materials for secondary lithium-ion batteries, *Electrochim. Acta* **2009**, *54*, 7464-7570.

- [25] T. F. Yi, Y. Xie, L. J. Jiang, J. Shu, C. B. Yue, A. N. Zhou, M. F. Ye, Advanced electrochemical properties of Mo-doped $\text{Li}_4\text{Ti}_5\text{O}_{12}$ anode material for power lithium ion battery, *RSC Adv.* **2012**, 2, 3541-3547.
- [26] T. F. Yi, J. Shu, Y. R. Zhu, X. D. Zhu, R. S. Zhu, A. N. Zhou, Advanced electrochemical performance of $\text{Li}_4\text{Ti}_{4.95}\text{V}_{0.05}\text{O}_{12}$ as a reversible anode material down to 0 V, *J. Power Sources* **2010**, 195, 285-288.
- [27] W. Lu, I. Belharouak, J. Liu, K. Amine, Electrochemical and thermal investigation of $\text{Li}_{4/3}\text{Ti}_{5/3}\text{O}_4$ spinel, *J. Electrochem. Soc.* **2007**, 154, A114-A118.
- [28] Y. B. Ye, F. Ning, B. Li, Q. S. Song, W. Lv, H. Du, D. Zhai, F. Su, Q. H. Yang, F. Kang, Carbon coating to suppress the reduction decomposition of electrolyte on the $\text{Li}_4\text{Ti}_5\text{O}_{12}$ electrode, *J. Power Sources* **2012**, 202, 253-261.
- [29] D. Ahn, X. Xiao, Extended lithium titanate cycling potential window with near zero capacity loss, *Electrochem. Commun.* **2011**, 13, 796-799.
- [30] X. Meng, X. Q. Yang, X. Sun, Emerging applications of atomic layer deposition for lithium-ion battery, *Adv. Mater.* **2012**, 24, 3589-3615.
- [31] H. C. M. Knoop, M. E. Donders, M. C. M. van de Sanden, P. H. L. Notten, W. M. M. Kessels, Atomic layer deposition for nanostructured Li-ion batteries, *J. Vac. Sci. Technol. A* **2012**, 30, 010801.
- [32] S. M. George, Atomic layer deposition, *Chem. Rev.* **2010**, 110, 111-131.
- [33] X. Xiao, P. Lu, D. Ahn, Ultrathin multifunctional oxide coatings for lithium ion batteries, *Adv. Mater.* **2011**, 23, 3911-3915.
- [34] Y. He, X. Yu, Y. Wang, H. Li, X. Huang, Alumina-coated patterned amorphous silicon as the anode for a lithium-ion battery with high coulombic efficiency, *Adv. Mater.* **2011**, 43, 4938-4941.

- [35] Y. S. Jung, A. S. Cavanagh, L. A. Riley, S. H. Kang, A. C. Dillon, M. D. Groner, S. M. George, S. H. Lee, Ultrathin direct atomic layer deposition on composite electrodes for highly durable and safe Li-ion batteries, *Adv. Mater.* **2010**, *22*, 2172-2176.
- [36] E. Kang, Y. S. Jung, A. S. Cavanagh, G. H. Kim, S. M. George, A. C. Dillon, J. K. Kim, J. Lee, Fe₃O₄ nanoparticles confined in mesocellular carbon foam for high performance anode materials for lithium-ion batteries, *Adv. Funct. Mater.* **2011**, *21*, 2430-2438..
- [37] L. A. Riley, A. S. Cavanagh, S. M. George, Y. S. Jung, Y. Yan, S. H. Lee, A. C. Dillon, Conformal surface coatings to enhance high volume expansion Li-ion anode materials, *ChemPhysChem* **2010**, *11*, 2124-2130.
- [38] L. A. Riley, A. S. Cavanagh, S. M. George, S. H. Lee, A. C. Dillon, Improved mechanical integrity of ALD-coated composite electrodes for Li-ion batteries, *Electrochem. Solid-State Lett.* **2011**, *14*, A29-A31.
- [39] I. R. M. Kottogoda, Y. Kadoma, H. Ikuta, Y. Uchimoto, M. Wakihara, Enhancement of rate capability in graphite anode by surface modification with zirconia, *Electrochem. Solid-State Lett.* **2002**, *5*, A275-A278.
- [40] J. Cho, Y. S. Kim, T. J. Kim, B. Park, Zero-strain intercalation cathode for rechargeable Li-ion cell, *Angew. Chem. Int. Ed.* **2001**, *40*, 3367-3369.
- [41] C. Li, H. P. Zhang, L. J. Fu, H. Liu, Y. P. Wu, E. Rahm, R. Holze, H. Q. Wu, Cathode materials modified by surface coating for lithium ion batteries, *Electrochem. Acta* **2006**, *51*, 3872-3883.
- [42] J. Liu, X. Li, J. Yang, D. Geng, Y. Li, D. Wang, R. Li, X. Sun, M. Cai and M. W. Verbrugge, Microwave-assisted hydrothermal synthesis of nanostructured spinel Li₄Ti₅O₁₂ as anode materials for lithium ion batteries, *Electrochim. Acta* **2012**, *6*, 100-104.
- [43] D. M. Hausmann, E. Kim, J. Becker, R. G. Gordon, Atomic layer deposition of hafnium and zirconium oxides using metal amide precursors, *Chem. Mater.* **2002**, *14*, 4350-4358.

[44] J. Liu, X. Meng, M. N. Banis, M. Cai, R. Li, X. Sun, Crystallinity-controlled synthesis of zirconium oxide thin films on nitrogen-doped carbon nanotubes by atomic layer deposition, *J. Phys. Chem. C* **2012**, *116*, 14656-14664.

[45] H. Ge, N. Li, D. Li, C. Dai, D. Wang, Study on the theoretical capacity of spinel lithium titanate induced by low-potential intercalation, *J. Phys. Chem. C* **2009**, *113*, 6324-6326.

Supporting Information

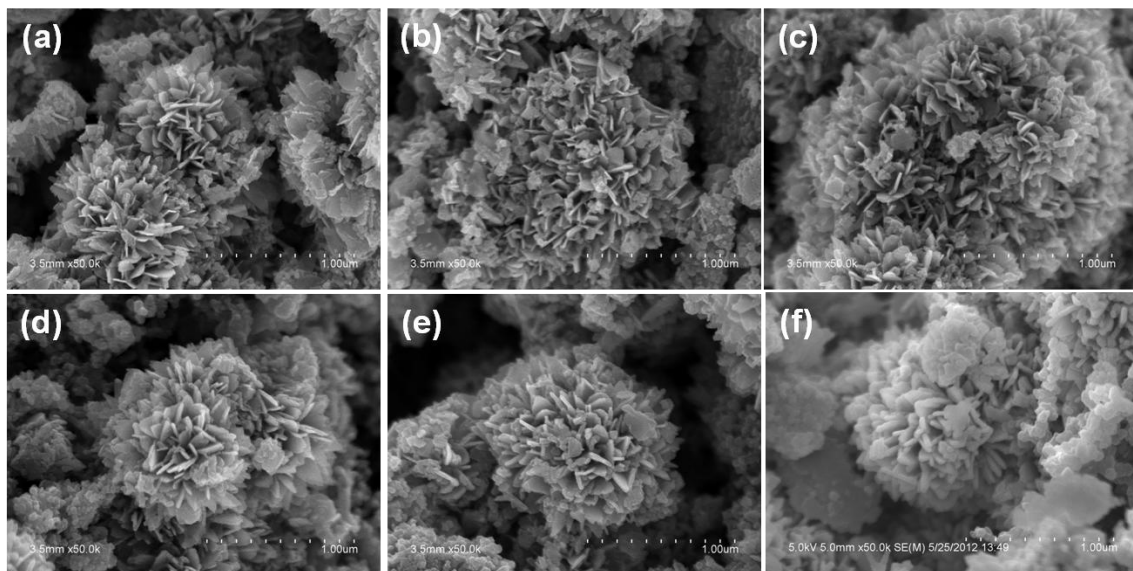


Figure SI-8.1 SEM images of LTO-0, LTO-1, LTO-2, LTO-5, LTO-10 and LTO-50 at low magnification.

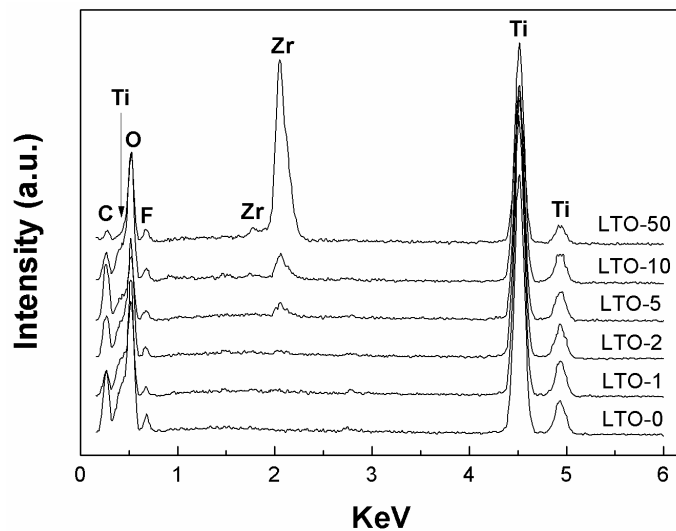


Figure SI-8.2 EDS spectra of LTO-0, LTO-1, LTO-2, LTO-5, LTO-10 and LTO-50.

Table SI-8-1 Potentials (V) of anodic peaks (ϕ_{pa}) and cathodic peaks (ϕ_{pc}) in the first five cycles

	1 st cycle		2 nd cycle		3 rd cycle		4 th cycle		5 th cycle	
	ϕ_{pa}	ϕ_{pc}	ϕ_{pa}	ϕ_{pc}	ϕ_{pa}	ϕ_{pc}	ϕ_{pa}	ϕ_{pc}	ϕ_{pa}	ϕ_{pc}
LTO-0	1.800	1.402	1.676	1.433	1.689	1.476	1.711	1.461	1.735	1.420
LTO-1	1.714	1.417	1.706	1.459	1.706	1.453	1.721	1.453	1.724	1.443
LTO-2	1.672	1.476	1.656	1.489	1.669	1.504	1.653	1.501	1.672	1.501
LTO-5	1.665	1.468	1.669	1.393	1.672	1.496	1.672	1.497	1.672	1.494
LTO-10	1.673	1.472	1.672	1.488	1.675	1.500	1.675	1.491	1.675	1.497
LTO-50	1.730	1.441	1.717	1.449	1.717	1.453	1.720	1.449	1.767	1.446

Chapter 9 Atomic Layer Deposited Aluminum Phosphate Thin Films on Nitrogen-Doped Carbon Nanotubes ^{‡‡}

Besides ZrO₂ developed in chapter 6 and 7 and applied in chapter 8, aluminum phosphate (AlPO₄) is another excellent coating material widely used in LIBs for surface modification. However, the deposition of AlPO₄ has been seldom reported.

Herein, Amorphous aluminum phosphate (Al_xP_yO_z) thin films were deposited on nitrogen-doped carbon nanotubes (NCNTs) by atomic layer deposition (ALD) at 150°C by combining subcycles of trimethylaluminum (TMA) – H₂O and trimethylphosphite (TMP) – O₃. TEM and HRTEM observation indicated uniform and conformal deposition of Al_xP_yO_z thin films on NCNTs. EDS analysis showed that the P/Al atomic ratio in Al_xP_yO_z thin films was controllable by varying the subcycle ratio between TMA – H₂O and TMP – O₃. The composition was determined to be Al_{1.3}PO_{5.1} by XPS for aluminum phosphate prepared using sequence of 1 × (TMA – H₂O) – 20 × (TMP – O₃). The thickness of Al_{1.3}PO_{5.1} thin film was linearly dependent on ALD cycles, with growth per cycle of 1.9 Å/cycle. XPS and XANES studies disclosed the existence of P-O-Al structure in Al_{1.3}PO_{5.1}, similar as that in standard AlPO₄. In addition, thermal stability testing showed that the oxidation resistance of NCNTs could be greatly improved by coating with 50-cycle Al_{1.3}PO_{5.1} (16 nm in thickness).

Keywords: Atomic layer deposition; aluminum phosphate; carbon nanotubes; low temperature deposition.

^{‡‡} Part of this chapter has been published in *RSC Adv.* **2013**, *3*, 4492-4495.

9.1 Introduction

Aluminium phosphate (AlPO_4) has long been known as a catalyst support for numerous catalytic applications [1, 2]. AlPO_4 itself has been used to catalyze the dehydration of methanol to dimethyl ether, which is a clean alternative fuel for diesel engines and a potential aerosol propellant in the cosmetics industry [3]. AlPO_4 coating on cathodes has been considered as an effective strategy to improve both the safety and cycle-performance of lithium secondary batteries [4]. In addition, AlPO_4 protective layer has been shown to inhibit the oxidation of carbonaceous materials [5].

AlPO_4 has been generally synthesized through a co-precipitation process followed by heat treatment previously [1-5]. Unfortunately, this route is incapable of achieving uniform aluminium phosphate thin film and lacks flexibility to tune its chemical composition (P/Al ratio). Uniformity and tunable composition have been proven to play a critical role in determining practical applications of AlPO_4 [3-6]. Recently, atomic layer deposition (ALD) has been emerging as a powerful technique for thin film deposition [7, 8]. Unlike other physical or chemical vapour deposition processes, ALD employs alternative precursor doses and self-limiting surface reactions, which result in material growth of one monolayer (or less) per cycle. Thus, ALD offers exquisite control over the thickness and composition of thin films. However, there have been very few studies on the preparation of aluminium phosphate by ALD [9-11]. Aluminium phosphate was found to form in P-doped aluminium oxide with P doping greater than 10 wt% at 450 and 500 °C using AlCl_3 or aluminium n-propoxide, 2-methyl-2-propanol and P_2O_5 as precursors [10]. However, the high deposition temperature seriously hinders its applications, especially for sensitive substrates. In another study, aluminium phosphate was obtained from AlCl_3 and trimethylphosphate at deposition temperatures between 150 and 400 °C [11]. This route simplifies ALD process by sacrificing the controllability on the chemical composition of aluminium phosphates. Moreover, the use of metal chlorides is undesirable in ALD process, because it may lead to corrosion of ALD system caused by HCl generated during reaction and leave Cl impurity in the deposited films [11, 12].

Herein, we report a new ALD approach to fabricate amorphous aluminium phosphate ($\text{Al}_x\text{P}_y\text{O}_z$) thin films. It is featured with low-temperature deposition, controllable film

thickness, variable film composition, and free of metal chlorides. $\text{Al}_x\text{P}_y\text{O}_z$ thin films are deposited by combining subcycles of Al_2O_3 and PO_x , and one ALD cycle consists of 1 Al_2O_3 subcycle and n PO_x subcycles ($5 \leq n \leq 20$), as schematically shown in Figure 9.1. The popular trimethylaluminum (TMA)- H_2O is adopted for the Al_2O_3 subcycle, and trimethylphosphite (TMP)- O_3 is used for the PO_x subcycle. The composition (P/Al ratio) of $\text{Al}_x\text{P}_y\text{O}_z$ thin films is controlled by varying PO_x subcycles while keeping Al_2O_3 subcycle unchanged.

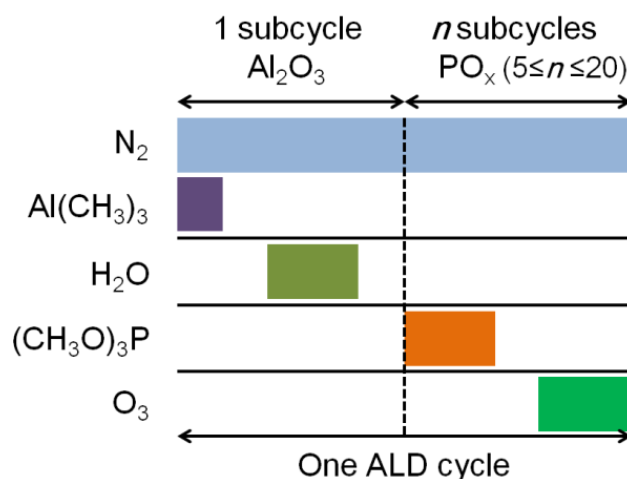


Figure 9.1 Illustration of ALD process for aluminum phosphate.

9.2 Experimental Section

9.2.1 Material synthesis

Nitrogen-doped carbon nanotubes (NCNTs) directly grown on carbon papers were used as the substrates for the deposition of aluminum phosphates, because of their high quality and clean surface. The as-prepared NCNTs were loaded into the reaction chamber of ALD system (Savannah 100, Cambridge Nanotech Inc., USA). The deposition of aluminum phosphates were achieved by alternatively supplying TMA – H_2O and TMP – O_3 . All precursors were kept at room temperature. The pulse time for TMA, H_2O , TMP and O_3 was 0.5 s, 1 s, 1s and 1s respectively, and the purge time was 15 s after each pulsing. 150 °C was chosen as deposition temperature. The ratio between Al_2O_3 subcycle and PO_x subcycle varied from 1:5, to 1:10 and 1:20, and 50 ALD cycles were applied in each sample.

9.2.1 Material characterization

The morphology and structure of the deposited thin films were characterized by a field-emission scanning electron microscope (SEM, Hitachi S4800) equipped with energy dispersive X-ray spectroscopy (EDS) and high-resolution transmission electron microscope (HRTEM, JEOL 2010 FEG). The phase was analyzed using micro X-ray diffraction (XRD, Bruker D8, Co - $K\alpha$ source, $\lambda = 1.7892 \text{ \AA}$). Compositions and element analysis was carried out in Kratos Axis Ultra Al (alpha) X-ray photoelectron spectrometer (XPS) operated at 14 kV. The X-ray absorption near-edge structure (XANES) spectroscopy experiment was conducted on the Variable Line Spacing Plane Grating Monochromator (VLS PGM) beamline at the Canadian Light Source (CLS) located at the University of Saskatchewan in Saskatoon.

9.3 Results and Discussion

The initial NCNTs have diameters of about 60 nm (Figure 9.2a) and exhibit typical bamboo-like structure (see Figure SI-9.1). Figure 9.2b shows a SEM image of a 100-cycle $\text{Al}_x\text{P}_y\text{O}_z$ thin film deposited on NCNTs using the sequence of $1 \times (\text{TMA} - \text{H}_2\text{O}) - 20 \times (\text{TMP} - \text{O}_3)$. It is apparent from Figure 9.2 (b) and (c) that the coating of the thin film is uniform and conformal on NCNTs, and the diameter of the nanotubes increases to ~ 100 nm. Selected area diffraction pattern (SAD) in Figure 9.2c indicates that the 100-cycle $\text{Al}_x\text{P}_y\text{O}_z$ thin film is amorphous, which is confirmed by XRD pattern (Figure SI-9.2) and HRTEM image in Figure 9.2d. From Figure 9.2d, the thickness of $\text{Al}_x\text{P}_y\text{O}_z$ thin film is measured to be 16.4 nm. Figure 9.2e presents EDS elemental line-scanning result of the 100-cycle $\text{Al}_x\text{P}_y\text{O}_z$ thin film from scanning transmission electron microscopy (STEM). Figure 9.2e clearly indicates the homogeneous distribution of Al, P and O elements along carbon nanotube. XPS analysis shows that the composition of Al, P and O elements is 15.4, 11.5 and 57.8 at.% respectively, as shown in Figure 9.2f (deconvolution of Al 2p, P 2p and O 1s peaks is provided in Figure SI-9.3). Thereby, the chemical formula is determined to be $\text{Al}_{1.3}\text{PO}_{5.0}$ for the aluminium phosphate thin film deposited using ALD sequence of $1 \times (\text{TMA} - \text{H}_2\text{O}) - 20 \times (\text{TMP} - \text{O}_3)$.

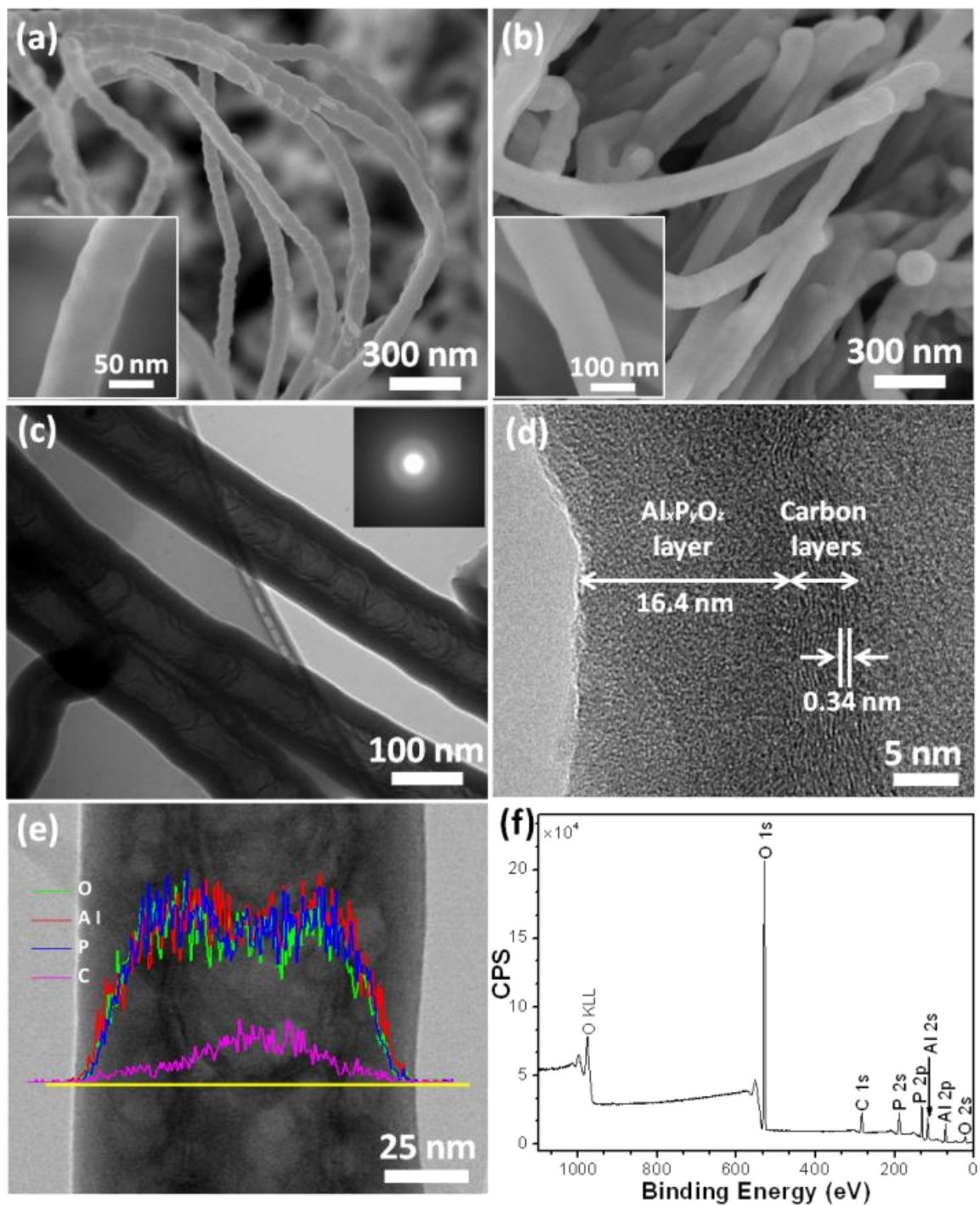


Figure 9.2 (a) SEM image of NCNTs; (b) SEM image, (c) TEM image, (d) HRTEM image, (e) STEM-EDS line-scanning and (f) XPS spectrum of NCNTs coated with 100-cycle $\text{Al}_x\text{P}_y\text{O}_z$ thin film deposited using sequence of $1 \times (\text{TMA} - \text{H}_2\text{O}) - 20 \times (\text{TMP} - \text{O}_3)$.

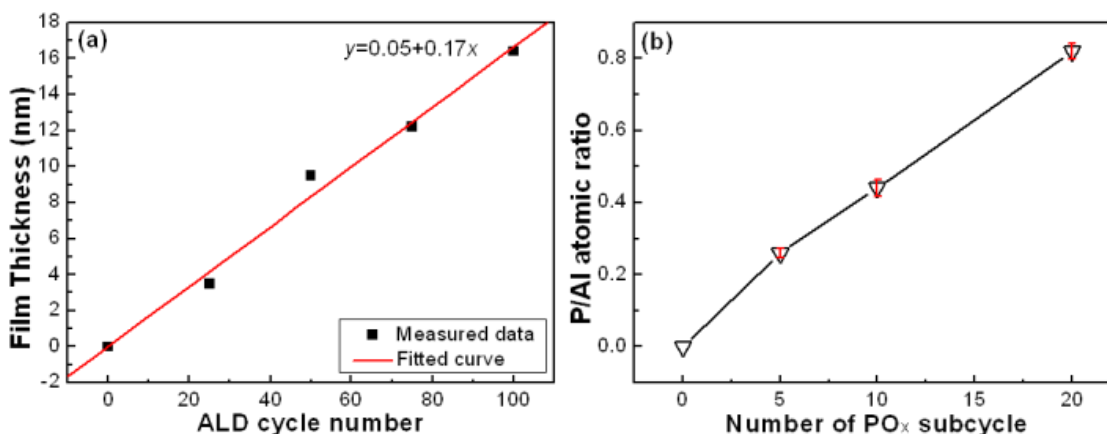


Figure 9.3 (a) Film thickness of $\text{Al}_{1.3}\text{PO}_{5.0}$ as a function of ALD cycle number and (b) P/Al atomic ratio in $\text{Al}_x\text{P}_y\text{O}_z$ thin films deposited using $1 \times (\text{TMA} - \text{H}_2\text{O}) - n \times (\text{TMP} - \text{O}_3)$ ($n = 5, 10$ and 20).

$\text{Al}_{1.3}\text{PO}_{5.0}$ thin films produced with 25, 50 and 75 ALD cycles are also examined, and their uniformity on NCNTs is observed in TEM and HRTEM images (Figure SI-9.4). The thickness of the thin film is measured to be 3.5, 9.5 and 12.2 nm for $\text{Al}_{1.3}\text{PO}_{5.0}$ deposited with 25, 50 and 75 ALD cycles respectively. Then film thickness is plotted as a function of ALD cycles in Figure 9.3a. The film thickness has a linear relationship with ALD cycle number, indicating the self-limiting nature of this ALD process. Growth per cycle for the $\text{Al}_{1.3}\text{PO}_{5.0}$ thin film at 150 °C is determined to be 1.7 Å/cycle by fitting the data in Figure 9.3a linearly. Thus, an aluminium phosphate thin film with desirable thickness can be easily obtained by choosing appropriate ALD cycle number. The growth rate of $\text{Al}_{1.3}\text{PO}_{5.0}$ is slightly higher than that of aluminium phosphate deposited by ALD from AlCl_3 and trimethylphosphate (1.4 Å/cycle) at the same deposition temperature [11].

To demonstrate the flexibility to modify the composition of $\text{Al}_x\text{P}_y\text{O}_z$ through this ALD approach, we use the subcycle number of PO_x varying from 20 to 10 and 5, while the Al_2O_3 subcycle is kept unchanged. The average P/Al atomic ratio of each sample is obtained from 10 EDS results (Figure SI-9.5), and is plotted as a function of PO_x subcycle number in Figure 9.3b. One can see that the P/Al atomic ratio decreases from ~ 0.8 to 0.4 to 0.3, when PO_x subcycle is reduced from 20 to 10 to 5 respectively. It is worth noting that the P/Al ratio in $\text{Al}_x\text{P}_y\text{O}_z$ thin films could be adjusted to be either higher

or lower by changing the subcycle number of PO_x in this ALD receipt. It also should be mentioned that the growth rate of $\text{Al}_x\text{P}_y\text{O}_z$ thin films would be reduced with lowering P/Al atomic ratio or PO_x subcycle number (Figure SI-9.6), due to less contribution of PO_x subcycle to the thin film.

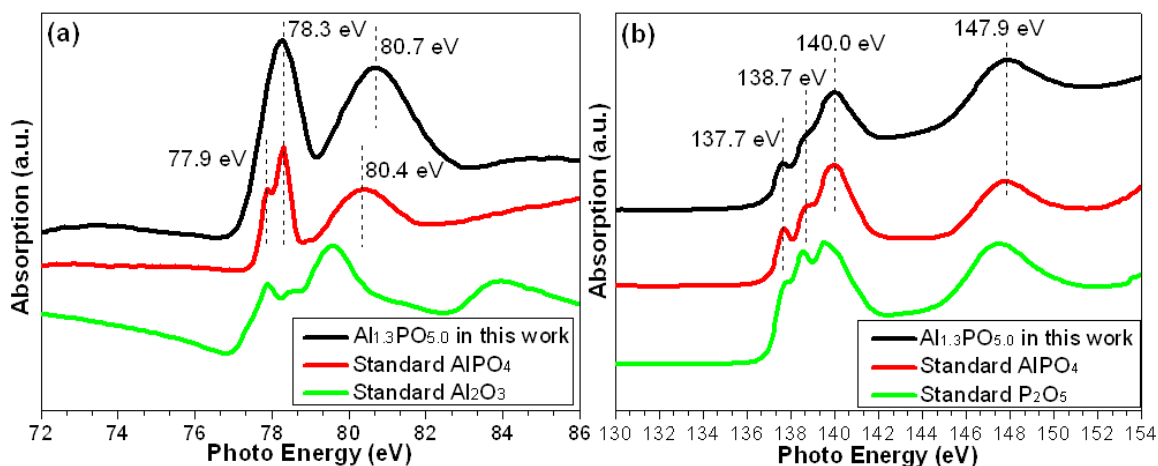


Figure 9.4 XANES Al L_{3,2}-edge (a) and P L_{3,2}-edge (b) spectra of Al_{1.3}PO_{5.0} in this work, and standard AlPO₄, Al₂O₃ and P₂O₅.

The structure of the amorphous Al_{1.3}PO_{5.0} thin film is analyzed by XANES spectroscopy. Figure 9.4 displays XANES at the Al L_{3,2}-edge and P L_{3,2}-edge for Al_{1.3}PO_{5.0}, in comparison with standard crystalline AlPO₄, Al₂O₃ and P₂O₅. Figure 9.4a indicates that Al_{1.3}PO_{5.0} has very similar Al L_{3,2}-edge spectrum to standard AlPO₄, except that the first transition of Al_{1.3}PO_{5.0} exhibits only one broad peak at 78.3 eV, instead of two well resolved peaks at 77.9 and 78.3 eV for standard AlPO₄. This observation is attributable to the amorphous state of Al_{1.3}PO_{5.0} [15]. The first transitions in Al_{1.3}PO_{5.0} could be assigned to transitions from the Al spin-orbit split 2p orbitals to the unoccupied densities of states of 3s character (L₃ and L₂ edges), and the second one corresponds to transitions from the Al 2p to the upper bands and is sometimes referred to as a multiple scattering resonance of which the energy position relative to the threshold is related to the inter-atomic distance (r) between Al and its nearest neighbouring atom O with a $\sim 1/r^2$ correlation [16]. A small shift in this resonance to higher energy indicates that the Al-O inter-atomic distance is shorter in Al_{1.3}PO_{5.0} compared to AlPO₄ albeit very slightly. It should be noted that the Al L_{3,2}-edge spectrum of Al_{1.3}PO_{5.0} distinctly differs from that of

Al_2O_3 , owing to different local bonding environment of the Al sites, *i.e.* P-O-Al in $\text{Al}_{1.3}\text{PO}_{5.0}$ and Al-O-Al in Al_2O_3 [15]. In Figure 9.4b, $\text{Al}_{1.3}\text{PO}_{5.0}$ and standard AlPO_4 exhibit the same four peaks centred at 137.7, 138.7, 140.0 and 147.9 eV in the P $L_{3,2}$ -edge XANES spectrum, suggesting the same coordination of P (P-O-Al) in both samples and that the local structure of the PO_4 moiety remains intact. The result is in agreement with P $L_{3,2}$ -edge XANES spectrum reported for AlPO_4 in literature [17]. The P $L_{3,2}$ -edge XANES spectrum of $\text{Al}_{1.3}\text{PO}_{5.0}$ is apparently different from P_2O_5 (P-O-P). XANES result provides strong evidence of P-O-Al bonds existing in amorphous $\text{Al}_{1.3}\text{PO}_{5.0}$ thin film prepared by ALD.

9.4 Conclusions

In conclusion, we report a new low-temperature ALD process to synthesize aluminium phosphate thin films on NCNTs in a well-controlled manner. The film thickness of aluminium phosphates is tunable at nanoscale lever by simply varying the ALD cycle number, and the film composition (P/Al ratio) is tailored by changing the subcycle ratio between Al_2O_3 and PO_x during the ALD process. The strategy reported in this work is applicable to the development of other metal phosphates (FePO_4 , TiPO_4) and phosphate-containing compounds (NASICON-type all-solid-state electrolyte, $\text{LiM}_2(\text{PO}_4)_3$ (M = Ti, Zr, Ge and Hf)), which will be key components in the next-generation of microbatteries.

Acknowledgements

The authors acknowledge the support of Natural Sciences and Engineering Research Council of Canada (NSERC), Canada Research Chair (CRC) Program, Foundation for Innovation (CFI), Ontario Research Fund (ORF), Canadian Light Source (CLS) at University of Saskatchewan, and University of Western Ontario.

References

- [1] T. T. P. Cheung, K. W. Willcox, M. P. Mcdaniel, M. M. Johnson, The structure of coprecipitated aluminophosphate catalyst supports, *J. Catal.* **1986**, *102*, 10-20.

- [2] M. A. Aramendia, V. Borau, C. Jim énez, J. M. Marinas, J. A. Pajares, Preparation of Pd/AlPO₄, Pd/AlPO₄-SiO₂, Pd/AlPO₄- γ -Al₂O₃ and study of their catalytic activity for the reduction of nitrobenzene by hydrogen transfer, *J. Catal.* **1982**, 78, 188-196.
- [3] F. Yaripour, M. Mollavali, Sh.M. Jam, H. Atashi, Catalytic dehydration of methanol to dimethyl ether catalyzed by aluminum phosphate catalysts, *Energy Fuels* **2009**, 23, 1896-1900.
- [4] J. Cho, Y. W. Kim, B. Kim, J. G. Lee, B. Park, A breakthrough in the safety of lithium secondary batteries by coating the cathode material with AlPO₄ nanoparticles, *Angew. Chem. Int. Ed.* **2003**, 42, 1618-1621.
- [5] C. R. Maier, L. E. Jones, The influence of aluminum phosphates on graphite oxidation, *Carbon* **2005**, 43, 2272-2276.
- [6] V. S. Kumar, A. H. Padmasri, C. V. V. Satyanarayana, I. A. K. Reddy, B. D. Raju, K. S. R. Rao, Nature and mode of addition of phosphate precursor in the synthesis of aluminum phosphate and its influence on methanol dehydration to dimethyl ether, *Catal. Commun.* **2006**, 7, 745-751.
- [7] S. M. George, Atomic layer deposition: an overview, *Chem. Rev.* **2010**, 110, 111-131.
- [8] R. L. Puurunen, Surface chemistry of atomic layer deposition: a case study for the trimethylaluminum/water process, *J. Appl. Phys.* **2005**, 97, 121301-121352.
- [9] M. Nieminen, L. Niinistö, R. Lappalainen, Determination of P/Al ratio in phosphorus-doped aluminum oxide thin films by XRF, RBS and FTIR, *Mikrochim. Acta* **1995**, 119, 13-22.
- [10] M. Tiita, E. Nykänen, P. Soininen, L. Niinistö, M. Leskelä, R. Lappalainen, Preparation and characterization of phosphorus-doped aluminum oxide thin films, *Mater. Res. Bull.* **1998**, 33, 1315-1323.

- [11] J. Hänninen, J. Holopainen, F. Munnik, M. Heikkilä, M. Ritala, M. Leskelä, Atomic layer deposition of aluminum and titanium phosphates, *J. Phys. Chem. C* **2012**, *116*, 5920-5925.
- [12] W. H. Nam, S. W. Rhee, Atomic layer deposition of ZrO₂ thin films using dichlorobis[bis-(trimethylsilyl)amido] zirconium and water, *Chem. Vap. Deposition* **2004**, *10*, 201-205.
- [13] X. Meng, Y. Zhong, Y. Sun, M.N. Banis, R. Li, X. Sun, Nitrogen-doped carbon nanotubes coated by atomic layer deposited SnO₂ with controlled morphology and phase, *Carbon* **2011**, *49*, 1133-1144.
- [14] J. Liu, X. Meng, M. N. Banis, M. Cai, R. Li, X. Sun, Crystallinity-controlled synthesis of zirconium oxide thin films on nitrogen-doped carbon nanotubes by atomic layer deposition, *J. Phys. Chem. C* **2012**, *116*, 14656-14664.
- [15] Y. F. Hu, R. K. Xu, J. J. Dynes, R. I. R. Blyth, G. Yu, L. M. Kozak, P. M. Huang, Coordination nature of aluminum (oxy) hydroxides formed under the influence of tannic acid studied by X-ray absorption spectroscopy, *Geochim. Cosmochim. Acta* **2008**, *72*, 1959-1969.
- [16] M. Kasrai, M. E. Fleet, T. K. Sham, G. M. Bancroft, K. H. Tan, J. R. Brown, A XANES study of the S L-edge in sulfide minerals: application to interatomic distance determination, *Solid State Commun.* **1988**, *68*, 507-511.
- [17] J. Kruse, P. Leinweber, K. U. Eckhardt, F. Godlinski, Y. Hu, L. Zuin, Phosphorus L_{2,3}-edge XANES: overview of reference compounds, *J. Synchrotron Rad.* **2009**, *16*, 247-259.

Supporting Information

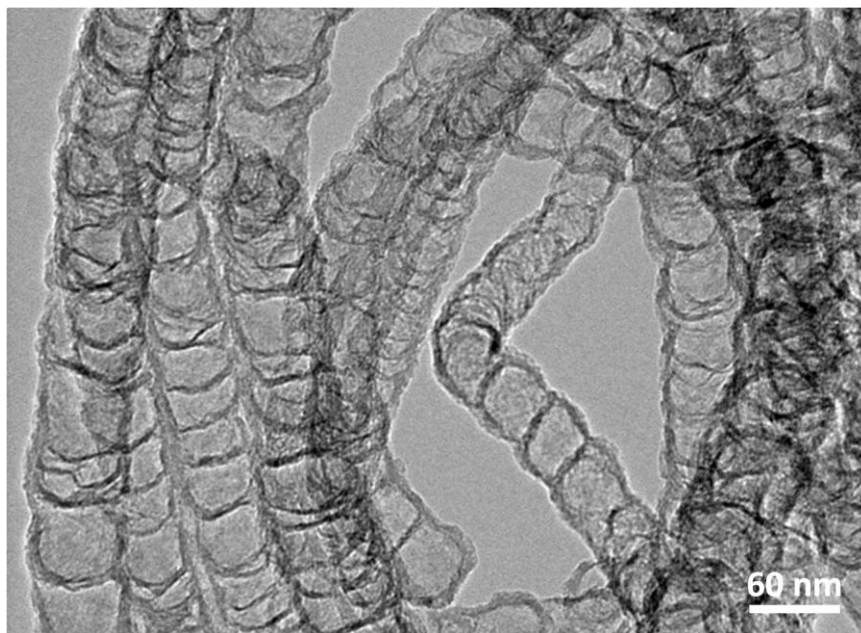


Figure SI-9.1 TEM image of NCNTs.

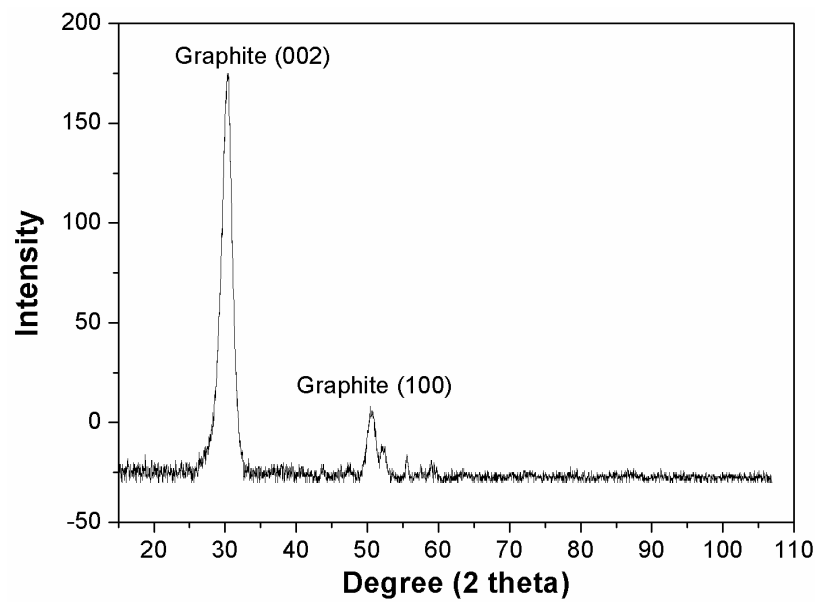


Figure SI-9.2 XRD pattern of NCNTs coated with 100-ALD cycle aluminum phosphate using sequence of $1 \times (\text{TMA} - \text{H}_2\text{O}) - 20 \times (\text{TMP} - \text{O}_3)$.

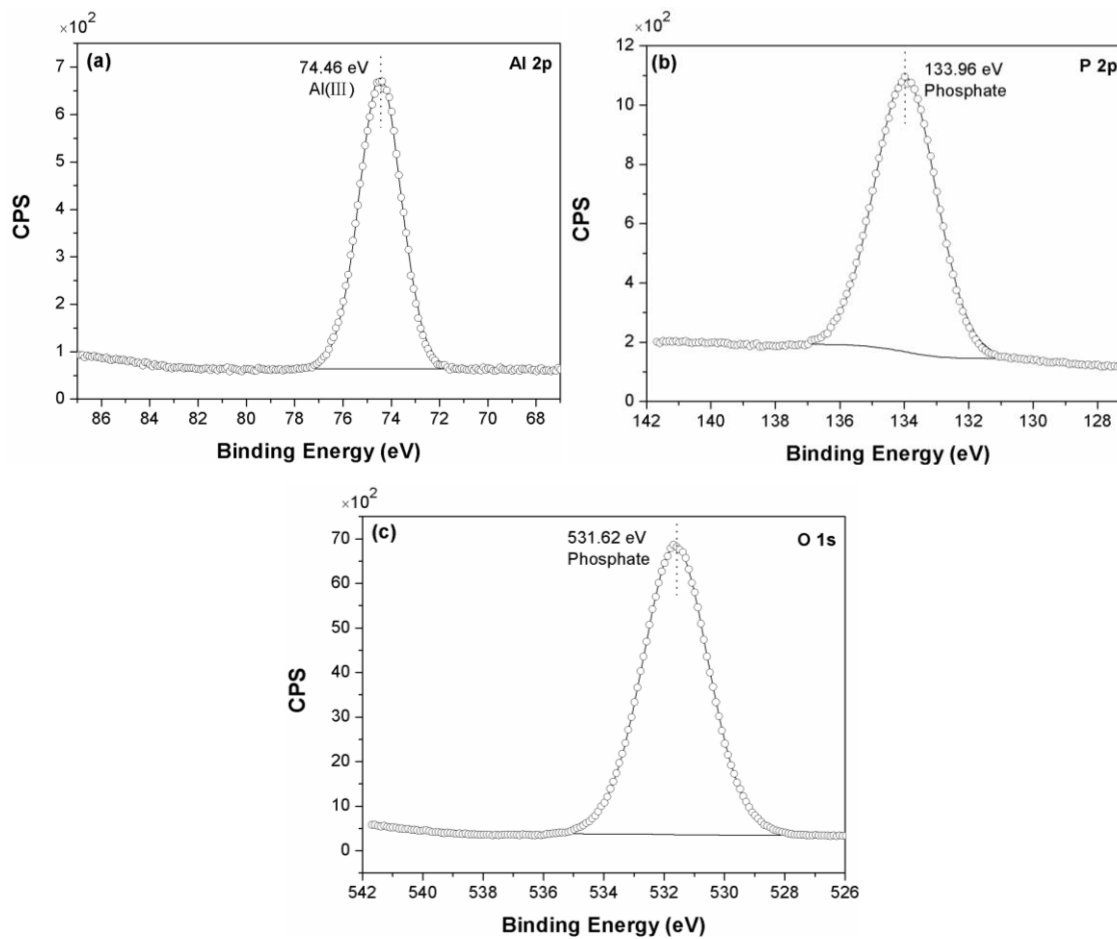


Figure SI-9.3 Deconvolution of Al 2p, P 2p and O 1s peaks together with theoretical fits and background.

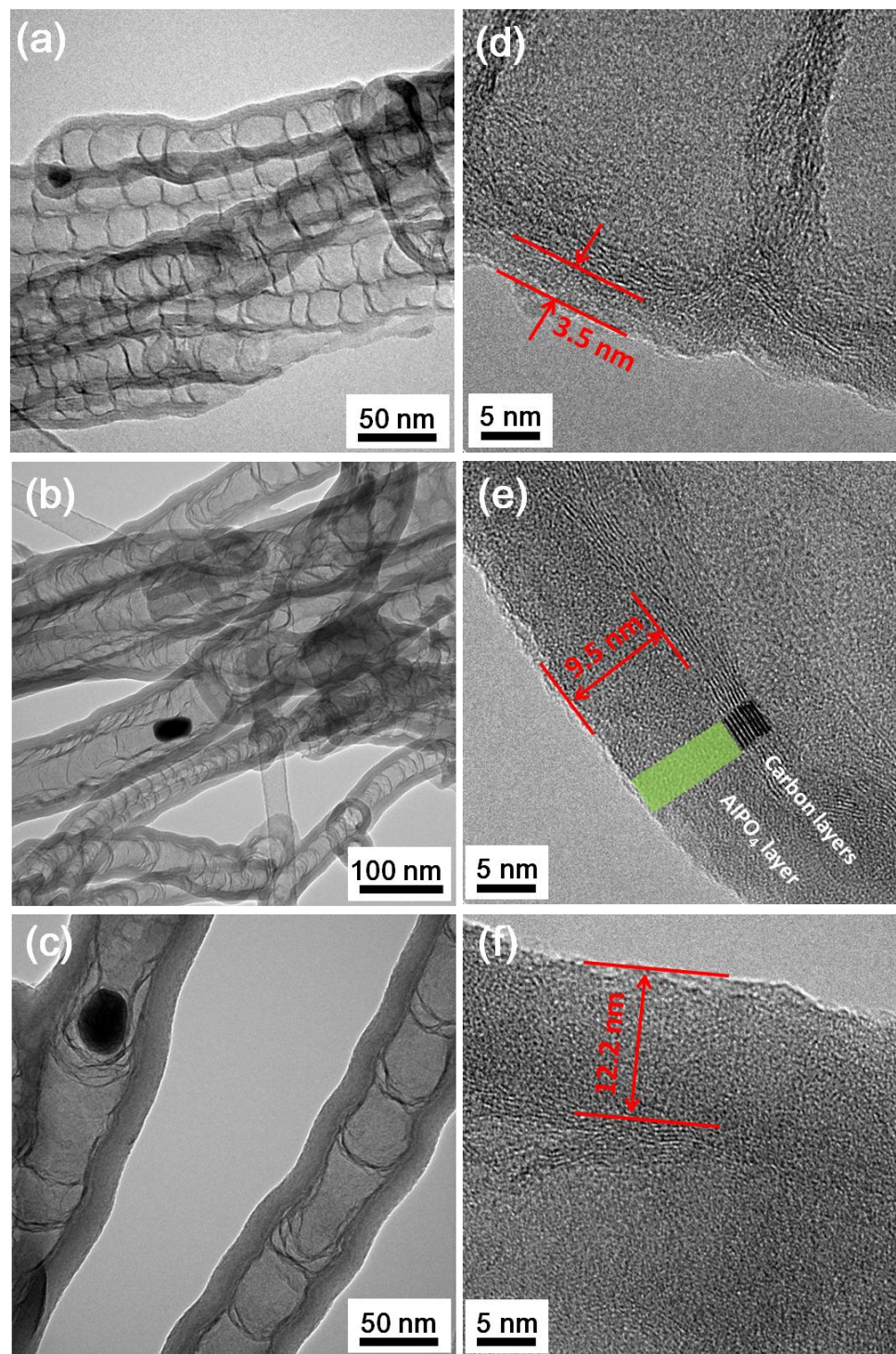


Figure SI-9.4 TEM (a-c) and HRTEM (d-f) images of NCNTs coated with thin films using sequence of $1 \times (\text{TMA} - \text{H}_2\text{O}) - 20 \times (\text{TMP} - \text{O}_3)$ for 25 (a, d), 50 (b, e), and 75 (c, f) ALD cycles.

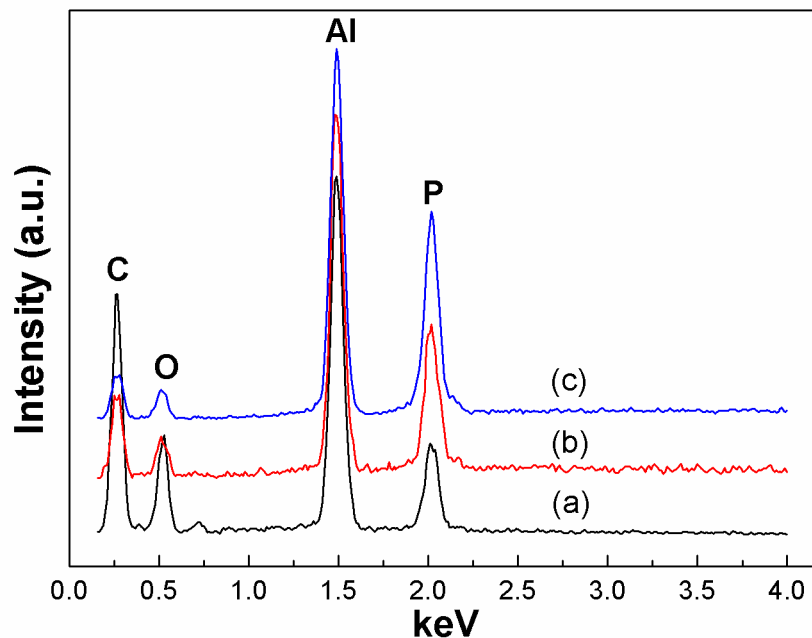


Figure SI-9.5 EDS results of NCNTs coated with 50-ALD cycle aluminum phosphates using sequences of (a) $1 \times (\text{TMA} - \text{H}_2\text{O}) - 5 \times (\text{TMP} - \text{O}_3)$; (b) $1 \times (\text{TMA} - \text{H}_2\text{O}) - 10 \times (\text{TMP} - \text{O}_3)$ and (c) $1 \times (\text{TMA} - \text{H}_2\text{O}) - 20 \times (\text{TMP} - \text{O}_3)$.

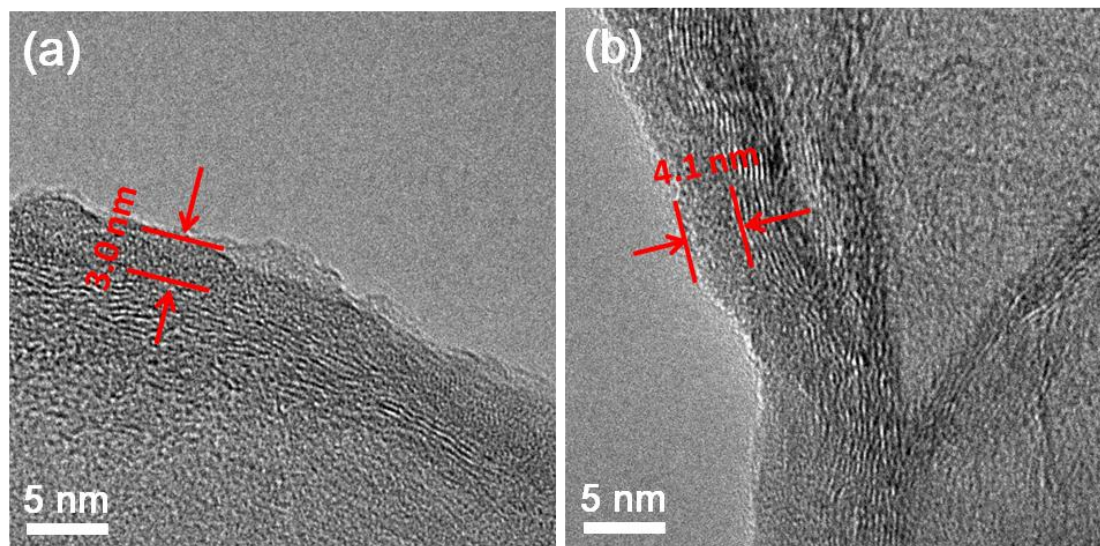


Figure SI-9.6 HRTEM images of NCNTs coated with 50-cycle $\text{Al}_x\text{P}_y\text{O}_z$ thin films using sequence of (a) $1 \times (\text{TMA} - \text{H}_2\text{O}) - 5 \times (\text{TMP} - \text{O}_3)$ and (b) $1 \times (\text{TMA} - \text{H}_2\text{O}) - 10 \times (\text{TMP} - \text{O}_3)$.

Chapter 10 Atomic Layer Deposition of Lithium Tantalate Solid-State Electrolytes

For surface-modification in LIBs, the desirable coating materials should have both good electronic and ionic conductivities, in order to insure efficient diffusion of electron and lithium ions in the electrodes. From this point, ALD-ZrO₂ and ALD-AlPO₄, as presented in chapters 6-9, are still not ideal for surface-modification, since both of them are poor electronic and ionic conductors. Recent studies showed the possibility of using solid-state electrolytes, which has good ionic conductivity, as coating materials in LIBs. Therefore, it is urgent to develop solid-state electrolyte by ALD.

In this chapter, lithium tantalate solid-state electrolyte thin films were grown by atomic layer deposition (ALD) at 225 °C using subcycle combination of $1 \times \text{Li}_2\text{O} + n \times \text{Ta}_2\text{O}_5$ ($1 \leq n \leq 10$). The Li/Ta ratio in the lithium tantalate thin films was controlled by varying Ta₂O₅ subcycles (n) while keeping Li₂O subcycle constant at 1. X-ray photoelectron spectroscopy analysis revealed that the composition of the lithium tantalate thin films was Li_{12.3}TaO_z, Li_{5.1}TaO_z and Li_{0.6}TaO_z, when Ta₂O₅ subcycles (n) equaled 1, 6 and 10, respectively. All lithium tantalate thin films displayed a linear relationship between film thickness and ALD cycle number, indicating self-limiting nature of the ALD process. The growth rate per ($1 \times \text{Li}_2\text{O} + n \times \text{Ta}_2\text{O}_5$) cycle of Li_{12.3}TaO_z, Li_{5.1}TaO_z and Li_{0.6}TaO_z was determined to be 2.2, 5.2 and 7.3 Å/cycle, respectively. Furthermore, the lithium tantalate thin films grown by ALD showed excellent uniformity and conformity, when deposited in anodic aluminum oxide template with an aspect ratio of ~ 300. Impedance testing showed that the as-grown Li_{5.1}TaO_z thin film exhibited a lithium-ion conductivity of 2×10^{-8} S/cm at 299 K, with activation energy of ~ 0.55 eV.

Keywords: Atomic layer deposition; lithium tantalate; solid-state electrolyte; thin-film battery.

10.1 Introduction

Microelectronic devices are becoming increasingly incorporated into our daily activities. A great deal of effort has been devoted to developing autonomous devices, such as medical implants, self-powered integrated circuits and micro-electromechanical systems, which need be driven by an on-board power supply system [1, 2]. Lithium-ion batteries (LIBs) are a preferable energy supply distribution medium for these types of applications, due to their ability to deliver high energy density [2]. In particular, all-solid-state LIBs have drawn great attention from various industries, since they can permit greater flexibility in the design of batteries, provide improved intrinsic safety due to the absence of liquid electrolytes, and facilitate miniaturization of microelectronic devices [1-3]. During the past decade or so, researches in the field of all-solid-state LIBs have been primarily focused on two-dimensional (2D) thin film batteries [4, 5]. However, it is becoming difficult for 2D thin film batteries to meet the elevated power consumption demand in modern microelectronic devices, due to their limited energy density per unit area [2]. One effective strategy to increase the capacity per unit area ($\mu\text{A h cm}^{-2}$) of all-solid-state LIBs is developing three-dimensional (3D) microbatteries instead of 2D thin film batteries. 3D microbatteries can offer significantly increased specific surface area of active materials in the same areal footprint as 2D thin film batteries, and maintain short path lengths for the diffusion of lithium ion, thereby rendering greatly enhanced battery capacity per unit area [2, 3]. Given the advantages and demand of 3D microbatteries, various concepts for their design have been proposed [1-3, 6-9]. However, it is still challenging to fabricate real 3D microbatteries, partly due to the great limitations of conventional deposition techniques employed in the fabrication of 2D thin film batteries, such as physical vapor deposition (PVD), chemical vapor deposition (CVD) and electrochemical deposition. One of the most difficult, but crucial steps in the fabrication of 3D microbatteries is the deposition of conformal and pinhole-free thin films onto 3D structures. The thin films required in 3D microbatteries must be perfect and free of cracks or pinholes, which will result in short circuits and failure of batteries. It has been realized that the key to achieving as-desired thin films in 3D architectures is the use of a deposition technique that is inherently self-limiting [8, 10].

Atomic layer deposition (ALD) has been known as a thin film technique being capable of depositing high-quality films in 3D structures [11]. Unlike other film deposition methods, such as PVD or CVD, ALD employs self-limiting surface reactions *via* alternating, saturated precursor doses [12, 13]. As a consequence, ALD provides exquisite control over the thickness of thin films, and the thin films deposited by ALD have excellent conformality and uniformity, even in 3D substrates with aspect ratio in excess of 1000 [14]. These unique features make ALD a suitable technique for fabricating 3D microbatteries, and its potential has been demonstrated recently [15-17]. For example, anatase TiO₂ thin film with 17 nm thickness was deposited by ALD directly on aligned aluminum nanorods, which served as current collectors [15]. The 3D TiO₂ nanoelectrode exhibited a capacity 10 times higher than traditional 2D TiO₂ electrode in the same areal footprint, and showed excellent rate capability and stability in 50 charge-discharge cycling. V₂O₅ thin films were deposited using ALD on micropillars coated with TMV/Ni, forming hierarchical 3D electrodes [17]. The conformal V₂O₅ thin films on the 3D micropillar electrodes enabled much higher energy density and faster charge-discharge rate than those on a planar substrate. Even though no real 3D microbatteries have been manufactured by ALD, given the aforementioned exclusive advantages, it is expected that ALD will play an important role in fabricating 3D microbatteries in the near future.

Advancement in 3D microbatteries by ALD is highly reliant on the development of battery materials, *i.e.* anodes, solid-state electrolytes and cathodes [18, 19]. Some ALD-derived materials (mainly metal oxide such as TiO₂, SnO₂, V₂O₅) have been adopted as anodes or cathodes in 3D microbatteries [18, 19]. However, there have been very few reports on the synthesis of solid-state electrolytes by ALD [20-26]. It was not until 2009 that research relevant to solid-state electrolytes deposited by ALD started to emerge, when the ALD process for Li₂O was first investigated [25]. Asltonen *et al.* [21] applied ALD to grow lithium lanthanum titanate (LLT) electrolytes at 225 °C by combining subcycles of TiO₂ (TiCl₄-H₂O), La₂O₃ (La(thd)₃-O₃) and Li₂O (LiO^tBu-H₂O). The LLT thin film deposited at saturation conditions had a composition of Li_{0.32}La_{0.30}TiO_z, with amorphous structure. The LLT thin film was crystallized after annealing at 800 °C in oxygen for 3h. Later on, Li₂O-Al₂O₃ thin films were fabricated by the same group using ALD of Li₂O (LiO^tBu-H₂O) and Al₂O₃ (TMA-O₃) [22]. The thickness of the Li₂O-Al₂O₃

thin film was found to depend on ALD cycles linearly, yielding a growth rate of 2.8 Å/cycle. Hänninen *et al.* [22, 24] described the deposition of lithium phosphate and lithium silicate thin films by ALD. The lithium phosphate was deposited between 225 and 350 °C using trimethyl phosphate and either of LiHMDS or LiO^tBu, and the lithium silicate was grown in a temperature range of 150 to 400 °C from LiHMDS and O₃. In both cases, the growth rate and composition of the thin films were dependent on deposition temperature. Furthermore, Li₃N was deposited by ALD from LiN(SiMe₃)₂ and NH₃ at 167 °C, showing a growth rate of 0.95 Å/cycle [25]. Even though progresses on ALD synthesis of solid-state electrolytes have been made, investigation on their lithium-ion conductivity was seldom conducted. Only Asltonen *et al.* [22] presented a lithium-ion conductivity of 1×10^{-7} S cm⁻¹ (at 300 °C) for Li₂O-Al₂O₃ thin film, which had been annealed at 700 °C for 5h. Unfortunately, the high operating temperature and post-annealing requirement seriously hinders application of the Li₂O-Al₂O₃ thin film. The post-annealing process increases the risk of cracking in solid-state electrolytes, leading to short circuits and failure of 3D microbatteries. Therefore, it is essential that the solid-state electrolyte thin films are prepared in a “gentle” manner to avoid cracking.

To fulfill the objective above, lithium tantalate was selected as the solid-state electrolyte to be deposited by ALD in this work. Lithium tantalate has the advantages of: (1) being lithium-ion conductive with amorphous structure. Previous work has found that amorphous lithium tantalate rather than crystalline one was conductive of lithium ions [27, 28]. The ALD-deposited lithium tantalate would show disordered structure due to the low deposition temperature (225 °C) used herein [20-24]. It was expected that the lithium tantalate grown by ALD could be a lithium-ion conductor at the as-deposited condition, saving post-treatment process and avoiding possible cracking of thin films during this process; (2) displaying acceptable lithium-ion conductivity (10^{-5} - 10^{-8} S/cm) and (3) negligible electronic conductivity at room temperature [27, 28]. In summary, this work realized the deposition of lithium tantalate thin films by ALD technique, for the first time. The synthesized lithium tantalate thin films were featured with not only precisely controlled film thickness, but well-tuned film composition. Most importantly, the lithium tantalate thin films by ALD, at the as-deposited state, exhibited moderate lithium-ion conductivity at room temperature, with no requirement of further treatments. Furthermore,

the ALD approach reported herein could achieve uniform and conformal lithium tantalate thin films in a 3D architecture. It is believed that the lithium tantalate thin films deposited by ALD, would have great potential as solid-state electrolytes in 3D microbatteries.

10.2 Experimental Section

All lithium tantalate thin films were deposited at 225 °C in Savannah 100 ALD system (Cambridge Nanotech Inc) by combining ALD subcycles of Li₂O and Ta₂O₅. The Li₂O subcycle consisted of alternating pulses of lithium tertbutoxide (LiO^tBu, (CH₃)₃COLi) and H₂O, while the Ta₂O₅ subcycle consisted of alternating pulses of tantalum(V) ethoxide (Ta(OEt)₅, Ta(OC₂H₅)₅) and H₂O. The source temperatures for LiO^tBu, Ta(OEt)₅ and H₂O were 170, 190 and 23 °C, respectively. The system pipelines were heated to 190 °C in order to prevent condensation of the precursors. The pulse times of LiO^tBu and Ta(OEt)₅ were varied from 0.2 to 1.5 s, while the pulse time of H₂O remained at 1 s. All precursor pulses were separated by a 10 s nitrogen purge. One ALD cycle was executed using a pulsing sequence of 1 × [LiO^tBu (0.2-1.5 s)-purge (10 s)-H₂O (1 s)-purge (10 s)]-*n* × [Ta(OEt)₅ (0.2-1.5 s)-purge (10 s)-H₂O (1 s)-purge (10s)], which was expressed as 1 × Li₂O + *n* × Ta₂O₅ (1 ≤ *n* ≤ 10) in brief. All lithium tantalate thin films were deposited on planar Si (100) and glass substrates. Anodic aluminum oxide (AAO, Anodisc 13, Whatman) template with aspect ratio of ~300 was chosen as a 3D substrate. All characterizations were carried out on the Si (100) substrate except otherwise noted.

The thicknesses of the lithium tantalate thin films were measured from the cross sections of Si (100) using field-emission scanning electron microscopy (SEM, Hitachi-4800). The thicknesses of the thin films were obtained by taking average of 10 values measured at different locations of each sample. The compositions of the lithium tantalate thin films were analyzed by using X-ray photoelectron spectroscopy (XPS) using Kratos Axis Ultra Al (alpha) spectrometer. The phases of the lithium tantalate thin films on the glass substrate were identified using micro X-ray diffraction (XRD, Bruker D8, Co-K α source, $\lambda=1.7892\text{\AA}$). The Ta L₃ edge X-ray absorption near edge structure (XANES) measurements were performed on the 06ID superconducting wiggler hard X-ray microanalysis (HXMA) beamline at the Canadian Light Source (CLS) with a premirror -

double crystal monochromator – postmirror configuration using Si (111) crystals and Rh mirrors. CLS operates at 2.9 GeV with 175 mA injection current and the beamline wiggler was running at 1.5 T. Measurements were made at room temperature in transmission mode for Ta foil with ion chambers filled with 100% of N₂, and in fluorescence mode for the lithium tantalate thin films using a 32-element Ge detector.

To prepare the sample for impedance testing, ~ 50 nm Au layer was first sputtered on the glass substrate in a Polaron sputtering system under 2 kV for 9 min, and then the lithium tantalate thin film was deposited on top of the Au layer using a pulsing sequence of $400 \times (1 \times \text{Li}_2\text{O} + 6 \times \text{Ta}_2\text{O}_5)$. Following the ALD deposition, the as-prepared sample was immediately transferred into the Polaron sputtering system for coating of another Au layer (~ 50 nm in thickness). The thickness of the lithium tantalate thin film (or the distance between the two Au layers) was measured to be ~ 200 nm, and the area of lithium tantalate thin film was 5 mm \times 5 mm. The impedance spectra at different temperatures were obtained by applying 50 mV in a frequency range of 200 kHz-10 Hz on a CHI Electrochemistry workstation. The sample was left to stabilize at each temperature for 30 min before acquiring data.

10.3 Results and Discussion

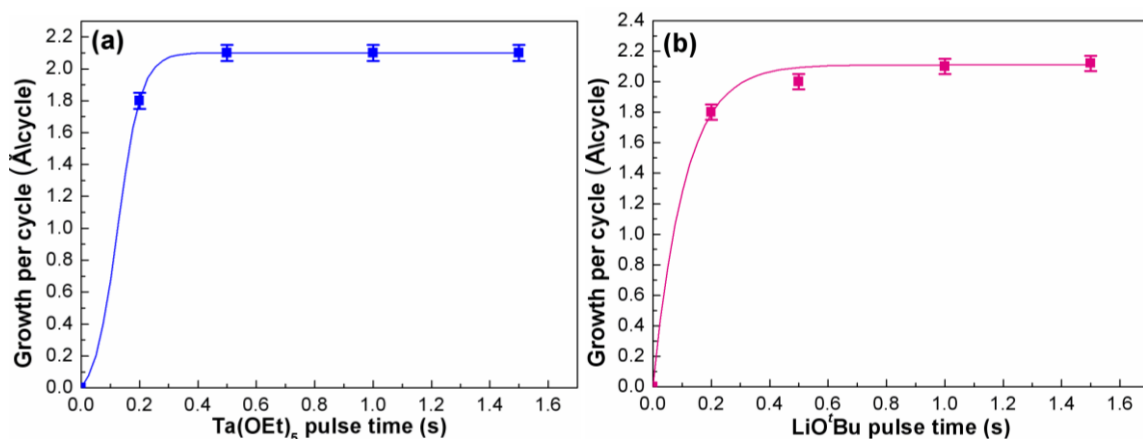


Figure 10.1 Growth per cycle of the lithium tantalate thin film as a function of (a) Ta(OEt)₅ pulse time and (b) LiO^tBu pulse time using a pulsing sequence of $400 \times (1 \times \text{Li}_2\text{O} + 1 \times \text{Ta}_2\text{O}_5)$. The lines serve as guides to the eye.

Figure 10.1 shows the effect of LiO^tBu and $\text{Ta}(\text{OEt})_5$ pulse times on the growth per cycle (GPC) of the lithium tantalate system deposited using a pulsing sequence of $(1 \times \text{Li}_2\text{O} + 1 \times \text{Ta}_2\text{O}_5)$. It can be seen that the GPC stabilizes at around $2.1 \text{ \AA}/\text{cycle}$, when pulse times for $\text{Ta}(\text{OEt})_5$ and LiO^tBu are longer than 0.5 and 1 s respectively. Thus, $\text{Ta}(\text{OEt})_5$ and LiO^tBu pulse lengths of 0.5 and 1 s, respectively, are sufficient to achieve saturated growth of the lithium tantalate thin film, and are chosen to be employed in subsequent experiments.

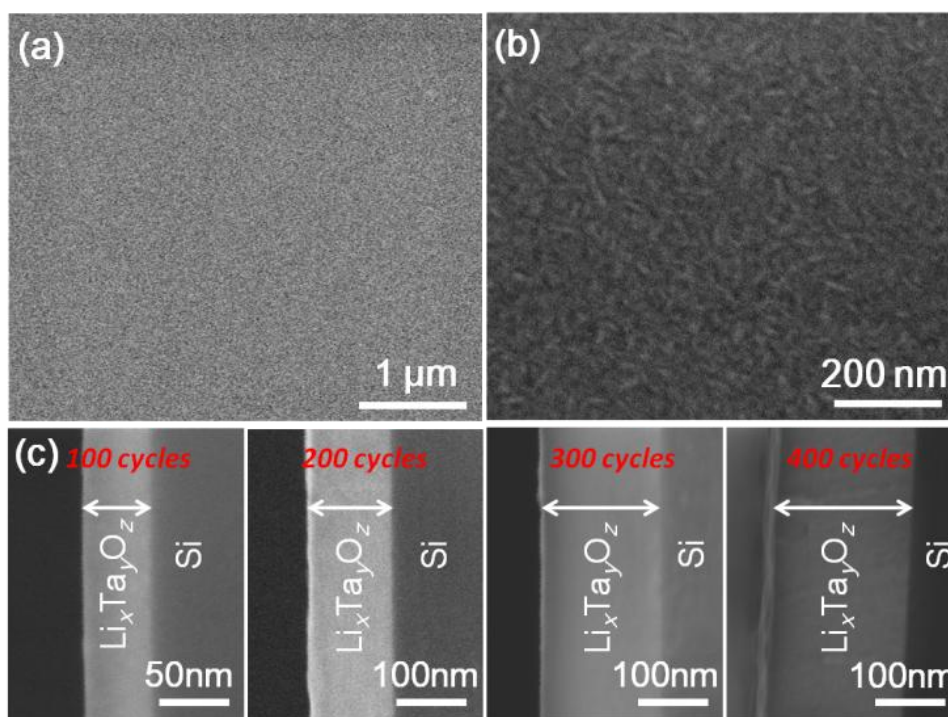


Figure 10.2 SEM morphology of lithium tantalate thin film deposited using a pulsing sequence of $(1 \times \text{Li}_2\text{O} + 6 \times \text{Ta}_2\text{O}_5)$: (a, b) top view of 400-cycle thin film, and (c) cross-section views of the thin films deposited with different ALD cycles.

The lithium tantalate thin films are deposited using pulsing sequences of $1 \times \text{Li}_2\text{O} + n \times \text{Ta}_2\text{O}_5$ ($n = 1, 6$ and 10), where subcycle number of Ta_2O_5 (n) is varied in order to change film composition (Li/Ta ratio). The morphologies of the as-deposited thin films are examined by SEM. Figure 10.2 displays the result of the lithium tantalate thin film deposited using a pulsing sequence of $1 \times \text{Li}_2\text{O} + 6 \times \text{Ta}_2\text{O}_5$ as an example. From top-view observation in Figure 10.2a, it can be seen that 400-cycle lithium tantalate thin film

is uniformly coated on the whole Si substrate, with a slight roughness associated with the film surface (Figure 10.2b). Cross-sectional views in Figure 10.2c clearly show the thicknesses of the lithium tantalate thin films deposited with different ALD cycles (low-magnification images included in Figure SI-10.1 of the Supporting Information). The thickness measurements by SEM are plotted as a function of ALD cycle number in Figure 10.3. XRD analysis (Figure SI-10.2 of the Supporting Information) reveals amorphous structure of the as-grown lithium tantalate thin films.

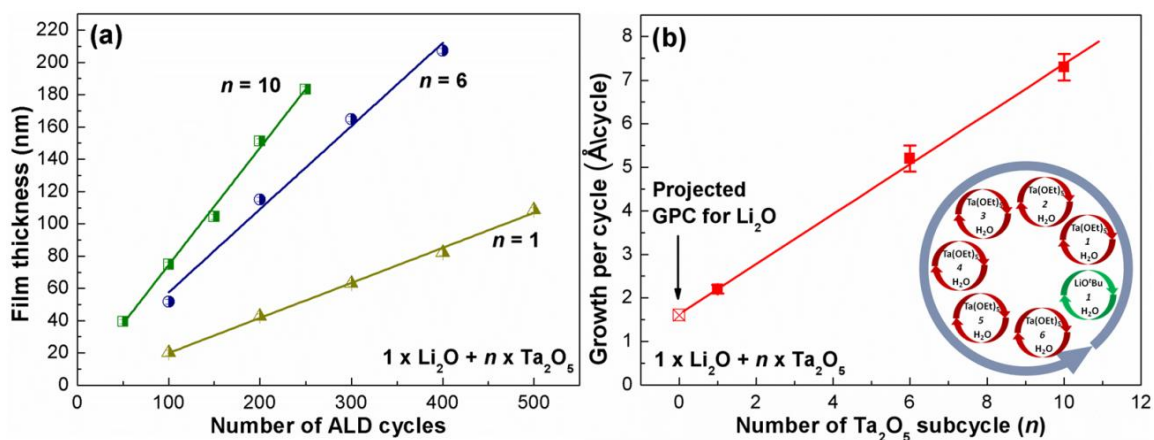
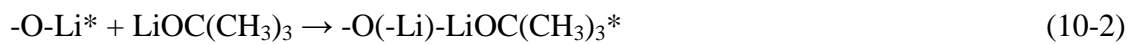
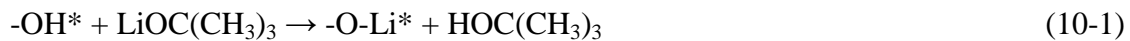


Figure 10.3 (a) Thickness of the lithium tantalate thin films as a function of ALD cycles and (b) the growth per cycle of the lithium tantalate thin films as a function of Ta_2O_5 subcycle number, using pulsing sequences of $1 \times \text{Li}_2\text{O} + n \times \text{Ta}_2\text{O}_5$ ($n = 1, 6$ and 10).

Figure 10.3a shows the ALD-cycle dependence of lithium tantalate film thickness when different pulsing sequences are employed. It is clear that the lithium tantalate film thickness is linearly dependent with ALD cycle, demonstrating the self-limiting behavior during the ALD process. By fitting the data in Figure 10.3a linearly, the GPC of the lithium tantalate thin film is calculated to be 2.2, 5.2 and 7.3 Å/cycle, where n equals to 1, 6 and 10, respectively, in one ($1 \times \text{Li}_2\text{O} + n \times \text{Ta}_2\text{O}_5$) cycle (as plotted in Figure 10.3b). From Figure 10.3b, one can see that the GPC of the lithium tantalate thin films increases monotonously with Ta_2O_5 subcycle number (n) in one complete ALD cycle ($1 \times \text{Li}_2\text{O} + n \times \text{Ta}_2\text{O}_5$). This trend indicates that the GPC of the lithium tantalate thin films is a linear combination of the GPC of the Li_2O subcycle and Ta_2O_5 subcycle. Thereby, two parameters could be extracted from the best-linear-fit in Figure 10.3b: the slope

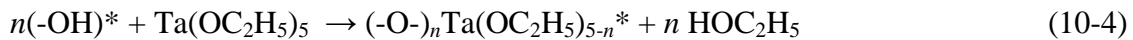
represents the GPC of the Ta₂O₅ subcycle ($\sim 0.5 \text{ \AA}/\text{cycle}$), while the y-axis intercept of the linear fit represents the GPC of solely the Li₂O subcycle ($\sim 1.7 \text{ \AA}/\text{cycle}$). The GPC of the Li₂O and Ta₂O₅ subcycles obtained herein have good agreement with reported values of Li₂O at $1.7 \text{ \AA}/\text{cycle}$ [29], and Ta₂O₅ at $0.4 \text{ \AA}/\text{cycle}$ [22]. A better understanding of the ALD process can be derived from looking at the reaction mechanism for each subcycle. As proposed by Asltonen *et al.* [22] during the Li₂O subcycle, the LiO^tBu pulse leads to the formation of two layers, resulting in a high GPC of the Li₂O subcycle:



where an asterisk denotes surface species. During the water pulse, the surface species generated in Equation (2) are converted to hydroxide groups [22, 30]:



During the Ta₂O₅ subcycle, the following surface reaction occurs [31]:



Therefore, the surface reactions during one complete ($1 \times \text{Li}_2\text{O} + n \times \text{Ta}_2\text{O}_5$) cycle would occur in the following sequence Equations (10-1)(10-2) \rightarrow (10-3) \rightarrow (10-4)ⁿ \rightarrow (10-5). One can find that the film surfaces after Li₂O and Ta₂O₅ subcycles are terminated with the same functional groups (-OH). Thus, the surface species available after each Li₂O subcycle are readily reactive sites for the succeeding Ta₂O₅ subcycle, and *vice versa*. This condition insures that the Li₂O and Ta₂O₅ subcycles in the combined ALD process proceed in the same manner as in each binary oxide, therefore leading to the similar GPC of Li₂O and Ta₂O₅ in the ternary system as in each binary system. The self-limiting characteristic of the Li₂O and Ta₂O₅ subcycles takes responsible for the linear relationship between the lithium tantalate film thickness and ALD cycles (Figure 10.3a), and between the GPC of the lithium tantalate films on Ta₂O₅ subcycle number (Figure 10.3b). It is worth mentioning that in a ternary or quaternary system deposited by ALD,

the GPC of the combined oxide processes is usually lower than what is expected from a linear combination of the GPC of each binary oxide [21, 32]. For example, the average GPC of La-Ti-O films grown by combining La_2O_3 and TiO_2 subcycles was found to be below the theoretical GPC calculated from individual growth rate of La_2O_3 ($0.28 \text{ \AA}/\text{cycle}$) and TiO_2 ($0.52 \text{ \AA}/\text{cycle}$) [21]. The reason was most likely due to the difference in the surface chemistry between the preceding and the succeeding subcycles, which could alter the GPC of one or each binary system when they are combined. This difference was more obvious in Li-La-Ti-O system, which was fabricated using Li_2O , La_2O_3 and TiO_2 subcycles. It was found that the pulsing order of the three subcycles had a substantial influence on the Li-La-Ti-O films. The films grown by using a sequence of TiO_2 - La_2O_3 - Li_2O was less rough and more uniform than that deposited using a TiO_2 - Li_2O - La_2O_3 pulsing sequence [21]. Thus, precursor combination and pulsing sequence should be carefully selected when depositing thin films composed of two or more ALD subcycles. From the calculation in [Figure 10.3b](#), one can find that the GPC of the Ta_2O_5 subcycle ($\sim 0.5 \text{ \AA}/\text{cycle}$) is slightly higher than that of binary Ta_2O_5 ($0.4 \text{ \AA}/\text{cycle}$) reported in the literature [22]. The higher GPC of Ta_2O_5 in our case might be due to denser regeneration of hydroxide groups after each Li_2O subcycle (Equation (10-3)) than those produced after each Ta_2O_5 subcycle (Equation (10-5)). Another reason that cannot be excluded is the possibility of physisorbed water remaining on the surface after reaction (10-3) or/and reaction (10-5). Physisorbed water may lead to CVD-like growth of thin film during the $\text{Ta}(\text{OEt})_5$ pulse, thus leading to a higher GPC of Ta_2O_5 than expected.

The structure of amorphous materials is difficult to be probed and determined by diffraction-based techniques due to the lack of long-range order. By contrast, X-ray spectroscopy is sensitive to the local environment of the element to be examined, and thus is ideal and powerful for analyzing amorphous materials [33]. By comparing the X-ray spectra of unknown and reference materials, it is possible to gain insight into the structure of non-crystalline materials [33, 34]. Thus, XANES and XPS techniques were employed to study the structure or/and composition of the amorphous lithium tantalate thin films deposited by ALD in this work. [Figure 10.4](#) displays XANES at Ta L_3 edge for the lithium tantalate thin films, in comparison with reference crystalline LiTaO_3 and pure Ta. The peak at the L_3 edge arises from Ta $2p_{3/2}$ to unoccupied Ta 5d states via

dipole transition and its intensity is expected to be higher in LiTaO_3 and exhibits a blue shift since Ta is in a higher oxidation state (d charge depletion). In Figure 10.4, it can be seen that all the lithium tantalate thin films have very similar Ta L_3 -edge spectrum to reference LiTaO_3 , except that the lithium tantalate thin films exhibit one broad peak at ~ 9886.5 eV, instead of two well-resolved peaks at 9884.5 and 9886.8 eV for reference crystalline LiTaO_3 [35]. This slight difference is attributable to the amorphous state of the lithium tantalate thin films [36, 37]. In Figure 10.4, it is also obvious that the Ta L_3 -edge XANES of the lithium tantalate thin films are remarkably different from that of pure Ta metal as expected. The XANES result indicates that the Ta in lithium tantalate thin films have similar chemical binding (Li-O-Ta) as that in reference LiTaO_3 with a noticeable broadening due to disorder.

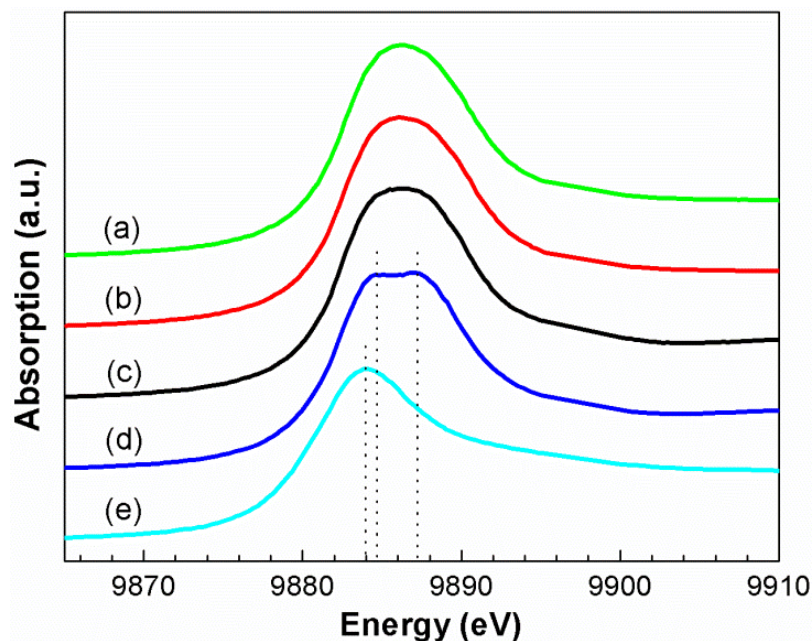


Figure 10.4 Ta L_3 -edge XANES spectra of lithium tantalate thin films deposited using pulsing sequences of $1 \times \text{Li}_2\text{O} + n \times \text{Ta}_2\text{O}_5$ where (a) $n = 1$, (b) $n = 6$, (c) $n = 10$; (d) reference crystalline LiTaO_3 , and (e) pure Ta.

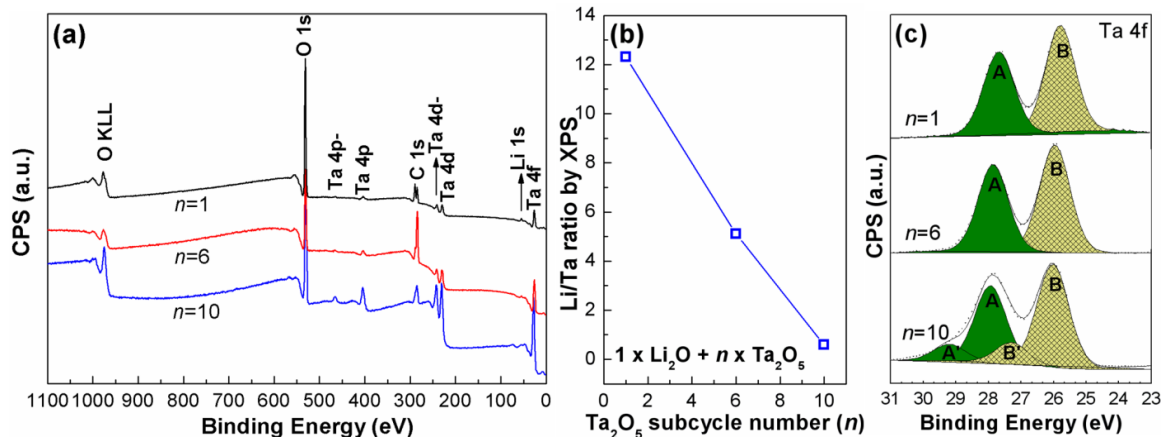


Figure 10.5 (a) XPS survey of the lithium tantalate thin films deposited using pulsing sequences of $1 \times \text{Li}_2\text{O} + n \times \text{Ta}_2\text{O}_5$ ($n = 1, 6$ and 10); (b) Li/Ta ratio in the thin films as a function of Ta_2O_5 subcycle number (n); and (c) deconvolution of Ta 4f spectra. In (c), the components A and A' correspond to the Ta 4f_{5/2} lines, and the components B and B' correspond to the Ta 4f_{7/2} lines.

Compositions of the lithium tantalate thin films were analyzed by XPS, and the results are displayed in Figure 10.5. XPS survey in Figure 10.5a indicates the presence of Li, Ta and O elements in all the lithium tantalate thin films (their atomic percentages listed in Table SI-10.1 of the Supporting Information). The chemical formula is determined as $\text{Li}_{12.3}\text{TaO}_z$, $\text{Li}_{5.1}\text{TaO}_z$ and $\text{Li}_{0.6}\text{TaO}_z$, for the lithium tantalate thin film deposited using a Ta_2O_5 subcycle of 1, 6, and 10 respectively, while Li_2O was kept constant at 1. XPS data reveals that the Li/Ta ratio of the lithium tantalate thin films decreases with increasing Ta_2O_5 subcycle number, as plotted in Figure 10.5b. Figure 10.5c illustrates the chemical environment of Ta element in the lithium tantalate thin films by analyzing Ta 4f spectrum. For $\text{Li}_{12.3}\text{TaO}_z$ and $\text{Li}_{5.1}\text{TaO}_z$, the Ta 4f spectrum is fitted into one set of doublet Ta 4f_{5/2} (peak A) and Ta 4f_{7/2} (peak B). The positions of Ta 4f_{5/2} (peak A) and Ta 4f_{7/2} (peak B) are centered at 27.7 and 25.8 eV for $\text{Li}_{12.3}\text{TaO}_z$, and at 27.9 and 26.0 eV for $\text{Li}_{5.1}\text{TaO}_z$, respectively. The slight shift of Ta 4f_{5/2} (peak A) and Ta 4f_{7/2} (peak B) is due to the stoichiometry change from $\text{Li}_{12.3}\text{TaO}_z$ to $\text{Li}_{5.1}\text{TaO}_z$. The positions of the Ta 4f_{5/2} (peak A) and Ta 4f_{7/2} (peak B) are very close to those reported in stoichiometric LiTaO_3 film [38], revealing that the Ta element in $\text{Li}_{12.3}\text{TaO}_z$ and $\text{Li}_{5.1}\text{TaO}_z$ has a similar chemical binding (Li-O-Ta) as stoichiometric LiTaO_3 . Deconvolution of Ta 4f peak of $\text{Li}_{0.6}\text{TaO}_z$ is

composed of two pairs of doublets. The one pair of Ta $4f_{5/2}$ (peak A) and Ta $4f_{7/2}$ (peak B) at lower binding energy is consistent with those in $\text{Li}_{5.1}\text{TaO}_z$. The other pair of Ta $4f_{5/2}$ (peak A') and Ta $4f_{7/2}$ (peak B') at higher binding energy are located at 29.2 and 27.3 eV respectively, which are very close to the binding energy of Ta element in stoichiometric Ta_2O_5 [39]. This result indicates that the Ta in $\text{Li}_{0.6}\text{TaO}_z$ exists in two types of chemical environments, *i.e.* Li-O-Ta and Ta-O-Ta, which make up 82% and 18% respectively. Besides the above elements, carbon is also detected in all thin films prepared (Figure 10.5a). The presence of carbon can be addressed to organic carbons in C-C, C-H (284.8 eV), C-OH, C-O-C (286.3 eV), O-C=O (288.8 eV) and C=O (287.2 eV) (see Figure SI-10.3 of the Supporting Information). The source of carbon is a result of ligand residue of ALD precursors, as well as hydrocarbons present in ambient air [40]. In $\text{Li}_{12.3}\text{TaO}_z$, another major source of carbon impurity is carbonate (290.1 eV) (Figure SI-10.3 of the Supporting Information), which is commonly found in lithium-containing thin films produced by ALD [22, 40]. Carbonate present results from a reaction between Li_2O and ambient carbon dioxide when the thin films are exposed to air [30], and thereby should predominantly reside on the topmost surface of the thin film [22, 40]. In $\text{Li}_{5.1}\text{TaO}_z$ and $\text{Li}_{0.6}\text{TaO}_z$, carbonate only accounts for 4-6% of the carbon impurity, compared to 40% in $\text{Li}_{12.3}\text{TaO}_z$ (Figure SI-10.3 of the Supporting Information). This difference could be explained by the fact that more Ta_2O_5 subcycles were used in ALD process of $\text{Li}_{5.1}\text{TaO}_z$ and $\text{Li}_{0.6}\text{TaO}_z$ than $\text{Li}_{12.3}\text{TaO}_z$, and resultant thicker Ta_2O_5 layer in the former films can better prevent the reaction of Li_2O with ambient carbon dioxide. $\text{Li}_{5.1}\text{TaO}_z$ thin film is chosen to be further studied in terms of the lithium-ion conductivity, because it is stable in air and easy for operation. More importantly, the excess Li content in $\text{Li}_{5.1}\text{TaO}_z$ thin film is beneficial for lithium-ion conduction according to previous studies [28, 41].

Lithium-ion conductivity of 400-cycle $\text{Li}_{5.1}\text{TaO}_z$ thin film (~ 200 nm thick) was assessed by using electrochemical impedance spectroscopy. Figure 10.6a shows Cole-Cole plots of the $\text{Li}_{5.1}\text{TaO}_z$ thin film measured at different temperatures. It can be seen that each Cole-Cole plot consists of one semicircle in the high frequency region and an inclined tail in the low frequency region. The former semicircle could be assigned to the bulk resistance of $\text{Li}_{5.1}\text{TaO}_z$ solid-state electrolyte [27], while the latter is attributable to the polarization at electrode-electrolyte interface [42]. It is worth noting that the inclined tail in the case

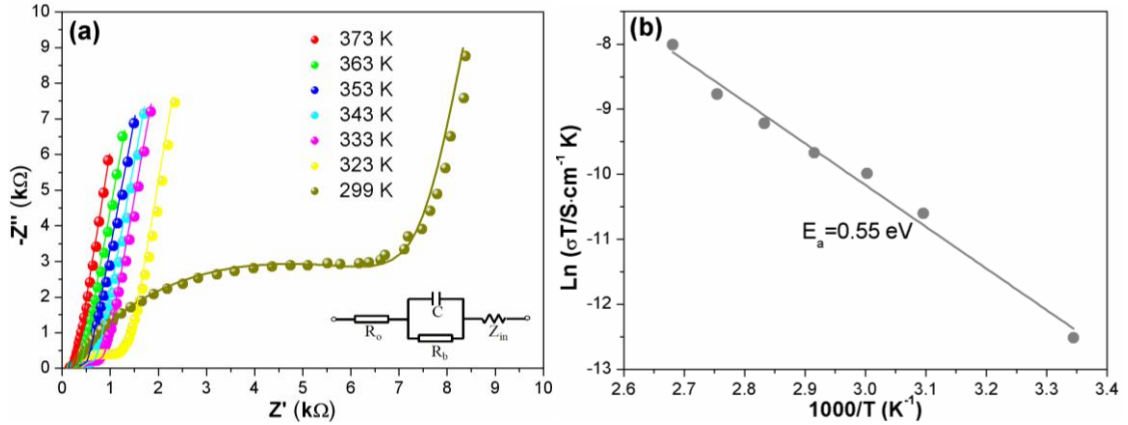


Figure 10.6 (a) Impedance plots of the $\text{Li}_{5.1}\text{TaO}_z$ thin film measured at different temperatures (inset shows the equivalent circuit for fitting); (b) Arrhenius plot of the ionic conductivity of the $\text{Li}_{5.1}\text{TaO}_z$ thin film.

of ionic blocking electrodes (such as Au used herein) is typical indication of that the investigated solid-state electrolyte is predominately ionic conductor in nature [42, 43]. The Cole-Cole plots could be well-resolved using the equivalent circuit inset in Figure 10.6a, in which R_b and C represents the bulk resistance and the resultant capacitance of the $\text{Li}_{5.1}\text{TaO}_z$ solid-state electrolyte respectively, Z_{in} denotes the polarization impedance of the electrode-electrolyte interface, and R_o is the ohmic resistance of the electrodes [27]. R_b values are obtained in Figure 10.5a at different temperatures, and the ionic conductivity of the $\text{Li}_{5.1}\text{TaO}_z$ solid-state electrolyte is derived from following equation [44]:

$$\sigma = d/AR_b \quad (10-6)$$

where σ is the ionic conductivity, d is the thickness of the $\text{Li}_{5.1}\text{TaO}_z$ film, and A is the area of the $\text{Li}_{5.1}\text{TaO}_z$ film between Au electrodes. The ionic conductivity of $\text{Li}_{5.1}\text{TaO}_z$ varies from 1.2×10^{-8} to 9.0×10^{-7} S/cm, at temperatures between 299 and 373 K. Furthermore, variation of the ionic conductivity with temperature is shown in an Arrhenius representation according to [44, 45]:

$$\sigma T = \sigma_0 \exp[-E_a/(kT)] \quad (10-7)$$

where E_a denotes the activation energy, k Boltzmann constant, T absolute temperature and σ_0 is a constant. Activation energy of ~ 0.55 eV is obtained by fitting the temperature-dependence of the lithium-ion conductivity in Figure 10.6b. Comparison is made between $\text{Li}_{5.1}\text{TaO}_z$, Li_xTaO_y prepared by RF sputtering, and $\text{Li}_2\text{O}-\text{Al}_2\text{O}_3$ grown by ALD in Table 10-1. It can be found that the lithium-ion conductivity of $\text{Li}_{5.1}\text{TaO}_z$ (2×10^{-8} S/cm at 299 K) is comparable with that of amorphous Li_xTaO_y prepared by RF sputtering (8×10^{-8} S/cm at 300 K) [27]. For the $\text{Li}_2\text{O}-\text{Al}_2\text{O}_3$, its lithium-ion conductivity was estimated to be around 1×10^{-7} S/cm at 573 K, and no data at room temperature was reported [22]. Furthermore, the $\text{Li}_2\text{O}-\text{Al}_2\text{O}_3$ exhibits a much higher activation energy (2.9 eV) than $\text{Li}_{5.1}\text{TaO}_z$ (0.55 eV) and amorphous Li_xTaO_y (0.25 eV). The lithium-ion conductivity of $\text{Li}_{5.1}\text{TaO}_z$ is considerably low compared with popular solid-state electrolytes (such as NASICON-type, Garnet-type [46, 47]) in 2D batteries. Nevertheless, to be applicable in 3D microbatteries, a solid-state electrolyte should be able to be deposited uniformly on a 3D architecture. Successful achievement of this goal will allow for significantly reduced ionic conductivity to be a tolerable consequence [27].

Table 10-1 Comparison of lithium tantalate and $\text{Li}_2\text{O}-\text{Al}_2\text{O}_3$ solid-state electrolytes.

Solid-state electrolyte	Substrate type	Li^+ conductivity	Activation energy	Preparation method	Ref.
Amorphous Li_xTaO_y	ITO film (planar)	8×10^{-8} S/cm (at 300 K)	0.25 eV	RF sputtering	[28]
$\text{Li}_2\text{O}-\text{Al}_2\text{O}_3$	Sapphire/Si(111) (planar)	1×10^{-7} S/cm (at 573 K)	2.90 eV	ALD	[22]
Amorphous $\text{Li}_{5.1}\text{TaO}_z$	Si(100)/glass (planar); AAO (3D aspect ratio ~ 300)	2×10^{-8} S/cm (at 299 K)	0.55 eV	ALD	Herein

The capability of the ALD process to achieve the above goal is demonstrated by depositing 100-cycle $\text{Li}_{5.1}\text{TaO}_z$ thin film on an AAO template with aspect ratio of ~ 300 , as shown in Figure 10.7. Top-view images in Figure 10.7 (a, b) indicate that the $\text{Li}_{5.1}\text{TaO}_z$ thin film is uniformly and conformally coated around the pores of the AAO template. Furthermore, cross-section examination (as seen in Figure 10.7 (c, d)) shows that the inner surface of the pores is covered by a tubular thin film of $\text{Li}_{5.1}\text{TaO}_z$. The thickness of the $\text{Li}_{5.1}\text{TaO}_z$ thin film is measured as ~ 50 nm from the top (Figure 10.7b) and the side

(Figure 10.7d). The BSE images in Figure 10.7 clearly illustrate that the ALD process developed herein is capable of depositing desirable lithium tantalate thin films in high-aspect-ratio substrates, as required in 3D microbatteries.

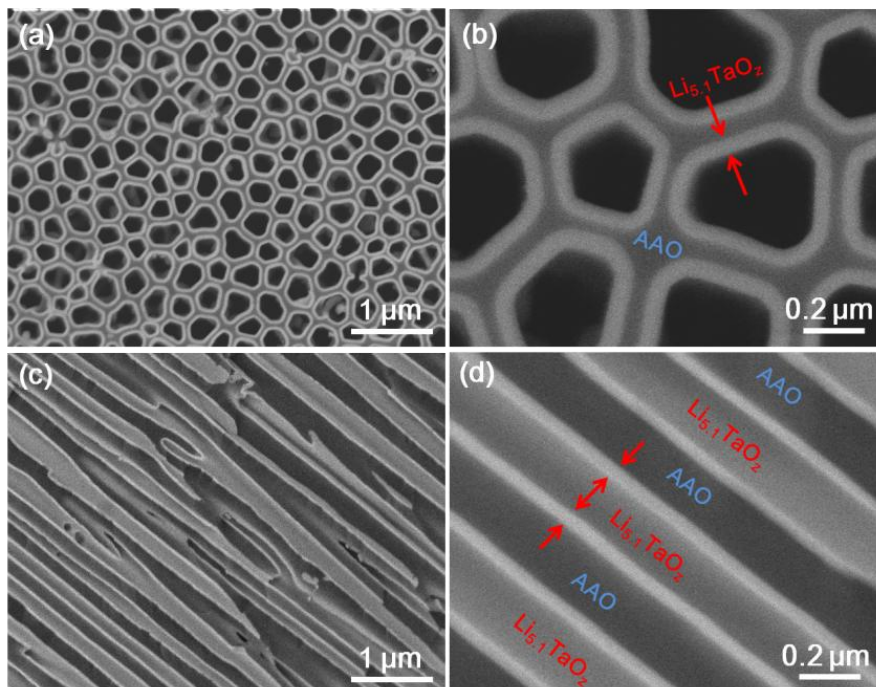


Figure 10.7 Backscattered electron (BSE) images of 100-cycle $\text{Li}_{5.1}\text{TaO}_z$ thin film deposited in AAO template: (a, b) top-view and (c, d) cross-section view.

10.4 Conclusions

Lithium tantalate thin films have been deposited by means of ALD through combining subcycles of Li_2O ($\text{LiO}^t\text{Bu-H}_2\text{O}$) and Ta_2O_5 ($\text{Ta}(\text{OEt})_5\text{-H}_2\text{O}$). All lithium tantalate thin films were deposited at 225 °C, and they were amorphous at as-deposited state. The growth of the lithium tantalate thin films by ALD was proven to be a self-limiting process. Composition (Li/Ta ratio) of the lithium tantalate thin films was controlled by changing the subcycle ratios of Li_2O to Ta_2O_5 (1 to 1, 1 to 6 and 1 to 10). Both XPS and XANES analysis confirmed that Ta element in the lithium tantalate thin films had similar chemical environment as that in reference LiTaO_3 . The as-grown lithium tantalate thin film using 1 Li_2O and 6 Ta_2O_5 subcycles exhibited a lithium-ion conductivity of 2×10^{-8} S/cm at room temperature. Moreover, the ALD process developed in this work

successfully deposited lithium tantalate thin films with excellent uniformity and conformality in a 3D AAO template with an aspect ratio of ~ 300 . Given the aforementioned unique advantages, the lithium tantalate thin films prepared by ALD might find potential applications as solid-state electrolytes in 3D lithium-ion microbatteries, which is very promising power supply system for next-generation microelectronic devices.

Acknowledgements

This work was supported by General Motors of Canada, Natural Sciences and Engineering Research Council of Canada (NSERC), Canada Foundation for Innovation (CFI), Ontario Research Fund (ORF), Canadian Light Source (CLS) at University of Saskatchewan and University of Western Ontario.

References

- [1] J. W. Long, B. Dunn, D. R. Rolison, H. S. White, Three-dimensional battery architectures, *Chem. Rev.* **2004**, *104*, 4463-4492.
- [2] M. Roberts, P. Johns, J. Owen, D. Brandell, K. Edstrom, G. E. Enany, C. Guery, D. Golodnitsky, M. Lacey, C. Lecoer, H. Mazor, E. Peled, E. Perre, M. M. Shaijumon, P. Simon, P.-L. Taberna, 3D lithium ion batteries – from fundamentals to fabrication, *J. Mater. Chem.* **2011**, *21*, 9876-9890.
- [3] J. F. M. Oudenhoven, L. Baggetto, P. H. L. Notten, All-solid-state lithium-ion microbatteries: A review of various three-dimensional concepts. *Adv. Energy Mater.* **2011**, *1*, 10-33.
- [4] J. B. Bates, N. J. Dudney, B. Neudecker, A. Ueda, C. D. Evans, Thin-film lithium and lithium-ion batteries, *Solid State Ionics* **2000**, *135*, 33-45.
- [5] J. L. Souquet, M. Duclot, Thin film lithium batteries, *Solid State Ionics* **2002**, *148*, 375-379.

- [6] T. S. Arthur, D. J. Bates, N. Cirigliano, D. C. Jhonson, P. Malati, J. M. Mosby, E. Perre, M. T. Rawls, A. L. Prieto, B. Dunn, Three-dimensional electrodes and battery architectures, *MRS Bull.* **2011**, *36*, 523-531.
- [7] P. H. L. Notten, F. Roozeboom, R. A. H. Niessen, L. Baggetto, 3-D integrated all-solid-state rechargeable batteries, *Adv. Mater.* **2007**, *19*, 4564-4567.
- [8] B. Dunn, J. W. Long, D. R. Rolison, Rethinking multifunction in three dimensions for miniaturizing electrical energy storage, *Electrochem. Soc. Interface* **2008**, *17*, 49-53.
- [9] D. Golodnitsky, M. Nathan, V. Yufit, E. Strauss, K. Freedman, L. Burstein, A. Gladkikh, E. Peled, Progress in three-dimensional (3D) Li-ion microbatteries, *Solid State Ionics* **2006**, *177*, 2811-2819.
- [10] D. R. Rolison, J. W. Long, J. C. Lytle, A. E. Fischer, C. P. Rhodes, T. M. Mcevoy, M. E. Bourg, A. M. Lubers, Multifunctional 3D nanoarchitectures for energy storage and conversion, *Chem. Soc. Rev.* **2009**, *38*, 226-252.
- [11] C. Bae, H. Shin, K. Nielsch, Surface modification and fabrication of 3D nanostructures by atomic layer deposition, *MRS Bull.* **2011**, *36*, 887-897.
- [12] S. M. George, Atomic layer deposition: an overview, *Chem. Rev.* **2010**, *110*, 111-131.
- [13] R. L. Puurunen, Surface chemistry of atomic layer deposition: a case study for the trimethylaluminum/water process, *J. Appl. Phys.* **2005**, *97*, 121301.
- [14] J. W. Elam, D. Routkevitch, P. P. Mardilovich, S. M. George, Conformal coating on ultrahigh-aspect-ratio nanopores of anodic alumina by atomic layer deposition, *Chem. Mater.* **2003**, *15*, 3507-3517.
- [15] S. K. Cheah, E. Perre, M. Rooth, M. Fondell, A. Hårsta, L. Nyholm, M. Boman, T. Gustafsson, J. Lu, P. Simon, K. Edström, Self-supported three-dimensional nanoelectrodes for microbattery applications, *Nano Lett.* **2009**, *9*, 3230-3233.

- [16] K. Gerasopoulos, X. Chen, J. Culver, C. Wang, R. Ghodssi, Self-assembled Ni/TiO₂ nanocomposite anode synthesized via electroless plating and atomic layer deposition on biological scaffolds, *Chem. Commun.* **2010**, 46, 7349-7351.
- [17] K. Gerasopoulos, E. Pomerantseva, M. McCarthy, A. Brown, C. Wang, J. Culver, R. Ghodssi, Hierarchical three-dimensional microbattery electrodes combining bottom-up self-assembly and top-down micromachining, *ACS Nano* **2012**, 6, 6422-6432.
- [18] X. Meng, X.-Q. Yang, X. Sun, Emerging applications of atomic layer deposition for lithium-ion battery studies, *Adv. Mater.* **2012**, 24, 3589-3615.
- [19] H. C. M. Knoop, M. E. Donders, M. C. M. van de Sanden, P. H. L. Notten, W. M. M. Kessels, Atomic layer deposition for nanostructured Li-ion batteries, *J. Vac. Sci. Technol. A* **2012**, 30, 010801.
- [20] M. Putkonen, T. Aaltonen, M. Alnes, T. Sajavaara, O. Nilsen, H. Fjellvåg, Atomic layer deposition of lithium containing thin films, *J. Mater. Chem.* **2009**, 19, 8767-8771.
- [21] T. Aaltonen, M. Alnes, O. Nilsen, L. Costelle, H. Fjellvåg, Lanthanum titanate and lithium lanthanum titanate thin films grown by atomic layer deposition, *J. Mater. Chem.* **2010**, 20, 2877-2881.
- [22] T. Aaltonen, O. Nilsen, A. Magras, H. Fjellvåg, Atomic layer deposition of Li₂O-Al₂O₃ thin films, *Chem. Mater.* **2011**, 23, 4669-4675.
- [23] J. Häkkinen, J. Holopainen, F. Munnik, T. Hatnpää, M. Heikkilä, M. Ritala, M. Leskelä Lithium phosphate thin films grown by atomic layer deposition, *J. Electrochem. Soc.* **2012**, 159, A259-A263.
- [24] J. Häkkinen, F. Munnik, T. Hatnpää, J. Holopainen, M. Ritala, M. Leskelä Study of amorphous lithium silicate thin films grown by atomic layer deposition, *J. Vac. Sci. Technol. A* **2012**, 30, 01A106.
- [25] E. Østreg, P. Vajeeston, O. Nilsen, H. Fjellvåg, Atomic layer deposition of lithium nitride and carbonate using lithium silylamide, *RSC Adv.* **2012**, 2, 6315-6322.

- [26] D. J. Comstock, J. W. Elam, Mechanistic study of lithium aluminum oxide atomic layer deposition, *J. Phys. Chem. C* **2013**, *117*, 1677-1683.
- [27] A. M. Glass, K. Nassau, T. J. Negran, Ionic conductivity of quenched alkali niobate and tantalate glasses, *J. Appl. Phys.* **1978**, *49*, 4808-4811.
- [28] Z. Li, X. Chen, X. Hu, The preparation of ionic conductance of nano-amorphous Li_xTaO_y thin film, *J. Phys. D: Appl. Phys.* **1996**, *29*, 2740-2744.
- [29] K. Kukli, M. Ritala, M. Leskelä Atomic layer epitaxy growth of tantalum oxide thin films from $\text{Ta}(\text{OC}_2\text{H}_5)_5$ and H_2O , *J. Electrochem. Soc.* **1995**, *142*, 1670-1675.
- [30] A. S. Cavanagh, Y. Lee, B. Yoon, S. M. George, Atomic layer deposition of LiOH and Li_2CO_3 using Lithium t-butoxide as the lithium source, *ECS Trans.* **2010**, *33*, 223-229.
- [31] K. Kukli, J. Aarik, A. Aidla, H. Siimon, M. Ritala, M. Leskelä In situ study of atomic layer epitaxy growth of tantalum oxide thin films from $\text{Ta}(\text{OC}_2\text{H}_5)_5$ and H_2O , *Appl. Surf. Sci.* **1997**, *112*, 236-242.
- [32] O. Nilsen, E. Rauwel, H. Fjellvåg, A. Kjekshus, Growth of $\text{La}_{1-x}\text{Ca}_x\text{MnO}_3$ thin films by atomic layer deposition, *J. Mater. Chem.* **2007**, *17*, 1466-1475.
- [32] F. Gitmans, Z. Sitar, P. Günter, Growth of tantalum oxide and lithium tantalate thin films by molecular beam epitaxy, *Vacuum* **1995**, *46*, 939-942.
- [33] M. W. Gaultois, A. P. Grosvenor, XANES and XPS investigations of the local structure and final-state effects in amorphous metal silicates: $(\text{ZrO}_2)_x(\text{TiO}_2)_y(\text{SiO}_2)_{1-x-y}$, *Phys. Chem. Chem. Phys.* **2012**, *14*, 205-217.
- [34] S. Yang, D. Wang, G. Liang, Y. M. Yiu, J. Wang, L. Liu, X. Sun, T.-K. Sham, Soft X-ray XANES studies of various phases related to LiFePO_4 based cathode materials, *Energy Environ. Sci.* **2012**, *5*, 7007-7016.

- [35] T. W. Kim, S. G. Hur, A. R. Han, S.J. Hwang, J. H. Choy, Effect of bond covalency on the lattice stability and fatigue behavior of ferroelectric bismuth transition-metal oxides, *J. Phys. Chem. C* **2008**, *112*, 3434.
- [36] Y. F. Hu, R. K. Xu, J. J. Dynes, R. I. R. Blyth, G. Yu, L. M. Kozak, P. M. Huang, Coordination nature of aluminum (oxy)hydroxides formed under the influence of tannic acid studied by X-ray absorption spectroscopy, *Geochim. Cosmochim. Acta* **2008**, *72*, 1959-1969.
- [37] J. Liu, Y. Tang, B. Xiao, T.-K. Sham, R. Li, X. Sun, Atomic layer deposition aluminum phosphate thin films on N-doped CNTs, *RSC Adv.* **2013**, *3*, 4492-4495.
- [38] E. Atanassova, G. Tyuliev, A. Paskaleva, D. Spassov, K. Kostov, XPS study of N₂ annealing effect on thermal Ta₂O₅ layers on Si, *Appl. Surf. Sci.* **2004**, *225*, 86-99.
- [39] V. Miikkulainen, O. Nilsen, M. Laitinen, T. Sajavaara, H. Fjellvåg, Atomic layer deposition of Li_xTi_yO_z thin films, *RSC Adv.* **2013**, *3*, 7537-7542.
- [40] A. M. Glass, K. Nassau, Lithium ion conduction in rapidly quenched Li₂O-Al₂O₃, Li₂O-Ga₂O₃, and Li₂O-Bi₂O₃ glasses, *J. Appl. Phys.* **1980**, *51*, 3756-3761.
- [41] A. Huanosta, A. R. West, The electrical properties of ferroelectric LiTaO₃ and its solid solutions, *J. Appl. Phys.* **1987**, *61*, 5386-5391.
- [42] R. Murugan, V. Thangadurai, W. Weppner, Fast lithium ion conduction in Garnet-type Li₇La₃Zr₂O₁₂, *Angew. Chem. Int. ed.* **2007**, *46*, 7778-7781.
- [43] J. B. Goodenough, Solid electrolytes, *Pure & Appl. Chem.* **1995**, *67*, 931-938.
- [44] A. R. West, Solid electrolytes, *Ber. Bunsenges. Phys. Chem.* **1989**, *93*, 1235-1241.
- [45] K. Takada, Progress and prospective of solid-state lithium batteries, *Acta Mater.* **2013**, *61*, 759-770.
- [46] V. Thangadurai, W. Weppner, Recent progress in solid oxide and lithium ion conducting electrolytes research, *Ionics* **2006**, *12*, 81-92.

Supporting Information

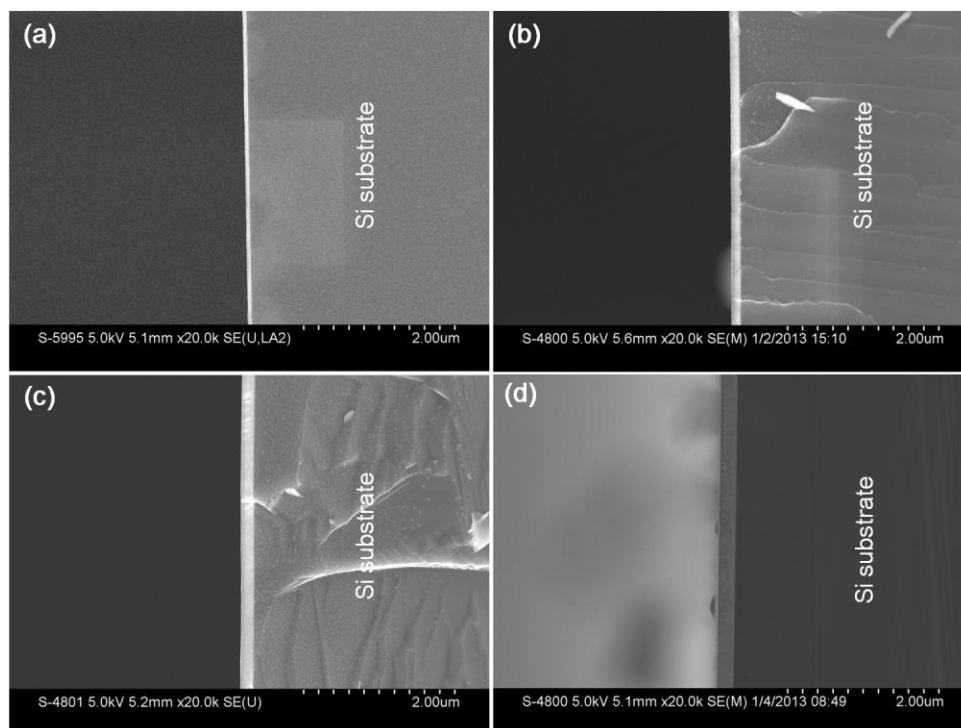


Figure SI-10.1 Low-magnification SEM images of the lithium tantalate thin film deposited using pulsing sequence of $1 \times \text{Li}_2\text{O} + 6 \times \text{Ta}_2\text{O}_5$ with (a) 100, (b) 200, (c) 300 and (d) 400 ALD cycles.

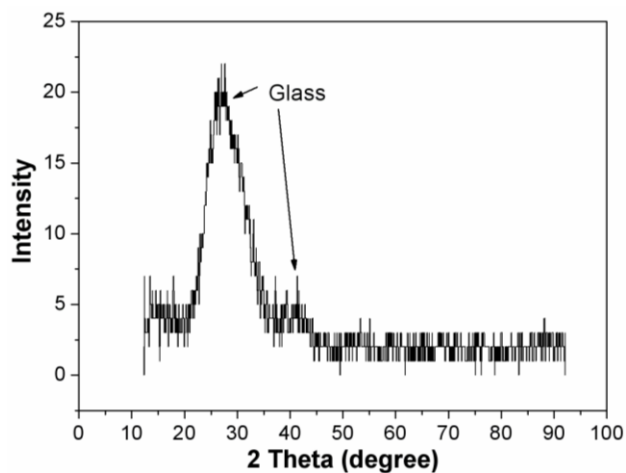


Figure SI-10.2 XRD pattern of 400-cycle lithium tantalate thin film deposited using pulsing sequence of $1 \times \text{Li}_2\text{O} + 6 \times \text{Ta}_2\text{O}_5$ on the glass substrate.

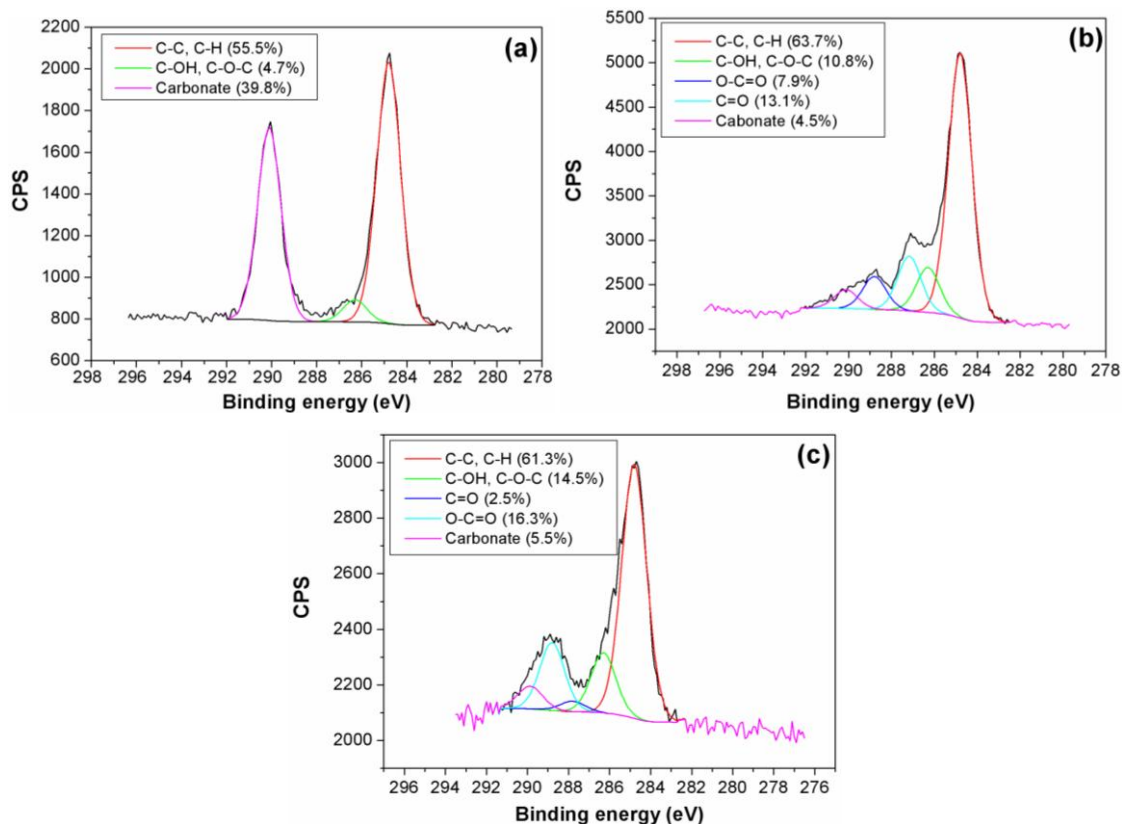


Figure SI-10.3 Deconvolution of C 1s/4 spectrum of the lithium tantalate thin films deposited using pulsing sequences of (a) $1 \times \text{Li}_2\text{O} + 1 \times \text{Ta}_2\text{O}_5$, (b) $1 \times \text{Li}_2\text{O} + 6 \times \text{Ta}_2\text{O}_5$ and (c) $1 \times \text{Li}_2\text{O} + 10 \times \text{Ta}_2\text{O}_5$.

Table SI-10.1 Elemental compositions of lithium tantalate thin films deposited using pulsing sequences of $1 \times \text{Li}_2\text{O} + n \times \text{Ta}_2\text{O}_5$ ($n = 1, 6$ and 10) as measured by XPS

Ta ₂ O ₅ subcycle (<i>n</i>)	Ta (at.%)	Li (at.%)	O (at.%)	C (at.%)	Chemical formula
1	1.9	23.4	44.9	29.3	Li _{12.3} TaO _z
6	3.1	15.9	27.3	53.7	Li _{5.1} TaO _z
10	9.8	5.9	49.2	35.1	Li _{0.6} TaO _z

Chapter 11 Conclusions and Perspectives

11.1 Conclusions

A series of experiments were conducted in this thesis to synthesize various nanostructured anode materials, and to develop surface-modification materials for electrode materials. The applications of some developed materials in LIBs were demonstrated. This thesis covered topics of material synthesis, growth characteristics, underlying mechanisms, and LIB performance.

Various nanosized anode materials, including nitrogen-doped carbon nanotubes (NCNTs), phosphorus-nitrogen doped carbon nanotubes (PNCNTs) and lithium titanate ($\text{Li}_4\text{Ti}_5\text{O}_{12}$), were produced using different methods, including ultrasonic spray pyrolysis, floating catalyst chemical vapor deposition (FCCVD), and microwave-assisted hydrothermal (MH) method. Relations between the microstructure of the nanosized anode materials and experimental parameters were found out, and the growth mechanisms of these materials were explored. In addition, the electrochemical performance of the prepared nanosized anode materials was investigated in some cases.

Firstly, NCNTs were produced from a mixture solution of imidazole and acetonitrile using ultrasonic spray pyrolysis. This work detailedly investigated different experimental parameters, including solution concentration, injection rate and amplitude of ultrasonic processor, on the morphology, internal structure, nitrogen content, defect density, growth rate and yield of NCNTs. It was revealed that the structure and nitrogen content could be easily controlled by adjusting the ratio between imidazole and acetonitrile.

Secondly, PNCNTs were prepared by a FCCVD method using triphenylphosphine (TPP) as phosphorus precursor. The result showed that the diameter and wall thickness of PNCNTs could be controlled by using different TPP amounts. Further study disclosed that the structural change of nanotubes was due to the shape change of the catalyst particles, with the addition of TPP. PNCNTs with P content of 1.9 at.% was obtained.

This work provided valuable information and insightful opinion about P doping in carbon nanotubes, which has been seldom investigated in open literatures.

Thirdly, nanoflower-like and nanoparticle $\text{Li}_4\text{Ti}_5\text{O}_{12}$ were synthesized by a MH method, and applied as anode materials for LIBs. Electrochemical evaluations indicated that nanoflower-like $\text{Li}_4\text{Ti}_5\text{O}_{12}$ exhibited better LIB performance than nanoparticle one, owing to its unique structure and high specific surface area. It could deliver a reversible capacity of ~ 140 mAh/g at 1.1C after 100 cycles. This MH synthesis method was energy-efficient and fast, suitable for industrial applications.

In the next part, various surface-modification materials, including ZrO_2 , AlPO_4 and LiTaO_3 solid state electrolyte, were deposited by atomic layer deposition (ALD) on NCNTs, graphene nanosheets (GNS), Si (100) and anodic aluminum oxide (AAO) template. ALD enabled highly flexibility and controllability of ZrO_2 , AlPO_4 and LiTaO_3 solid state electrolyte, in terms of the film thickness, composition, and/or crystallinity.

ZrO_2 was deposited on NCNTs and GNS by ALD using (dimethylamido) zirconium (IV) and water as precursors. The as-deposited ZrO_2 were controllable in the crystallinity and morphology. Increasing deposition temperature led to more crystalline feature of ZrO_2 on both NCNTs and GNS. Moreover, low ALD cycles resulted in ZrO_2 nanoparticles, while high ALD cycles trended to form ZrO_2 nanofilms. Growth of ZrO_2 on both NCNTs and GNS showed a transition from an island-growth mode to a layer-by-layer growth mode with increasing ALD cycles. Difference in the transition ALD cycles was observed between NCNTs and GNS, due to different densities of reactive sites on their surfaces. This work provided detailed information about how to controllably deposit ZrO_2 by ALD.

Following the above work, study was further carried out to improve the LIB performance of nanoflower-like $\text{Li}_4\text{Ti}_5\text{O}_{12}$ using ZrO_2 coating by ALD. The thickness of ZrO_2 coating layer was precisely tuned by different ALD cycles at nanoscale level. Systemic electrochemical testings revealed that the performance of $\text{Li}_4\text{Ti}_5\text{O}_{12}$ in an extended voltage range (0.1-2.5 V) could be enhanced by ZrO_2 coatings with no more than 5 ALD cycles. Impedance measurement disclosed that the improvement was attributed to the influence of ZrO_2 coating on the formation of solid-electrolyte interphase (SEI) on

$\text{Li}_4\text{Ti}_5\text{O}_{12}$. This work gave a good example of the applications of surface-modification materials developed ALD in LIBs.

Besides ZrO_2 , another good coating material AlPO_4 was developed by ALD in this work. Amorphous aluminum phosphate was deposited by ALD using combined subcycles of Al_2O_3 (trimethylaluminium- H_2O) and PO_x (trimethylphosphite- O_3). The film composition (P/Al ratio) was tunable by changing the subcycle ratio of Al_2O_3 to PO_x . Using 1 Al_2O_3 subcycle and 20 PO_x subcycle, aluminum phosphate with a composition of $\text{Al}_{1.3}\text{PO}_{5.0}$ was obtained. The structure of $\text{Al}_{1.3}\text{PO}_{5.0}$ was confirmed by X-ray photoelectron spectroscopy and X-ray absorption near-edge structure spectroscopy. The thickness of $\text{Al}_{1.3}\text{PO}_{5.0}$ had a linear dependence on ALD cycles, showing typical self-limiting characteristic.

At last, amorphous lithium tantalate thin films were deposited by ALD using subcycle combination of $1 \times \text{Li}_2\text{O} + n \times \text{Ta}_2\text{O}_5$ ($1 \leq n \leq 10$). The Li/Ta ratio in the thin films was controlled by varying Ta_2O_5 subcycle n while keeping Li_2O subcycle constant at 1. The growth of all the thin films showed typical ALD self-limiting behaviors. Furthermore, the thin film grown using $1 \times \text{Li}_2\text{O} + 5 \times \text{Ta}_2\text{O}_5$ exhibited a lithium-ion conductivity of 2×10^{-8} S/cm at 299 K. This property made lithium tantalate more advantageous than ZrO_2 and AlPO_4 for surface-modification purpose in LIBs. In addition, this kind of lithium tantalate by ALD showed excellent uniformity and conformity in 3D AAO template. Therefore, the lithium tantalate developed in this work was very promising solid-state electrolyte in all-solid-state LIBs as well.

11.2 Perspectives

Despite advancements made in this thesis, further research and breakthrough is in need in order to obtain high-performance electrode materials for EV LIBs. Some suggestions are provided in the following part.

First of all, this thesis achieved successful doping of CNTs with N and P. Further studies needs to be carried out on testing the LIB performance of N doped CNTs and P and N co-doped CNTs. Especially, the research on using P doping CNTs as anode materials is rare, and the influence of P doping on the LIB performance of CNTs is still not clear.

Moreover, it would be interesting to investigate and clarify the effect of N and P doping contents on the LIB performance of CNTs, and the working mechanisms.

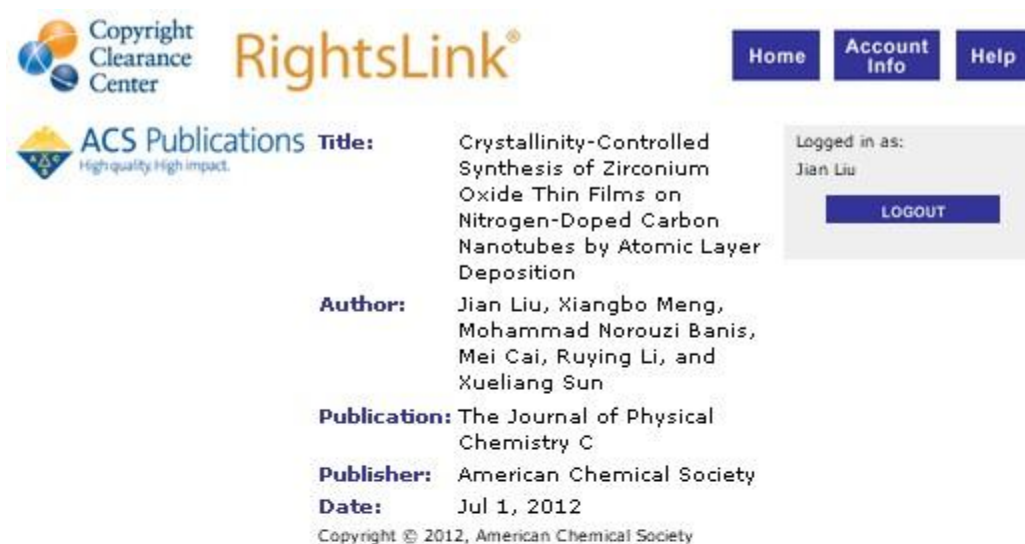
Secondly, three surface-modification materials, including ZrO_2 , AlPO_4 and LiTaO_3 , have been successfully developed by ALD in this thesis. Further studies need to be focused on applying these materials to enhance the LIB performance of both the anode and cathode, in terms of cycling stability, rate capability, coulombic efficiency, and safety. In addition, more efforts should be devoted to understanding and disclosing underlying mechanism for performance improvement by surface modification *via* ALD.

At last, ALD has been demonstrated to be able to deposit solid-state electrolytes in 3D substrates, compared with conventional film deposition techniques. Given its exceptional advantages, ALD has great potentials for fabrication of 3D all-solid-state microbatteries. ALD could be a suitable technique for making real 3D microbatteries, which has proven to be very difficult for other film deposition techniques. Advancement in this field relies on the development of active materials, *i.e.* the anode, cathode and solid-state electrolytes by ALD. In particular, it is really challenging for ALD to deposit the cathode and solid-state electrolytes, which usually contain multi-elements and thereby require combination of a few ALD processes.

Appendices

Appendix A: Permission from American Chemical Society (ACS) for Published Article

Published article: Jian Liu, Xiangbo Meng, Mohammad N. Banis, Mei Cai, Ruying Li, Xueliang Sun. Crystallinity-controlled synthesis of zirconium oxide thin films on nitrogen-doped carbon nanotubes by atomic layer deposition. *J. Phys. Chem. C* **2012**, *116*, 14656-14664. (<http://pubs.acs.org/doi/abs/10.1021/jp3028462>)



The screenshot shows the ACS RightsLink interface. At the top left is the Copyright Clearance Center logo. In the center is the RightsLink logo. On the top right are navigation buttons for Home, Account Info, and Help. Below the logos is the ACS Publications logo with the tagline "High quality. High impact." The main content area displays the following information:

Title: Crystallinity-Controlled Synthesis of Zirconium Oxide Thin Films on Nitrogen-Doped Carbon Nanotubes by Atomic Layer Deposition

Author: Jian Liu, Xiangbo Meng, Mohammad Norouzi Banis, Mei Cai, Ruying Li, and Xueliang Sun

Publication: The Journal of Physical Chemistry C

Publisher: American Chemical Society

Date: Jul 1, 2012

At the bottom of the page, it says "Copyright © 2012, American Chemical Society". On the right side, there is a user login box showing "Logged in as: Jian Liu" and a "LOGOUT" button.

PERMISSION/LICENSE IS GRANTED FOR YOUR ORDER AT NO CHARGE

This type of permission/license, instead of the standard Terms & Conditions, is sent to you because no fee is being charged for your order. Please note the following:

- Permission is granted for your request in both print and electronic formats, and translations.
- If figures and/or tables were requested, they may be adapted or used in part.
- Please print this page for your records and send a copy of it to your publisher/graduate school.
- Appropriate credit for the requested material should be given as follows: "Reprinted (adapted) with permission from (COMPLETE REFERENCE CITATION). Copyright (YEAR) American Chemical Society." Insert appropriate information in place of the capitalized words.
- One-time permission is granted only for the use specified in your request. No additional uses are granted (such as derivative works or other editions). For any other uses, please submit a new request.

Appendix B: Permission from Royal Society of Chemistry (RSC) for Published Article

Published Article: Jian Liu, Yongji Tang, Biwei Xiao, Tsun-Kong Sham, Ruying Li, Xueliang Sun. Atomic layer deposited aluminium phosphate thin films on N-doped CNTs. *RSC Adv.* **2013**, 3, 4492-4495. - Reproduced by permission of The Royal Society of Chemistry. (<http://pubs.rsc.org/en/content/articlelanding/2013/RA/C3RA23320K>)

Author Use of Own Material in Theses and Dissertations

Authors of articles in RSC journals or chapters in RSC books do not need to formally request permission to reproduce their article or book chapter in their thesis or dissertation. For all cases of reproduction the correct acknowledgement should be given in the caption of the reproduced material. The acknowledgement depends on the RSC publication in which the material was published. The form of the acknowledgement to be included in the caption can be found on the page entitled Acknowledgements to be used by RSC authors.

Please ensure that your co-authors are aware that you are including the paper in your thesis. (Source: <http://www.rsc.org/AboutUs/Copyright/Permissionrequests.asp>)

Appendix C: Permission from Elsevier for Published Article

Published Articles:

- (1) Jian Liu, Xiangbo Meng, Yuhai Hu, Dongsheng Geng, Mohammad N. Banis, Mei Cai, Ruying Li, Xueliang Sun. Controlled synthesis of zirconium oxide on graphene nanosheets by atomic layer deposition and its growth mechanism. *Carbon* **2013**, *52*, 74-82.
- (2) Jian Liu, Xifei Li, Mei Cai, Ruying Li, Xueliang Sun. Ultrathin atomic layer deposited ZrO₂ coating to enhance the electrochemical performance of Li₄Ti₅O₁₂ as an anode material. *Electrochim. Acta* **2013**, *93*, 195-201.
- (3) Jian Liu, Xifei Li, Jinli Yang, Dongsheng Geng, Yongliang Li, Dongniu Wang, Ruying Li, Xueliang Sun, Mei Cai, Mark W. Verbrugge. *Electrochim. Acta* **2012**, *63*, 100-104.
- (4) Jian Liu, Hao Liu, Yong Zhang, Ruying Li, Guoxian Liang, Michel Gauthier, Xueliang Sun. Synthesis and characterization of phosphorus-nitrogen doped multiwalled carbon nanotubes. *Carbon* **2011**, *49*, 5014-5021.
- (5) Jian Liu, Yong Zhang, Mihnea I. Ionescu, Ruying Li, Xueliang Sun. Nitrogen-doped carbon nanotubes with tunable structure and high yield produced by ultrasonic spray pyrolysis. *Appl. Surf. Sci.* **2011**, *257*, 7837-7844.

Elsevier Authors' Rights

How authors can use their own journal articles

Authors publishing in Elsevier journals have wide rights to use their works for teaching and scholarly purposes without needing to seek permission.

Table of Authors' Rights

	Preprint version (with a few exceptions- see below *)	Accepted Author Manuscript	Published Journal Articles
Inclusion in a thesis or dissertation	Yes	Yes with full acknowledgement of final article	Yes with full acknowledgement of final article

(Source: <http://www.elsevier.com/authors/author-rights-and-responsibilities>)

Curriculum Vitae

Name: Jian Liu

Post-secondary Education and Degrees: Department of Mechanical and Materials Engineering
The University of Western Ontario, London, ON, Canada
2009-2013 Ph.D.

State Key Laboratory for Advanced Metals and Materials
University of Science and Technology Beijing, Beijing, P.R. China
2006-2009 Master.

Department of Materials Science and Technology
Sichuan University, Chengdu, P.R. China
2002-2006 B.E.Sc.

Honors and Awards: Western Engineering Scholarship
The University of Western Ontario, Canada
2010-2013

Chinese Government Award for Outstanding Self-financed
Students Abroad
2012

Related Work Experience Teaching Assistant
The University of Western Ontario
2010-2013

Publications:*(A) Peer-reviewed Journal Papers Based on This Thesis (First Author)*

1. **Jian Liu**, Yongji Tang, Biwei Xiao, Tsun-Kong Sham, Ruying Li, Xueliang Sun. Atomic layer deposited aluminium phosphate thin films on N-doped CNTs. *RSC Adv.* **2013**, 3, 4492-4495.
2. **Jian Liu**, Xiangbo Meng, Yuhai Hu, Dongsheng Geng, Mohammad N. Banis, Mei Cai, Ruying Li, Xueliang Sun. Controlled synthesis of zirconium oxide on graphene nanosheets by atomic layer deposition and its growth mechanism. *Carbon* **2013**, 52, 74-82.
3. **Jian Liu**, Xifei Li, Mei Cai, Ruying Li, Xueliang Sun. Ultrathin atomic layer deposited ZrO_2 coating to enhance the electrochemical performance of $Li_4Ti_5O_{12}$ as an anode material. *Electrochim. Acta* **2013**, 93, 195-201.
4. **Jian Liu**, Xiangbo Meng, Mohammad N. Banis, Mei Cai, Ruying Li, Xueliang Sun. Crystallinity-controlled synthesis of zirconium oxide thin films on nitrogen-doped carbon nanotubes by atomic layer deposition. *J. Phys. Chem. C* **2012**, 116, 14656-14664.
5. **Jian Liu**, Xifei Li, Jinli Yang, Dongsheng Geng, Yongliang Li, Dongniu Wang, Ruying Li, Xueliang Sun, Mei Cai, Mark W. Verbrugge, Microwave-assisted hydrothermal synthesis of nanostructured spinel $Li_4Ti_5O_{12}$ as anode materials for lithium ion batteries, *Electrochim. Acta* **2012**, 63, 100-104.
6. **Jian Liu**, Hao Liu, Yong Zhang, Ruying Li, Guoxian Liang, Michel Gauthier, Xueliang Sun. Synthesis and characterization of phosphorus-nitrogen doped multiwalled carbon nanotubes. *Carbon* **2011**, 49, 5014-5021.
7. **Jian Liu**, Yong Zhang, Mihnea I. Ionescu, Ruying Li, Xueliang Sun. Nitrogen-doped carbon nanotubes with tunable structure and high yield produced by ultrasonic spray pyrolysis. *Appl. Surf. Sci.* **2011**, 257, 7837-7844.

8. **Jian Liu**, Mohammad N. Banis, Xifei Li, Andrew Lushington, Mei Cai, Ruying Li, Tsun-Kong Sham, Xueliang Sun. Atomic layer deposition of lithium tantalate solid-state electrolytes. 2013, submitted.

(B) Peer-reviewed Journal Papers Related to This Thesis (Co-author)

9. Xiangbo Meng, **Jian Liu**, Xifei Li, Mohammad N. Banis, Jinli Yang, Ruying Li, Xueliang Sun. Atomic layer deposited $\text{Li}_4\text{Ti}_5\text{O}_{12}$ on nitrogen-doped carbon nanotubes. *RSC Adv.* **2013**, 3, 7285-7288.
10. Xifei Li, Xiangbo Meng, **Jian Liu**, Dongsheng Geng, Yong Zhang, Mohammad N. Banis, Yongliang Li, Jinli Yang, Ruying Li, Xueliang Sun, Mei Cai, Mark W. Verbrugge. Tin oxide with controlled morphology and crystallinity by atomic layer deposition on graphene nanosheets for enhanced lithium storage. *Adv. Funct. Mater.* **2012**, 22, 1647-1654.
11. Jinli Yang, Jiajun Wang, Xifei Li, Dongniu Wang, **Jian Liu**, Guoxian Liang, Michel Gauthier, Yongliang Li, Dongsheng Geng, Ruying Li, Xueliang Sun. Hierarchically porous LiFePO_4 /nitrogen-doped carbon nanotubes composite as a cathode for lithium ion batteries. *J. Mater. Chem.* **2012**, 22, 7537-7543.
12. Xifei Li, **Jian Liu**, Yong Zhang, Yongliang Li, Hao Liu, Xiangbo Meng, Jinli Yang, Dongsheng Geng, Dongniu Wang, Ruying Li, Xueliang Sun. High concentration nitrogen doped carbon nanotube anodes with superior Li^+ storage performance for lithium rechargeable battery application. *J. Power Sources* **2012**, 197, 238-245.
13. Yongliang Li, Jiajun Wang, Yong Zhang, Mohammad N. Banis, **Jian Liu**, Dongsheng Geng, Ruying Li, Xueliang Sun. Facile controlled synthesis and growth mechanisms of flower-like and tubular MnO_2 nanostructures by microwave-assisted hydrothermal method. *J. Colloid Interface Sci.* **2012**, 369, 123-128.

14. Xiangbo Meng, Dongsheng Geng, **Jian Liu**, Ruying Li, Xueliang Sun. Controllable synthesis of graphene-based titanium dioxide nanocomposites by atomic layer deposition. *Nanotechnology* **2011**, 22, 165602.
15. Yongliang Li, Jiajun Wang, Xifei Li, **Jian Liu**, Dongsheng Geng, Jinli Yang, Ruying Li, Xueliang Sun. Nitrogen-doped carbon nanotubes as cathode for lithium-air batteries. *Electrochem. Commun.* **2011**, 13, 668-672.
16. Dongsheng Geng, Songlan Yang, Yong Zhang, Jinli Yang, **Jian Liu**, Ruying Li, Tsun-Kong Sham, Xueliang Sun, Siyu Ye, Shanna Knights. Nitrogen doping effects on the structure of graphene. *Appl. Surf. Sci.* **2011**, 257, 9193-9198.
17. Xiangbo Meng, Dongsheng Geng, **Jian Liu**, Mohammad N. Banis, Yong Zhang, Ruying Li, Xueliang Sun. Non-aqueous approach to synthesize amorphous/crystalline metal oxide-graphene nanosheet hybrid composites. *J. Phys. Chem. C* **2010**, 114, 18330-18337.
18. Xifei Li, **Jian Liu**, Xiangbo Meng, Yongji Tang, Ruying Li, Mei Cai, Xueliang Sun. Significant impact on cathode performance of lithium-ion batteries by precisely controlled metal oxide coatings via atomic layer deposition. 2013, submitted.

(C) *Previous publications*

19. **Jian Liu**, Xiping Song, Pei Pei, Guoliang Chen. Hydrogen storage properties of Mg-50 vol.% V_{7.4}Zr_{7.4}Ti_{7.4}Ni composite prepared by spark plasma sintering. *Int. J. Hydrogen Energy* **2009**, 34, 4365-4370.
20. **Jian Liu**, Xiping Song, Pei Pei, Guoliang Chen. Hydrogen storage performance of Mg-based composites prepared by spark plasma sintering. *J. Alloys Compd.* **2009**, 486, 338-342.
21. Pei Pei, Xiping Song, **Jian Liu**, Anna Song, Peilong Zhang, Guoliang Chen. Study on the hydrogen desorption mechanism of a Mg-V composite prepared by SPS. *Int. J. Hydrogen Energy* **2012**, 37, 984-989.

22. Pei Pei, Xiping Song, **Jian Liu**, Ming Zhao, Guoliang Chen. Improving hydrogen storage properties of Laves Phase related BCC solid solution alloy by SPS preparation method. *Int. J. Hydrogen Energy* **2009**, *34*, 8597-8602.
23. Pei Pei, Xiping Song, **Jian Liu**, Guoliang Chen, Xiubo Qin, Baoyi Wang. The effect of rapid solidification on the microstructure and hydrogen storage properties of $V_{35}Ti_{25}Cr_{40}$ hydrogen storage alloy. *Int. J. Hydrogen Energy* **2009**, *34*, 8094-8100.
24. Xiping Song, Peilong Zhang, Pei Pei, **Jian Liu**, Rucheng Li, Guoliang Chen. The role of spark plasma sintering on the improvement of hydrogen storage properties of Mg-based composites. *Int. J. Hydrogen Energy* **2010**, *35*, 8080-8087.

(D) Conference presentation and abstracts

1. **Jian Liu**, Xifei Li, Xiangbo Meng, Yuhai Hu, Dongniu Wang, Ruying Li, Xueliang Sun. Atomic-layer-deposition synthesis of energy nanomaterials and their applications in lithium-ion batteries. **96th Canadian Chemistry Conference**, May 26-30, 2013, Quebec city, Quebec, Canada.
2. **Jian Liu**, Xifei Li, Mei Cai, Ruying Li, Xueliang Sun. Ultrathin atomic layer deposited ZrO_2 coating to enhance the electrochemical performance of $Li_4Ti_5O_{12}$ as an anode material. **223rd ECS Meeting**, May 12-16, 2013, Toronto, Canada.
3. **Jian Liu**, Xifei Li, Xiangbo Meng, Dongsheng Geng, Yuhai Hu, Ruying Li, Xueliang Sun. Atomic layer deposition synthesis of energy nanomaterials and their applications in lithium-ion batteries. **CAMBR (The Center for Advanced Materials and Biomaterials Research), Distinguished Lecturer and Reserach DAY**, Nov. 13th, 2012, London, ON, Canada.
4. **Jian Liu**, Xifei Li, Ruying Li, Xueliang Sun. A new technique – atomic layer deposition and its applications in lithium-ion batteries for EVs and HEVs. **3rd Annual NANO ONTARIO Conference**, Oct. 11-12, 2012, Waterloo, ON, Canada.

5. **Jian Liu**, Xifei Li, Xiangbo Meng, Dongsheng Geng, Mohammad N. Banis, Yuhai Hu, Ruying Li, Xueliang Sun. Atomic-layer-deposition synthesis of energy nanomaterials and their applications in lithium-ion batteries. *24th Canadian Materials Science Conference*, June 5-8, 2012, London, ON, Canada.
6. **Jian Liu**, Xifei Li, Liang Li, Ruying Li, Mei Cai, Xueliang Sun. Novel nanostructured $\text{Li}_4\text{Ti}_5\text{O}_{12}$ as anode materials for lithium-ion battery applications. *16th International Meeting on Lithium Batteries*. June 17-22, 2012, Jeju, Korea.
7. **Jian Liu**, Xifei Li, Xiangbo Meng, Dongsheng Geng, Mohammad N. Banis, Yuhai Hu, Ruying Li, Xueliang Sun. Atomic-layer-deposition synthesis of energy nanomaterials and their applications in lithium-ion batteries. *12th International Conference on Atomic Layer Deposition*. June 17-20, 2012, Dresden, Germany.
8. **Jian Liu**, Xueliang Sun. Crystallinity-controlled coating of ZrO_2 and Co_3O_4 on carbon nanotubes by atomic layer deposition. *61st Canadian Chemical Engineering Conference*. Oct. 23-26, 2011, London, ON, Canada.
9. **Jian Liu**, Xiangbo Meng, Xifei Li, Mohammad N. Banis, Ruying Li, Xueliang Sun. Atomic layer deposition of crystalline/amorphous cobalt oxide on nitrogen-doped carbon nanotubes and application in lithium ion batteries. *11th International Conference on Atomic Layer Deposition*. June 26-29, 2011, Cambridge, Massachusetts, USA.